UNIVERSITY OF LONDON THESIS

Degree PhD Year 2006 Name of Author BENLACHTAR Yannis

UCL DEPARTMENT OF ELECTRONIC
& ELECTRICAL ENGINEERING

UCL

Advanced Performance Monitoring in All-Optical Networks

Yannis Benlachtar

A thesis submitted to the University of London for the degree of
Doctor of Philosophy (Ph.D.)

Department of Electronic and Electrical Engineering
University College London
January 2006

ProQuest LLC
789 East Eisenhower Parkway
P.O. Box 1346
Ann Arbor, MI 48106-1346

"God is the Light of the heavens and the earth. The similitude of His light is as a niche wherein is a lamp. The lamp is in a glass. The glass is as it were a shining star. (This lamp is) kindled from a blessed tree, an olive neither of the East nor of the West, whose oil would almost glow forth (of itself) though no fire touched it. Light upon light. God guideth unto His light whom He will. And God speaketh to mankind in allegories, for God is Knower of all things" Quran [24:35]

To my mother

Abstract

This thesis investigates advanced optical performance monitoring approaches for future all-optical networks using the synchronous sampling technique. This allows for improved signal quality estimation, fault management and resource allocation through improved control of transmission at the physical layer level.

Because of the increased transparency in next generation networks, it is not possible to verify the quality of the signal at each node because of the limited number of optical-electrical-optical conversions, and therefore new non-intrusive mechanisms to achieve signal quality monitoring are needed. The synchronous sampling technique can be deployed to estimate the bit error rate, considered an important quality measure, and hence can be utilised to certify service level agreements between operators and customers. This method also has fault identification capabilities by analysing the shapes of the obtained histograms. Each impairment affects the histogram in a specific way, giving it a unique shape that can be used for root cause analysis. However, chromatic dispersion and polarisation mode dispersion (PMD) can have similar signatures on the histograms obtained at decision times. A novel technique to unambiguously discriminate between these two sources of degradation is proposed in this work. It consists of varying the decision times so that sampling also occurs at both edges of the eye diagram. This approach is referred to as three-section eye sampling technique. In addition, it is shown that this method can be used to accurately assess first order polarisation mode dispersion and can simultaneously estimate the differential group delay (DGD) and the power splitting ratio between the two states of polarisation. Since synchronous sampling is employed, the effect of PMD on the sampling times is also investigated. For the first time, closed form relationship between the shift in sampling time, the DGD and the power splitting ratio between the polarisation states is obtained. Three types of high-Q filter based clock recovery circuits are considered: without pre-processing circuits that can be used for RZ format and with an edge detector or a squarer pre-processing circuits suitable for NRZ format. Moreover, this technique can be used to monitor chromatic dispersion and a large monitoring range of more than 1750ps/nm is experimentally demonstrated at 10Gbit/s. Since it can monitor PMD and dispersion, this method can be deployed to control dynamic PMD or dispersion compensators. Furthermore, this technique offers easy and quick inline eye mask testing and timing jitter assessment.

Acknowledgements

First I would like to express my gratitude to my supervisors and acknowledge their contributions to for the successful completion of this work. I am eternally grateful to my direct supervisor Dr. Robert Killey for giving me the possibility of conducting this research and providing me with invaluable help and encouragement. His friendliness, in-depth knowledge of the subject and personal commitment have been inspirational for the good progress of my thesis. I benefited greatly from his constant guidance and suggestions and it has been a great pleasure to work under his supervision. I am also indebted to my co-supervisor Prof. Polina Bayvel for her feedback and constructive advice. She has always been a source of guidance and motivation and I will always be grateful for that. Last but not least, I am very thankful for the help and assistance of my industrial supervisor Alan McGuire. I benefited greatly from his knowledge and his pragmatic suggestions and solutions.

I am deeply grateful to BT in Martlesham (Ipswich) for funding my PhD studentship. I also would like to thank all the people in the Polaris building (BT) for making my internship enjoyable and fruitful. In particular, I thank Mark Scopes for his invaluable help, encouragement and continuous feedback. I would also like to thank Shehzad Mirza and Sergio Inglima for their help and assistance.

Special thanks go to Dr. Benn Thomsen and Dr. Seb Savory for their help with some of the analytical work of chapter 6 and Dr. Vitaly Mikhailov for his experimental advice in the laboratory. I am also very grateful to Giancarlo G. Gavioli for presenting my work at several conferences

I owe a lot of gratitude to my "second family", my colleagues of the Optical Networks Group and the Ultrafast Photonics Group in room 808 for creating such an amazing atmosphere for work and fun. We shared so many unforgettable moments in and outside the office (e.g. beating the Italian team in football 9 times out of 10...) and that made all the difference to beat the weather and the PhD blues.

Finally, I can never thank my family enough, especially my mother and "Tonton" Abdellali Blikaz, for everything they have done for me. God bless them all.

Table of Contents

Abstract 2

Acknowledgements 3

Chapter 1 Introduction 7

Chapter 2 Theory 14

2.1 Introduction 14

2.2 Theory of Impairments 14

2.2.1 Distortion 14

2.2.2 Noise 33

2.3 Measurement of System Performance 38

2.3.1 Q-Factor 38

2.3.2 Bit Error Rate 39

2.3.3 Eye Closure Penalty 40

2.4 Summary 42

Chapter 3 Literature Review 43

3.1 Introduction 43

3.2 OPM Application 44

3.2.1 Operator Handover 44

3.2.2 Protection and Restoration 45

3.2.3 Impairment-based Routing 46

3.2.4 Fault Management 47

3.3 OPM Reference Model 48

3.4 Optical Performance Monitoring Techniques 49

3.4.1 Spectral Methods 51

3.4.2 Sampling Methods 65

3.5 Summary 82

Chapter 4 Synchronous Sampling Technique for Performance Monitoring 83

4.1 Introduction 83

4.2 Monitoring Circuit 84
4.3 Impairment Signatures on Synchronously Obtained Histograms 84
4.3.1 Crosstalk Signature on Histograms 84
4.3.2 Dispersion Signature on the Histograms 89
4.3.3 PMD Signature on the Histograms 91
4.4 Investigation of the Sampling Technique to Monitor a WDM System 94
4.4.1 ASE Noise Experiment 96
4.4.2 Laser Drift Experiment 100
4.4.3 Summary and Conclusions 102
4.5 Histogram Method to Estimate Gaussian Noise Using Deconvolution 103
4.5.1 Deconvolution Algorithm 103
4.5.2 Numerical Simulation 106
4.5.3 Experimental validation 109
4.6 Summary 112

Chapter 5 PMD Effects on the Clock Recovery 113

5.1 Introduction and Problem Formulation 113
5.2 Clock Recovery Circuits 114
5.2.1 High-Q Filter 115
5.2.2 Phase-Lock Loop (PLL) 116
5.3 The Effect of PMD on the Sampling Time 117
5.3.1 The System and PMD Model 117
5.3.2 No Pre-processing Circuit 117
5.3.3 Using a Squarer 121
5.3.4 Using an Edge Detector 126
5.4 Summary 135

Chapter 6 Three-Section Eye Sampling Technique 137

6.1 Introduction 137
6.2 The System and PMD Model 138
6.3 Three-section Eye Diagram Sampling Technique 139
6.3.1 Concept 139
6.3.2 Eye Reconstruction 140

6.3.3 Sampling Circuit Configuration *143*
6.4 First-Order PMD Monitoring 144
6.4.1 Concept *145*
6.4.2 Simulation Results *148*
6.4.3 Experimental Validation *152*
6.5 Chromatic Dispersion Monitoring 158
6.5.1 Concept *159*
6.5.2 Theoretical Results *162*
6.5.3 Experimental Validation *166*
6.6 Potential Utilisation of the Three-Point Sampling Technique 171
6.6.1 Inline Mask Measurement *171*
6.6.2 Inline Transmitter Monitoring *173*
6.7 Summary 175

Chapter 7 Summary and conclusions 177

Chapter 8 Appendices 182

8.1 Appendix 1: Digital Performance Monitoring 182
8.2 Appendix 2: PMD Effects on Clock Recovery Modules without Pre-processing Circuits 187
8.3 Appendix 3: PMD Effects on Clock Recovery Modules with Squarer Pre-processing Circuits 190
8.4 Appendix 4: PMD Effects on Clock Recovery Modules with Edge Detection Pre-processing Circuits 196
8.5 Appendix 5: Hyperbolic Tangent Approximation 203
8.6 Appendix 6: Split-Step Fourier Algorithm 206
8.7 Appendix 7: Relationship between the BER and Noise Figure of EDFAs 208
8.8 Appendix 8: Glossary 210

Chapter 9 References 212

Chapter 1 Introduction

In the last few years, there has been a considerable increase in demand for higher bandwidth and more reliable data and voice services. This growth in demand will be further accentuated with the introduction of next generation services such as TV over broadband and on-demand entertainment (videos, film, music ...etc). At present, access networks are keeping the gigabit per second core/metro transmission rates away from the end users because the "last mile" connection to premises is achieved using some form of digital subscriber loop (DSL) which provides only a few megabit per second connection over the copper wires. However this bottleneck is gradually removed by slowly replacing the copper wires by fibre optic cables, a process that will ultimately lead to a substantial increase in demand for more bandwidth in the core network. The expected deployment of fibre to the premises over the next few years is shown in Figure 1.1. In addition, traditionally only large corporations could afford to own or lease a fibre that directly connects them to the network of the service provider but this fibre to the business connectivity is gradually making its way to smaller and smaller businesses [Gre'01]. This anticipated explosion in bandwidth demand is certainly beneficial for operators and service providers who witnessed a decline in traditional fixed telephony revenues. However, augmenting the network capacity comes with an increased cost that customers are unwilling to share since they are not prepared to pay significantly more for a higher bandwidth [Dav'02]. This sees network operators with almost flat revenues and higher expenditure. This burden dictates novel methods of increasing the network capacity while lowering the cost per unit of bandwidth by up to a factor of 10 [Dav'02].

There are two possible approaches to enlarge network capacity: increase the bitrate and/or increase the number of wavelengths. Most of the core/backhaul networks are already operating at either 2.5Gbit/s or 10Gbit/s and upgrading them to 40Gbit/s is currently impractical because the technology is still immature. In addition, increasing the bitrate by a factor of 4 will lead to a cost increase by a factor of 2.5 [Dav'02]. A more realistic approach in achieving higher capacity is to migrate to dense WDM systems. This results in installing more transponders and hence the cost will increase proportionally with the number of wavelengths. Although the capacity will rise, this approach will fall short of providing the drastic cost reduction needed for the viability

of such investments. Unless transponder prices fall sharply, the only possible solution is to move to truly transparent photonic networks. A substantial decline in the prices of network equipment is highly unlikely since electronic-based products have a learning curve of 70 to 80% [Dav'05]. In other words, the unit price of such equipment drops by 70 to 80% for every doubling of cumulative production volume. Therefore, the only remaining realistic solution is to reduce the number of optical-electrical-optical (OEO) conversions and implement transparent all-optical networks. It was recently suggested to bypass the WDM metro nodes and connect the photonic core network with the customers via long reach passive optical networks (LR-PON) [Hor'05]. The metro equipment is replaced by simpler nodes consisting of optical amplifiers and power splitters.

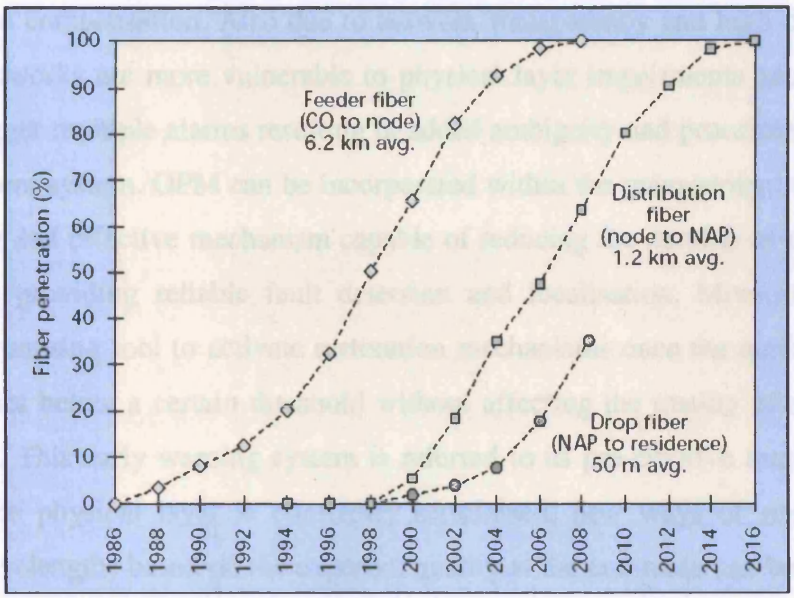

Figure 1.1 Expected deployment of fibre to the premises [Gre'01]. CO: central office; NAP: network access point

While the advantages of moving to more transparent and higher bitrate networks are attractive, tighter constraints are placed on the transmission margins and engineering rules that govern network design nowadays. Added complexities such as dynamic link reconfiguration, fault localisation and restoration have to be addressed. Current networks are based on simple linear engineering rules and heavily rely on the design and the allocated margins to provide an acceptable service quality. The signal quality is verified by ensuring that different network elements are functioning properly. This is achieved by means of indirect indicators such as drive currents, power loss, over temperature and frequency drift. This is no longer valid for future all-optical networks and more sophisticated monitoring and diagnosis tools are needed. Optical

performance monitoring (OPM) is the enabling technology to improve the control and management of next generation optical networks.

Because of the increased transparency, it is impossible to verify the quality of the signal at each node in the network and hence new non-intrusive mechanisms are required. OPM can be initially utilised to certify the service level agreement (SLA) between the provider and the customer, traditionally achieved by means of digital methods such as bit-interleaved parity (BIP) checking in SONET/SDH. Additionally, If OPM can monitor physical signal impairments, it can therefore be used for dynamic distortion compensation or regeneration. As most systems are upgraded to operate at 10Gbit/s, impairments such as polarisation mode dispersion (PMD) are best handled through active compensation. Also due to network transparency and high data rates, all-optical networks are more vulnerable to physical layer impairments and a single fault may trigger multiple alarms resulting in added ambiguity and processing time of the management system. OPM can be incorporated within the management system to achieve a fast and effective mechanism capable of reducing the number of redundant alarms while providing reliable fault detection and localisation. Moreover, OPM could be a promising tool to activate restoration mechanisms once the quality of the signal degrades below a certain threshold without affecting the quality of service at the end node. This early warning system is referred to as pre-emptive maintenance. Finally, as the physical layer is constantly scrutinised, new ways of routing and allocating wavelengths based on the expected quality at the end-node can be obtained (impairment-based routing). For example, high-priority traffic can be dynamically routed through high-quality optical channels.

The goal of this work is to investigate optical performance monitoring methods that can be deployed in next generation all-optical networks and examine the techniques that best satisfy the abovementioned expectations. More precisely, we will be considering OPM using synchronous sampling monitoring approach. We will demonstrate that this technique can be utilised for signal quality measurement (BER/Q-factor), fault identification and assessment of PMD and chromatic dispersion.

Overview of the thesis

Since this work deals with performance monitoring, some of the root causes of signal degradation are examined in **chapter 2**. Optical impairments are divided into two categories: noise and distortion. Noise includes transmitter noise, receiver noise and amplified spontaneous emission noise generated by optical amplifiers. Distortion on the other hand, contains effects such as fibre dispersion, nonlinearities, crosstalk and polarisation-mode dispersion (PMD). This is not an exhaustive list of impairments but it represents the dominant effects reported in the literature. Different impairments introduce different anomalies in the network and it is crucial to comprehend how they, either individually or collectively, affect the optical channels and hence how they influence the performance monitoring techniques. Finally, various techniques for characterising and quantifying of signal quality and system performance are presented. These include metrics such as the Q-factor, the bit error rate (BER) and eye closure penalty.

Chapter 3 provides an overview of the various techniques of optical performance monitoring (OPM) for WDM networks proposed in the literature. It starts by reviewing the multiple applications of OPM that will empower the control and management of future all-optical networks. Applications such as quality monitoring, service handover, fault management, restoration and routing and wavelength assignment can potentially be provided by OPM methods. These techniques are divided into two main groups: spectral methods and sampling methods. Spectral methods are further subdivided into optical and electrical spectrum techniques. Similarly, the sampling approach is subdivided into synchronous and asynchronous methods. The advantages and limitations of each technique are also discussed.

The synchronous sampling monitoring technique is investigated in **chapter 4**. We begin by examining the patterns of different impairments such as crosstalk, chromatic dispersion and polarisation mode dispersion (PMD) on the sampled histograms. Each source of degradation has a special signature that can be used to identify and localise the faults in the network. The accuracy of this technique in determining the health of a network is then verified on a commercial WDM system. Two impairments, amplified spontaneous emission (ASE) noise and in-band crosstalk, are introduced in a network

operating with different protocols including Gigabit Ethernet, fibre channel and (2.5Gbit/s) SONET/SDH. The performance of the sampling method is assessed and compared to the built-in digital methods. Finally a histogram deconvolution method that can be applied to evaluate the Gaussian noise without prior knowledge of the transmission path is introduced. This can be used to separate the contribution of distortion from the contribution of noise.

Since this work deals with synchronous sampling, the effect of PMD on the clock recovery and thus on decision time has to be characterised. The PMD-induced phase shift of sampling time is investigated in **chapter 5**. Closed form relationships between the shift in sampling time, the differential group delay (DGD) and the power splitting ratio between the principal states of polarisation are obtained for different clock and data recovery (CDR) circuit configurations. The high-Q filter based clock configurations considered include CDR without a pre-processing circuit and CDR with a squarer and edge detector pre-processing circuits.

In **chapter 6**, a novel sampling method which consists of taking the histogram at three different sections of the eye diagram is introduced. Using the obtained histograms, PMD signature on the eye can be detected and unambiguously discriminated from the effects of chromatic dispersion. In addition, this approach allows the assessment of PMD and chromatic dispersion. Both the DGD and the state of polarisation of the signal and the residual chromatic dispersion can be accurately estimated. As a result, this technique can also be deployed for active compensation or regeneration. Finally, other useful applications such as inline eye mask testing and timing jitter evaluation are outlined.

List of Publications

1. Y. Benlachtar, R. I. Killey and P. Bayvel "The Effects of Polarization-Mode Dispersion on the Phase of the Recovered Clock", to be published in the IEEE Journal of Lightwave Technology, November 2006

2. Y. Benlachtar, R. I. Killey and P. Bayvel "Chromatic Dispersion Monitoring Using Synchronous Sampling", IEEE Optical Fiber Communications Conference (OFC) 05-10 March 2006, California, OWK4

3. Y. Benlachtar, R. I. Killey and P. Bayvel "Effects of first-order polarisation-mode dispersion on clock recovery", IEE Electronics Letters, October 2005, Volume 41, Issue 21, pp: 1190-1192

4. Y. Benlachtar, R. I. Killey and P. Bayvel "Experimental Investigation of Three-Point Sampling Technique for the Estimation of First Order PMD", European Conference on Optical Communications (ECOC), 25-29 September 2005, Glasgow, We4.P.100

5. Y. Benlachtar, M. Scopes, R. I. Killey and P. Bayvel "Novel Eye Monitoring Technique for Detection of First Order PMD", IEEE Conference on Lasers and Electro-Optics (CLEO/QELS) 2005 in Baltimore. JThE77. May 22 - May 27, 2005

6. Y. Benlachtar, R. I. Killey and P. Bayvel "Novel Three-Point Sampling Technique for Detection of First Order PMD", e-Photon ONe Winter School on Optical Core Network Technologies, Aveiro, 23-25 February 2005. Portugal

7. Y. Benlachtar, R. I. Killey and P. Bayvel "Experimental Investigation of a Deconvolution Technique for Identification of Channel Impairment", IEEE Lasers and Electro-Optics Society (LEOS) 2003.Volume: 1, pp:146 - 147 vol.1, 2003

8. Y. Benlachtar, R. I. Killey and P. Bayvel "Novel Histogram Method for Estimating Gaussian White Noise in Optical Channels and Its Application in Identifying

Different Sources of Degradation", Postgraduate Research Conference in Electronics, Photonics, Communications and Software (PREP2003), 14-16 April 2003, Exeter University, UK

9. Y. Benlachtar, R. I. Killey and P. Bayvel "Identification of Sources of Degradation in Optical Channels Using Deconvolution Technique", IEEE Optical Fiber Communications Conference 2003 (OFC), vol.1, pp:109 – 110, 23-28 March 2003, Atlanta, USA

Chapter 2 Theory

2.1 Introduction

This chapter mainly covers the fundamentals of signal degradation during transmission and its impact on the detected data. Optical channels are affected by two types of impairments: noise and distortion. Noise includes transmitter noise, receiver noise and amplified spontaneous emission noise generated by optical amplifiers. Distortion contains effects such as fibre dispersion, nonlinearities, Kerr effects, crosstalk and polarisation-mode dispersion (PMD). These two types of impairment have different origins and different effects, and the way in which they limit system performance is discussed in section 2.2. Section 2.3 considers the various techniques for the characterisation and quantisation of signal quality and system performance.

2.2 Theory of Impairments

Optical channels are affected by two types of degradation: noise and distortion. The first part of this section deals with distortion which includes fibre dispersion, self-phase modulation, crosstalk and polarisation-mode dispersion (PMD). The second subsection introduces the three main sources of noise: transmitter noise, receiver noise and amplified spontaneous emission noise generated by optical amplifiers.

2.2.1 Distortion

2.2.1.1 Dispersion

Fibre dispersion originates from the fact that the refractive index of the fibre is frequency dependent. This causes different wavelengths (frequencies) to travel at different velocities leading to pulse broadening and thus to inter-symbol interference (ISI). We will consider in this section two different but complementary approaches to describe this broadening: a *phenomenological* approach that assumes that the spectral width is dominated by the optical source and a *pulse shape* approach which relies on the width and the shape of the input waveform

a) Phenomenological approach

The optical source in a high-speed communication system is typically a single-mode diode laser with non-zero spectral width. The latter is increased by modulating the signal pulse. In single mode fibre, the group velocity associated with the fundamental

mode is frequency dependent. As a result, different spectral components of the pulse travel at slightly different speeds leading to pulse broadening, a phenomenon referred to as group velocity dispersion, intramodal dispersion or simply fibre dispersion. Assuming $\Delta\omega$ is the spectral width of a pulse going through a fibre of length L. The different spectral components arriving at different times at the fibre output result in pulse broadening given by:

$$\Delta T = L\beta_2\Delta\omega \tag{2.1}$$

The parameter β_2 is known as the group velocity dispersion (GVD) parameter. The spectral width can also be represented by the range of wavelengths $\Delta\lambda$ emitted by the optical source. In this case, the equation given above can be rewritten as:

$$\Delta T = DL\Delta\lambda \tag{2.2}$$

where

$$D = -\frac{2\pi c}{\lambda^2}\beta_2 \tag{2.3}$$

D is the dispersion parameter and is expressed in units of ps/(nm.km). Notice that when β_2 is positive D is negative which is referred to as normal dispersion. Conversely when β_2 is negative, D is positive and is referred to as anomalous dispersion. There are two underlying effects that contribute to fibre dispersion: material dispersion and waveguide dispersion. D can be written as the sum of these two parameters i.e. $D = D_M + D_W$ where D_M is the material dispersion coefficient and D_W is the waveguide dispersion coefficient.

Material dispersion results from the nonlinear dependence of the refractive index (n) with respect to the wavelength in doped silica as shown in Figure 2.1. It is related to the characteristic resonance frequencies at which the material absorbs the electromagnetic radiation. The group index n_g defined by $n_g = n + \omega(dn/d\omega)$ is also shown.

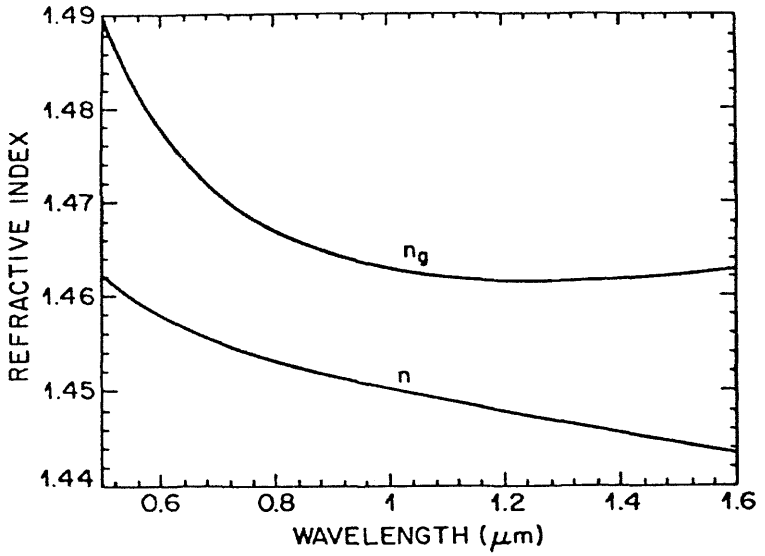

Figure 2.1 Variation of refractive index n and group index n_g with wavelength for fused silica [Agr'02]

D_M is related to the slope of n_g and is defined as [Agr'02]:

$$D_M = \frac{1}{c}\frac{dn_g}{d\lambda} \tag{2.4}$$

Waveguide dispersion is rooted in the wavelength-dependent relationships of the group velocity to the core diameter and the difference in index between the core and the cladding. The contribution of the waveguide dispersion D_W to the dispersion parameter D is given by [Agr'02]:

$$D_W = -\frac{2\pi\Delta}{\lambda^2}\left[\frac{n_{2g}^2}{n_2\omega}\frac{Vd^2(Vb)}{dV^2} + \frac{dn_{2g}}{d\omega}\frac{d(Vb)}{dV}\right] \tag{2.5}$$

where n_{2g} is the group index of the cladding material, V is the normalised frequency and b is the normalised propagation constant. Unlike D_M, D_W is negative in the entire wavelength range 0-1.6 μm. Figure 2.2 shows D_M, D_W and their sum D for a typical single-mode fibre. Dispersion is almost zero at wavelengths near 1300 nm in single mode fibre where the two mechanisms, material dispersion and waveguide dispersion, cancel one another. The zero-dispersion region can be shifted to longer wavelengths by using this combination between material and waveguide dispersion. This is achieved by controlling the core radius, the core-cladding index difference and the refractive index profile. In dispersion shifted fibre (DSF) the zero-dispersion wavelength is set to approximately 1550 nm.

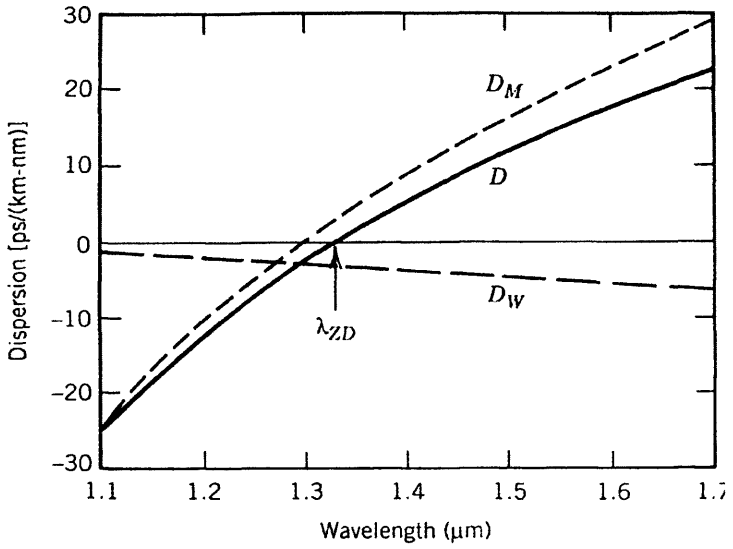

Figure 2.2 Total dispersion D and contributions D_M, D_W for a conventional single-mode fibre [Agr'02]

Pulse Shape Approach

In this approach we assume that pulse broadening depends on the width and the shape of the input waveform and will be estimated using the pulse Fourier spectrum. The basic propagation equation that governs pulse evolution inside a single mode fibre is given by the nonlinear Schrödinger (NLS) equation defined as [Agr'01]:

$$i\frac{\partial A}{\partial z}+\frac{i\alpha}{2}A-\frac{\beta_2}{2}\frac{\partial^2 A}{\partial T^2}+\gamma|A|^2A=0 \tag{2.6}$$

where a frame of reference moving with the pulse at group velocity v_g is used. α is the signal attenuation due to fibre loss, β_2 the group velocity dispersion parameter and γ is the nonlinear coefficient. In the case of the pulse evolving in a purely dispersive medium (i.e. $\gamma = 0$ and $\alpha = 0$) the NLSE becomes:

$$i\frac{\partial A}{\partial z}=\frac{\beta_2}{2}\frac{\partial^2 A}{\partial T^2} \tag{2.7}$$

This equation is solved by using the Fourier transform method whose general solution is given by:

$$\tilde{A}(z,\omega)=\tilde{A}(0,\omega).\exp\left(\frac{i}{2}\beta_2\omega^2 z\right) \tag{2.8}$$

where $\tilde{A}$ is the Fourier transform of A. Alternatively the above equation can be rewritten in the time domain as:

$$A(z,T) = \Im^{-1}\left\{\tilde{A}(0,\omega).\exp\left(\frac{i}{2}\beta_2\omega^2 z\right)\right\} \tag{2.9}$$

where $\Im^{-1}$ represents the inverse Fourier transforms. The above equation shows that GVD changes the phase of each spectral component differently (frequency dependent) and even though it does not alter the pulse spectrum, it may modify the pulse shape. Consider an example of a Gaussian pulse with the optical field given by:

$$A(0,T) = \exp\left(-\frac{T^2}{2T_0^2}\right) \tag{2.10}$$

where T_0 is the half-width at 1/e intensity point. Carrying out the transformations in equation 2.9, the optical amplitude at any distance z along the fibre can be shown to be:

$$A(z,T) = \frac{T_0}{\sqrt{T_0^2 - i\beta_2 z}}\exp\left(-\frac{T^2}{2(T_0^2 - i\beta_2 z)}\right) \tag{2.11}$$

It can be seen that the Gaussian pulse maintains its shape but its width T_z increases to:

$$T_z = T_0\sqrt{1+\left(\frac{z}{L_D}\right)^2} \tag{2.12}$$

where $L_D = \frac{T_0^2}{|\beta_2|}$ is the dispersion length. Figure 2.3 illustrates how a Gaussian pulse broadens inside a fibre as a function of the dispersion length.

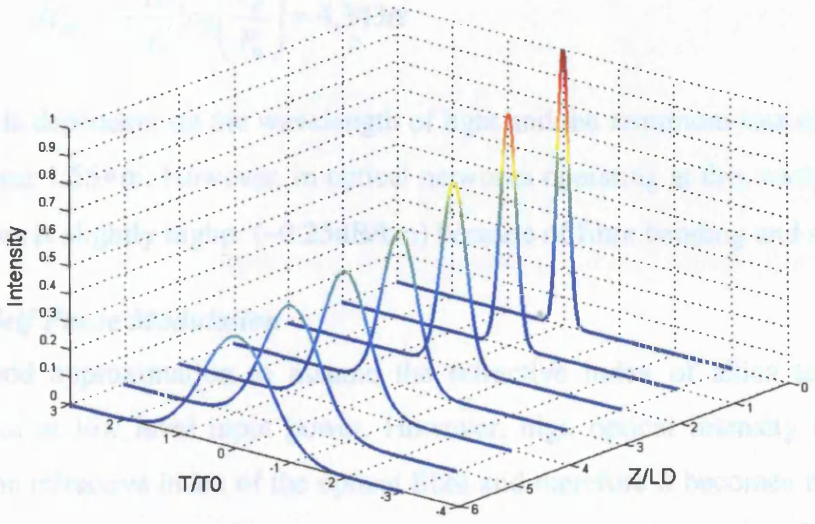

Figure 2.3 Dispersion-induced broadening of a Gaussian-shaped pulse

Dispersion limits the distance over which the signal can be detected error free and this is described by the dispersion limit factor D_{lim} in ps/nm. The approximate dispersion limit in a non-return to zero (NRZ) signal generated by a chirp-free external modulator is given by [Ber'02]:

$$D_{\text{lim}}(ps/nm) \approx \frac{104000}{B^2} \tag{2.13}$$

where B is the bitrate in Gbit/s. Hence in a 10Gbit/s system, residual dispersion should be kept below 1040ps/nm, equivalent to approximately 61km of single mode fibre (SMF). This limit changes with the square of the bitrate and becomes only 65ps/nm (~3.8km of SMF) at 40Gbit/s. This value is even smaller for signals with larger optical bandwidth such as return-to-zero (RZ) and directly modulated signals.

In equation 2.7 the effect of fibre loss was ignored. Although it does not affect the above analysis, fibre loss indirectly contributes to the degradation of an optical signal through optical amplifiers. These are periodically used in optical networks to compensate for signal attenuation in order to meet the minimum required sensitivity of the deployed receivers. Fibre loss which is caused mainly by material absorption and Rayleigh scattering, can be described by the following equation:

$$P_{out} = P_{in}\exp(-\alpha L) \tag{2.14}$$

where P_{in} is the input power, L the fibre length and α is the attenuation constant. It is customary however to express α in units of dB/km and it is related to the linear α by:

$$\alpha_{dB} = -\frac{10}{L}\log\left(\frac{P_T}{P_0}\right) = 4.343\alpha \tag{2.15}$$

Fibre loss is dependent on the wavelength of light and the minimum loss of 0.2dB/km is found near 1.55•m. However, in optical networks operating at this wavelength, the average loss is slightly higher (~0.25dB/km) because of fibre bending and splicing

2.2.1.2 Self Phase Modulation

It is a good approximation to assume the refractive index of silica to be power independent at low level input power. However, high optical intensity temporarily changes the refractive index of the optical fibre and therefore it becomes necessary to include a non-linear contribution so that the new refractive index is given by [Agr'97]:

$$n_j' = n_j + \bar{n}_2(P/A_{eff}) \quad , j=1, 2 \tag{2.16}$$

where j=1 refers to the core and j=2 refers the cladding, n_j is the linear index coefficients and $\bar{n}_2$ is the non-linear index coefficient (approx. 2.3 10^{-20} m^2/W). Because of this nonlinear property, a high intensity pulse leads to a time-changing index which causes a self-induced phase modulation of the input pulse. This phenomenon is called self phase modulation (SPM) since the phase shift Φ_{NL} is induced by the optical field itself. The maximum nonlinear phase shift is governed by [Agr'97]:

$$\Phi_{NL} = \gamma P_{in} L_{eff} \tag{2.17}$$

where L_{eff} is the effective interaction length given by $L_{eff} = [1-\exp(-\alpha L)]/\alpha$ (α is the attenuation coefficient) and $\gamma = k_0\bar{n}_2/A_{eff}$ (typically ~ $1W^{-1}km^{-1}$). A_{eff} is the effective mode cross section, also referred to as the effective core area. Going back to the NLSE given in equation 2.6 and setting $\beta_2 = 0$, the output pulse affected by SPM is found to be [Agr'01]:

$$A(L,T) = A(0,T).\exp\left(i\phi_{NL}(L,T)\right) \tag{2.18}$$

and

$$\phi_{NL}(L,T) = \left|A(0,T)\right|^2\left(L_{eff}/L_{NL}\right) \tag{2.19}$$

The nonlinear length is defined as $L_{NL} = (\gamma P_0)$. Equation 2.18 shows that SPM induces an intensity-dependent phase shift but does not alter the pulse shape.

SPM causes the generation of new optical frequencies resulting in a spectral broadening of the pulse propagating through the fibre. These frequencies are generated on the rising and the falling edges of the pulse where the rate of change in the intensity is the highest as shown in Figure 2.4. The bandwidth of the newly generated frequencies is proportional to the product of the nonlinear coefficient and the time derivative of the optical intensity.

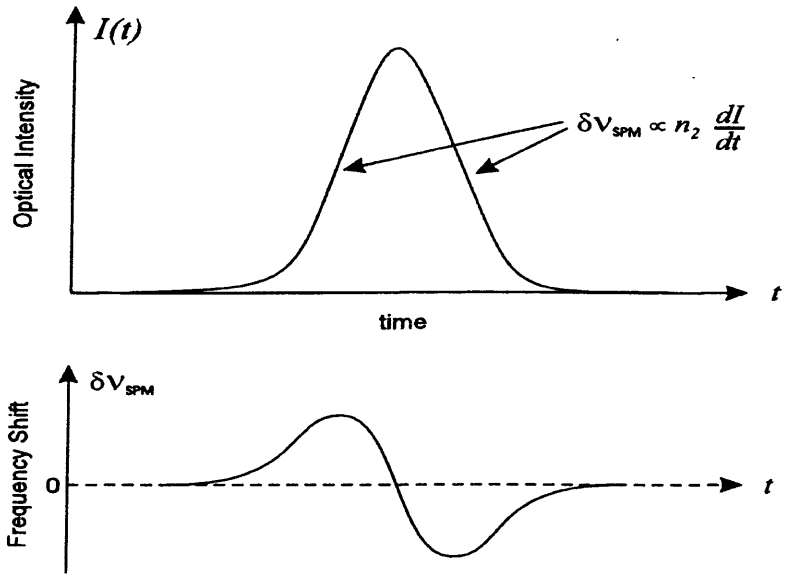

Figure 2.4 SPM generates new frequencies at the rising and falling edges of the pulse [Der'98]

SPM can be a serious limiting factor for optical communication systems although it can be used in soliton based systems to counteract the effects of dispersion. The critical power is the power that causes the optical spectrum of the pulse to double in width due to nonlinear frequency generation. Since it depends on the interaction length along the fibre, it is convenient to express the SPM limit as a power-length product and can be approximated by [Der'98]:

$$P_{cr} L_{eff} \cong \frac{\lambda A_{eff}}{\pi n_2} \tag{2.20}$$

P_{cr} is the critical peak pulse power. For a standard telecommunication fibre the power-length product is equal to 1.5W.km (λ=1.55μm, A_{eff}= 70μm, n_2=2.3 10^{-20} m^2/W). The effective length can be limited by either fibre dispersion or fibre attenuation.

Generally SPM and GVD act simultaneously on the travelling signal and their combined effect depends on the dispersion sign. In the normal dispersion regime (D<0), their effects lead to an enhancement in the rate of the pulse broadening compared with GVD alone. This is explained by the fact that SPM generates new frequency components that travel at different speeds resulting in an acceleration of pulse broadening. In the anomalous dispersion regime (D>0) however, the pulse broadening progresses at a much lower pace than in the absence of SPM because the two phenomena produce opposite chirps. As a consequence, GVD and SPM cancel each other out.

The intensity dependence of the refractive index causes another nonlinear distortion in WDM systems named cross phase modulation (XPM). This occurs when multiple signals are multiplexed together and the intensity changes in one signal cause phase or frequency modulation in another channel. The nonlinear phase shift not only depends on the power of that channel but also on the power of other channels. The phase shift for the jth channel is given by [Agr'97]:

$$\Phi_j^{NL} = \gamma L_{eff}\left(P_j + 2\sum_{m\neq j}^{M} P_m\right) \tag{2.21}$$

M is the total number of channels and P_j is the power at the jth channel. The factor 2 in the above equation indicates that XPM is twice as effective as SPM for the same amount of power. The total phase shift not only depends on the power in all channels but also on the bit pattern of adjacent channels. Assuming equal channel powers, the worst case in terms of phase shift occurs when all channels simultaneously carry 1 bits. In this case the phase shift is given by [45]:

$$\Phi_j^{NL} = (\gamma/\alpha)(2M-1)P_j \tag{2.22}$$

If the GVD effects are negligible, XPM does not affect the performance in IM/DD systems. However, with non-zero dispersion, amplitude distortion results due to the phase-to-intensity conversion. It therefore has a large impact on systems using ASK modulation format where the phase shift depends on the bit pattern.

2.2.1.3 Crosstalk

Crosstalk is one of the main sources of degradation in WDM systems [Ian'99] and consists of a transfer of power from one channel to another. This occurs because of the imperfect characteristics of various optical components such as demultiplexers and optical switches and is referred to as linear crosstalk. It can also occur because of nonlinear effects such as light scattering, FWM or XPM and this type of crosstalk is referred as nonlinear crosstalk.

Linear crosstalk can be divided into two categories depending on its origin: in-band crosstalk and out-of-band crosstalk. Out-of-band crosstalk occurs when a fraction of the power of neighbouring channels interferes with the main channel at the receiver

because of the non-perfect characteristics of optical filters and demultiplexers. Since it is incoherent in nature, out-of-band crosstalk is relatively easy to correct. In-band crosstalk however, is more difficult to correct because of its coherent nature and usually occurs in the routing process or when adding and dropping optical channels.

Because out-of-band crosstalk occurs in the detection process, the incident optical power of N channels at the photodetector when the mth channel is selected can be written as [Agr'97]:

$$P = P_m + \sum_{n \neq m}^{N} T_{mn} P_n \tag{2.23}$$

where P_m is the power of the main channel and T_{mn} is the filter transmittivity of the channel n when m is selected. Crosstalk occurs when $T_{mn} \neq 0$ and it is incoherent because it only depends on the power of the neighbouring channels. The above equation can be rewritten in terms of the photocurrent generated by the receiver as [Agr'97]:

$$I = R_m P_m + \sum_{n \neq m}^{N} R_n T_{mn} P_n = I_{ch} + I_X \tag{2.24}$$

where R_m and R_n are the photodetector responsivity for the m^{th} and n^{th} channels respectively. The worst penalty occurs when all interfering channels are carrying 1 bits simultaneously. The power penalty, defined as the additional power required at the receiver to counteract the effects of crosstalk, can be calculated using two approaches: the eye closure approach and the BER approach. In the first approach, I_{ch} needs to be increased by a factor of δ_X in order to keep the same eye opening. In the worst case the power penalty is given by [Agr'97]:

$$\delta_X = 1 + I_X / I_{ch} \tag{2.25}$$

In the BER approach, the power penalty is calculated by finding the increase in I_{ch} needed to maintain a certain value of BER. By treating I_X as a random variable, the BER is given by [Agr'97]:

$$BER = \frac{1}{4}\left[erfc\left(\frac{I_1 - I_D}{\sigma_1\sqrt{2}}\right) + erfc\left(\frac{I_D - I_0}{\sigma_0\sqrt{2}}\right)\right] \tag{2.26}$$

where $I_0 = I_X$, $I_1 = I_{ch} + I_X$ and $I_D = I_{ch}(1+X)/2$ corresponds to the worst case scenario ($X=\sum_{n\neq m}^{N} T_{mn}$). Finally, the BER is obtained by averaging over the distribution of I_X.

In-band crosstalk on the other hand can originate from waveguide-grating routers (WGR) or add-drop multiplexers/demultiplexers. The total optical field incident on the detector in this case is [Agr'97]:

$$E_m(t) = \left(E_m + \sum_{n\neq m}^{N} E_n \right) \exp(-i\omega_m t) \tag{2.27}$$

where E_m is the desired signal. Because of the coherent nature of in-band crosstalk, two beating terms can be identified: signal-crosstalk and crosstalk- crosstalk although the latter is low and can be neglected. Since phases fluctuate randomly, the receiver current can be written as [Agr'97]:

$$I(t) = R(P_m + \Delta P) \tag{2.28}$$

In this case crosstalk can be treated as intensity noise and the power penalty is [Agr'97]:

$$\delta_X = -10\log(1 - r_X^2 Q^2) \tag{2.29}$$

where $r_X = P_n/P_m(N-1)$.

2.2.1.4 Polarisation Mode dispersion (PMD)

Concept

In single mode optical fibres, signal energy at a given wavelength is resolved into two orthogonal polarisation modes. Ideally these two modes encounter the same refractive index and have the same group delay. However, due to manufacturing imperfection and mechanical stress, the fibre core is in fact non-circular, resulting in birefringence, a difference in the group velocity of the two orthogonal modes. This slight difference in the propagation velocity leads to pulse broadening, a phenomenon known as polarisation-mode dispersion (PMD). The difference in propagation time between the different modes is referred to as differential group delay (DGD) $\Delta\tau$. This is illustrated in Figure 2.5(a) where the two polarisation states have different arrival times at the fibre output.

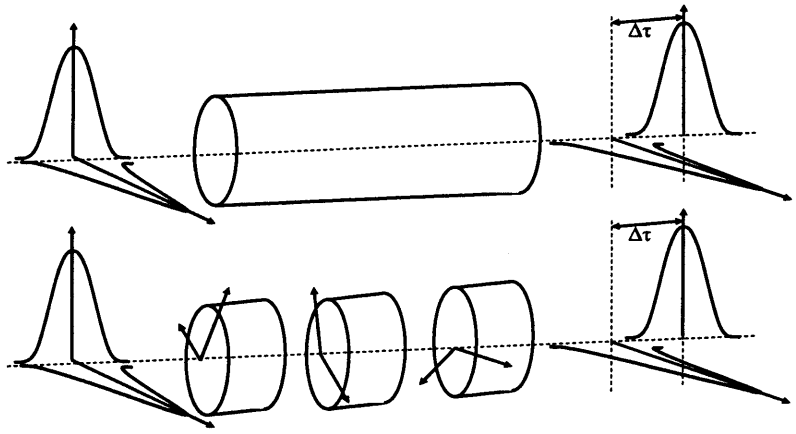

Figure 2.5 Conceptual time-domain model of PMD in a) a short fibre b) a long fibre with polarisation mode coupling

In a long fibre, the birefringence does not remain constant and hence the DGD is not additive. This can be represented by a series of random length birefringent segments of random rotations [Der'98] as illustrated in Figure 2.5(b). The fast and the slow polarisation mode emerging from one segment is projected onto the next one with different fast and slow axis, a process known as *polarisation-mode coupling*. This is dependent on environmental conditions such as mechanical stress, splicing or can be caused by components such as isolators. Due to mode coupling, each section may add or subtract from the DGD and on average this increases with square root of the distance [Kog'02]. Optical fibres are usually characterised by their PMD parameter D_{PMD} with typical values in the range 0.1-1 ps/km$^{1/2}$. For minimal effects on the eye diagram in an intensity modulated NRZ system, the mean value of PMD should be kept below one-tenth of the bit period, or 10ps for 10Gbit/s systems [Hau'04].

Representation of Polarised light

Polarised light can be represented using two distinct models: Jones model and Stokes model. These will be considered in turn in the following discussion.

Polarised light can be represented mathematically by a projection of the electric field on the x-y axis as demonstrated in Figure 2.6(a). The two components are given by:

$$\begin{cases} E_x(z,t) = E_{0x}\cos(\tau + \delta_x) \\ E_y(z,t) = E_{0y}\cos(\tau + \delta_y) \end{cases} \tag{2.30}$$

where $\tau = \omega t - kz$ is called the propagator and $\delta_{x,y}$ represents the phase. The pattern traced by the electric field is shown in Figure 2.6(b) and is given by:

$$\frac{E_x^2}{E_{0x}^2}+\frac{E_y^2}{E_{0y}^2}-2\frac{E_xE_y}{E_{0x}E_{0y}}\cos\delta=\sin^2\delta \tag{2.31}$$

where $\delta=\delta_y-\delta_x$. The above equation describes an ellipse but can also represent in certain special cases a circle or a line.

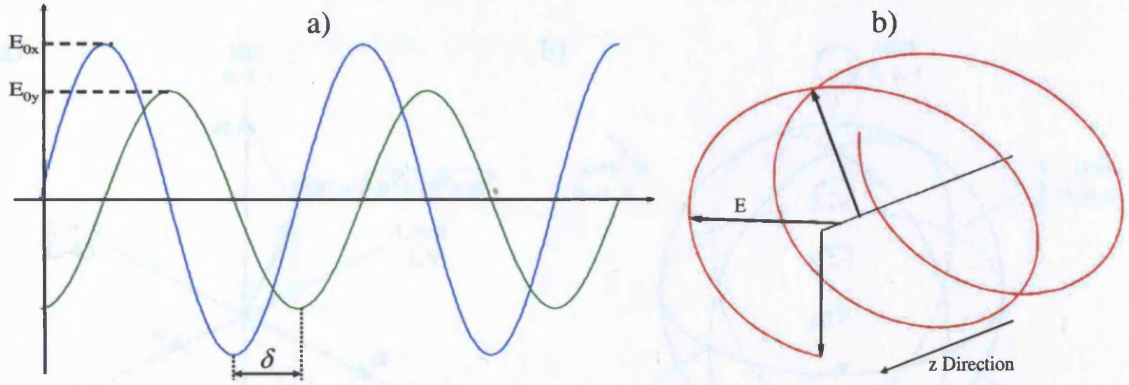

Figure 2.6 a) Electrical field of a polarised light in terms of the x-y coordinate b) The polarisation ellipse traced by the electrical field

Equation 2.29 can be rewritten using a two-element complex vector (Jones calculus) representation. This is given by the Jones vector which has the form:

$$E=\begin{pmatrix}E_x\\E_y\end{pmatrix}=\begin{pmatrix}E_{0x}\exp(i\delta_x)\\E_{0y}\exp(i\delta_y)\end{pmatrix} \tag{2.32}$$

The Jones vector is limited to the description of fully polarised light. To describe a partially polarised light, the Stokes model is preferred.

In the Stokes model, polarised light is described by four quantities which represent the power output of four polarisation filters. The first filter passes all states equally and is used to measure the relative power (S_0) of the signal. The second filter is a linear polarizer that gives the power of the vertical (LV) or horizontal (LH) polarised components (S_1). The third filter is also a linear polarizer but provides the power of the light at +45° (L+45) or -45° (L-45) and is denoted S_2. The fourth filter is a circular filter that indicates the right (RC) or left circular (LC) polarisation (S_3). The Stokes vector is generally represented by the following array:

$$S=\begin{bmatrix}S_0\\S_1\\S_2\\S_3\end{bmatrix} \tag{2.33}$$

The Stokes vector is usually represented in a 3 dimensional coordinate system, as illustrated in Figure 2.7(a), using the normalised Stokes parameter which are given by:

$$s1 = \frac{S_1}{S_0},\ s2 = \frac{S_2}{S_0},\ s3 = \frac{S_3}{S_0} \tag{2.34}$$

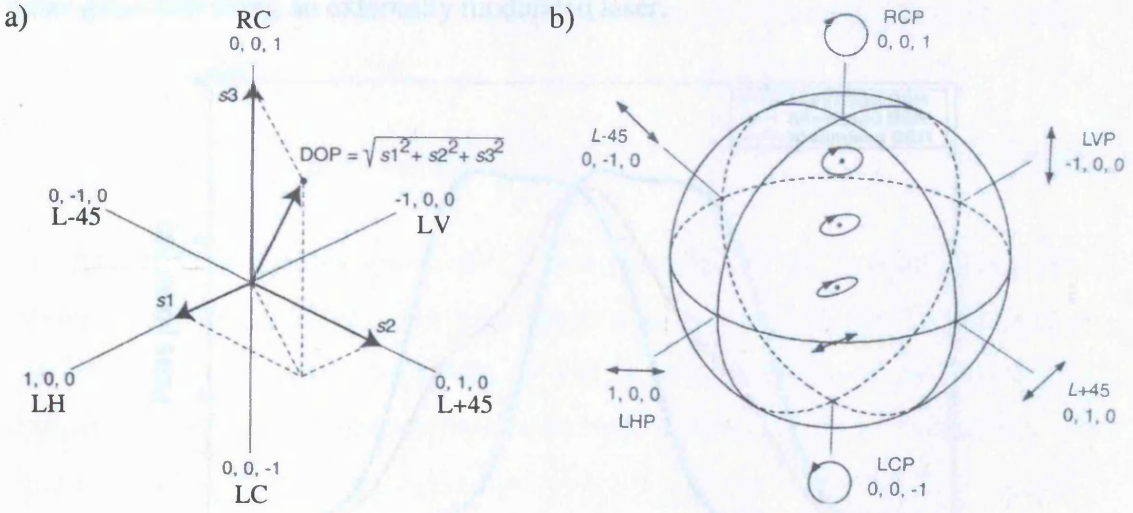

Figure 2.7 a) Orthogonal representation of normalised Stokes parameter b) Poincare sphere [Der'98]

Any optical signal can be fully polarised, partially polarised or unpolarised. The degree of polarisation (DOP) parameter describes the ratio between the polarised part and the unpolarised part of the signal and is given by:

$$DOP = \frac{P_{Polarised}}{P_{Polarised} + P_{Unpolarised}} \tag{2.35}$$

The degree of polarisation can be expressed in terms of Stokes parameters as:

$$DOP = \frac{\sqrt{S_1^2 + S_2^2 + S_3^2}}{S_0} = \sqrt{s_1^2 + s_2^2 + s_3^2} \tag{2.36}$$

Fully polarised light (e.g. output of a laser) has a DOP = 1 and a partially polarised light has a DOP<1. It is more convenient to represent the signal polarisation and its DOP in a normalised sphere. This is referred to as the Poincaré sphere and is shown in Figure 2.7(b). Any state of polarisation can be uniquely represented by a point on the sphere. The distance of the point from the centre gives the DOP of the signal and it ranges from zero to unity at the surface of the sphere.

Principal States Model

As mentioned before, a long fibre can be considered as a concatenation of birefringent sections with random orientations that either add or subtract from the DGD. However, there exists a couple of orthogonal input polarisation states for which the output pulse is undistorted to the first order. This is illustrated in Figure 2.8 for a 10Gbit/s NRZ pulse generated using an externally modulated laser.

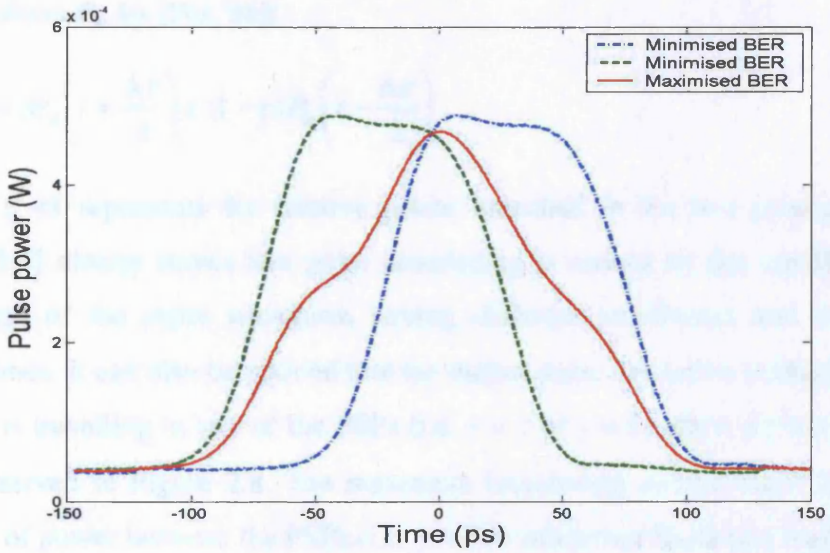

Figure 2.8 Output pulse shapes for three polarisation launches of a NRZ signal at 10Gbit/s with a DGD of 50ps. The two undistorted pulses (dashed and dash-dot) were aligned on the fast and slow PSP's

A polarisation controller was utilised to control the polarisation launch into a first order PMD emulator that created a 50ps DGD. A detailed explanation of the PMD emulator is given in section 5.3.4.2. It can be observed from the figure above that there are two input polarisation states for which the output waveform is undistorted, albeit arriving at different times. These polarisation launches give minimum BER. Also shown, an input polarisation state that gives maximum pulse broadening and therefore a maximum BER. The two polarisation states that lead to undistorted waveform, to the first order, are called principal states of polarisation (PSP) and they are orthogonal in the absence of polarisation-dependent loss (PDL). The PSPs can be used as a building block to describe PMD using either Jones or Stokes calculus. This model is known as the *principal state model* and provides both time and frequency domain characterisation of PMD. Starting with the time domain description of PMD, the fast and slow PSPs can be characterised by the unit Jones vectors $|p_+\rangle$ and $|p_-\rangle$

respectively. The output electrical field from a fibre with PMD to the first order can be written as [Kog'02]:

$$\vec{E}_{out}(t) = a_+ |p_+\rangle E_{in}\left(t - \frac{\Delta\tau}{2}\right) + a_- |p_-\rangle E_{in}\left(t + \frac{\Delta\tau}{2}\right) \tag{2.37}$$

where a_+ and a_- are complex coefficients that describes the launch power in each PSP ($|a_+|^2 + |a_-|^2 = 1$). After square law detection, the output waveform P_{out} is related to the input waveform P_{in} by [Poo'86]:

$$P_{out} = \gamma P_{in}\left(t + \frac{\Delta\tau}{2}\right) + (1-\gamma)P_{in}\left(t - \frac{\Delta\tau}{2}\right) \tag{2.38}$$

where $0 < \gamma < 1$ represents the relative power launched in the two principle states. Equation 2.37 clearly shows that pulse broadening is caused by the combination of two replicas of the input waveform having different amplitudes and arriving at different times. It can also be noticed that the output pulse can arrive undistorted if all the power is travelling in one of the PSPs (i.e. $\gamma = 1$ or $\gamma = 0$) albeit shifted by $\pm\Delta\tau/2$ as was observed in Figure 2.8. The maximum broadening occurs when there is an equal split of power between the PSPs (i.e. $\gamma = 0.5$) and hence leads to a maximisation of the BER. While the time-domain description of the PMD involves pulses, the frequency-domain characterisation considers a continuous single frequency wave. Using Stokes analysis, the output polarisation $\hat{t}$ is related to the input polarisation $\hat{s}$ by:

$$\hat{t} = R\hat{s} \tag{2.39}$$

where R is a 3×3 rotation matrix representing the transfer function of the fibre. Using the principal states model, the PMD can be characterised by the vector:

$$\vec{\tau} = \Delta\tau\hat{p} \tag{2.40}$$

where $\Delta\tau$ is the differential group delay and $\hat{p}$ is the unit Stokes vector of the output PSP's. $\vec{\tau}$ is a function of the optical frequency. The PSPs, the PMD vector and the output polarisation state can be graphically represented on the Poincaré sphere as illustrated in Figure 2.9. The principal states of polarisation are orthogonal and are situated at 180° from each other. The PMD vector has a magnitude of $\Delta\tau$ and points toward the slower PSP.

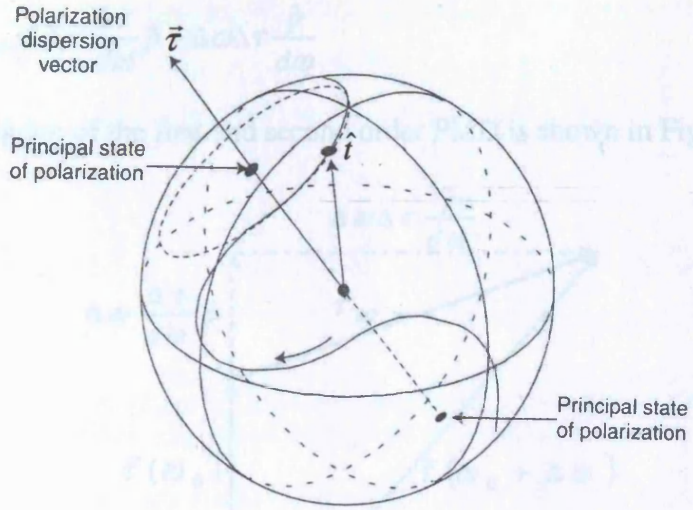

Figure 2.9 PMD representation in three-dimensional Stokes space [Der'98]

The output polarisation ($\hat{t}$) is frequency dependent and this dependency can be obtained by taking the derivative of equation 2.39:

$$\frac{d\hat{t}}{d\omega} = \vec{\tau} \times \hat{t} \tag{2.41}$$

where × represents the cross product. The above equation says that for a fixed input polarisation, and as the wavelength is varied, the output polarisation rotates around the principal states axis. The rate of rotation of the output state of polarisation around the PSP axis is proportional to the DGD. If $\hat{t}$ is aligned with the PSP axis then there will be no rotation and hence no change in the output polarisation. This is in fact the frequency definition of the principal states of polarisation which expresses that the PSP is the input polarisation state for which the output polarisation state is independent of the wavelength.

Second Order PMD

The PMD vector varies with varying optical frequency in both magnitude and direction. For a signal with a large bandwidth, its PMD vector can be expressed, using the Taylor expansion, as [Kog'02]:

$$\vec{\tau}(\omega_0 + \Delta\omega) = \vec{\tau}(\omega_0) + \frac{\vec{\tau}(\omega_0)}{d\omega}\Delta\omega + ... \tag{2.42}$$

The first term in the above equation represents first order PMD whereas the second term is the second order PMD. It is given by:

$$\vec{\tau}_{SO} = \Delta\omega\frac{\Delta\tau}{d\omega}\hat{p} + \Delta\omega\Delta\tau\frac{\hat{p}}{d\omega} \tag{2.43}$$

A schematic diagram of the first and second order PMD is shown in Figure 2.10

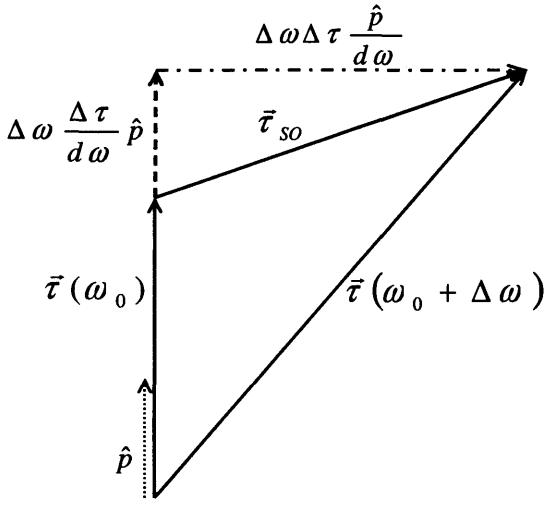

Figure 2.10 Schematic diagram of the first and the second order PMD

The first term in equation 2.43 is a vector parallel to the PSP unit vector ($\hat{p}$) and its magnitude follows the change in DGD with the wavelength. This leads to a polarisation-dependent pulse compression or broadening referred to as *polarisation-dependent chromatic dispersion* (PCD). In other words, the effective chromatic dispersion of the fibre can change depending on the polarisation of the signal and is given by:

$$DL_{Eff} = DL \pm \tau_\lambda\,,\ \tau_\lambda(ps/nm) = \frac{1}{2}\frac{d\Delta\tau}{d\lambda} \tag{2.44}$$

The ± sign depends on whether or not the vector is pointing in the direction of the PSP vector. The second term in equation 2.42 is a vector perpendicular to the PSP unit vector and represents the rotation of the PSP's with frequency. In other words, it describes the PSP depolarisation and results in pulse distortion such as overshoot and the generation of satellite pulses. This is demonstrated in Figure 2.11 where a 10Gbit/s 2^5 PRBS is affected by PMD (first and second order) with $\Delta\tau$ = 71ps, $\Delta\tau/d\omega$ = 1.3ps/GHz and a PSP rotation of 10.8°/GHz [Fra'98a].

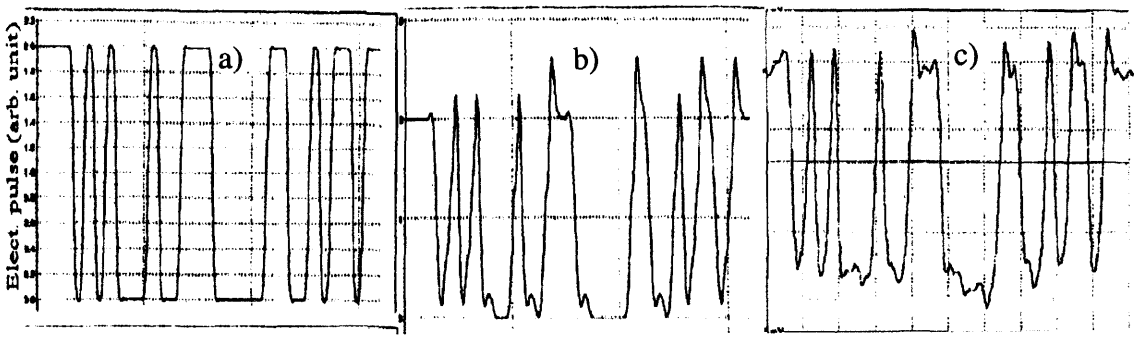

Figure 2.11 a) 2^5 input bit sequence b) Numerical simulation of second order PMD ($\Delta\tau$=71ps) c) Experimental waveform affected by second order PMD ($\Delta\tau$=71ps) [Fra'98a]

In order to comprehend the underlying reason for waveform distortion and the generation of satellite pulses due to second order PMD, one should look at the time impulse response of the latter. The time impulse response for first order PMD was given in equation 2.37. The time description of first and second order PMD is given by [Fra'98b]:

$$E_{out}(t)=\frac{1}{2\sqrt{2}}\left\{\left(au^*+bu\right)\left[E_{out}^{+}\left(t+\frac{\Delta\tau}{2}\right)+E_{out}^{-}\left(t-\frac{\Delta\tau}{2}\right)\right]\right.$$
$$+au\left[E_{out}^{+}\left(t-2k+\frac{\Delta\tau}{2}\right)+E_{out}^{-}\left(t-2k-\frac{\Delta\tau}{2}\right)\right]$$
$$\left.+bu^*\left[E_{out}^{+}\left(t+2k+\frac{\Delta\tau}{2}\right)+E_{out}^{-}\left(t+2k-\frac{\Delta\tau}{2}\right)\right]\right\} \qquad (2.45)$$

$$E_{out}^{\pm}=\Im^{-1}\left\{\tilde{E}_{in}(\omega)\exp(-\alpha z)\exp\left(-\beta(\omega)z\pm\Delta\tau'\omega^2/2\right)\right\} \qquad (2.46)$$

where a and b are the complex coefficients ($a^2+b^2=1$), u = [1,j], u* = [1,-j] and $2k$ is the linear PSP rotation with frequency, $\Delta\tau'=d\Delta\tau/d\omega$, β ($=\beta_0+\beta_1\omega+\beta_2\omega^2/2+....$) is the fibre propagation constant, α is fibre attenuation and $\tilde{E}_{in}$ is the Fourier transform of the input field E_{in}. It can be seen from the above equation that with second order PMD, there are six filtered replicas of the input pulse for each polarisation axis [Fra'99]. While $\Delta\tau'$ asymmetrically broadens the replicas, the rotation 2k creates overshoot and satellite pulses which ensures that there is always energy in both polarisation states even when one axis is excited at the input.

Power Penalties Due to First-Order PMD

First order PMD can be represented by a differential group delay time $\Delta\tau$ between orthogonally polarised components of the input power waveform expressed by equation 2.38. Since the two polarisation components arrive at different times, the output pulses broadens after square-law detection. If the input root mean square (rms) width is $\sigma 1$, the output rms width σ_2 is given by [Poo'91]:

$$\sigma_2^2 = \sigma_1^2 + \Delta\tau^2\gamma(1-\gamma) \tag{2.47}$$

The impairment caused by this effect can be expressed as a power penalty in dB [Kog'02]:

$$penalty(dB) = \left(\frac{A}{T}\right)^2 \Delta\tau^2\gamma(1-\gamma) \tag{2.48}$$

where T is the bit period. *A* is dimensionless parameter and depends on the pulse shape, modulation format and receiver characteristics such as the electrical bandwidth and the predominant noise type. For optically pre-amplified receivers, *A* ranges between 10 and 70 for NRZ format and between 10 and 40 for RZ. It can be deduced from the above equation that power penalty increases with increasing DGD or when γ tends to 0.5. Conversely, the penalty decreases with small $\Delta\tau$ or when γ approaches 1 or 0 (i.e. when the majority of the power is travelling on one polarisation axis).

2.2.2 Noise

2.2.2.1 Transmitter Noise

The output from a semiconductor laser suffers from fluctuations in its intensity, phase and frequency even when biased with a constant current. The most dominant noise however is the intensity noise. Intensity noise occurs from the optical interference between the stimulated emission laser signal and the spontaneous emission generated within the laser cavity leading to power fluctuations. Laser sources such as distributed feedback (DFB) lasers and Fabry-Perot (FP) laser diodes typically exhibit intensity noise whose value depends on pump levels and feedback conditions. The optical receiver converts the power fluctuation into current fluctuations which add to those generated by shot and thermal noise. Intensity noise can also be generated by non-laser sources such as erbium doped-fibre amplifiers (EDFA's). They generate amplified spontaneous emission (ASE) whose intensity noise statistics differ from that of a laser and will be discussed in section 2.2.2.3.

It is useful to describe and compare intensity noise as a ratio of noise power in a 1Hz bandwidth normalised by the DC signal power as it becomes independent of any attenuation or the absolute power reaching the photodetector. This ratio is referred to as relative intensity noise (RIN) and is defined as [Der'98]:

$$RIN = \frac{<\Delta i^2>}{I_{dc}} \qquad [\mathrm{Hz}^{-1}] \tag{2.49}$$

where $<\Delta i^2>$ is the time averaged intensity noise power in a 1Hz bandwidth and I_{dc} is the average DC intensity. The intensity noise standard deviation is given by [Agr'97]:

$$\sigma_I = RP_{in}r_I \tag{2.50}$$

where r_I is a measure of the noise level and is related to the relative intensity noise of the transmitter as

$$r_I^2 = \frac{1}{2\pi}\int_{-\infty}^{\infty} RIN(\omega)d\omega \tag{2.51}$$

2.2.2.2 *Receiver Noise*

Optical receivers convert the incident light into an electric current. This current is not constant and fluctuates even if the optical signal has a constant power. The fluctuation is considered as noise since it contains no information and is introduced by two fundamental noise mechanisms: thermal noise and shot noise.

Thermal noise (also known as Johnson noise) should be considered in any detection process as it is generated by the receiver electronics. The load resistor in the front end of the receiver adds current fluctuation due to the random thermal motion of electrons. This can be considered as being generated by a current noise source as shown in Figure 2.12.

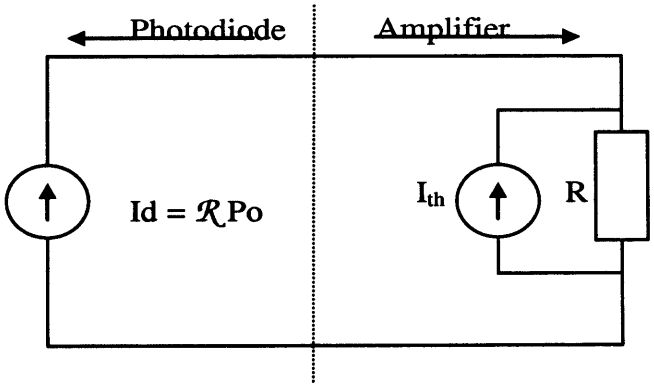

Figure 2.12 Modelling of thermal noise source

The thermally generated rms current noise i_{th} in a 1Hz bandwidth is given by [Der'98]:

$$i_{th} = \sqrt{\frac{4kT}{R}} \quad [A/\sqrt{Hz}] \tag{2.52}$$

where R is the resistance, k is the Boltzman's constant and T is the temperature in Kelvin. The amount of noise also depends on the front-end design as some receivers contain pre- and main amplifiers. If the noise figure F_n of the amplifiers is considered, a general formula for the noise variance is given by [Agr'97]:

$$\sigma_T^2 = \frac{4KT}{R} F_n \Delta f \tag{2.53}$$

Δf is the effective noise bandwidth.

Shot noise results from the fact that electrons in an electrical current arrive at random times. It usually becomes significant when a small signal is being measured in the presence of a large DC background. In fact shot noise is one of the dominant sources of noise when coherent detection schemes are used, where a small AC current is usually detected with a large DC current due to the local oscillator. The rms shot noise current in a 1Hz bandwidth is given by [Der'98]:

$$i_s = \sqrt{2qI_p} \tag{2.54}$$

And the noise variance is given by [Agr'97]:

$$\sigma_S^2 = 2qI_P \Delta f \tag{2.55}$$

I_p is the average current, q is the charge of an electron and Δf is the effective noise bandwidth.

Unlike thermal noise, the shot noise level depends on the signal current and above a certain DC threshold, shot noise value exceeds the fixed thermal noise (assuming fixed temperature). In fact, for a photodetector connected to a resistor, the shot noise starts to exceed thermal noise when the voltage across the resistor becomes greater then 52mV [Der'98]. This voltage is independent of the value of the resistor used.

2.2.2.3 *Amplified Spontaneous Emission (ASE) Noise*

Amplifier noise is the dominant noise in WDM networks and can be the ultimate limiting factor for long-haul systems. It is generated from the amplified spontaneous emission (ASE) of the optical amplifiers. In an EDFA, amplification occurs when the incident signal light interacts with the exited erbium atoms distributed along the fibre core. This gives rise to additional photons with the same optical phase and direction as the incident signal (stimulated emission). However, some of the exited atoms that do not interact with the signal decay to the ground state resulting in spontaneous emission with random phase and direction. Up to 1% of the spontaneously emitted photons are captured by the propagating mode of the optical fibre then amplified as they travel inside the doped fibre resulting in amplified spontaneous emission [Bec'99]. Since the detector will convert all photons into electrons, spontaneous emission of amplifiers will give rise to an electrical signal that must be considered as noise since it contains no information. Writing the total optical field as the sum of a signal field $\vec{E}_s$ and spontaneous emission noise field $\vec{E}_n$:

$$\vec{E}_{total} = \vec{E}_s + \vec{E}_n \tag{2.56}$$

The photodetection processes is a nonlinear square-law process and the photocurrent I is therefore:

$$I \sim \left(\vec{E}_{total}\right)^2 = E_s^2 + E_n^2 + 2\vec{E}_s \cdot \vec{E}_n \tag{2.57}$$

The first term on the right hand side of the above equation is the signal power, the second term is the noise power, also referred to as spontaneous-spontaneous beat noise and the last term is the signal-spontaneous beat noise. Notice that when a one is received, the data is affected by both spontaneous-spontaneous and signal-spontaneous beat noise whereas if a zero is detected, in which E_s is close to zero, the photocurrent is influenced by the spontaneous-spontaneous beat noise only. Interference between signal light and ASE is similar in many aspects to heterodyne detection where two frequencies are mixed together to generate a different frequency. Also, the signal will only beat with ASE components that are in the same polarisation state. Since ASE is typically unpolarised, only one half will contribute to the signal-spontaneous beat noise density. The effect of ASE noise on the photocurrent can be diminished by placing a narrow optical filter before the detector so that only the

bandwidth corresponding to the signal is converted. The total ASE power originating from a single mode EDFA, with two propagating modes of polarisation, is governed by [Bec'99]:

$$P_{ASE} = 2n_{sp}h\nu(G-1)\Delta\nu_{opt} \tag{2.58}$$

Where n_{sp} is the population-inversion factor (also called spontaneous emission factor), ν the optical frequency, $\Delta\nu_{opt}$ the optical bandwidth, G the amplifier gain, and h is the Planck's constant. The factor n_{sp} is a measure of the quality of the inversion of optical amplifier and its value ranges from 1 (complete inversion) to 4. This factor also determines by how much the signal to noise ratio deteriorates due to ASE noise. This is quantified in terms of amplifier noise figure F_n defined as [Agr'02]:

$$F_n = \frac{SNR_{in}}{SNR_{out}} \tag{2.59}$$

Where SNRs refer to the electrical power generated when an ideal receiver is used (i.e. 100% quantum efficiency). Usually the signal spontaneous beat noise is the dominant noise in amplified systems and the noise figure in this case is given by [Des'02]:

$$F_n = 2n_{sp}\frac{(G-1)}{G} + \frac{1}{G} \tag{2.60}$$

The second term in the right hand side represents the contribution of shot noise at the receiver. For large gains, the above equation can be simplified to:

$$F_n = 2n_{sp} \tag{2.61}$$

For a fully inverted amplifier (ideal amplifier with n_{sp} =1) the noise figure is equal to 3dB. Most optical amplifiers have a noise figure that lies between 5 and 8 dB [Agr'97].

The photocurrent generated at the detector using equation 2.56 can be written as:

$$I = I_s + \Delta I \tag{2.62}$$

where I_s is the current of the signal and ΔI represents current fluctuation originating from the spontaneous-spontaneous and signal-spontaneous beat noise (ignoring shot and thermal noise). The variance of the current fluctuation can be written as:

$$\sigma^2 = \sigma^2_{sig-sp} + \sigma^2_{sp-sp} \tag{2.63}$$

The variance of the signal-spontaneous beat noise is governed by [Agr'97]:

$$\sigma^2_{sig-sp} = 2(q\eta)^2 F_n \frac{\Delta f}{h\nu} G^2 P \tag{2.64}$$

where Δf is the electrical bandwidth and η is the quantum efficiency of the receiver. It is clear from the above equation that using amplifiers with small noise figure and deploying electrical filters helps in reducing current fluctuation and thus reduces the error probability. The variance of the spontaneous-spontaneous beat noise is given by:

$$\sigma^2_{sp-sp} = (q\eta F_n)^2 \Delta f \Delta \nu_{opt} G^2 \tag{2.65}$$

Unlike signal-spontaneous, spontaneous-spontaneous noise is not dependent on the input power and can be minimised by using an optical filter to reduce the optical bandwidth $\Delta\nu_{opt}$. For a single optical amplifier, the equivalent electrical signal to noise ratio (SNR) assuming noise at the output of the amplifier is dominated by the signal-spontaneous beat noise is given by [Bec'99]:

$$SNR = \frac{GP_{in}}{4h\nu n_{sp} B_e (G-1)} \tag{2.66}$$

where B_e is the electrical bandwidth. It can be noticed that the electrical SNR is independent of the amplifier gain when G >>1 and is only determined by the noise figure. In a system with many cascaded amplifiers, the equivalent electrical SNR is obtained by multiplying n_{sp} by the number of amplifiers.

2.3 Measurement of System Performance

In digital transmission systems, many techniques to measure the performance of a system were developed. These can be used to compare system design trade offs or the effect of transmission impairments on the overall system. We will consider three metrics in this work: the Q-factor, the bit error rate (BER) and the eye closure penalty (ECP)

2.3.1 Q-Factor

The Q-factor is the most practical way to measure the quality of a signal and is sensitive to transmission impairments. Assuming that ISI effects are negligible compared to the noise and the marks and spaces rails have Gaussian distributions, the Q factor at a decision circuit is defined as:

$$Q = \frac{|\mu_1 - \mu_2|}{\sigma_1 + \sigma_2} \tag{2.67}$$

where $\mu_{0,1}$ are the means and $\sigma_{0,1}$ are the standard deviations of the zeros and the ones (Figure 2.13). Estimating signal quality using the Q-factor should be taken with caution since any strong signal distortion (due to dispersion for example) may lead to erroneous interpretation. For instance, heavy presence of inter-symbol interference (ISI) causes pessimistic Q factor estimation [Fis'97]. Assuming the main source of noise is the signal-spontaneous beat noise and a large duty cycle intensity-modulated format is used, the Q-factor is related to the optical SNR by the following expression [Ess'02]:

$$OSNR = \frac{Q^2 B_e}{B_0} \frac{1+r}{\left(1-\sqrt{r}\right)^2} \tag{2.68}$$

where B_o is the optical bandwidth, B_o the electrical bandwidth and r is the extinction ratio.

2.3.2 Bit Error Rate

The bit error rate (BER) is the ratio of the number of incorrectly received bits to the total number of bits within a certain time interval. This can be obtained by means of a bit-error detector where each received bit is compared to the one sent (assuming it is known) or by using the sub-error rate method [Ber'93]. It consists of varying the decision threshold (I_D) around the ones and zeros rails and comparing the decisions with the ones of a fixed threshold. This technique is explained in more details in section 3.4.2.1 of the next chapter. The method has advantages of speed, repeatability and wide dynamic range [Fis'97].

Assuming a Gaussian distribution of the marks and spaces rails, the BER of a channel at decision threshold I_D is given by [Agr'97]:

$$BER(I_D) = \frac{1}{4}\left[erfc\left(\frac{I_1 - I_D}{\sigma_1\sqrt{2}}\right) + erfc\left(\frac{I_D - I_0}{\sigma_0\sqrt{2}}\right)\right] \tag{2.69}$$

where *erfc()* is the complementary error function and can be approximated by the following expression [Ber'93]:

$$erfc(x) \approx \frac{1}{x\sqrt{2\pi}} \exp\left(\frac{-x^2}{2}\right) \tag{2.70}$$

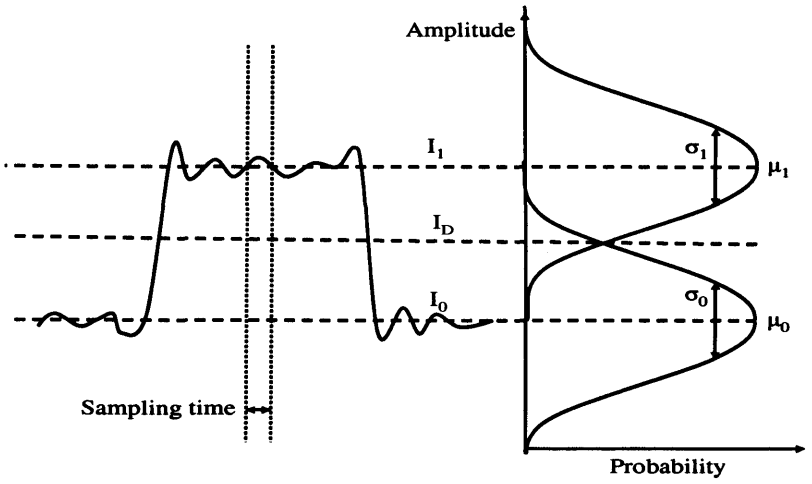

Figure 2.13 A received noisy signal with its histogram

It can be seen that the BER is dependent on the decision threshold. However, the latter is optimised to give the minimum BER which occurs when:

$$I_D = \frac{\sigma_0 I_1 + \sigma_1 I_0}{\sigma_0 + \sigma_1} \tag{2.71}$$

Hence the optimum BER using the above decision threshold is given by:

$$BER = \frac{1}{2} erfc\left(\frac{Q}{\sqrt{2}}\right) \approx \frac{\exp\left(-Q^2/2\right)}{Q\sqrt{2\pi}} \tag{2.72}$$

Direct measurement of the BER is impractical because with current standards (10^{-15}) it will take days to detect a single error in one channel. The Q-factor on the other hand is quick and easy to evaluate and directly related to the BER. This is why the Q-factor is such a powerful measurement tool.

2.3.3 Eye Closure Penalty

In the absence of noise, the shape of the eye diagram becomes a reliable indicator of the effects of distortion on the quality of the signal [Ess'02]. One way of measuring this distortion is the eye closure penalty (ECP). It is determined by measuring the height P_R of the highest rectangle that can be fitted inside the eye diagram as demonstrated in Figure 2.14. The rectangle width represents 20% of the bit period to allow for jitter in the decision times due to the clock recovery. The eye closure penalty is given by [Ess'02]:

$$ECP = -10\log\left(\frac{P_R}{2P_{ave}}\right) \tag{2.73}$$

where P_{ave} is the average power of the signal.

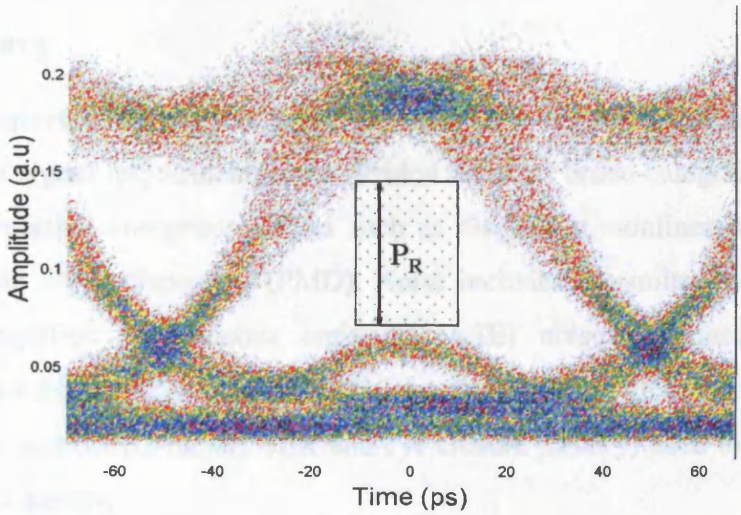

Figure 2.14 Determination of the eye closure penalty using a box of width 20% of the bit period. Eye diagram of a 10Gbit/s signal after 60km of single mode fibre

The ECP is very useful to compare the transmission performance of various modulation formats. The relationship between the ECP and the Q penalty (QP) is not linear and depends on the nature of the degradation and the modulation format. It was shown in [Dow'05] that for NRZ systems and assuming a symmetrical eye closure from the top and bottom, the Q-penalty is related to the ECP by:

$$QP = ECP.\frac{1+\sqrt{\frac{ECP-1}{ECP+1}}}{\sqrt{1+\frac{ECP-1}{ECP+1}}} \tag{2.74}$$

For RZ formats, two crucial assumptions have to be made. The undistorted RZ pulses are treated as Gaussians with e^{-1} pulse width of $2\times T_u$ and the distorted pulses are also treated as Gaussians having the same energy but with widths of $2\times T_d$. The relationship between the QP and the ECP in this case is given by [Dow'05]:

$$QP = \frac{ECP}{\sqrt{\frac{T_d}{T_u}}}\cdot\frac{\left(1+\sqrt{2}\cdot\exp\left[\frac{-(T_B/T_d)^2}{2}\right]\right)}{\left(1+\sqrt{2}\cdot\exp\left[\frac{-(T_B/T_u)^2}{2}\right]\right)} \tag{2.75}$$

where T_B is the bit period.

2.4 Summary

This chapter covered the theory of signal degradation in optical transmission systems. The sources of signal impairments were divided into two broad categories: distortion and noise. Distortion comprises effects such as dispersion, nonlinearities, crosstalk and polarisation mode dispersion (PMD). Noise includes transmitter noise, receiver noise and amplified spontaneous emission (ASE) noise generated by optical amplifiers. Also described in this chapter are the coherent ways of detecting an optical signal and few metrics (Q-factor, BER and eye closure penalty) used to evaluate and compare signal quality.

Fibre dispersion originates from the fact that the refractive index of the fibre is frequency dependent. This causes different wavelengths (frequencies) to travel at different velocities leading to pulse broadening and thus to inter-symbol interference (ISI). In addition, this refractive index also changes with optical intensity which leads to the modulation of any intensity-modulated signal with relatively high power, a phenomenon referred to as self-phase modulation (SPM). Generally, SPM and fibre dispersion interact together to either compress or broaden even more the optical pulses. Another phenomenon that causes pulse broadening is polarisation mode dispersion (PMD). There are two propagating modes in single mode fibres, and because of the imperfection (non-circularity) of the fibre core, these modes travel at different velocities. The impairments mentioned so far are due to the propagation of the signal in the fibre but degradation can also originate from the imperfect characteristics of various optical components. Crosstalk, which consists of a transfer of power from one channel to another, is introduced by demultiplexers, optical switches and filters. Noise on the other hand is mainly introduced in the network by the spontaneous emission (ASE) of the optical amplifiers. This could be the ultimate limiting factor for long-haul WDM system transmissions since it degrades the signal to noise ratio (SNR). All these impairments have negative effects on the quality of the transmission in a network and have to be monitored so that they are either compensated or isolated. Different monitoring schemes have been proposed for this purpose and they are discussed in the next chapter.

Chapter 3 Literature Review

3.1 Introduction

In the last few years, there has been a considerable increase in demand for higher bandwidth and more reliable data and voice services. From a network operator point of view, the cost of delivering better services has been increasing while they have seen their revenues stagnating because customers were unwilling to pay more. The figure of a factor of 2.5 increase in cost for a factor of 4 increase in bitrate is often mentioned [Dav'02]. The only way to remain profitable is to substantially cut costs by up to 1 fold. One realistic way of achieving this goal is the deployment of truly photonic networks in order to reduce the number of optical/electrical/optical transponders which usually represent between 50% and 70% of the investment in wavelength division multiplexed (WDM) networks. While the advantages of moving to more transparent and higher bitrate networks are attractive, tighter constraints are placed on the transmission margins and engineering rules that govern network design nowadays. Added complexities such as dynamic link reconfiguration, fault localisation and restoration have to be addressed. All these issues put optical performance monitoring (OPM) under the spotlight as an enabling technology for future all-optical networks. It is a potential technique to realise such networks through improved fault management and better control of transmission at the physical layer level. The primary function of any OPM method is to determine the signal quality either in the optical domain or the electrical domain. Ideally, it should be non-intrusive, bitrate and protocol independent, format transparent, cheap, fast and accurate. However, no such technique currently exists and the challenge is to find a good trade-off between cost, accuracy, transparency and versatility. The topic of OPM has been covered in the literature since the introduction of flexible optical networks in the early 1990's [Hil'93] and has taken many synonymous appellations such as "optical parameter monitoring" or "analogue symbol monitoring" (ASM). Nowadays OPM is mainly regarded as a tool used to control optical or electrical compensators in order to mitigate impairments. However, it has myriad other applications, some of which are described in the next section. Section 3.3 discusses a proposed idea of dividing up OPM into three distinct layers based on their functionality. This taxonomy separates OPM objectives into channel management, channel quality monitoring and protocol monitoring. Section 3.4

reviews the different OPM methods reported in the literature. It is divided into two sections: spectral methods and sampling methods.

3.2 OPM Application

3.2.1 Operator Handover

A widely perceived application of performance assessment is optical channel monitoring to verify the service quality agreement between the network operator and the customer commonly known as SLA (service level agreement). This could be extended to provide a "warranty label" between network operators to avoid disagreement when handing over the services. Traditionally these level agreements and other quality of service (QoS) measurements are based on the digital bit/block error mechanisms (please refer to Appendix 1 for more information). For instance, SONET/SDH has built-in overhead within their frame structure to measure error performance at Section, Line and Path layers (B1, B2, and B3 bytes) and it is relatively easy to measure the health of a network at the end points as well as in the in-between segments of the SONET/SDH network. However this necessitates the complete termination then regeneration of the signal, a concept that is becoming unacceptable in future low-cost optical networks. Additionally, and although this technique detects errors occurring within the digital frame, it does not provide any information about the root cause of the degradation making fault localisation an awkward operation to achieve. Moreover, this method is protocol-aware which does not make it suitable in a transparent environment.

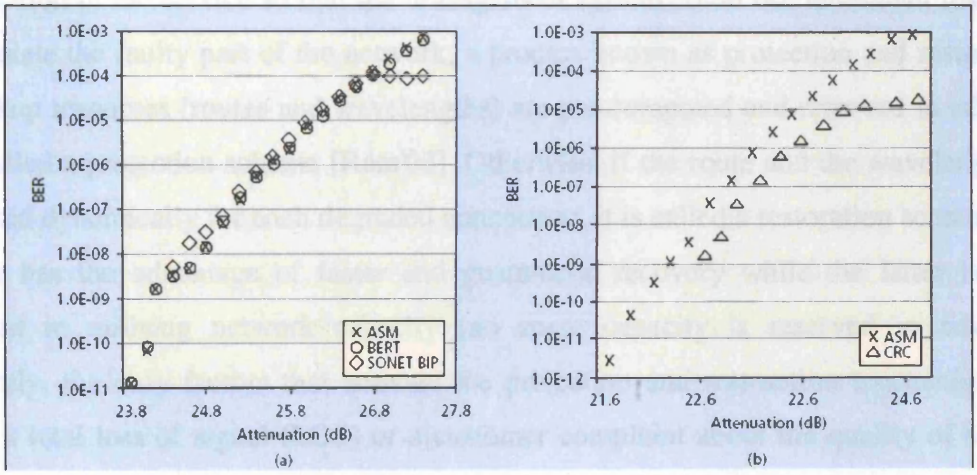

Figure 3.1 (a) experimental data of 622 Mb/s BER measurement using SONET OC-12 BIP-8, ASM and a BERT (baseline). (b) experimental data comparing ASM and CRC for a 1.25Gb/s GbE link [Par'02].

Protocol independent services such as Digital Wrappers and Generic Framing Procedure (GFP) have been introduced recently to bring the technology one step closer to realising the original vision of optical transport networks (OTNs) [Bon'00]. However they all suffer from the fact that no information about the root cause can be extracted from them. As a result, OPM can potentially be utilised as a way to certify service quality agreement in transparent networks. A comparison between the digital and analogue quality monitoring was conducted by [Par'02] and the results are shown in Figure 3.1. Figure 3.1a shows BER measurements of SONET BIP-8, ASM and a baseline bit error rate test (BERT) at a bitrate of 622 Mb/s. It can be seen that ASM and BIP-8 give the same BER up to an attenuation of 27dB, above this level of attenuation there will be so many errors that some of them will go undetected by the digital method. Figure 3.1b shows a comparison between the ASM method and the cycle redundancy check (CRC) method in a Giga-bit Ethernet (GbE) network operating a bitrate of 1.25Gb/s. It can be observed that there is a small offset between the two curves, which means that ASM method detects errors before the CRC method. This is due to the fact that approximately 20% of the bits in the frame and interframe gaps are not included in the CRC calculations. As a consequence, any errors occurring in those bits will not be counted and the BER will not be affected immediately.

3.2.2 Protection and Restoration

In addition, any performance monitoring system should be able to detect anomalies or degradation in the service so that the management system could use redundant resources and isolate the faulty part of the network, a process known as protection and restoration. If backup resources (routes and wavelengths) are pre-computed and reserved in advance, it is called a protection scheme [Ram'03]. Otherwise, if the route and the wavelength are allocated dynamically for each degraded connection, it is called a restoration scheme. The former has the advantage of faster and guaranteed recovery while the latter is more efficient in utilising network capacity (no spare capacity is reserved in advance). Currently, the only factors that activate the protection and restoration mechanisms are either a total loss of signal (LOS) or a customer complaint about the quality of service. The latter case is particularly costly for network providers because they are liable for some kind of compensation [Jin'04]. OPM may be a promising tool to activate restoration mechanisms once the quality of the signal degrades below a certain threshold without affecting the QoS at the end node. Furthermore, it can also be used for dynamic allocation

of resources by estimating QoS before transmission. This point leads us to the next potential use of OPM: impairment-aware routing.

3.2.3 Impairment-based Routing

Impairment-aware routing in wavelength-routed optical networks has become an important topic since the deployment of all-optical transparent networks became a reality. Traditionally, the routing and wavelength assignment (RWA) algorithms were based on the shortest path algorithm in opaque networks because the signal is regenerated at every node and the quality of service is always maintained. However this is no longer valid in the next generation networks where little or no optical-electrical-optical (OEO) conversions are possible. A new concept of blocking probability is also introduced. Network-layer blocking occurs when a light path cannot be setup due to unavailable resources such as a wavelength or a free route. With the impairment-aware routing method, blocking also means physical layer blocking and happens when a light path suffers from an unacceptably high BER. In a dynamic network, the end-to-end transmissions experience different degradations depending on the assigned light path. Additionally, these impairments are also dynamic and depend, for example, on the traffic load (crosstalk, cross phase modulation (XPM)...) and temperature (polarisation mode dispersion (PMD) and chromatic dispersion (CD)). Traditional RWA algorithms might provision a light path with the lowest number of nodes but fall short on the signal-quality requirement. This is where physical-layer based RWA algorithms become important and should be incorporated into the control plane [Muk'04]. In this area, the impairments are classified into two categories: linear and non-linear. Linear effects are independent of signal power or traffic load and affect wavelengths individually [Str'01]. These include amplified spontaneous emission (ASE) noise, PMD and CD. Non-linear effects are significantly more complex to incorporate in routing algorithms and include impairments such as four-wave mixing (FWM), self phase modulation (SPM) and XPM. Many routing algorithms have been proposed depending on the most dominant sources of degradation. It has been argued in [Ali'02] that the number of regenerators can be significantly reduced using a PMD-aware routing protocol. In the high-speed Italian network, the number of regenerators can be reduced by up to 50% assuming legacy high-PMD fibre ($0.5ps/\sqrt{km}$) represents more than 50% of installed fibre [Ali'01]. In [Lev'01] on the other hand, the routing algorithm is based on calculating the optical signal-to-noise ratio (OSNR) and the noise figure of the light path before transmission. It has been shown that

this method outperforms the shortest path algorithm in terms of blocking probability but parameters such as amplifier gain and saturation power or multiplexer/demultiplexer (MUX/DEMUX) and switch losses can have a significant impact on the network performance [Maf'04]. The full incorporation of non-linear effects into the routing mechanism has proved very complex. A full treatment of these constraints requires an exhaustive knowledge of the physical layer such as residual dispersion in each span, signal power and fibre type and the actual state of the network such as channel spacing and the number of channels in use. This evidently increases the complexity of the algorithm and reduces its scalability. A potential solution to this was proposed by [Car'05] and consists of converting the non-linear penalties based on the number of wavelengths, channel spacing and power in each channel into OSNR penalties. Another solution proposed by [Pen'03] treats the interaction between the linear and non-linear effects statistically and can accurately predict the BER for a distance up to 2000km.
It is clear that impairment-aware routing is indispensable for future all-optical networks because it offers clear advantages such as lower blocking probability, cost reduction and guaranteed QoS. In the long term, the ultimate solution to the network scalability problem is the true integration of OPM into the decision and routing process.

3.2.4 Fault Management

Fault management of optical networks deals with the prevention, detection and reaction to failures [Car'05]. Reaction to failure through restoration was discussed previously and we only deal with troubleshooting and fault localisation in this section. Due to network transparency and high data rates, all-optical networks have become more vulnerable to physical layer impairments. Signals propagating from ingress to egress nodes may take different routes, and in case of a single fault, may trigger multiple alarms resulting in added ambiguity and processing time of the management system. It is therefore crucial to design a fast and effective management system that is capable of reducing the number of redundant alarms while providing reliable fault detection and localisation [Sav'02]. This subject is widely covered in the literature and there is a general consensus that OPM is the enabling technology for the successful implementation of fault management. However they diverge in answering two crucial and closely related questions concerning what to monitor and where to monitor. To answer the first question from the fault management point of view, one should look at the root causes of a network outage. These can be divided into component faults and transmission impairments. The former include single

or multiple component malfunctions due to damage, aging or bad configuration. A good example of component generated fault would be an EDFA pump laser failure. This will result in a drop in power at a certain node in the network leading to an excess noise in the subsequent amplification stage. Conversely if there is an increase in the pump laser power, it will result in a rise in the output optical power, generating non-linear effects such as SPM and XPM. Transmission impairments which include noise and distortion have been discussed in the previous chapter and should also be considered in any fault diagnosis. Previous work on fault localisation assumed centralised management and only considered optical power or optical spectrum analysis as inputs for their system [Kat'95] [Sav'03]. In [Kat'01] for example, the central manager periodically checks all source and destination powers using a probe channel and routing table information. If the power at any node is out of the expected range than the fault is localised. In [Mas'00] on the other hand, an efficient alarm filtering algorithm based on alarm correlation binary trees was introduced in order to narrow down the possible sources of degradation. It has been extended recently to include crosstalk and wavelength misalignment [Mas'05]. The optimal locations for monitoring equipment are places where they cover the maximum number of network elements while triggering the least number of alarms in case of a failure. This also depends on network topology and the desired monitoring parameters. For instance in a mesh topology, if the monitoring parameter is optical power, then the OPM devices can be placed at intermediary nodes where many light paths can be covered. However, if distortion is the main parameter then the OPM equipment should be installed at the end nodes.

It is true that integrating OPM in a network leads to higher capital expenditure but this will be amortised in the long term through saving in operational costs.

3.3 OPM Reference Model

OPM can be broken into three distinct layers as shown in Figure 3.2 [Kil'04]. The first layer is the transport or WDM channel management layer monitoring which involves establishing the optical domain characteristics necessary for channel management at the WDM level. This includes real time detection of channel presence, wavelength registration, power levels and spectral OSNR. The second level, which is the optical signal or channel quality layer monitoring, tunes into a single wavelength and determines the quality of that specific channel. It comprises parameters such as the analogue eye

opening and eye statistics, analogue BER, Q-factor, electrical SNR and distortions affecting the channel such as dispersion, timing jitter and non-linear effects.

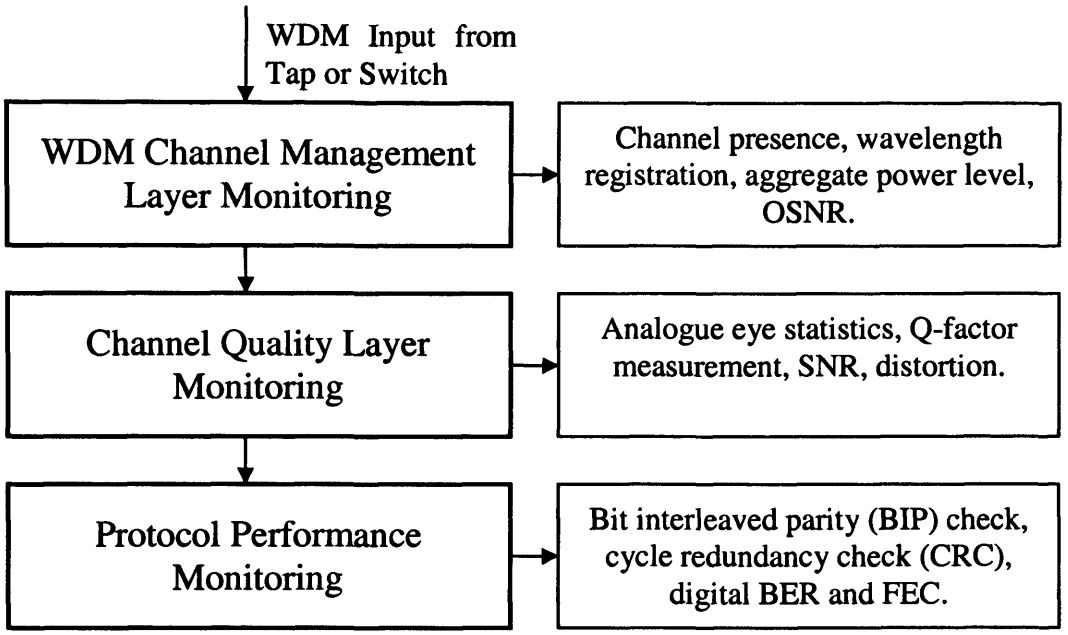

Figure 3.2 Three layers of OPM reference model

The third level of the OPM reference level is protocol performance monitoring (PPM). This implies scrutinising the end to end performance of an optical channel and estimating the BER by means of Error Detection Code (EDC) methods. These include BIP-8 for SONET/SDH and digital wrappers (ITU-T recommendation G.907) and CRC for generic framing procedure (GFP). For more information on these methods, refer to appendix 1. Most analogue performance monitoring methods that will be discussed in the next section fall into either layer 1 or layer 2 of this OPM reference model. One exception to the rule are pilot tones where they can be used for channel detection and registration (layer 1) and for distortion monitoring (layer 2).

3.4 Optical Performance Monitoring Techniques

Future all optical networks (AON) will transport a variety of voice, data and video signals over optical channels regardless of their format or bit rate. One major obstacle in these networks is the transparent implementation of performance monitoring, fault localisation and network management. Optical channels are affected by two types of degradation: noise and distortion. Distortion includes chromatic dispersion, PMD and fibre non-linearities whereas noise is mainly generated by amplifiers (ASE), semiconductors (thermal and shot noise) and interferometric crosstalk.

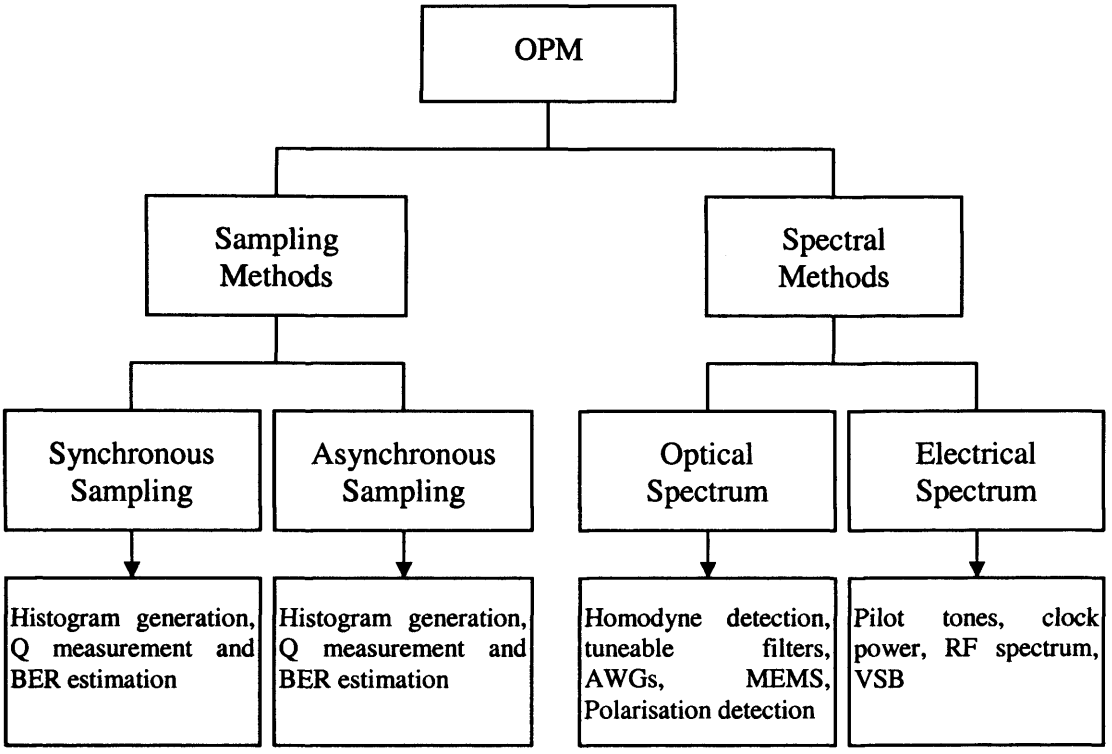

Figure 3.3 Taxonomy of optical performance monitoring methods

Numerous OPM techniques to detect these impairments have been proposed and can be divided into two categories: spectral methods and sampling methods as illustrated in Figure 3.3. The former is further divided into optical and electrical techniques. The optical spectrum is measured by using highly sensitive optical components and can provide OSNR and channel identification. Unfortunately, there is not a strong correlation between the optical spectrum measurements and the end-node signal quality since it does not measure signal distortion. Electrical spectrum monitoring, which assesses the encoded signal, is a better measure of the signal quality because it is sensitive to both noise and distortion. This includes pilot tones, clock power and vestigial side bands (VSB). Sampling methods on the other hand are divided into synchronous and asynchronous techniques. They are both used to measure the Q-factor which is strongly related to the BER and thus sensitive to the same impairments as the end-node receiver. The asynchronously-generated histogram differs from the synchronous one as it also samples the transitions between the marks and the spaces, making it more difficult to evaluate their average levels and the noise level around them.

3.4.1 Spectral Methods

3.4.1.1 Optical Spectrum Methods

Intuitively the most direct approach of implementing OPM in optical networks is to measure the optical spectrum and determine the optical power and the OSNR of each wavelength. This can easily be achieved using an optical spectrum analyser (OSA) and not surprising all the OPM methods that fall into this category can simply be considered as small and low cost OSAs. They typically use three types of technology: filters, either tuneable such as Fabry-Perot or fixed such as fibre Bragg grating, Micro-Electro-Mechanical Systems (MEMS) and homodyne/heterodyne detection.

3.4.1.1.1 Homodyne Detection

This method is used to monitor each optical carrier frequency, its relative power and its adjacent noise level. It has a very high wavelength resolution and is suitable for densely spaced optical channels application [Amr'99]. Its configuration setup is shown in Figure 3.4. A local tuneable laser is swept across the entire spectrum and each time it coincides with a channel frequency, a pulse signal is generated. This signal is proportional to the power of the channel and the local oscillator. An optical polarisation scrambler is used at the output of the frequency swept laser in order to avoid the influence of possible polarisation mismatch.

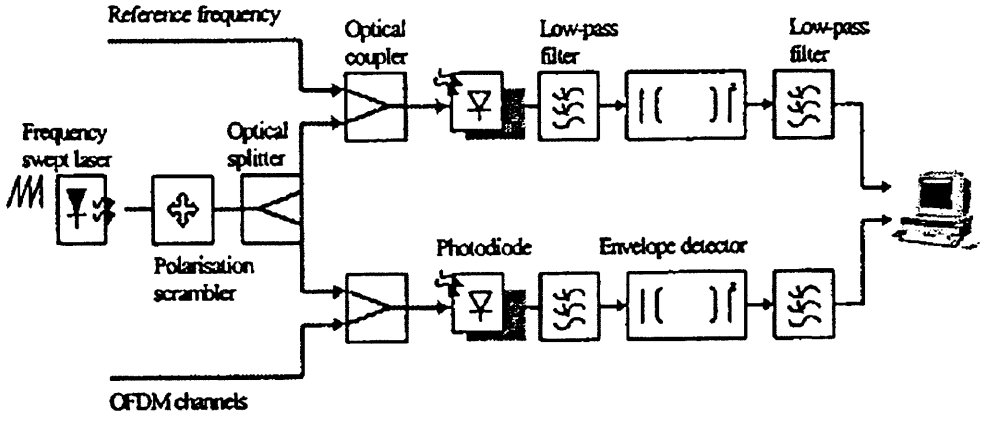

Figure 3.4 Homodyne detection configuration setup [Amr'99]

An optional branch of reference frequencies can also be homodyned (as shown in the figure above) and the output compared to the output of the tapped WDM channel in order to obtain more information about their exact frequencies (by comparing the two pulses wrt time). This method is effective in detecting any channel absence and hence detects any transmission failure [Amr'00]. In addition this technique can estimate the relative power between an optical channel and the adjacent noise level and thus giving a first

estimate of the OSNR. Furthermore, it can potentially be used to detect out-of-band crosstalk if placed after an optical filter since any additional frequencies will be detected. Unfortunately no further studies are found in the literature about its accuracy, resolution or sensitivity range.

3.4.1.1.2 OSNR Monitoring Using Filters

Using optical filters is probably the most direct way of implementing OPM. Two types of filters have been widely reported in the literature: tuneable filters using mainly Fabry-Perot filters and arrayed waveguide grating (AWG) filters. The former, followed by a single photodetector, is tuned across the WDM range and relative powers are recorded. This allows the detection of operating channels and the estimation of their OSNR by comparing their relative power with the adjacent noise power. However this is very hard to achieve in densely spaced WDM since one needs a high-rejection filter with a very narrow bandwidth in order to detect the noise power without having leaks from adjacent channels. A novel method that utilises double-pass filtering and a tuneable reflector was recently proposed to solve this problem [Chu'04].

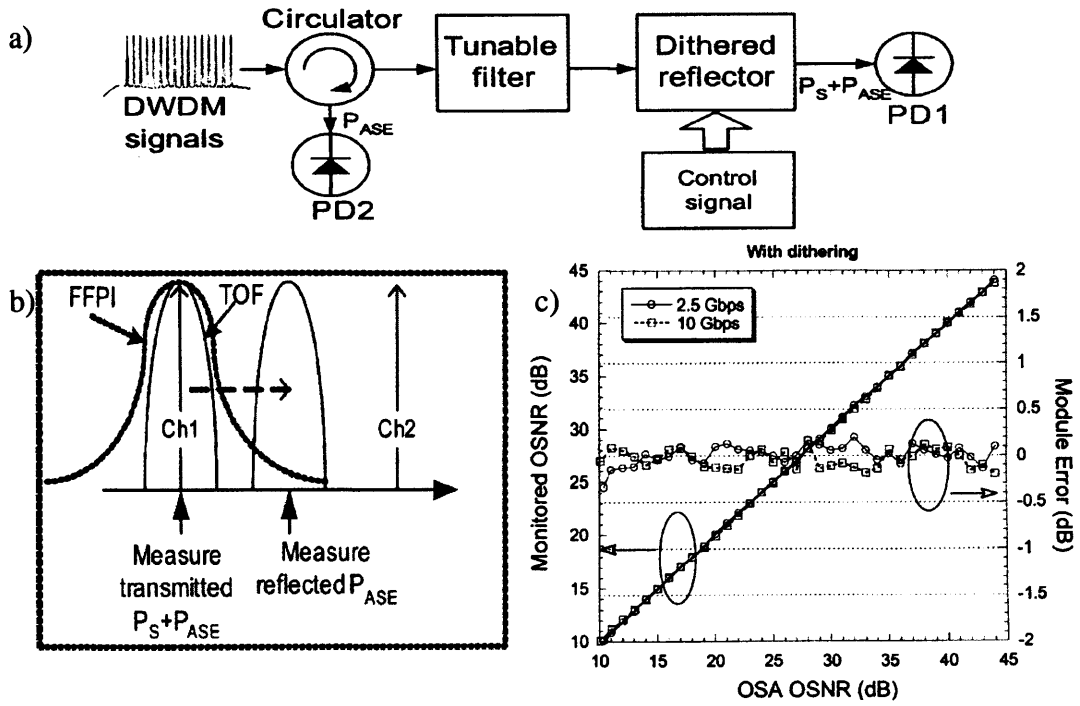

Figure 3.5 (a) Schematic diagram of the double-pass filtering method (b) Signal and noise power measurement mechanism (TOF: tuneable optical filter; FFPI: fibre Fabry-Perot interferometer) (c) Measured OSNR and corresponding errors for bitrate of 2.5 & 10Gbit/s [Chu'04]

It consists of passing the signal through a first stage of filtering to detect the combined ASE and signal powers then through a second stage of filtering where only the ASE power is measured. A schematic diagram is shown in Figure 3.5a. First the signal power

is measured at the output of the reflector (i.e. PD1) by aligning the tuneable filter to the channel position as depicted in Figure 3.5b. The reflector is then activated while the central frequency of the filter is shifted between the monitored and the adjacent channel. The signal therefore passes through a second filtering stage and is detected at the circulator output (i.e. PD2). This is equivalent to using two overlapping filters but without the attached cost of a second filter. A potential problem for the accuracy of this method arises from the circulator leakage and other reflections that might be detected at PD2 resulting in an overestimation of the noise power. This is solved by dithering the signal controlling the reflector so that the reflected signal is modulated and can easily be separated from any residual power. The measured OSNR using this technique is compared with OSNR obtained using a high-performance OSA in Figure 3.5c for bitrates of 2.5 and 10Gbit/s. It can be seen that it is very accurate (errors less than 0.4dB) for values ranging between 10 and 44dB.

The demultiplexing property of an AWG can also be used for channel identification. The AWG module is followed by a photodiode array where the position of each photo-detector is related to a particular wavelength. This property was extended to monitor OSNR by using one of the ports as a noise power monitor [Suz'99]. The experimental setup to monitor the OSNR of seven channels using an eight port AWG module is shown in Figure 3.6.

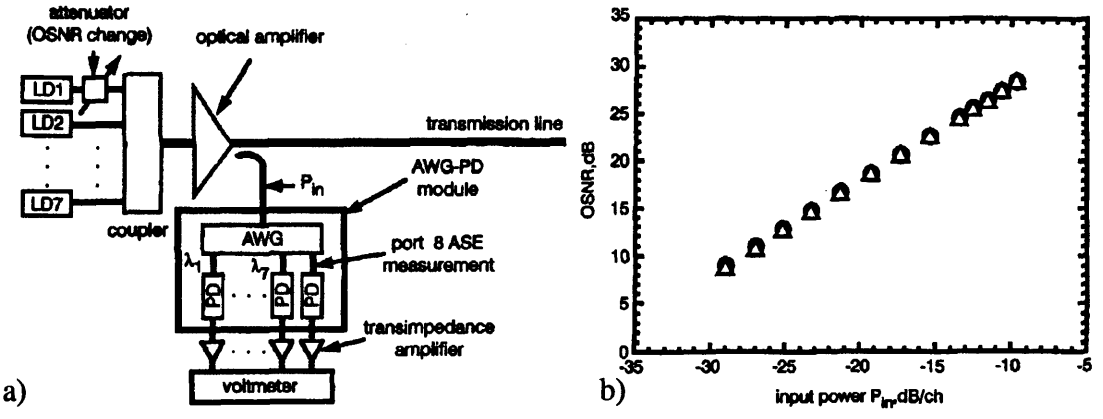

Figure 3.6 (a) Experimental setup for OSNR measurement (b) Measured OSNR using an OSA (circles) and the AWG module (triangles) [Suz'99]

The noise level generated by the optical amplifier is assumed to be flat across the entire spectrum and thus all the AWG ports will exhibit the same noise power. Port 8 of the AWG, which is not in use for optical communication, is utilised to measure the ASE noise level. The OSNR is obtained by comparing the output power of this port with the

power at the other ports. The good agreement between the results of this method and an OSA (resolution bandwidth of 0.1nm) is illustrated in Figure 3.6 for OSNR values ranging between 9 and 29dB.

It has been argued in [Nak'03] that MEMS technology offers superior resolution and speed than AWGs and tuneable filters for channel monitoring. OSNR sensitivity of more than 25dB was reported using this technology.

3.4.1.1.3 Polarisation Detection

By taking advantage of the fact that light emanating from a laser source is fully polarised whereas ASE noise is unpolarised, OSNR can be obtained by comparing the power of polarised and unpolarised light in WDM channels. Figure 3.7 shows the configuration of a PMD-immune method based on polarisation-nulling [Lee'01].

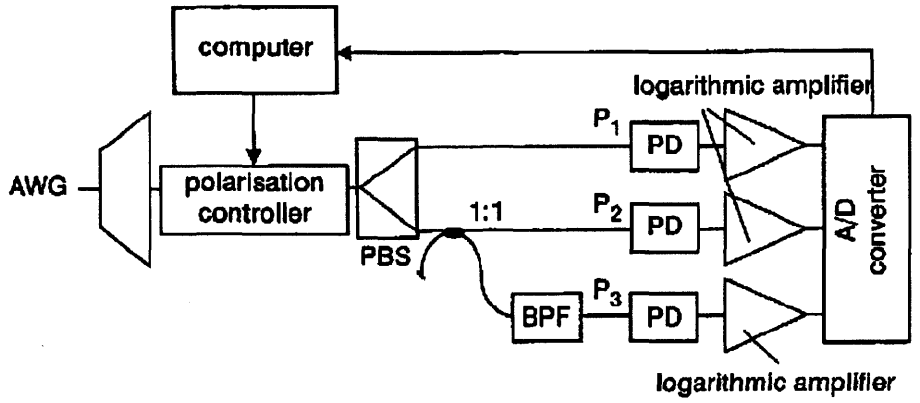

Figure 3.7 Schematic diagram of polarisation-nulling based technique for OSNR monitoring [Lee'01]. PBS: Polarisation Beam Splitter; BPF: Band-Pass Filter; PD: Photodiode

Assuming the polarisation beam splitter (PBS) has infinite extinction ratio and no PMD, the demultiplexed signal is split into two polarisation components, one containing the signal and a portion of ASE noise while the other contains just the remaining ASE noise. This is achieved by maximising the output power of one arm by means of a polarisation controller. However, since the PBS has a finite extinction ratio (~24dB) and PMD cannot be fully compensated for, there will be some leakage of the signal power (ε) in the ASE branch that must be considered for accurate OSNR estimation. To find ε, the ASE noise component is further divided into two equal parts with one part going through a narrow band-pass filter (BPF). Therefore the optical powers at the photodiodes can be described as:

$$\begin{cases} P_1 = P_S(1-\varepsilon) + 0.5P_{ASE} \\ P_2 = 0.5P_S\varepsilon + 0.25P_{ASE} \\ P_3 = 0.5P_S\varepsilon + 0.25\alpha P_{ASE} \end{cases}$$

where α is the passband width determined by the characteristics of the AWG and the BPF. By solving the above three simultaneous equations with three unknowns ε, P_S and P_{ASE}, the OSNR can be determined. The results show that this method can monitor OSNR with an accuracy of ±1dB for a range of 16-30dB.

Another polarisation method proposed in [Pem'04] relies on estimating the degree of polarisation (DOP) of the signal by evaluating the Stokes parameters as explained in the previous chapter (Section 2.2.1.4). DOP is the ratio between the power of the polarised component and the total power of the signal and thus is related to the OSNR by the following expression:

$$OSNR = \frac{DOP}{1-DOP}$$

This technique was experimentally tested and proved to be accurate for OSNR up to 26dB. However it is not clear how it will cope with signal depolarisation due to second order PMD or polarisation dependent loss (PDL). In addition, this method can also be used for PMD monitoring [Fra'99]. As explained in the previous chapter, the DOP of a fully polarised signal is equal to 1 whereas its value decreases to 0 for randomly scrambled light. Assuming a fully polarised light is launched at the transmitter, the DOP of the received channel after suffering from PMD decreases to values below 1 as explained in Figure 3.8.

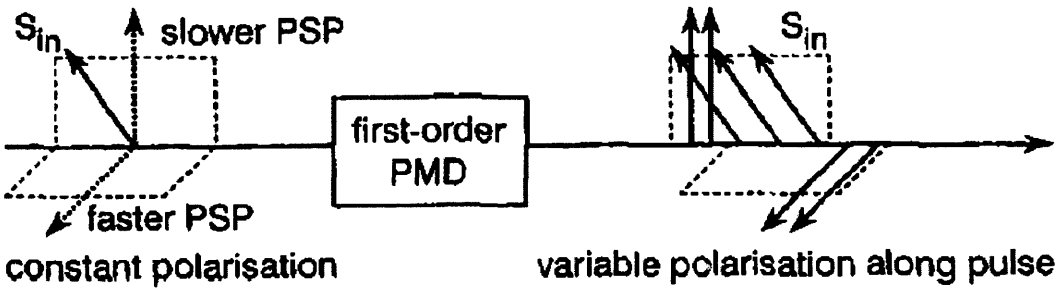

Figure 3.8 Impact of PMD on polarised light and its degree of polarisation [Fra'99]. PSP: Principal State of Polarisation

At the output of the link, the leading edge of the pulse is polarised along the fastest principal state of polarisation (PSP), the middle of the pulse has the same SOP as the input pulse while the trailing edge is polarised along the slowest PSP. As a result, the end

DOP is modified except when the launched pulse is polarised along one of the PSPs or when the differential group delay (DGD) is 0ps. Since the signal DOP decrease is dependent on the amount of signal pulse distortion caused by PMD, it can be used as a feedback signal for PMD compensation. It was demonstrated in [Kik'01] that using this method allows unambiguous PMD monitoring for a range of up to a DGD=110ps for 10Gbit/s systems (approximately equivalent to the bit period). The main advantage of this approach is its insensitivity to dispersion and modulation chirp. However, ASE noise and fibre non-linear effects (SPM and XPM) have significant effect on the DOP of a signal and can introduce measurement errors of up to 60ps [Kik'01].

3.4.1.1.4 Issues Related to Optical Spectrum Monitoring

OSNR monitoring is of paramount importance in the evaluation of optical amplifier performance and fault isolation throughout optical networks. Most of the monitoring techniques proposed in this area try to compare the signal power with the noise power adjacent to the channel. This may give erroneous results in case of dense WDM (DWDM) systems since there is no or little room to measure the noise between the channels as illustrated in Figure 3.9 [Kil'02].

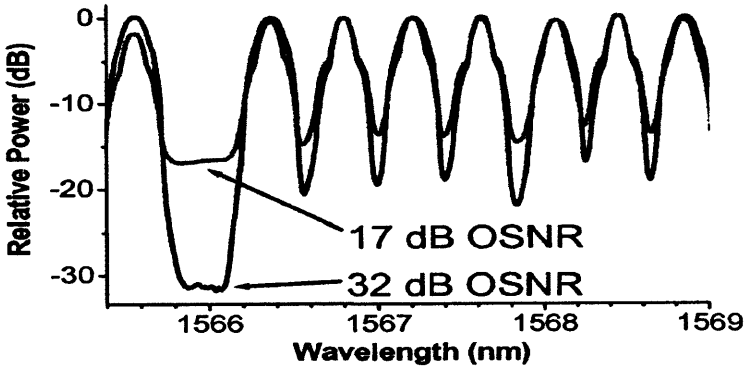

Figure 3.9 Optical spectrum of 10Gbit/s RZ data, 50GHz spacing DWDM channels with 17 and 32dB OSNR (0.1nm resolution bandwidth) [Kil'02]

It can be seen in Figure 3.9 that for a 10Gbit/s RZ system with 50 GHz channel spacing the actual noise level near 1566nm, where the channel has been switched off, is significantly different from the minimum optical power between the other channels especially at high OSNRs. This is further accentuated in switched networks where adjacent channels may have different propagation histories and where crosstalk may be added due to the imperfect characteristics of optical add drop multiplexers (OADMs) and optical cross-connects (OXCs). Polarisation analysis can be added to alleviate this

problem, but polarisation methods also depend on the filter technology and bandwidth utilised. Therefore there is a trade off between the wavelength density of the system and the accuracy of optical spectral monitoring of OSNR.

3.4.1.2 Electrical Spectrum Methods

Unlike the aforementioned techniques, electrical spectrum methods measure signal quality by assessing the amplitude power spectrum of the encoded data (without the optical carrier). Noise and distortion usually affect the magnitude of the power spectrum and by monitoring this amplitude variation, signal quality may be determined. The first technique discussed in this section consists of superimposing a low-frequency monitoring tone on the signal and using it as a base for impairment monitoring. The other methods measure either the clock amplitude of the signal or the phase-shift between the clock components.

3.4.1.2.1 Sub-Carrier Multiplexing/Pilot Tones

This technique consists of adding a tone (or a sub-carrier) to the baseband to determine the health of optical channels without knowing the origin or transport history of the data. By monitoring the pilot tone amplitude, parameters such as signal power, wavelength, OSNR, CD and PMD can be extracted [Ben'00]. Historically, any added tones in the kHz regime are called "pilot tones" and the ones in the MHz/GHz regime are labelled "sub-carrier multiplexing" and they are interchangeably used in the literature. The strength of this approach lies in the simplicity of processing low frequency signals and the fact that the tones travel the complete optical path with the baseband and thus suffer from the same noise and distortion. The use of this technique for optical-path supervision was successfully demonstrated in many experiments [Kon'99][Kwa'00].

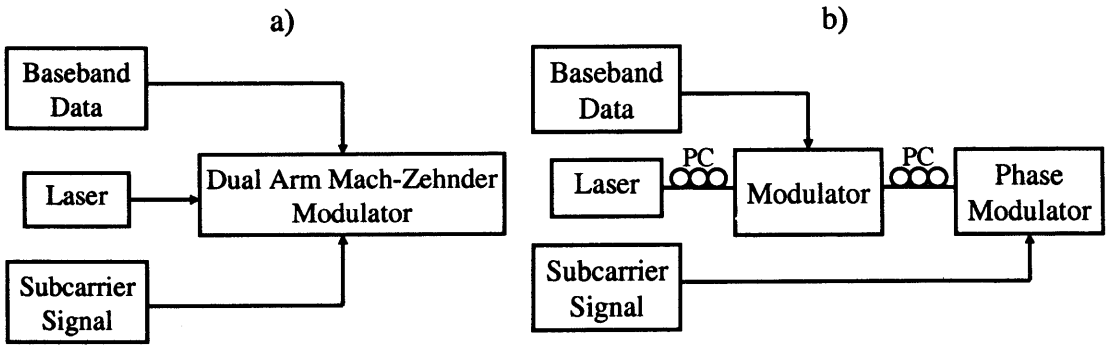

Figure 3.10 Pilot tone generation (a) Amplitude modulation only [Ros'00] (b) Amplitude or phase modulation [Pak'03]

The pilot tones are added by means of dual arm modulators or by cascading two modulators as shown in Figure 3.10. There are three possible ways of adding a tone to a signal: by amplitude modulation (AM), phase modulation (PM) and frequency modulation (FM). The monitoring capability of each modulation format will be discussed in turn.

AM Tones

The AM tone based technique is suitable for channel identification and overhead transmission since each channel is assigned an exclusive tone frequency [Ham'97]. It also offers OSNR monitoring capability through the measurement of the carrier-to-noise ratio (CNR) since they are linearly related. It has been shown in [Ben'00] that for an OSNR of less than 30 dB the pilot tone method gives the same results as with an OSA measurement. Additionally, dispersion introduces a phase shift between the lower and upper sidebands of the tone leading to a change in its RF amplitude after detection as illustrated in Figure 3.11.

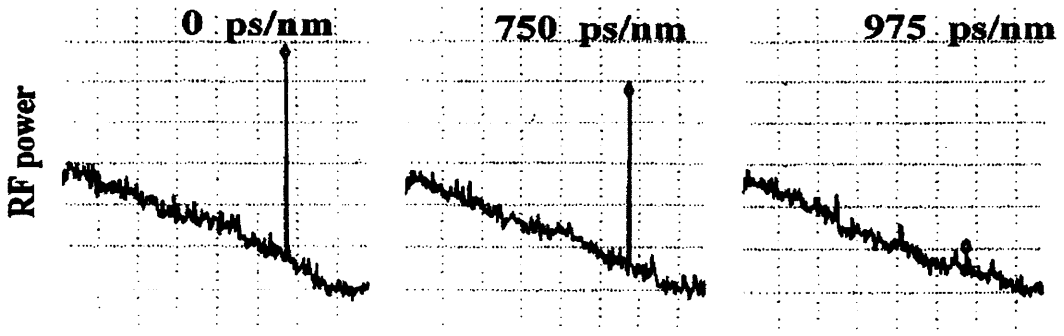

Figure 3.11 RF spectra of an 8GHz tone in a 10Gbit/s system with different dispersion values [Pet'02]

It can be seen from Figure 3.11 that the amplitude of the tone decreases as the dispersion increases and it is governed by the following equation [Pak'03]:

$$P_{AM} \propto m\cos\left(\frac{\pi DL\lambda^2 f^2}{c}\right)$$

where m is the modulation depth, f is the subcarrier frequency, λ is the carrier frequency, c is the speed of light and D is the dispersion parameter. The resolution of this technique can be improved by increasing the tone frequency, but this reduces the measurement range. For example, a 3GHz subcarrier gives a measurement range of about 7000ps/nm with a resolution of 1360ps/nm for every 1dB drop in power whereas a 9GHz tone has a range of only 675ps/nm but with 10ps/nm resolution [Per'02]. A potential problem with

this approach is that it needs a reference power level (at zero dispersion) that is used as a base for CD calculations. This might not be possible in dynamic networks where losses and power gains are randomly varying. This can be solved by modulating two tones for each channel and using their power ratio to eliminate any arbitrary power fluctuation [Ros'00]. Another approach is to measure the relative dispersion-induced delay between the subcarrier sidebands and the baseband [Dim'00]. It was shown that for a 2.5Gbit/s system and a 16.4GHz subcarrier, dispersion over a distance of 90km can be measured with fine and medium accuracy.

As for the baseband signal, the subcarrier tones are also affected by PMD. The latter affects the received subcarrier power in a similar way as dispersion although the tone amplitude is inversely proportional to the DGD. This could be exploited to our advantage in order to mitigate the deleterious effects of PMD. By measuring the amplitude of a single sideband of the subcarrier (Figure 3.12a), the contribution of CD can be eliminated [Nez'04a]. This also has another advantage as shown in Figure 3.12b.

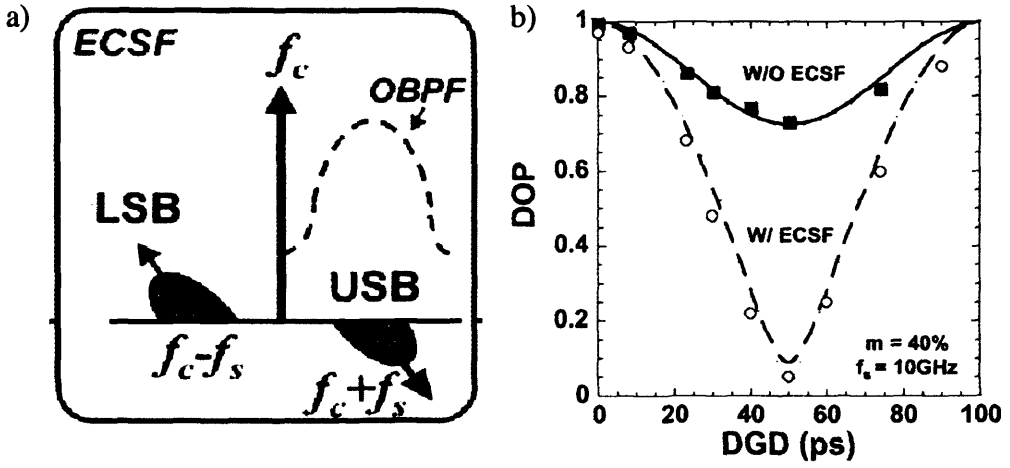

Figure 3.12 a) Using an optical bandpass filter (OBPF) to filter out a single sideband of the subcarrier (b) Subcarrier DOP sensitivity to DGD with filtering (circles) and without filtering (squares). Solid and dashed lines are the theoretical values [Nez'04a]

The tone's DOP sensitivity to DGD/PMD (squares) is typically negligible, due to the high optical power of the carrier compared to the subcarrier. By filtering out one sideband of the subcarrier, the sensitivity (circles) is significantly enhanced and therefore DOP-based DGD monitoring can be applied to pilot tones.

PM Tones

When a phase modulated optical signal propagates through a dispersive fibre, the phase difference between the optical carrier and the sidebands changes. This in turn results in a

fluctuation of the amplitude, a phenomenon known as phase modulation to amplitude modulation (PM-AM) conversion. After direct detection, the amplitude modulation index (m) of the detected current measured at the original phase modulation frequency (f_m) is given by [Mur'95]:

$$m = 4\sum_{n=0}^{\infty} J_n(m_\phi)J_{n+1}(m_\phi)\sin(2n+1)\theta$$

where $$\theta = \frac{\pi f_m^2 \lambda^2}{c} D(\lambda)L$$

J_n is the first kind Bessel function of order n, λ is the wavelength of the carrier, $D(\lambda)$ is group velocity dispersion, L is the fibre length and m_Φ is the phase modulation index. It is clear when looking at the above equations that the AM component is determined by the phase angle θ, which is a function of the DL product. As mentioned in the previous section, a good compromise between the AM tone frequency, range and resolution have to be found in order to monitor dispersion. This is not the case when using PM tones because the modulation index at the receiver increases (almost) linearly with dispersion even at low subcarrier frequencies as shown in Figure 3.13a [Pak'03]. This figure shows the measured modulation indices of an 8GHz AM tone and a 2GHz PM tone with a phase modulation depth of 0.09π.

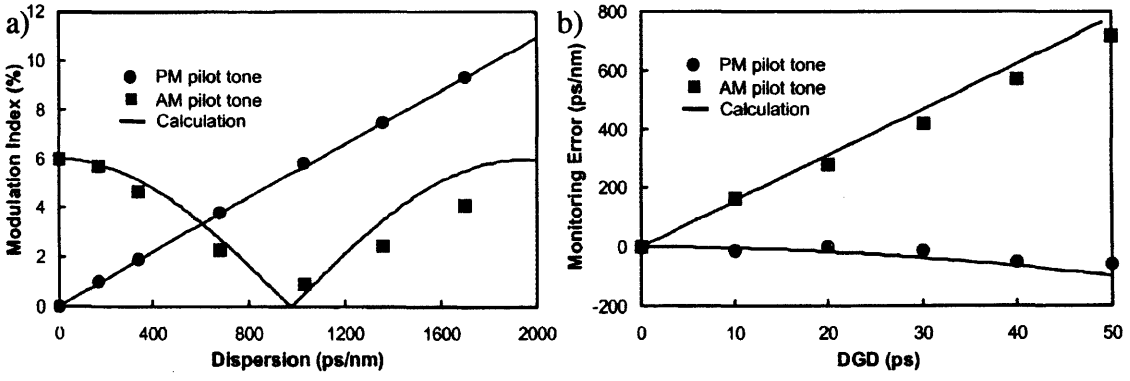

Figure 3.13 (a) Measured modulation index of pilot tones with varying dispersion (b) Monitoring errors due to PMD [Pak'03]

Moreover, the PM tone technique is more robust to the effect of PMD than AM tones. Figure 3.13b shows the monitoring errors when dispersion was set to zero and the DGD is incremented from 0 to 50ps. At a DGD=30ps, the error in monitoring CD using the AM method was 420ps/nm whereas it was only 30ps/nm for the PM. However, SPM also causes phase modulation of the signal and can have a significant impact on the PM

technique. It was demonstrated in [Pak'02a] that SPM-induced errors increase significantly with increasing tone frequency and a 30ps/nm error margin was observed using a 2GHz tone. This can be reduced to <7ps if a frequency between 300MHz and 1GHz is used [Pak'02a] although this would decrease the monitoring resolution.

FM Tones

Frequency modulated pilot tones are generated by slightly dithering the carrier frequency. This can be achieved by temperature dithering of DFB lasers or by using wavelength-tuneable sources (e.g. DBR laser). It has recently been demonstrated that this method could monitor wavelengths and powers of a WDM system with accuracies better than ±4GHz and ±1dB respectively even after 640km of SMF transmission [Pak'04]. The advantage of using this modulation technique is that, unlike with AM, it does not suffer from the generation of ghost tones due to stimulated Raman scattering (SRS) and EDFA cross gain modulation as will be discussed next.

Issues Related to Pilot Tones

Pilot tone performance is affected by the number of wavelengths operating in the network, the frequencies used and the modulation index [Ham'97]. The power spectral density (PSD) of the optical signal is the dominant noise for the pilot tone. When many optical signals are multiplexed (WDM), their PSDs are summed, leading to a degradation in the pilot-tone's carrier-to-noise ratio (CNR). The latter is proportional to 1/Ratio, which is defined as:

$$\text{Ratio} = N(N+1)/2$$

assuming that N optical signals, of equal optical powers, are multiplexed together.

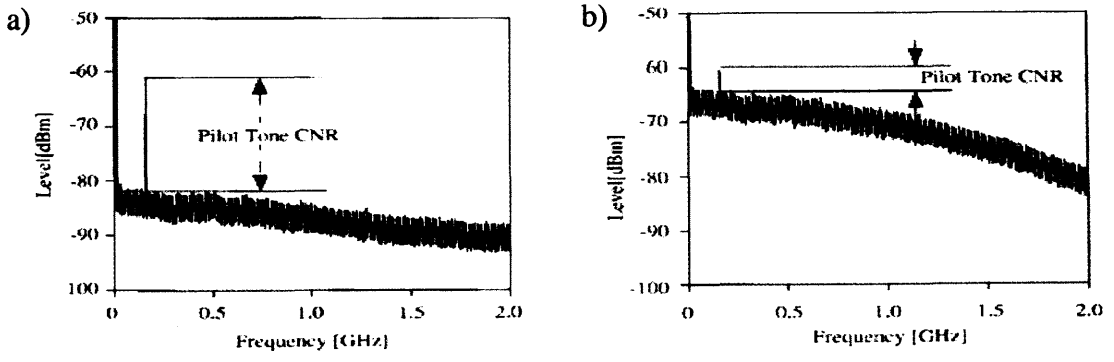

Figure 3.14 Pilot tone power spectral density at 2.5 Gb/s of (a) a single wavelength (b) 8 multiplexed wavelengths [Ham'97]

Hence the pilot tone CNR in a system with eight wavelengths is decreased by 15.5 dB compared to the value with a single wavelength. This example is shown in Figure 3.14. At a frequency of a few tens of kHz, the pilot tone performance is affected by the slow dynamic properties of the EDFAs [Sun'97]. The pilot tones that are superimposed on every optical channel experience cross-gain modulation and cross-phase modulation leading to the appearance of "ghost tones". These tones can cause errors and mislead the network management system. Additionally, ghost tones can also arise from the stimulated Raman scattering (SRS) as shown in [Chs'00]. These effects can seriously undermine the pilot-tone based monitoring technique (maximum transmission distance of 400km for a 32-channel WDM network) and can only be negligible for tone frequencies higher than 100 MHz. Increasing the tone frequency leads to an increase in the CNR of the pilot tone and, to a certain extent, a decrease in the power penalty on the optical signal. It was argued in [Ham'97] that the main optical signal power penalty is significantly improved only when the pilot tone frequency is over 1GHz in a 2.5Gbit/s network and 4GHz in a 10Gbit/s system. However at these frequencies the pilot tone technique is no longer simple and cheap because more complicated (high speed) circuitry needs to be deployed for tone detection in addition to transmitter modification. Finally, this technique should also work in networks where wavelength conversion is needed. However, the subcarriers need to be blocked and then reinserted after wavelength conversion because the tones are very sensitive to the converters nonlinear transfer function which may lead to a big variation in the amplitude of the pilot tones or to the appearance of ghost tones [Klo'98].

3.4.1.2.2 RF Clock-Power Detection

As with subcarrier multiplexing, RF clock-power extraction methods take advantage of the distortion-induced RF power fading/regeneration for monitoring purposes. Unlike the previous method, this one does not add a new tone but monitors the relative RF clock power at the receiver [San'96]. This is more advantageous since no transmitter modification is required. The electrical spectrum of a NRZ signal does not contain any element at the clock frequency because after quadratic detection, many frequency components in the optical spectrum beat with each other to cancel it out [Hei'03]. However this is no longer true in the presence of chromatic dispersion, since it introduces frequency-dependent optical phase shifts in the amplitude spectrum. As a result, a dispersion-dependent clock component appears in the electrical spectrum and this dependency is illustrated in Figure 3.15a [Pan'01].

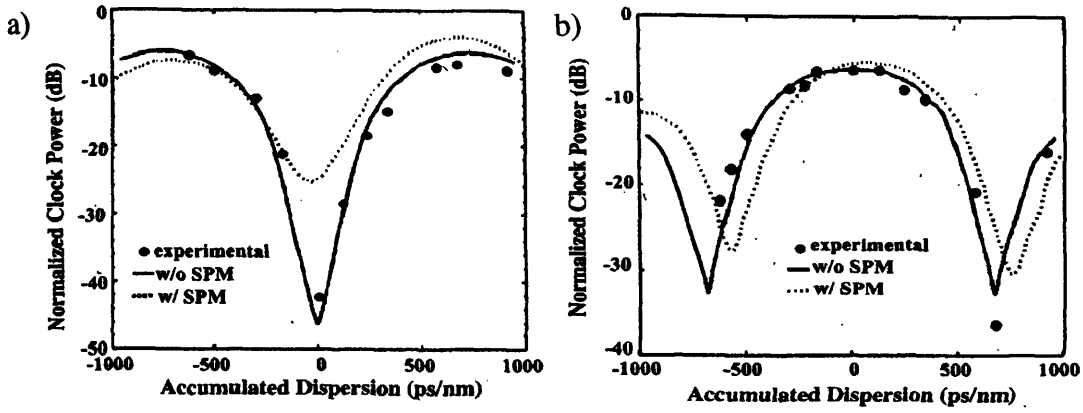

Figure 3.15 (a) NRZ clock regeneration as a function of dispersion in 10Gbit/s systems (b) RZ clock fading as a function of dispersion in 10Gbit/s systems [Pan'01]

It can be observed that the clock power changes unambiguously over a dynamic range of 30dB for dispersion up to ±850ps/nm at 10Gbit/s. Additionally, the curve is symmetrical wrt zero dispersion since both positive and negative dispersion have the same effects on non-chirped data. However non-linear effects disturb this symmetry and decrease the relative dynamic range to 20dB. RZ format on the other hand does contain a clock component in the electrical spectrum even without dispersion. Non-zero dispersion however leads to a fading in the clock power as demonstrated in Figure 3.15b. It can be seen that CD can be unambiguously monitored for a range up to ±620ps/nm at 10Gbit/s. The curves shown in the figure above are periodic and repeat each time the phase shift $\Delta\phi$ between the upper and lower sidebands of the clock is 2π. This shift is given by:

$$\Delta\phi = 2\pi \frac{\lambda_0^2}{c} B^2 DL$$

where B is the bitrate, D is the dispersion coefficient and L is the fibre length. The above equation shows the technique's dependency on the bitrate and it can be concluded that a fourfold increase in the bitrate leads to a decrease by a factor of 16 in the range. For instance, the range will decrease from 850ps/nm to 53ps/nm if the system is upgraded from 10 to 40Gbit/s. This range only represents 3km of standard single mode fibre (SMF) if D is assumed to be 17ps/nm.km. Although this method provides rapid dispersion monitoring, it is limited by the bitrate and deleterious effects such as PMD and non-linearities. It was suggested in [Nez'04b] that by filtering out one of the clock sidebands, the RF power will only be affected by PMD and loses sensitivity to CD. The asymmetric filtering operation is shown in Figure 3.16a while Figure 3.16b illustrates the relationship

between the normalised clock power and the DGD (with polarisation ratio γ=0.5) for NRZ.

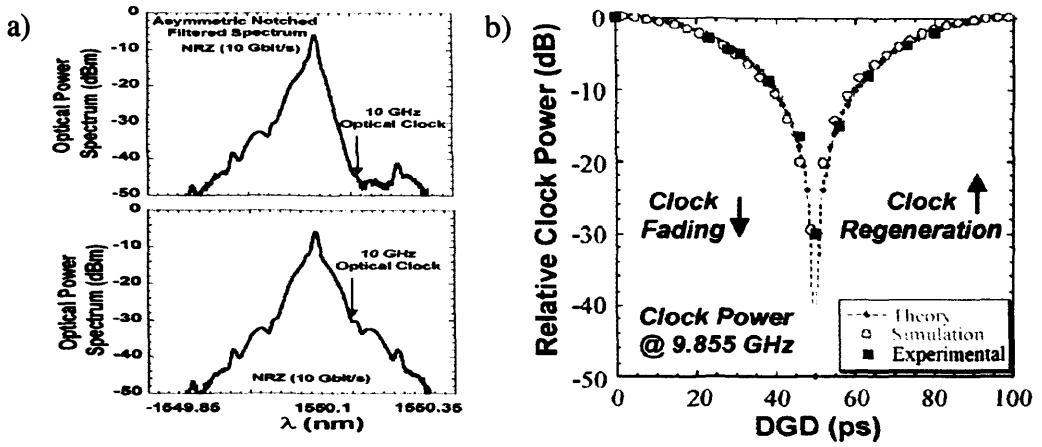

Figure 3.16 (a) Spectrum showing the asymmetric filtering of the clock sideband (b) Relative clock power as a function of DGD (worst case) [Nez'04b]

It can be seen that the clock power fades for DGD values ranging between 0 and 50ps and is regenerated from 50 to 100ps and therefore this method can only be unambiguously used up to a range of 50ps (half the bitrate). This relationship is also periodic and the range is dependent on the bitrate. For instance, in 40Gbit/s systems, the range is divided by 4 i.e. 12.5ps.

3.4.1.2.3 Clock Phase-Shift Detection

This technique uses an optical filter to select the upper and lower vestigial-sidebands (VSB) signals in the optical data of either RZ or NRZ format and monitor the relative clock phase-shift caused by dispersion as shown in Figure 3.17a [Yuq'02].

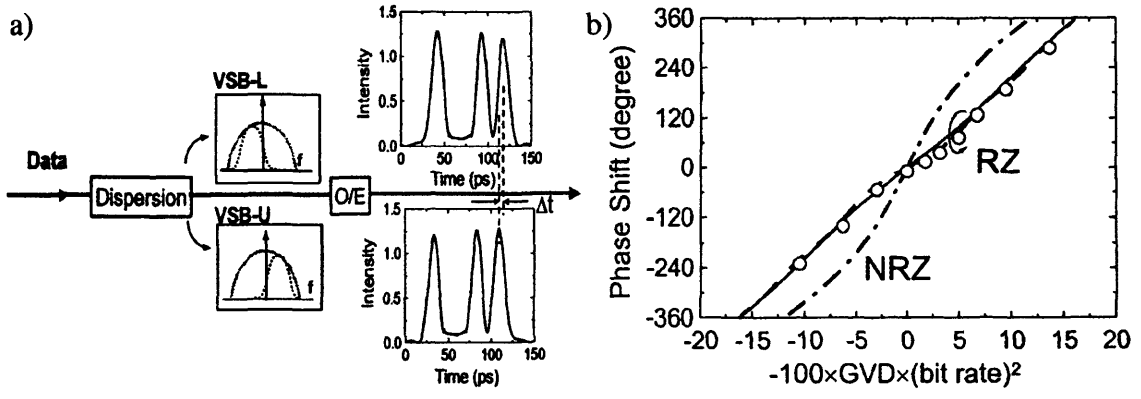

Figure 3.17 (a) CD monitoring using VSB (b) Phase shift between the two VSB signals as a function of dispersion for NRZ (dot-dash), RZ (solid) and experimental RZ (circles) at 10Gbit/s [Yuq'02]

Transmitted signals, either RZ or NRZ formats, have two optical sidebands which can be extracted using an optical filter with a bandwidth equal to the data bitrate. Since the two

sidebands occupy slightly different wavelengths, they undergo different propagation delays due to chromatic dispersion. This results in a clock phase shift $\Delta\Phi$ between the two copies given by:

$$\Delta\phi = 2\pi BDL\Delta\lambda$$

where B is the bitrate, DL is the accumulated dispersion and $\Delta\lambda$ is the effective wavelength shift between the two VSBs. The latter is a function of the modulation format and the filter parameters. The dispersion-induced phase shifts between the upper and lower sidebands for RZ and NRZ formats are shown in Figure 3.17b. The advantage of using this technique over the previous one (clock power detection) is that it is insensitive to PMD. As mentioned before, PMD leads to fading in the clock power of the single sideband but does not affect the phase shift between the two sidebands. On the other hand, if the attenuation of the clock power is considerably high then phase comparison becomes impossible. This could be solved by adding a clock recovery module after the optical filters in order to regenerate the clock. Another advantage of this method is that it has a slightly higher monitoring range of 1700ps/nm at 10Gbit/s. Unfortunately, and as with the previous method, the range scales with the square of the bitrate i.e. only 106ps/nm at 40Gbit/s.

The RF clock power and the VSB are very rapid methods (in ms) for dispersion and PMD monitoring and may be suitable for wavelength routed optical burst switched networks. However, they suffer from serious drawbacks the first of which is cost. These techniques require state of the art electrical and optical filters with high-rejection slopes that are expensive to acquire. In addition, it is impractical to utilise one monitoring circuit for each channel and therefore the optical filter has to be swept through the entire spectrum which makes the techniques relatively slow. Furthermore, they are bitrate and format dependent and their range scales poorly with the bitrate.

3.4.2 Sampling Methods

Sampling methods explore the statistical information of an optical signal to derive the histogram then the Q-factor which is strongly correlated to the bit error rate (BER) of a transmission channel. Unlike spectral methods, they are sensitive to noise effects and all sources of distortion and can be integrated into a single electronic circuit. Furthermore, they give the best bit error rate (BER) estimation which is the "bottom line" signal quality measure that is delivered to the customer or the client layer. However, they may be costly

in WDM networks when implemented in every network element since they need demultiplexing and opto-electrical conversion of the signal.

Sampling methods can be divided into two categories: synchronous and asynchronous. The latter has the advantage of performing sampling without the need for a clock recovery but loses accuracy and impairment details. Asynchronously-generated histograms contain the transition samples between the marks and the spaces which make signal quality monitoring more problematic. Synchronous sampling is the closest method to a full BER measurement and can be used to identify and evaluate different sources of degradation. In addition, the cost of the clock recovery circuit is not an issue since a multi-bitrate clock recovery can be bought for less than $150 nowadays. Before exploring how these methods are used to evaluate the signal quality, it is worth discussing how they are physically implemented. Some techniques are presented in section 3.4.2.1 to illustrate how histograms are obtained. Section 3.4.2.2 focuses on the effects of selected impairments on the eye diagram in general and the histogram in particular. Finally section 3.4.2.3 discusses how the signal quality is obtained from the synchronous and asynchronous techniques.

3.4.2.1 Sampling Circuits

Sampling can be performed electronically using post-detection decision circuits or optically using an electro-optic sampling module. Post detection (electrical) sampling techniques can be further divided into single decision or dual decision circuits as described below.

3.4.2.1.1 Electrical Sampling

Histograms can be generated using a single D-type flip-flop as shown in Figure 3.18. It consists of a photodiode, a variable decision-threshold flip-flop and a pulse counter. A clock recovery circuit can be used to feed the clock input of the flip-flop if synchronous sampling is desired; otherwise an external clock is used for asynchronous sampling.

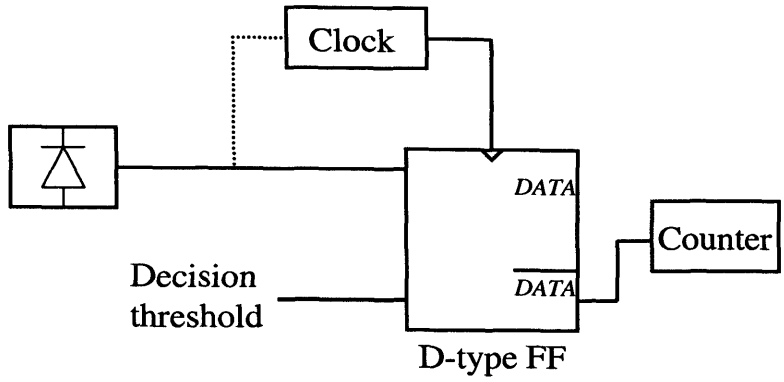

Figure 3.18 Single decision circuit configuration for histogram generation [Oht'99]

While the threshold level is swept through the eye at decision time, the number of samples that are taken as zeros is counted. This results in a step function as displayed in Figure 3.19a using numerical simulation [Oht'99]. After this, the first derivative of the data is taken and a histogram is obtained (Figure 3.19b).

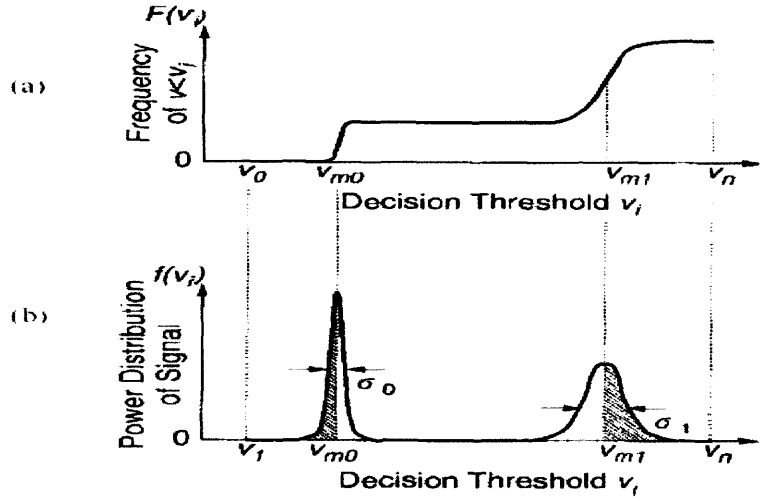

Figure 3.19 a) Number of spaces against threshold level b) Histogram [Oht'99]

This method has also been successfully verified experimentally where histograms affected by noise, dispersion and crosstalk were obtained [Dow'01]. Similarly, the histogram can be obtained using a dual decision circuit [Wie'00] as shown in Figure 3.20. In this configuration, the current output from the photodiode is split into two; one part is fed into a flip-flop with a fixed (reference) threshold level whereas the other part goes into a flip-flop that has a variable threshold. The outputs from the two flip-flops are then fed into an XOR gate. This turns to a high state only when the outputs from the two flip-flops are logically different. Like the single decision circuit, the clock inputs of the two

flip-flops can be connected either to a clock recovery circuit for synchronous sampling or an external clock for asynchronous sampling.

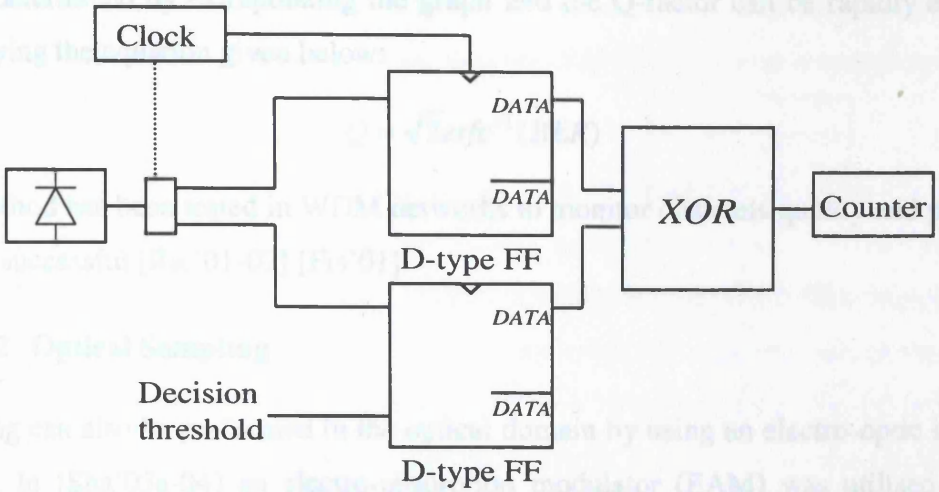

Figure 3.20 Dual decision circuit configuration for histogram generation [Wie'00]

While the threshold level of one of the flip-flops is swept through the eye, the number of ones output from the XOR gate is counted. In other words, the number of times the two decision circuits differ in their judgement (one or zero) is summed over the same decision threshold and a graph similar to Figure 3.21a is obtained. This technique was experimentally tested on a 2.5Gbit/s pseudo-random signal traversing 20 km of single mode fibre. 10dB of relative crosstalk (in-band) was introduced at the start of the link while an EDFA was placed at the end to boost the power of the signal. The output of the monitoring circuit is plotted in Figure 3.21b.

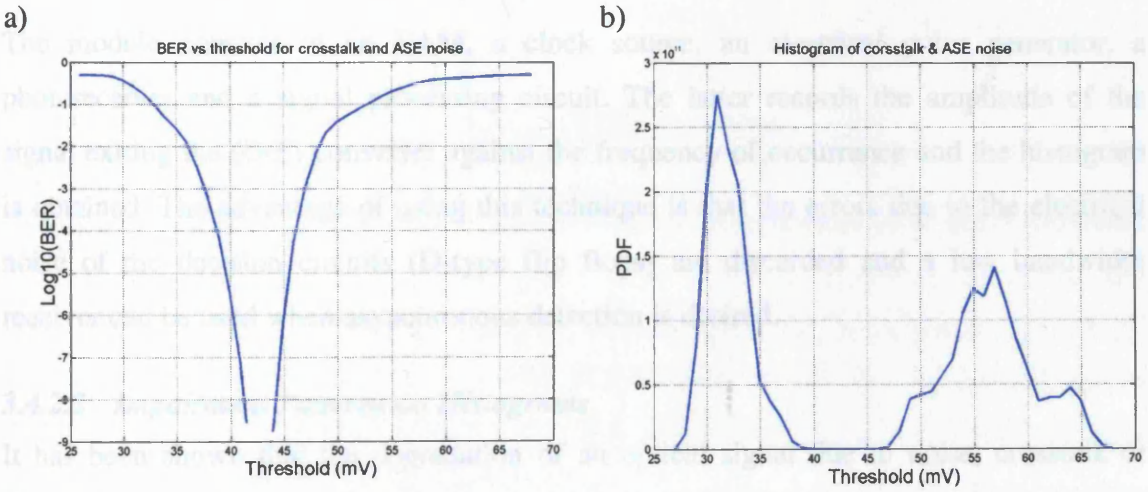

Figure 3.21 a) Number of errors against threshold level (log scale) b) Histogram

The histogram is obtained by taking the absolute value of the first derivative of the graph in Figure 3.21a (see Figure 3.21b). The advantage of this method over the single decision

one is that the number of counts from the XOR gate is significantly lower and therefore a (cheaper) low frequency counter can be utilised. In addition, the optimum decision level can be determined by extrapolating the graph and the Q-factor can be rapidly evaluated by applying the equation given below:

$$Q = \sqrt{2} erfc^{-1}(BER)$$

This method has been tested in WDM networks to monitor channels quality and proved to be very successful [Ric'01-02] [Fis'01].

3.4.2.1.2 Optical Sampling

Sampling can also be performed in the optical domain by using an electro-optic sampling module. In [Sha'03a-04] an electro-absorption modulator (EAM) was utilised for this purpose and a block diagram of the sampling circuit is shown in Figure 3.22.

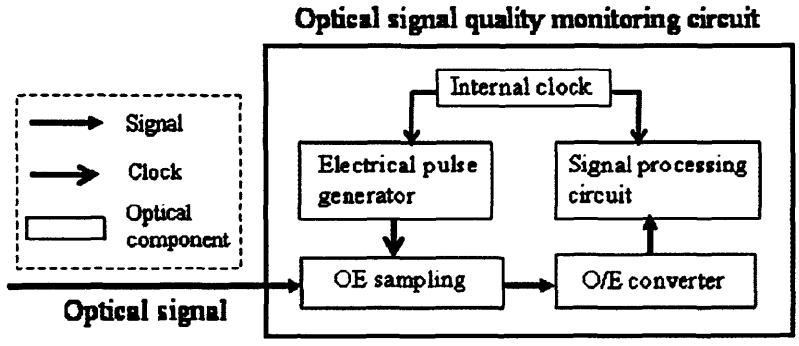

Figure 3.22 Block diagram of an optical sampling circuit [Sha'03a]

The module consists of an EAM, a clock source, an electrical pulse generator, a photoreceiver and a signal processing circuit. The latter records the amplitude of the signal exiting the (O/E) converter against the frequency of occurrence and the histogram is obtained. The advantage of using this technique is that the errors due to the electrical noise of the decision circuits (D-type flip flops) are discarded and a low bandwidth receiver can be used when asynchronous detection is desired.

3.4.2.2 Impairment Patterns on Histograms

It has been shown that the degradation of an optical signal due to noise, crosstalk or dispersion can be detected with high sensitivity by evaluating amplitude histograms [Han'98] [Mue'99]. It has also been shown that histograms, and especially the marks' histograms, take distinctive shapes (signatures) for each source of degradation.

As the perturbations act on the histograms in a distinguishable way, the definition of appropriate signatures should allow fast and reliable estimation of the transmission quality as well as the source of degradation. The effects of crosstalk, dispersion and ASE noise have been confirmed experimentally and are discussed in the subsequent sections.

3.4.2.2.1 Crosstalk

Crosstalk is one of the main sources of degradation in WDM systems [Ian'99] and consists of a transfer of power from one channel to another. This occurs because of the imperfect characteristics of various optical components such as demultiplexers and optical switches and is referred to as linear crosstalk. It can also occur because of nonlinear effects such as light scattering, FWM or XPM and this type of crosstalk is referred to as nonlinear crosstalk. The statistical effects of crosstalk on the histogram and especially on the marks' distribution have been extensively studied and lead to an arcsine distribution (U-shape) [Leg'96]. A 5Gbit/s experiment was carried out in [Mue'99] to define the effects of in-band crosstalk on the histogram and the results are shown in Figure 3.23.

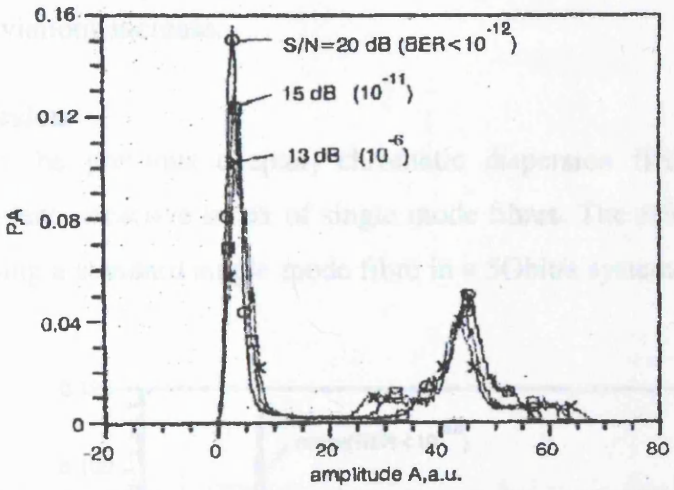

Figure 3.23 Asynchronous histograms of a 5Gbit/s channel affected by different levels of crosstalk [Mue'99]

It can be observed from the above graphs that the typical effect of intra-band crosstalk on the histogram is the appearance of a floor or a plateau around the marks curve and its width increases with increasing relative power of the interfering signal. This floor can be easily identified when BER < 10-12 [Mue'99].

3.4.2.2.2 ASE Noise

ASE noise is mainly introduced in the network by EDFAs and leads to the decrease in the signal to noise ratio of the signals. The effects of ASE noise on the histogram of a 5Gbit/s signal are shown in Figure 3.24.

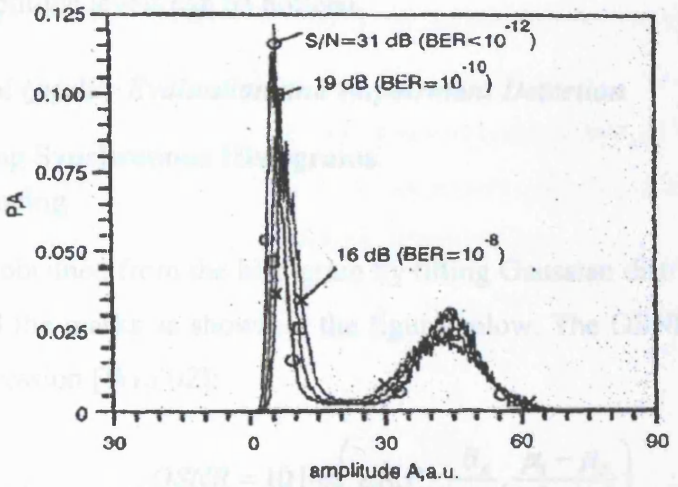

Figure 3.24 Asynchronous histograms of a 5Gbit/s channel affected by different level of ASE noise. S/N: optical signal-to-noise ratio measured by an OSA with a 0.1nm resolution bandwidth [Mue'99]

It can be observed that ASE noise gives a Gaussian shape to both the marks and spaces distributions. With decreasing OSNR, the peaks of these distributions diminish while their standard deviations increase.

3.4.2.2.3 Dispersion

As discussed in the previous chapter, chromatic dispersion finds its origin in the frequency-dependent refractive index of single mode fibres. The effects of dispersion on the histogram using a standard single mode fibre in a 5Gbit/s system are shown in Figure 3.25.

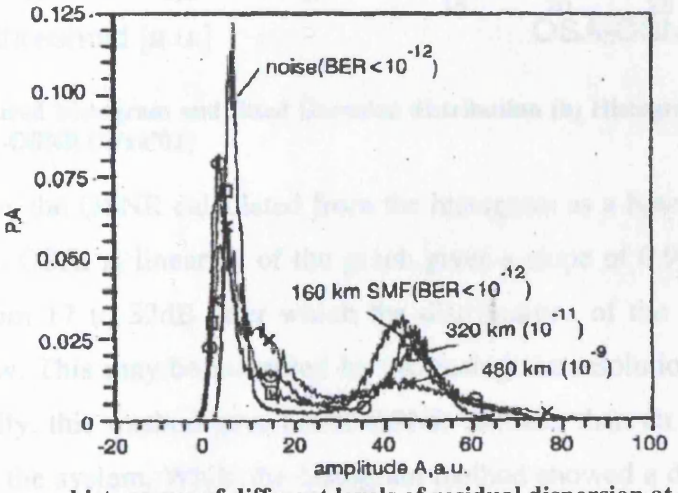

Figure 3.25 Asynchronous histograms of different levels of residual dispersion at 5Gbit/s [Mue'99]

The effect of dispersion on the asynchronous histogram is characterised by the increase of the standard deviation of both spaces and marks and an upward shift of the means of the zero levels. It can be seen that the zeros distribution is the most affected where two distinctive amplitude levels can be noticed.

3.4.2.3 Signal Quality Evaluation and Impairment Detection

3.4.2.3.1 Using Synchronous Histograms

OSNR Monitoring

OSNR can be obtained from the histogram by fitting Gaussian distributions to the PDF of the spaces and the marks as shown in the figure below. The OSNR is then given by the following expression [Wra'02]:

$$OSNR = 10\log\left(z.R.P_{ave}.\frac{B_E}{B_O}.\frac{\mu_1-\mu_0}{\sigma_1^2+\sigma_0^2}\right)$$

where z is the photodiode impedance, R is the responsivity, P_{ave} is the average optical power, B_E and B_O are the electrical and optical bandwidths.

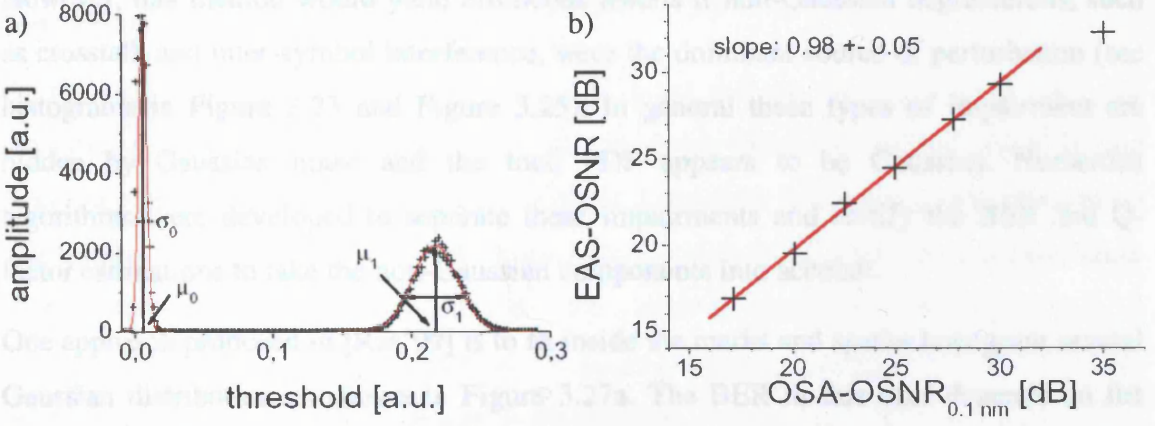

Figure 3.26 a) Measured histogram and fitted Gaussian distribution (b) Histogram-measured OSNR as a function of OSA-OSNR [Wra'02]

Figure 3.26b shows the OSNR calculated from the histogram as a function of the OSNR measured using an OSA. A linear fit of the graph gives a slope of 0.98±0.05 for OSNR values ranging from 17 to 32dB after which the distributions of the marks and spaces become too narrow. This may be increased by increasing the resolution of the sampling device. Additionally, this method gave better OSNR estimate than an OSA when FWM was introduced in the system. While the histogram method showed a decrease in OSNR, the OSA was "blind" to the change introduced by FWM.

BER/ Q-Factor Measurement

Using the histogram, the Q-factor can be directly measured. This technique for in-service signal quality monitoring is simple and independent of the signal format. It can also be applied to small signal degradation due to distortion where the eye opening penalty is smaller than 0.6dB and to that which cannot be revealed by SNR monitoring [Oht'99]. Using this method, the standard deviation and the mean values of the mark/space rail of the eye pattern are derived. Assuming that the distribution of ASE noise approximates a Gaussian distribution, the Q-factor and BER are given by:

$$BER = \tfrac{1}{2} erfc\left(\frac{Q}{\sqrt{2}}\right)$$

$$Q = \frac{\mu_1 - \mu_0}{\sigma_1 + \sigma_0}$$

where μ_1, μ_0 and σ_1, σ_0 are the mean and standard deviation of the mark and space levels respectively.

However, this method would yield erroneous results if non-Gaussian degradations, such as crosstalk and inter-symbol interference, were the dominant source of perturbation (see histograms in Figure 3.23 and Figure 3.25). In general these types of impairment are hidden by Gaussian noise and the total PDF appears to be Gaussian. Numerous algorithms were developed to separate these impairments and rectify the BER and Q-factor estimations to take the non-Gaussian components into account.

One approach proposed in [Ras'99] is to fit inside the marks and spaces histogram several Gaussian distribution as shown in Figure 3.27a. The BER in this case depends on the combination of amplitudes, means and standard deviations of all the Gaussian fits inside the histogram and is given by:

$$BER = \frac{1}{2}\left[\sum_n H(I_{0,n}).erfc\left(\frac{D - I_{0,n}}{\sqrt{2}\sigma_{0,n}}\right) + \sum_m H(I_{1,m}).erfc\left(\frac{I_{1,m} - D}{\sqrt{2}\sigma_{1,m}}\right)\right]$$

where $\sigma_{0,n}, \sigma_{1,m}$ are the standard deviations and $I_{0,n}$, $I_{1,m}$ are the means of the zeros and the ones respectively. D is the threshold level and $\sum H(I)$ is the normalised amplitude of the Gaussian distributions so that:

$$\sum_{n} H(I_{0,n}) = \sum_{m} H(I_{1,m}) = 0.5$$

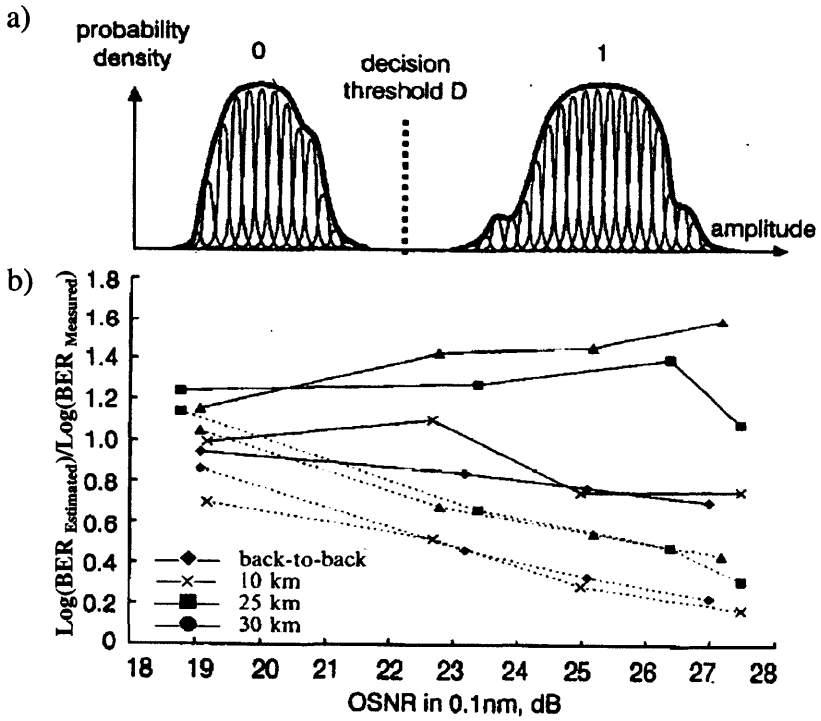

Figure 3.27 a) Superposition of Gaussian pulses on the histogram b) Ratio of estimated and measured BER against different OSNR for different fibre lengths (Dashed lines: Gaussian approximation; Solid lines: superposition of Gaussian)

Figure 3.27b shows the ratio between the estimated and the measured BER when the Gaussian estimation is used (dashed lines) and when using the equation above (solid lines) for different levels of noise and chromatic dispersion. It can be observed that when dispersion is the dominant source of degradation (at high OSNR) the first equation tends to overestimate the BER i.e. indicating that the quality is worse than what it actually is. It can be clearly seen that the method of superimposing Gaussian profiles leads to significant improvement in signal quality estimation.

Crosstalk Evaluation

Another approach proposed in [Wei'00a-b] is to subtract the Gaussian contribution from the total PDF using deconvolution. This will result in the separation of the contribution of noise from distortion and the potential identification of the different sources of impairment. As mentioned in the previous section each source of degradation affects the histogram in a specific way. However when a channel is degraded by more than one impairment, the final histogram is a convolution of their patterns. Figure 3.28a shows the marks' histogram when the signal is perturbed by 19dB relative in-phase crosstalk (solid line), half-bit out-of-phase crosstalk (dashed line) with a received power of -20dBm. The

dotted line represents the marks' distribution of 19dB in-phase crosstalk and a received power of -32dBm. Notice that due to the larger receiver noise, the plateau is now hidden.

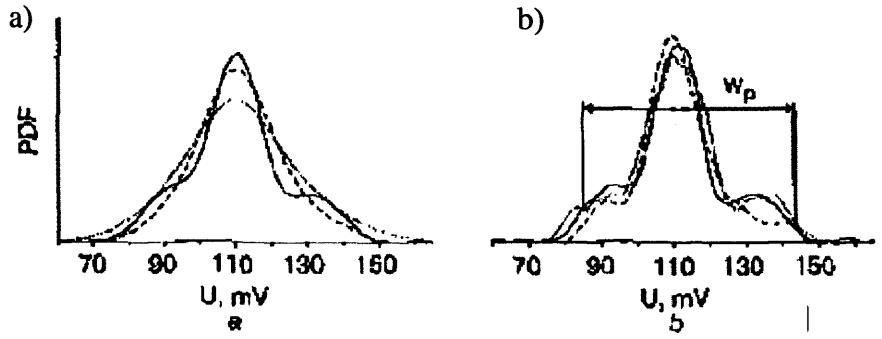

Figure 3.28 a) Histogram for 19dB in-phase crosstalk (solid), ½ bit out of phase (dashed), crosstalk and a large receiver noise (dotted). b) Histograms after deconvolution [Wei'00b]

The deconvolution is performed as follows; the measured PDF is smoothed by a Gaussian filter with width of $6/w_0$ where w_0 is the width of the central peak of the PDF. The Gaussian function is a normalised function with varying width since the exact amount of Gaussian noise in not known. For a width of the Gaussian much smaller than the one of the PDF, the deconvolved PDF has the same structure as the original. Unless the deconvolution function fits the actual Gaussian noise, the crosstalk PDF will remain hidden. The deconvolved histograms are shown in Figure 3.28b. It is observed that the plateaus can be easily identified and have equal widths regardless of the noise level. Finally the BER is calculated using Gaussian statistics for the noise and the expression given below for the crosstalk [Wei'00b].

$$BER = \frac{1}{2}\left(erfc\left(\frac{D-\mu_0}{\sigma_0}\right) + \frac{1}{2} erfc\left(\frac{\mu_1 - D}{\sigma_1}\right) + \right.$$

$$\left. \frac{1}{4} erfc\left(\frac{\mu_1 - D - \omega_p/2}{\sigma_1}\right) + \frac{1}{4} erfc\left(\frac{\mu_1 - D + \omega_p/2}{\sigma_1}\right)\right)$$

where D is the decision threshold, μ_1, μ_0 and σ_1, σ_0 are the means and standard deviations of the mark and space levels respectively and ω_p is the plateau width. The highest BER that can be measured using this method is 10^{-4} and it gives a better accuracy (two orders of magnitude) than the conventional Q-factor method. Furthermore, the width of the plateau (ω_p) can be used to evaluate the crosstalk level and it was shown that a relative crosstalk ranging between 16 and 22dB can be accurately measured [Wei'00b].

PMD Mitigation

A sampling-based technique for PMD mitigation was proposed in [Buc'01]. It consists of measuring the eye opening and using it as a feedback signal for a PMD compensator. The monitoring circuit used was a dual-decision circuit discussed in the previous section where an integrator was used as a counter after the XOR gate. The output of the integrator as a function of the decision threshold is depicted in Figure 3.29a for DGD = [0:70 ps] and γ=0.5 for a 10Gbit/s NRZ system.

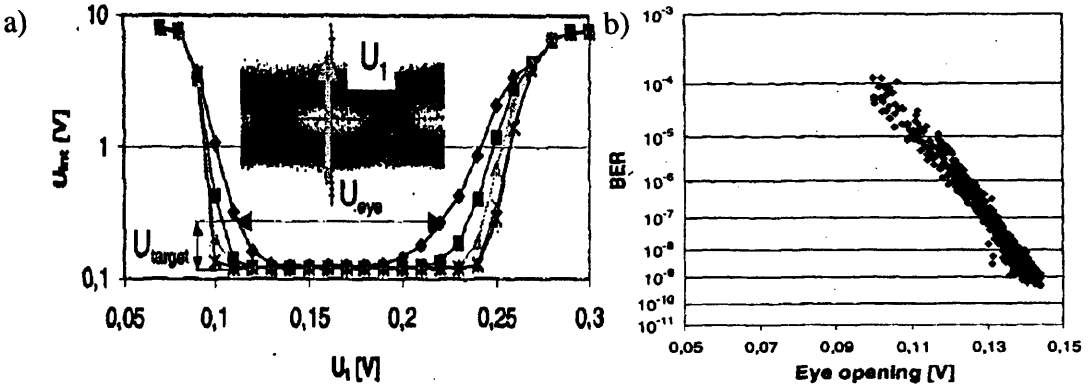

Figure 3.29 a) Integrator voltage vs. threshold level of monitoring circuit (b) BER vs. eye opening for all PMD statistics [Buc'01]

The eye opening here was defined as the difference in the threshold levels where the pseudo-error rate near the marks and spaces was 10^{-3}. Figure 3.29b shows the BER of the system as a function of the eye opening when PMD is randomly varied. Based on the relationship between the eye opening and PMD, this method can be used as a feedback system for a PMD compensator. Improvements of up to four orders of magnitude in the BER were reported. The technique was also successfully implemented in 40Gbit/s NRZ systems [Buc'02].

However, other impairments such as noise and dispersion also lead to eye closure and it is not clear how this approach would perform in such environments.

3.4.2.3.2 Using Asynchronous Histograms

BER/ Q-Factor Measurement

Achieving signal monitoring in a WDM system using asynchronous sampling has been a major area of research during the last few years [Sha'98] [And'01]. It provides a clear advantage over the previous method since it truly achieves bitrate transparency. Also it may be desirable where clock recovery is not possible due to heavy impairment such as an excessive amount of residual dispersion or PMD. The asynchronous histogram is obtained by sampling the signal at higher (over-sampling) or lower (under-sampling)

rates. However and as observed in the previous section, this also leads to sampling the signal transitions (from 0 to 1 or 1 to 0) which creates a floor between the marks and spaces histograms leading to an erroneous assessment of the Q factor. Furthermore this floor also depends on the sampling rate, the bit rate of the channel, the electrical and optical bandwidth and shape of the pulses used [And'04]. Most of the techniques found in the literature and reported here deal with the optimum approach of removing these cross-point data in order to correctly estimate the BER.

The first technique proposed in [Ras'99] was to cut the inner-histogram between the means of the zeros and the ones, then mirror the external parts around these two axes as shown in Figure 3.30a. Gaussian pulses are then fitted to the new histogram and the BER is calculated.

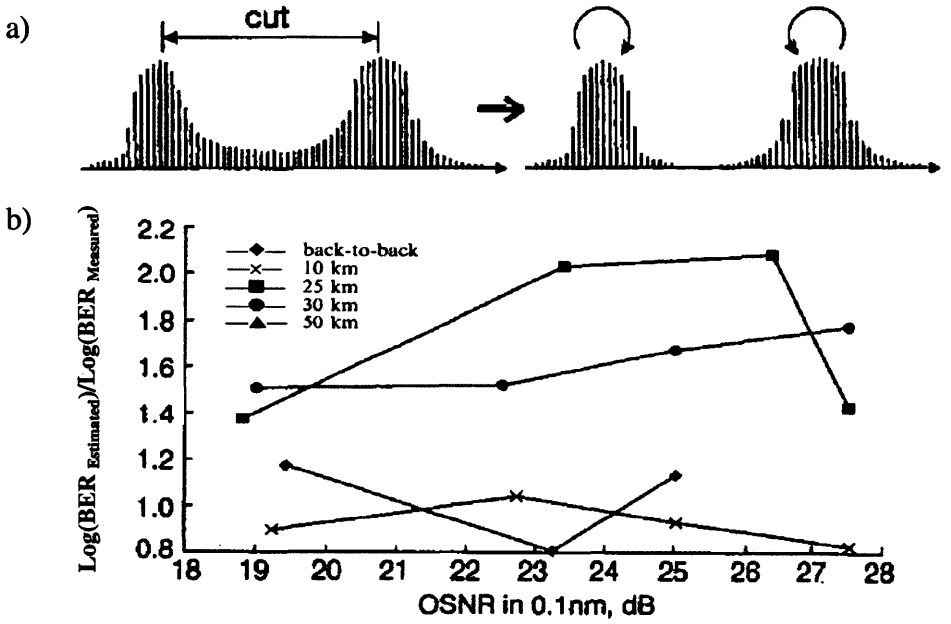

Figure 3.30 a) Cut and flip technique for asynchronous histograms [Ras'99]

Figure 3.30b shows the ratio between the estimated and the measured BER when using this technique on a system with varying OSNR and residual chromatic dispersion. It can be seen that when noise is the dominant effect (back-to-back and 10km fibre) this procedure gives accurate results. However when dispersion is the most dominant source of degradation (25 and 30km fibre) this method tends to underestimate the BER meaning that the signal quality is worse than calculated. This is because dispersion, or indeed distortion in general, affects the area between the two means to a greater extent, by creating multi-level patterns, than the external area.

A different approach proposed by [Sha'00] was to cut and delete the floor at a certain level of the eye opening and then calculate an average Q factor as shown in Figure 3.31.

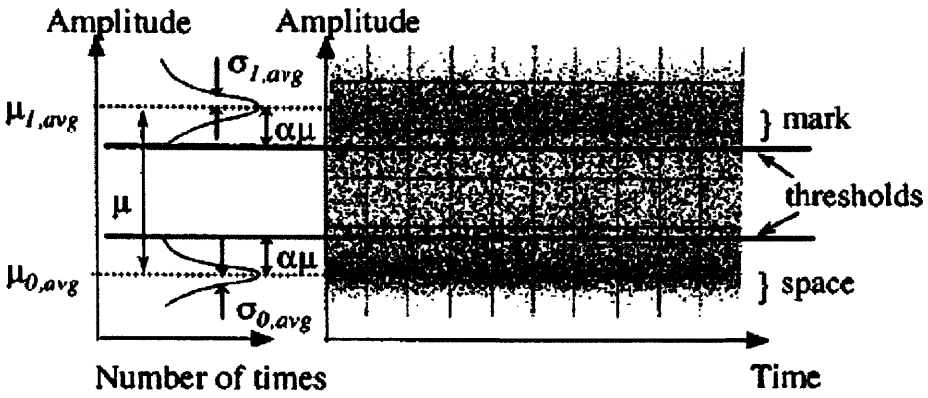

Figure 3.31 Cut and delete technique for asynchronous histograms [Sha'00]

This level is determined by α, a value between 0.1 and 0.5. If α is too small, the number of sampled points to determine the mean and standard deviation become insufficient whereas if it is too large then the standard deviation will include the sampled cross-points. It has been established experimentally that the optimum value for α to give a good correlation between the estimate and the real Q factor is 0.3 [Sha'02]. Figure 3.32 shows the correlation between the estimated and the real Q factor for different values of α (optical bandwidth = 4 x bitrate). The slope $\delta Q_{ave}/\delta Q$ when α=0.3 is 0.68.

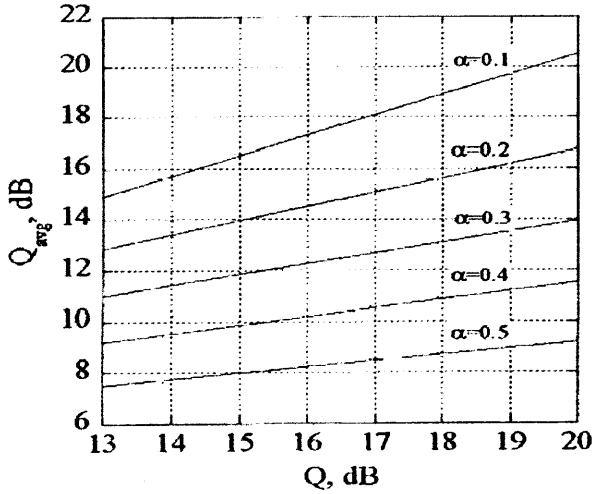

Figure 3.32 Dependence of Q_{avg} on Q for different α [Sha'02]

Although this technique shows a good correlation between the estimated and measured signal quality, it still has to be fully tested when perturbations come from distortion such as dispersion or crosstalk. In addition it may be used to determine the origin of the degradation. It has been argued in [Sha'03b] that the combination of the eye opening and

the standard deviation of the marks can be used in establishing the origin of the degradation as depicted in Figure 3.33.

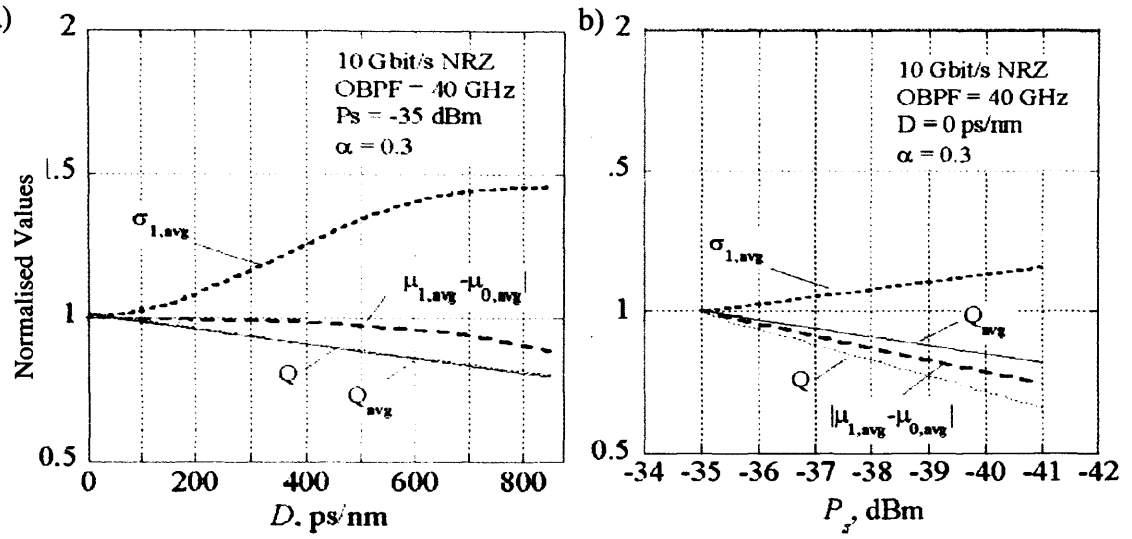

Figure 3.33 a) Dispersion and b) OSNR dependence of $\sigma_{1,ave}$ and $|\mu_{1,ave} - \mu_{0,ave}|$ [Sha'03]

Comparing Figure 3.33(a) and (b), we can see that $\sigma_{1,ave}$ increases more rapidly with increasing dispersion than with decreasing OSNR. On the other hand, $|\mu_{1,ave} - \mu_{0,ave}|$ decreases faster with decreasing OSNR than increasing dispersion. In addition the value $\sigma_{1,ave} - |\mu_{1,ave} - \mu_{0,ave}|$ is always greater than the reference level (i.e. 1) in the presence of dispersion and lower in the case of increasing noise. Therefore by evaluating the reference level of the eye opening and the marks' standard deviation at system installation and comparing them with the newly acquired parameters, the origin of the degradation can be determined. However this analysis only takes into account impairment due to noise and dispersion and ignores all other perturbations such as crosstalk, PMD and non-linearities.

Finally and unlike the aforementioned techniques, a new way of asynchronously estimating the Q factor without the need for cross-point removal has been proposed [And'04]. It relies on obtaining the pre-transmission histogram (i.e. at the transmitter) and convolving it with different Gaussian distributions, then comparing it with the histogram at the receiver. An example of a 40Gbit/s asynchronous histogram is illustrated in Figure 3.34.

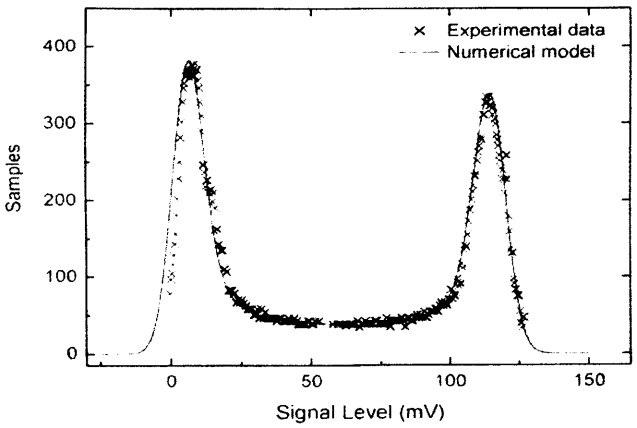

Figure 3.34 40Gbit/s asynchronous histogram (crosses) and the predicted curve (solid line) [And'04]

Although this technique can accurately estimate the quality of the signal without the need to remove cross-point data, it can only be utilised for high Q values (>8) and when noise is the only source of degradation. It might be extended to tackle distortion by convolving the histogram with pre-established distributions (e.g. crosstalk or dispersion) but it would be impracticable in real systems since it will necessitate "guessing" the right mix.

Crosstalk Evaluation

Intra-band crosstalk induced by a single source can be evaluated using asynchronous histograms. A numerical model to obtain the shape of the marks histogram affected by in-band crosstalk was developed [Lui'04]. By using this model and a reference histogram, obtained in the absence of impairments, an approximate histogram affected by crosstalk can be achieved. Finally the signal to crosstalk ratio (SCR) is acquired by fitting the calculated distribution to the experimental one. Figure 3.35 shows the accuracy of this technique.

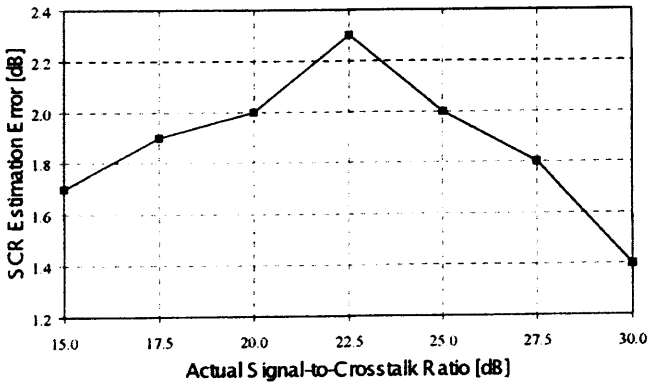

Figure 3.35 SCR estimation error as a function of the actual SCR [Lui'04]

It can be observed that SCR estimation errors under 2.4dB are obtained for a 15-30dB range.

Table 1 Summary of the main OPM methods and their impairment capabilities

	Homodyne Detection (Section 3.4.1.1.1)	Double-Pass Filtering (Section 3.4.1.1.2)	AWG (Section 3.4.1.1.2)	Polarisation Detection (Section 3.4.1.1.3)	Pilot Tones (Section 3.4.1.2.1)	RF Clock Power (Section 3.4.1.2.2)	Clock Phase Shift (Section 3.4.1.2.3)	Synchronous Sampling (Section 3.4.2.3.1)	Asynchronous Sampling (Section 3.4.2.3.2)
OSNR/ SNR	Range not known	Range: 10-44dB± 0.4dB	Range: 9-29dB	Range: 16-30dB± 1dB	Range up to 30dB	X	X	Range: 17-32dB	Range not known
Chromatic Dispersion	X	X	X	X	Range=675 ps/nm, Res = 10ps/nm (10Gbit/s)	Range up to 850ps/nm (10Gbit/s)	Range up to 1700ps/nm (10Gbit/s)	Sensitive	Sensitive
PMD	X	X	X	Range up to DGD=110ps (10Gbit/s)	Range up to DGD=50ps (10Gbit/s)	Range up to DGD=50ps (10Gbit/s)	X	Sensitive	Sensitive
Relative Crosstalk	Sensitive	X	X	X	X	X	X	Range: 16-22dB (with noise)	Range: 15-30dB without noise)
BER/Q	X	X	X	X	X	X	X	BER range: 10^{-4} to $<10^{-12}$	Q range: 9-16dB

3.5 Summary

Current networks are based on simple engineering rules that disregard rapid network reconfiguration and dynamic routing. In order to ensure quality of service, it is sufficient to verify that the different network elements are up and running. By checking certain indicators such as mains power loss, over-temperature or frequency drift, the signal quality may be assumed to be acceptable. However this is no longer valid in next generation all-optical networks where links are configured dynamically. Issues such as dynamic link reconfiguration, fault localisation and restoration need to be addressed. Optical performance monitoring (OPM), if integrated within the management system, can be a potential mechanism to enable the successful application of all-optical networks. A widely perceived application of performance assessment is optical channel monitoring to verify the service quality agreement between the network operator and the customer. This could be extended to provide a "warranty label" between network operators to avoid disagreement when handing over the services. In addition, any performance monitoring system should be able to detect anomalies or degradation in the service so that the management system could use redundant resources and isolate the faulty part of the network (protection). It can also be used by field engineers to rapidly localise and repair faults (fault localisation and troubleshooting). Performance monitoring can be used to anticipate major degradations of components or changes in working conditions that could affect the quality of transport services (pre-emptive maintenance). Furthermore, it may be used for impairment-based routing by estimating the expected QoS for a new path (connection setting up management).

OPM techniques can be divided into spectral and sampling methods. The former is further divided into optical spectrum methods and electrical spectrum methods. Similarly, sampling techniques can also be classified into synchronous sampling and asynchronous sampling. The different OPM approaches reported in the literature are summarised in Table 1. It can be noticed that, unlike spectral techniques, sampling techniques are sensitive to all types of noise and distortion and can be used to estimate the BER/Q-factor. They can be further developed to achieve precise root cause analysis and to include quantitative and qualitative estimation of chromatic dispersion and PMD. This will be studied in the next chapters.

Chapter 4 Synchronous Sampling Technique for Performance Monitoring

4.1 Introduction

Future all optical networks (AON) will transport a variety of voice and data signals over optical channels regardless of their format or bit rate. One major obstacle in these networks is the implementation of transparent performance monitoring, fault localization and network management. A variety of (analogue) monitoring schemes have been discussed in the previous chapter and most of them fall within two categories: spectral methods and sampling methods. The former, albeit simple and fast to implement, lack versatility and can only be used to monitor one or two sources of impairments. Additionally, they cannot be used to estimate the BER. Sampling methods on the other hand are sensitive to both noise and distortion and they usually utilize the statistical information of the signal to derive histograms and the bit error rate (BER). Furthermore, the histograms and especially the marks' histogram take a distinctive shape for every source of degradation [Mue'99] and this can be used to determine the cause of signal distortion during transmission. Indeed, identifying the sources of distortion is an important task in isolating faulty components, to anticipate major equipment degradation (pre-emptive maintenance), and to estimate quality of service for a new path (connection management). In this chapter we cover the synchronous sampling methods for performance monitoring. We start by describing, in section 4.2, the monitoring circuit deployed in the experiments of this chapter. In section 4.3, the effect of some major impairments such as chromatic dispersion, polarisation mode dispersion (PMD) and crosstalk on the obtained histograms are examined. This can be utilised to determine the origin of the degradation in signal quality. In section 4.4 we investigate the accuracy of this monitoring technique when implemented in deployed wavelength division multiplexed (WDM) systems. The performance of this method is assessed and compared with the in-built digital monitoring techniques of various protocols operating at different bitrates. In section 4.5 we introduce a deconvolution method that can be applied to the histograms in order to evaluate the Gaussian noise without prior knowledge of the transmission path. This can be used to separate the contribution of distortion from the contribution of noise and hence provide advanced root cause analysis.

4.2 Monitoring Circuit

A digital oscilloscope (Agilent 86100B Infiniium DCA) was used to emulate the dual decision monitoring circuit discussed in section 3.4.2.1. A small variation was introduced however, where two variable threshold were utilised instead of one fixed and one variable. The histogram was obtained by counting the number of hits detected between the upper and lower thresholds. The device had a 30GHz electrical bandwidth and a sampling aperture of 2ps was used. The voltage difference (q) between the two thresholds defined the quantisation noise introduced in the histograms. Assuming the output bin is defined by the voltage at its centre, the maximum quantisation error is found to be ±q/2. Quantisation error can be thought of noise which is added to an ADC of infinite resolution. It was shown in [Mel'92] that for large amplitude (compared to q), complex signals (containing many frequencies) the quantisation noise becomes white noise. It was also demonstrated that the signal-to-noise ratio is solely dependent on the number of bins (n) utilised (S/N(dB) = 1.76+6.02n). In our monitoring circuit we used 64 bins achieving a very high signal-to-noise ratio and hence quantisation noise effects on the histograms have been ignored.

4.3 Impairment Signatures on Synchronously Obtained Histograms

Different impairments give different patterns to histograms obtained at decision times using sampling performance monitoring techniques. Signatures of ASE noise, dispersion and crosstalk using asynchronous sampling were discussed in section 3.4.2.2. However, to the best of our knowledge, the signatures of these impairments and other distortions have not been reported in the literature for the case of synchronous sampling. This is investigated in this section. In addition, the signature of polarisation mode dispersion (PMD) is also studied and important characteristics that differentiate it from the pattern of chromatic dispersion are discussed.

4.3.1 Crosstalk Signature on Histograms

Crosstalk is one of the main sources of degradation in WDM systems [Ian'99] and consists of a transfer of power from one channel to another. This occurs because of the imperfect characteristics of various optical components such as demultiplexers and optical switches and is referred to as linear crosstalk. It can also occur because of nonlinear effects such as light scattering, FWM or XPM and this type of crosstalk is

referred as nonlinear crosstalk. Crosstalk can be classified into in-band (homodyne) crosstalk and out-of-band (heterodyne) crosstalk. The latter occurs when two signals of different wavelength reach the receiver because of the imperfect nature of optical filters and AWGs. In-band crosstalk on the other hand occurs between two channels of the same nominal wavelength and is common in WDM ring and bus networks that utilise add-drop multiplexers. The statistical effects of in-band crosstalk on the histogram and especially on the marks' distribution have been extensively studied, which has led to an arcsine distribution (U-shape) [Leg'96]. Two experiments, one at 2.5Gbit/s and one at 10Gbit/s, were carried out to investigate the in-band crosstalk pattern on the synchronously generated histograms. Two cases for each experiment were considered: the two interfering channels having the same bitrate and when the main channel having a higher bitrate. The four cases are summarised in Table 2.

Case	Main Channel	Interfering Channel
1	2.5 Gbit/s	2.5 Gbit/s
2	2.5 Gbit/s	1.062 Gbit/s
3	10 Gbit/s	2.5 Gbit/s
4	10 Gbit/s	10 Gbit/s

Table 2 Cases used to investigate the signature of crosstalk on the histogram

Additionally, in each case the PRBS used in the two interfering channels was altered in order to avoid any correlation and to imitate real life situations where different channels transporting different loads interfere with each other. Let us consider these cases one by one.

Case 1

The experimental setup for the case in which the two interfering channels are transmitted at 2.5Gbit/s is shown in Figure 4.1. The main channel (transmitter 1) consisted of SDH frames transporting a 2^{11}-1 pseudo-random bit sequence (PRBS) generated using an externally modulated laser. The crosstalk channel (transmitter 2) was also an SDH channel with a 2^{20} PRBS payload and was generated by directly modulating a distributed-feedback (DFB) laser.

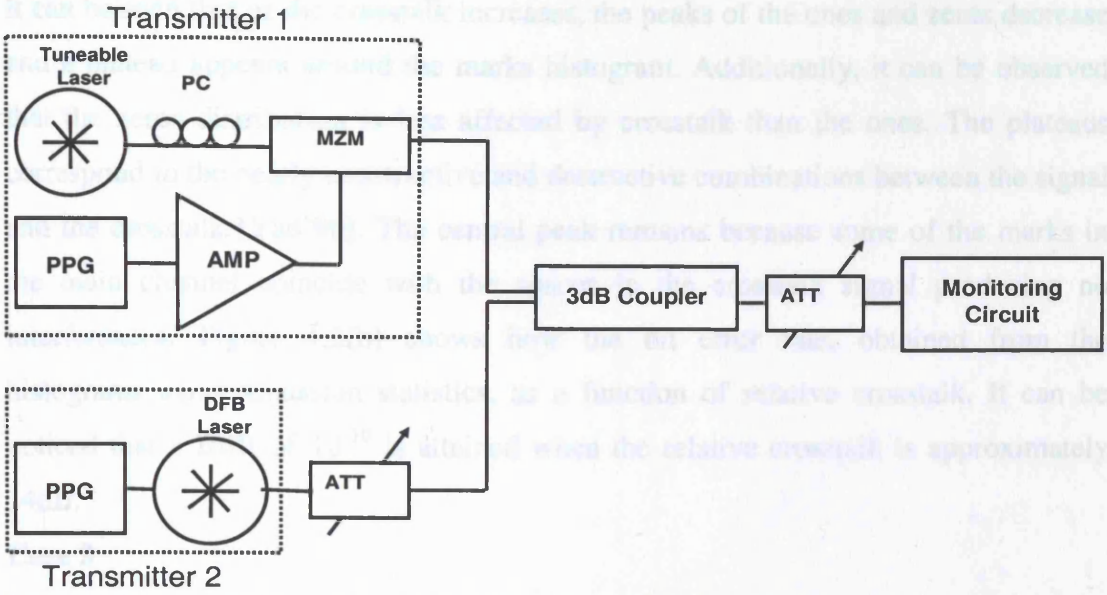

Figure 4.1 Experimental setup to investigate crosstalk signature on the histogram. PC: polarisation controller; PPG: pulse pattern generator; MZM: Mach-Zehnder modulator.

Two different pulse pattern generators (PPG) were utilised with different PRBS so that the two interfering signals are de-correlated and phase independent. This is a more realistic scenario compared with most experiments reported in the literature where the crosstalk channel is a delayed replica of the main channel [Leg'96] [Yad'98] [Wei'00a]. The wavelength used in this experiment for both transmitters was 1559nm and the power incident on the photodetector of the monitoring circuit was kept constant at -6dBm to avoid any change in the behaviour of the receiver. The back to back operation of the main channel was error-free. A variable attenuator was used to alter the amount of relative crosstalk which was increased from -30dB to -10dB. Figure 4.2(a) shows the normalised histograms of the different values of relative crosstalk.

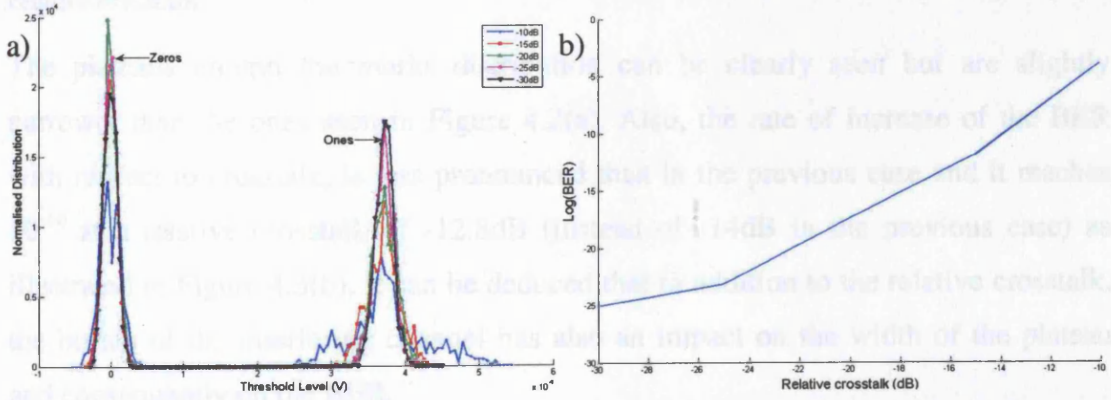

Figure 4.2 a) The effect of different crosstalk levels on the histogram of two interfering channels operating at 2.5Gbit/s b) The corresponding BER as a function of the relative crosstalk

It can be seen that as the crosstalk increases, the peaks of the ones and zeros decrease and a plateau appears around the marks histogram. Additionally, it can be observed that the zeros distribution is less affected by crosstalk than the ones. The plateaus correspond to the nearly constructive and destructive combinations between the signal and the crosstalk [Yad'98]. The central peak remains because some of the marks in the main channel coincide with the spaces in the crosstalk signal producing no interferences. Figure 4.2(b) shows how the bit error rate, obtained from the histograms using Gaussian statistics, as a function of relative crosstalk. It can be noticed that a BER of 10^{-10} is attained when the relative crosstalk is approximately 14dB.

Case 2

In this case the main channel was maintained at 2.5Gbit/s whereas the bitrate of the interfering channel was set to 1.062Gbit/s. The interfering signal consisted of Fibre Channel (FC) frames transporting a 2^{11} PRBS payload. Figure 4.3(a) shows the normalised histograms for the different values of relative crosstalk.

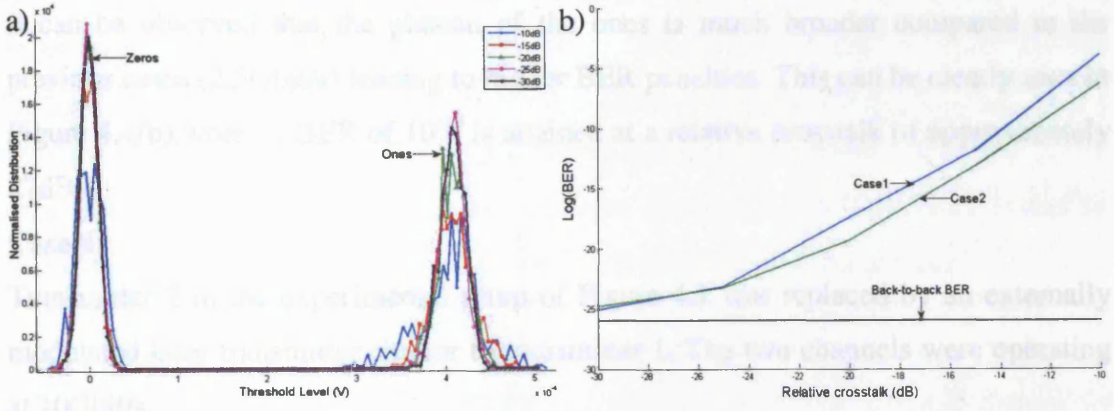

Figure 4.3 The effect of different crosstalk levels on the histogram of a 2.5Gbit/s channel interfering with a 1.062Gbit/s crosstalk channel b) The corresponding BER as a function of the relative crosstalk

The plateaus around the marks distribution can be clearly seen but are slightly narrower than the ones seen in Figure 4.2(a). Also, the rate of increase of the BER with respect to crosstalk, is less pronounced than in the previous case and it reaches 10^{-10} at a relative crosstalk of -12.8dB (instead of -14dB in the previous case) as illustrated in Figure 4.3(b). It can be deduced that in addition to the relative crosstalk, the bitrate of the interfering channel has also an impact on the width of the plateau and consequently on the BER.

Case 3

The main channel (transmitter 1) was upgraded to a SDH STM-64 protocol operating at 10Gbit/s and transporting a payload of an 2^{23} PRBS. The second channel consisted of SDH STM-16 frames (2.5Gbit/s) encapsulating a 2^{20} PRBS. The estimated back to back BER of transmitter 1 was 10^{-14}. The histogram of the main channel with respect to the relative crosstalk is shown in Figure 4.4(a).

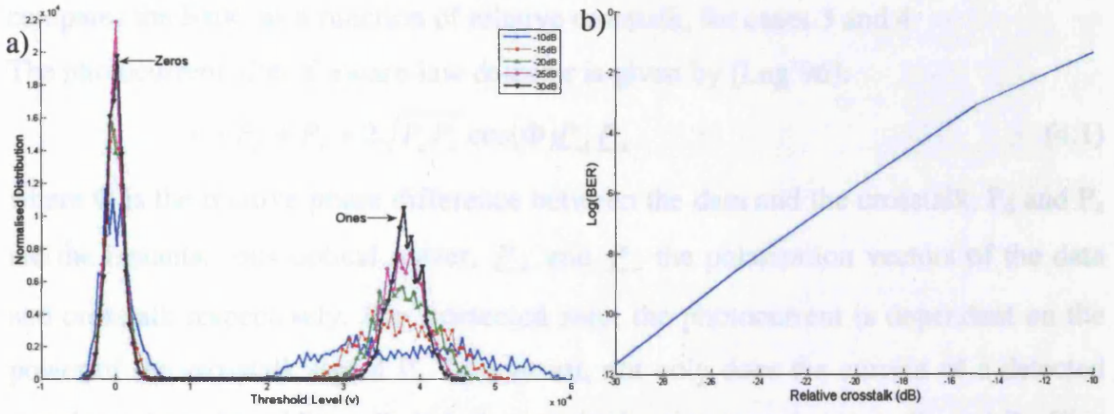

Figure 4.4 The effect of different crosstalk levels on the histogram of a 10Gbit/s channel interfering with a 2.5Gbit/s crosstalk channel b) The corresponding BER as a function of the relative crosstalk

It can be observed that the plateau of the ones is much broader compared to the previous cases (2.5Gbit/s) leading to higher BER penalties. This can be clearly seen in Figure 4.4(b) where a BER of 10^{-10} is attained at a relative crosstalk of approximately 27dB.

Case 4

Transmitter 2 in the experimental setup of Figure 4.1 was replaced by an externally modulated laser transmitter similar to transmitter 1. The two channels were operating at 10Gbit/s.

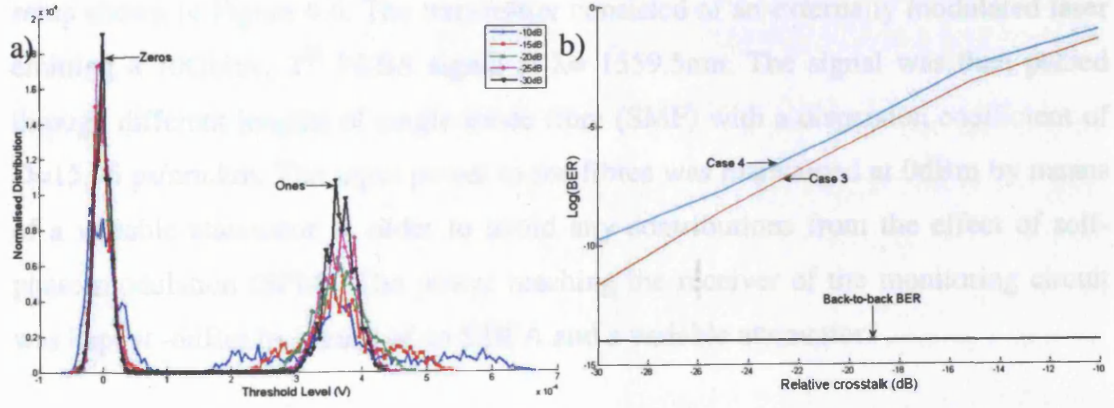

Figure 4.5 The effect of different crosstalk levels on the histogram of two interfering channels operating at 10Gbit/s b) Comparison between the BER as a function of the relative crosstalk for all cases

The main channel consisted STM-64 frames that encapsulated a 2^{23} PRBS whereas the interfering channel contained of STM-64 frames encapsulating a 2^{31} PRBS. Figure 4.5(a) shows the normalised histograms for different values of relative crosstalk. The distributions of ones and zeros are similar to the previous case although the plateaus of the marks are slightly wider. This can be clearly seen in Figure 4.5(b) which compares the BER, as a function of relative crosstalk, for cases 3 and 4.

The photocurrent after a square-law detector is given by [Leg'96]:

$$i \sim P_d + P_x + 2\sqrt{P_d P_x}\cos(\Phi)\underline{P}_d \underline{P}_x \tag{4.1}$$

where Φ is the relative phase difference between the data and the crosstalk, P_d and P_x are the instantaneous optical power, $\underline{P}_d$ and $\underline{P}_x$ the polarisation vectors of the data and crosstalk respectively. For a detected zero, the photocurrent is dependent on the power of the crosstalk signal P_x. In contrast, not only does the current of a detected one depend on the additive P_x but also on the beating term between P_d and P_x. This mixing can result in either a constructive or a destructive combination depending on the phase difference. This is why the histogram of the marks is more affected by crosstalk than the distribution of the spaces. In addition if the crosstalk channel operates at a lower bitrate than the main channel, the instantaneous power of the marks in this latter is likely to beat with the power of the transition edges of the crosstalk signal (since it has longer transition times). This will lead to a smaller deviation from P_d in equation 4.1 and therefore a slightly narrower plateau.

4.3.2 Dispersion Signature on the Histograms

The effect of dispersion on the histogram was investigated using the experimental setup shown in Figure 4.6. The transmitter consisted of an externally modulated laser emitting a 10Gbit/s, 2^{23} PRBS signal at λ= 1559.5nm. The signal was then passed through different lengths of single mode fibre (SMF) with a dispersion coefficient of D=15.96 ps/nm.km. The input power to the fibres was maintained at 0dBm by means of a variable attenuator in order to avoid any contributions from the effect of self-phase modulation (SPM). The power reaching the receiver of the monitoring circuit was kept at -6dBm by means of an EDFA and a variable attenuator.

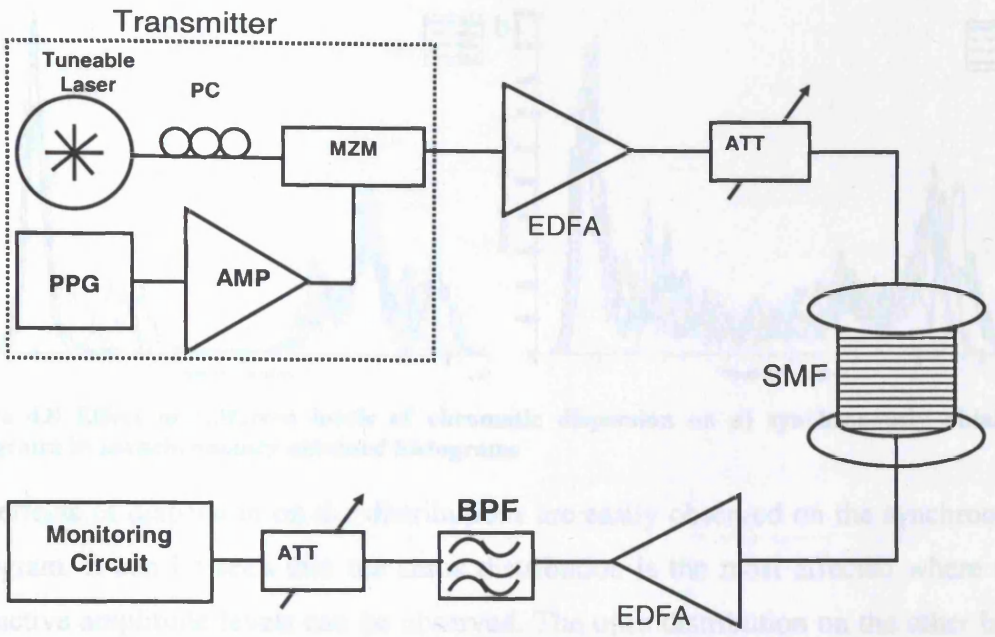

Figure 4.6 10Gbit/s experimental setup to investigate the signature of dispersion on the histograms. PC: polarisation controller; PPG: pulse pattern generator; MZM: Mach-Zehnder modulator; SMF: single mode fibre; BPF: bandpass filter

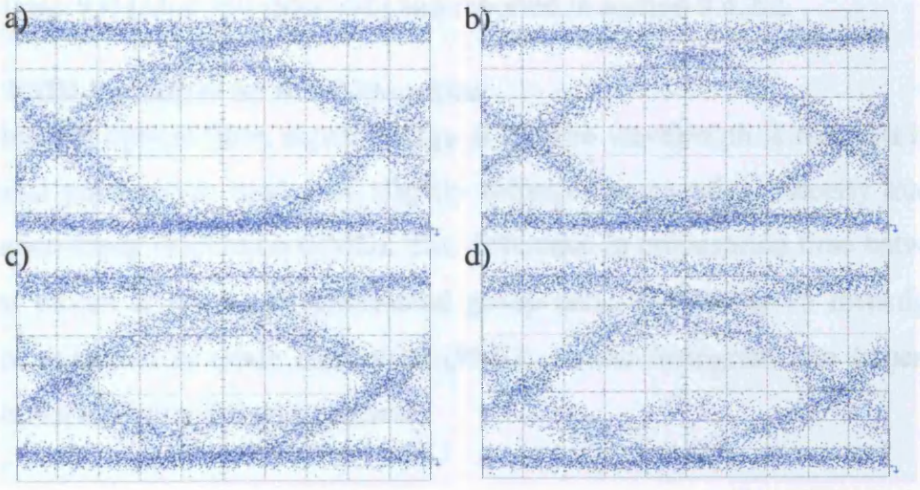

Figure 4.7 10Gbit/s eye diagram obtained using a 7.5GHz bandwidth receiver after a fibre length of a) 13km b) 26km c) 39km d) 50km

It can be observed that dispersion induces inter-symbol interference (ISI) as marks and spaces have multiple distinctive levels leading to an increase in the error probability. The corresponding synchronous and asynchronous histograms are shown in Figure 4.8

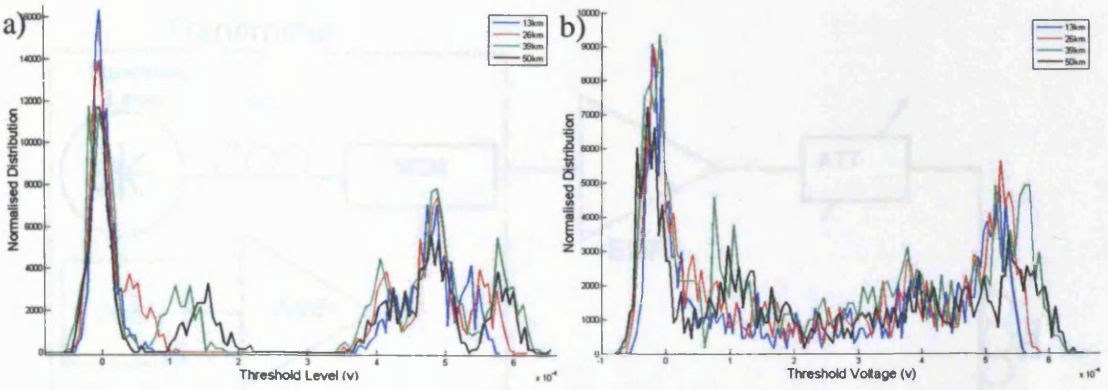

Figure 4.8 Effect of different levels of chromatic dispersion on a) synchronously obtained histograms b) asynchronously obtained histograms

The effects of dispersion on the distributions are easily observed on the synchronous histogram. It can be seen that the zeros distribution is the most affected where two distinctive amplitude levels can be observed. The ones distribution on the other hand is split into three levels. The effect of dispersion on the asynchronous histogram is characterised by the increase of the standard deviation of both spaces and marks and an upward shift of the means of the zero levels. This confirms previously published results [Han'98] [Mue'99] [Sha'03b] and reported in section 3.4.2.2.

4.3.3 PMD Signature on the Histograms

In singlemode optical fibre, signal energy at a given wavelength is resolved into two orthogonal polarisation modes of slightly different propagation velocity leading to polarisation-mode dispersion (PMD). The difference in propagation time between the different modes is known as differential group delay (DGD)$\Delta\tau$. To investigate the effect of polarisation mode dispersion (PMD) on the histogram, the experimental setup shown in Figure 4.9 was realised.

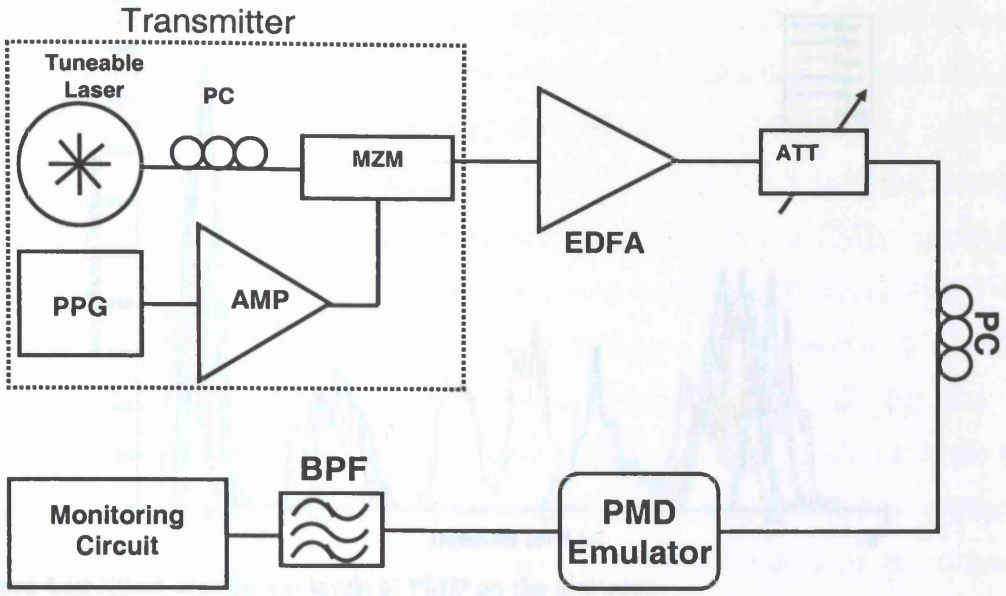

Figure 4.9 10Gbit/s experimental setup to investigate the signature of PMD on the histograms. PC: polarisation controller; PPG: pulse pattern generator; MZM: Mach-Zehnder modulator; BPF: bandpass filter

The 9.953Gbit/s, 2^{31} PRBS signal was passed through a 16-element *Yafo* PMD emulator capable of emulating first and second order PMD. This device consists of 16 birefringent elements connected by inter-element polarisation coupling. PMD can be adjusted by changing the polarisation coupling between elements, by changing the amount of birefringence in each element or a combination of both. A polarisation controller (PC) was placed at the input of the emulator to control the power splitting ratio between the two principal states of polarisation. The obtained histograms for various DGD's are shown in Figure 4.10. It can be observed that the PMD effect on the histogram is very similar to dispersion and in reality cannot be differentiated (compare this with Figure 4.8a).

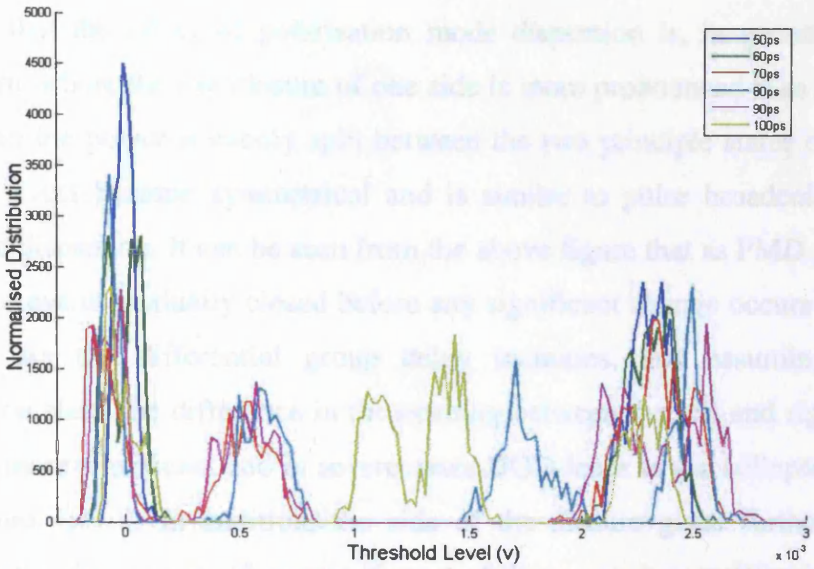

Figure 4.10 Effect of different levels of PMD on the histogram

Both phenomena split the marks distribution into two or three levels and add an extra level to the spaces distribution. The latter comes from the transfer of some of the ones energy to the adjacent zeros leading to inter-symbol interference (ISI). However, the two impairments may be separated by observing their general signature on the entire eye diagram rather than at its centre. Figure 4.11 illustrates the effects of first and second order PMD on the eye diagram.

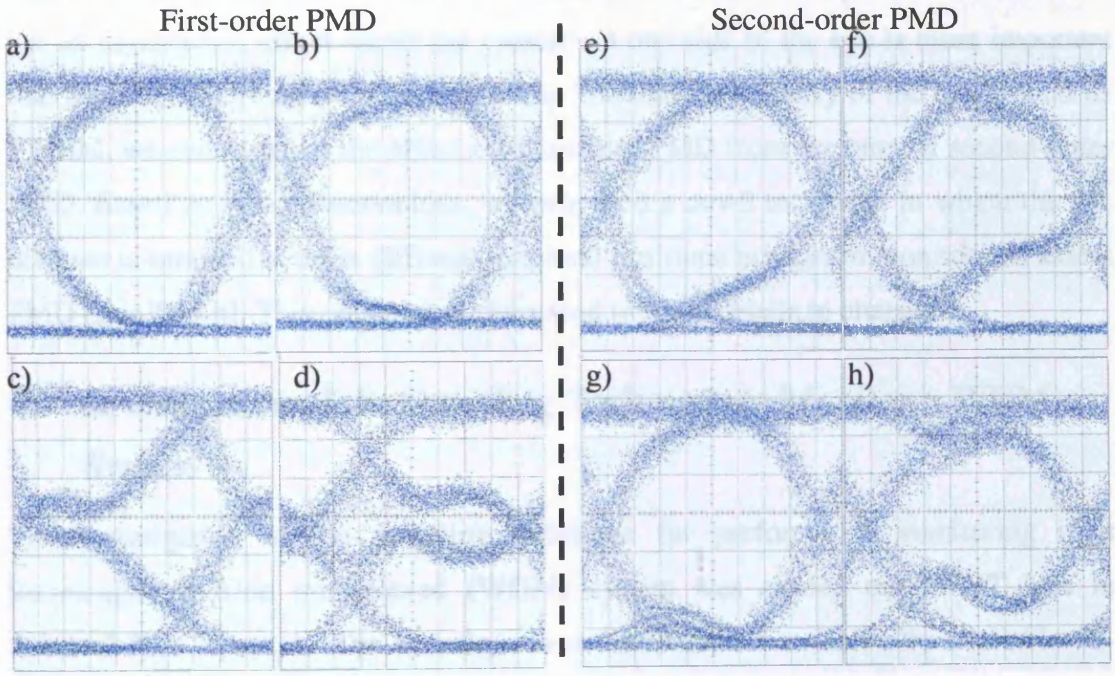

Figure 4.11 Effects of first order PMD on the eye diagram. a) Δτ=50ps, b) Δτ=60ps, c) Δτ=80ps, d) Δτ=100ps. Effects of second order PMD on the eye diagram. e) Δτ=62ps, f) Δτ=70ps, g) Δτ=85ps, h) Δτ=90ps

We note that the effect of polarisation mode dispersion is, in general, temporally asymmetric where the eye closure of one side is more pronounced than the other one. Only when the power is evenly split between the two principle states of polarization does the effect become symmetrical and is similar to pulse broadening caused by chromatic dispersion. It can be seen from the above figure that as PMD increases, one side of the eye is gradually closed before any significant change occurs on the rest of the eye. As the differential group delay increases, and assuming a constant polarisation state, the difference in the opening between the left and right hand sides becomes more significant and in severe cases DGD leads to the collapse of the entire eye (Figure 4.11d). In addition, the side of the closure gives further information regarding the distribution of power; if most of the power is travelling in the fast axis then the right-hand side of the eye is affected. Conversely, if most of the power is travelling in the slow axis then the closure starts from the left-hand side. Furthermore, it can be observed that, unlike second-order PMD, first-order PMD is symmetrical around the horizontal axis crossing the full-width at half maximum (FWHM) of the eye diagram. In conclusion, the signature of chromatic dispersion (CD) and PMD on the histogram taken at the centre of the eye diagram is very similar. To discriminate between them, we need to verify the vertical symmetry of the eye. Unlike CD, PMD has an asymmetric effect where the closure on one side of the eye is more important that the other. Moreover, by looking at the horizontal symmetry of the eye around its FWHM, we can separate the effect of first-order PMD from the ones of second-order PMD. Based on these observations, we proposed a novel technique in which the eye diagram is sampled at three different temporal positions in order to monitor and assess PMD [Ben'05a-b]. This approach is discussed in more details in chapter 6.

4.4 Investigation of the Sampling Technique to Monitor a WDM System

The investigation of the sampling technique for performance monitoring in a wavelength division multiplexed (WDM) system was carried out in BT labs in Adastral Park, Ipswich. The technique was tested on a commercially available 32-channel dense WDM (DWDM) metro system which supports various protocols operating at different bitrates. The experimental setup is shown in Figure 4.12.

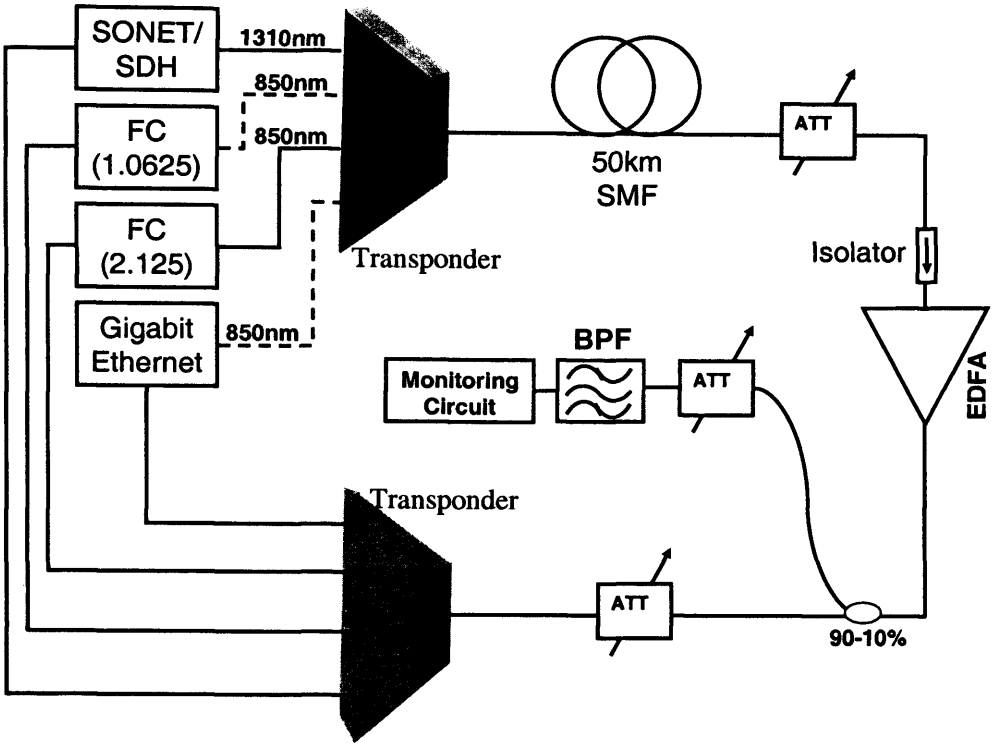

Figure 4.12 Investigation of the sampling monitoring technique in a commercial metro WDM system

Four simultaneous channels transporting four different protocols were utilised in this experiment. The protocols used were 2.5Gbit/s Synchronous Digital Hierarchy (SONET/SDH), 1.0625Gbit/s Fibre Channel (1 Gigabit FC), 2.125Gbit/s Fibre Channel (2 Gigabit FC) and 1.25Gbit/s Gigabit Ethernet (GbE). These were generated using separate emulators which were directly connected the local ports of the multiplexer/transponder. The SDH emulator was connected to the multiplexer via a single mode fibre (SMF) at a wavelength of 1310nm while the other emulators were linked by means of multimode fibres using a wavelength of 850nm. The transponder regenerated the data then transmitted it in the C band frequencies. The wavelengths utilised were 1531, 1533, 1555 and 1557nm for 2 Gigabit FC, SDH, GbE, and 1 Gigabit FC respectively. The data was passed through 50km of SMF (average metro network length) then boosted by means of an EDFA. The fibre span had an average fibre loss of 0.25dB/km and a dispersion coefficient of 16.9ps/nm.km. A small portion (10%) of the signal was tapped out for monitoring the quality of the signal. A tuneable 200GHz bandpass filter was deployed to select the different channels which were then sampled by a digital oscilloscope. The demultiplexer regenerated all the channels and reconverted them to their initial wavelengths. A variable attenuator was placed before the demultiplexer in order to keep the optical power constant at approximately -

6dBm. Finally the emulators received the data and performd a health check using their specific (digital) monitoring methods. In order to assess the performance of the sampling monitoring technique and compare it with the digital methods, two impairments were introduced in the network: ASE noise and in-band crosstalk.

ASE noise was generated by varying the input power to the EDFA by means of a variable attenuator. As the input power was decreased, the EDFA generated increasing amount of noise which ultimately led to errors in the detected data. The in-band crosstalk was generated by emulating a laser drift in one of the transmitters of the transponder. We caused one of the wavelengths to gradually shift towards an adjacent channel to verify how the system and our monitoring technique performed.

4.4.1 ASE Noise Experiment

The ASE noise in the system was increased by decreasing the input power to the EDFA using a variable attenuator as shown in Figure 4.12. The EDFA used in this experiment was a high gain amplifier (G = 37dB at P_{in} = -35dBm) with a noise figure of 5dB. We measured the power of the four channels reaching the EDFA without any attenuation. These were, including the insertion loss of the attenuator, -20dBm for 2 Gigabit FC, -13.5dBm for SDH, -18dBm for GbE and -16.5dBm for 1 Gigabit FC. As the attenuation was increased, the histogram of every channel was taken. These histograms were later used to estimate the system BER using Gaussian statistics. In addition, we also noted the BER given by the emulators which effectively represents the service quality estimated by the clients.

4.4.1.1 SONET/SDH Channel

The 1533nm channel was transporting SONET/SDH frames at 2.48832Gbit/s. The payload consisted of a 2^{20} PRBS (scrambled) data. SDH protocol has a digital technique to analyse errors called bit-interleaved parity-8 (BIP-8) (see Appendix 1).The BIP bin is transmitted one frame behind the corresponding data (one frame lag) to give the receiver time to calculate its own BIP code and compare them together (different BIP if an error occurred). The BER of the channel, as a function of the OSNR is plotted in Figure 4.13. It shows the BER taken from three different sources: the SDH emulator (red), the BER tester (green) and the sampling method (blue). The BER tester was used in the same position as the monitoring circuit in the experimental setup.

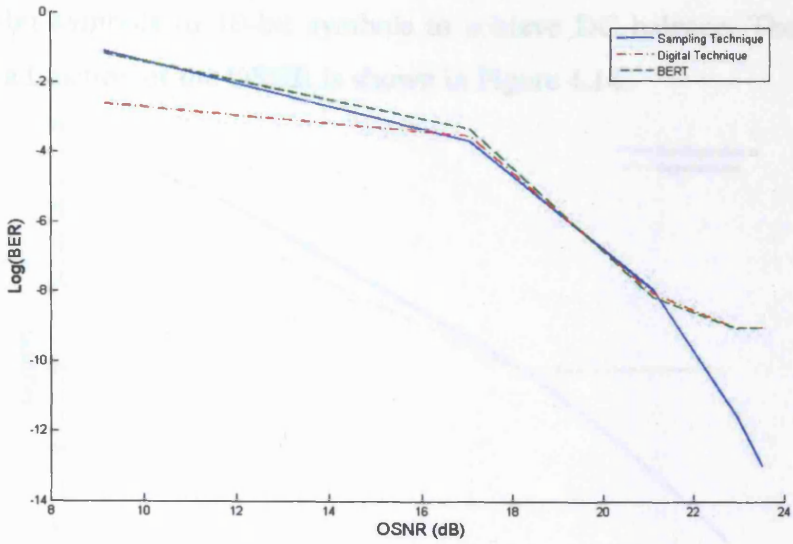

Figure 4.13 The BER of the SDH channel as a function of the OSNR (0.1nm resolution)

It can be observed that up to an OSNR of 23dB, the BER detector and the SDH BIP technique see a constant error-free transmission while the sampling method notices a slight degradation in the quality of the transmission where the BER increased from 10^{-13} to 10^{-12}. This reached 5×10^{-9} at OSNR = 21dB then rose to approximately 3.5×10^{-4} at OSNR = 17dB. All three approaches closely agree over this range. At an OSNR = 9dB, the digital technique indicates a BER of 2.5×10^{-3} whereas the sampling method and the BER tester detect a BER of 10^{-1}. This is due to the fact that at this level of BER, it is more probable that an even number of errors occurs in a single BIP bin and hence self-compensate. As a consequence, some errors can go undetected and therefore the estimated BER is lower than the actual one. We can conclude from this experiment that the sampling technique can accurately evaluate the BER of a channel and predict performance degradation before it affects the client's network. In other words, this method can also be utilised for pre-emptive maintenance.

4.4.1.2 1 Gigabit Fibre Channel

Fibre Channel (FC) was developed primarily to rapidly transfer data between workstations, mainframes, supercomputers, storage devices and other peripherals [Fci'05]. This protocol utilises cyclic redundancy checking (CRC) to ensure the integrity of the received packets (see Appendix A). A FC packet contains six fields: a header, a synchronisation field, start of frame (SOF), payload, CRC and the end of frame (EOF) field. The CRC is computed as a function of the header and the payload and does not include the rest. The FC used in this experiment transported a 2^{20} PRBS at 1.0625Gbit/s (λ= 1557.4nm). The 8b/10b mapping was enabled. This consists of

mapping 8-bit symbols to 10-bit symbols to achieve DC balance. The BER of the channel, as a function of the OSNR is shown in Figure 4.14.

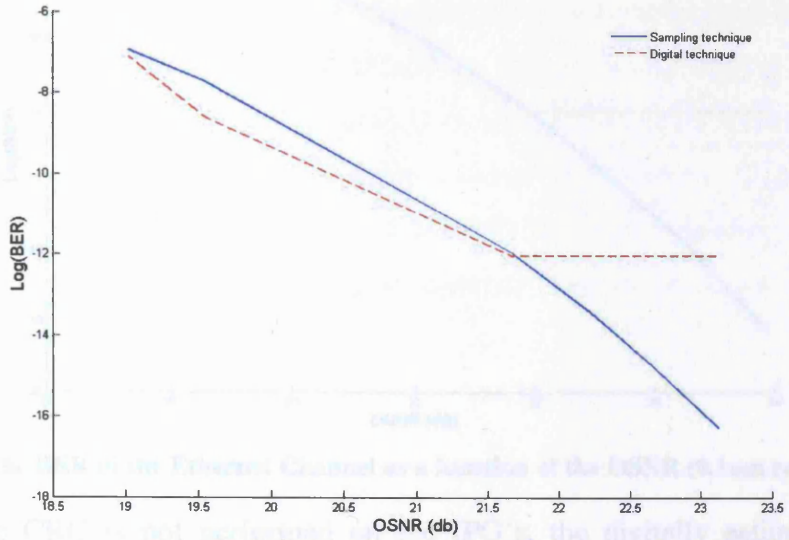

Figure 4.14 The BER of the 1 gigabit Fibre Channel as a function of the OSNR (0.1nm resolution)

Although there is a good correlation between the digital and the analogue techniques, the BER using the sampling approach is slightly higher. This is because, as mentioned earlier, the CRC is not performed on the entire frame and therefore some errors can go unnoticed. It can clearly be observed from the above figure how the sampling technique tracks the degradation in the performance before it becomes critical.

4.4.1.3 Gigabit Ethernet

Gigabit Ethernet is a transmission technology based on the Ethernet frame format and protocol which is the most widely implemented networking protocol today. Just as in Fibre Channel, it utilises CRC to check the integrity of the packets. Each Ethernet frame contains six fields: a preamble, destination (MAC) address, source address, length of the packet, payload and the CRC. In addition, Ethernet allows inter-packet gaps (IPG) which provide a brief recovery time between frames to allow devices to prepare for reception of the next frame. In our experiment, Ethernet was used to carry a 2^{20} PRBS load at 1.25Gbit/s (λ= 1555.7nm). The BER, as a function of the OSNR is shown in Figure 4.15

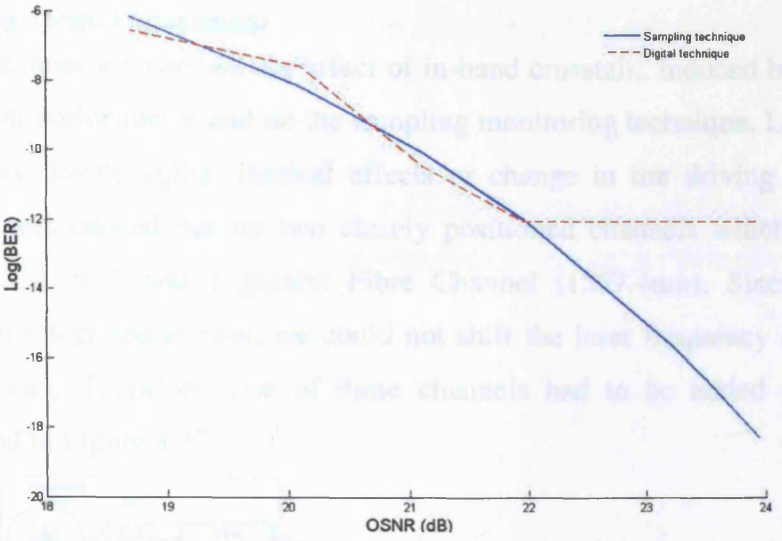

Figure 4.15 The BER of the Ethernet Channel as a function of the OSNR (0.1nm resolution)

Because the CRC is not performed on the IPG's, the digitally estimated BER is slightly smaller than using our analogue method.

4.4.1.4 2 Gigabit Fibre Channel

2 gigabit Fibre Channel is a faster version of the standard FC operating at 2.125Gbit/s. In our experiment, the 2G FC occupied the wavelength 1531nm and transported a payload of 2^{20} PRBS. The BER, as a function of the OSNR is shown in Figure 4.16.

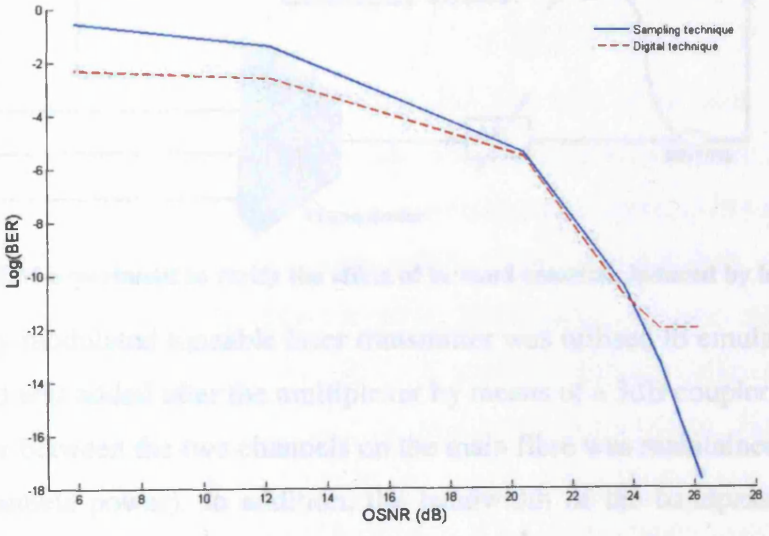

Figure 4.16 The BER of the 2 gigabit Fibre Channel as a function of the OSNR (0.1nm resolution)

Similarly to 1G FC, the BER using the CRC is slightly underestimated. The continuous degradation in the quality of the service can be clearly seen from the estimated BER using the sampling method.

4.4.2 Laser Drift Experiment

In this experiment we verified the effect of in-band crosstalk, induced by laser drift, on the system performance and on the sampling monitoring technique. Laser drift can be caused by device aging, thermal effects or change in the driving current. The experiment was carried out on two closely positioned channels which are Gigabit Ethernet (1555.7nm) and 1 gigabit Fibre Channel (1557.4nm). Since the WDM system is an integrated system, we could not shift the laser frequency directly from the transponder. Therefore, one of these channels had to be added externally as demonstrated in Figure 4.17.

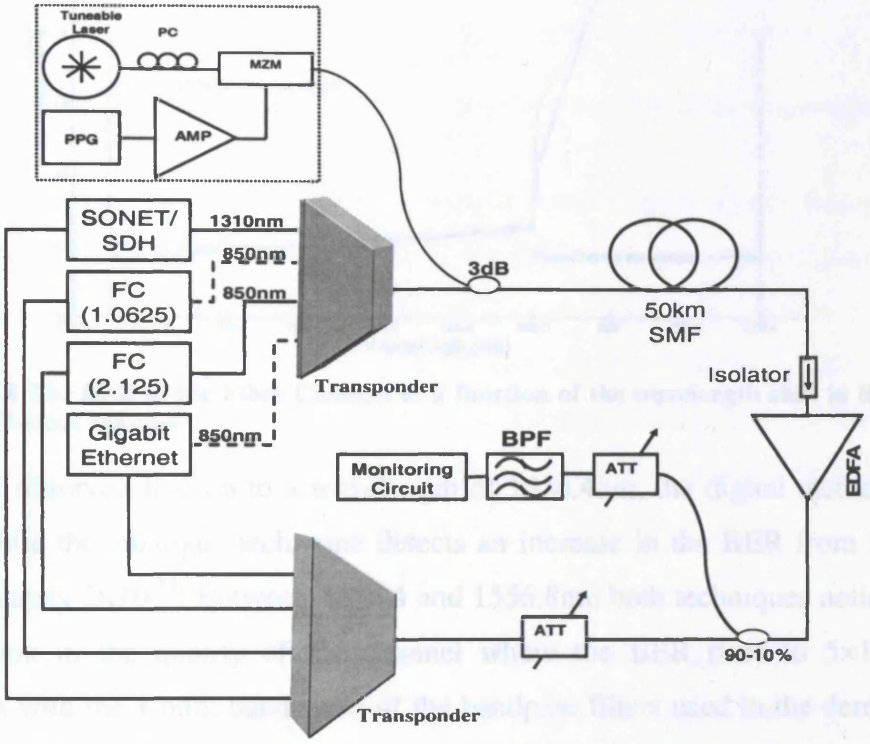

Figure 4.17 WDM experiment to verify the effect of in-band crosstalk induced by laser drift

An externally modulated tuneable laser transmitter was utilised to emulate one of the channels, and was added after the multiplexer by means of a 3dB coupler. The relative optical power between the two channels on the main fibre was maintained (see section 4.4.1 for channels power). In addition, the bandwidth of the bandpass filter in our monitoring circuit was changed to 100GHz. The first step was to eliminate the GbE channel from the local port of the multiplexer and directly introduce it on the main fibre. While the frequency of the tuneable laser was gradually increased from 1555.7nm to 1557.4nm, the FC signal was monitored by the sampling technique. The second step was to reintroduce the GbE channel and disconnect the FC channel from the local port. This was added directly to the link. The frequency of the tuneable laser

was gradually decreased from 1557.4nm towards 1555.7nm while monitoring the GbE channel.

4.4.2.1 Monitoring 1G Fibre Channel

Figure 4.18 shows the BER, obtained by the digital and the sampling techniques, of the FC channel as the wavelength of the adjacent GbE channel increases.

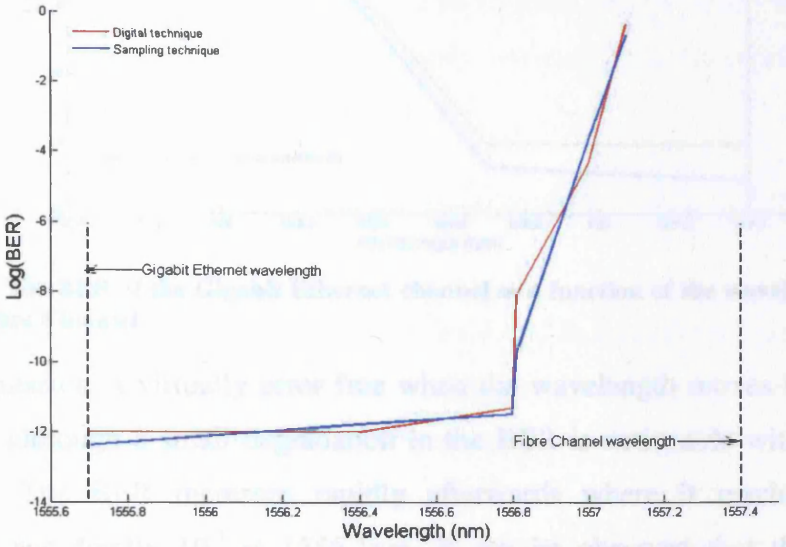

Figure 4.18 The BER of the Fibre Channel as a function of the wavelength shift in the adjacent Gigabit Ethernet channel

It can be observed that up to a wavelength of 1556.4nm, the digital method sees no errors while the analogue technique detects an increase in the BER from 5×10^{-13} to approximately 2×10^{-12}. Between 1556.4 and 1556.8nm both techniques notice a slight degradation in the quality of the channel where the BER rises to 5×10^{-12}. This coincides with the 1.6nm bandwidth of the bandpass filters used in the demultiplexer (1557.4 - 0.8= 1556.6nm). After this the BER increases dramatically where it goes from an average of 10^{-10} at 1556.81nm to 10^{-1} at 1557.1nm.

4.4.2.2 Monitoring Gigabit Ethernet

Figure 4.19 shows the BER, obtained by the digital and the sampling techniques, of the GbE channel as the wavelength of the adjacent FC channel decreases.

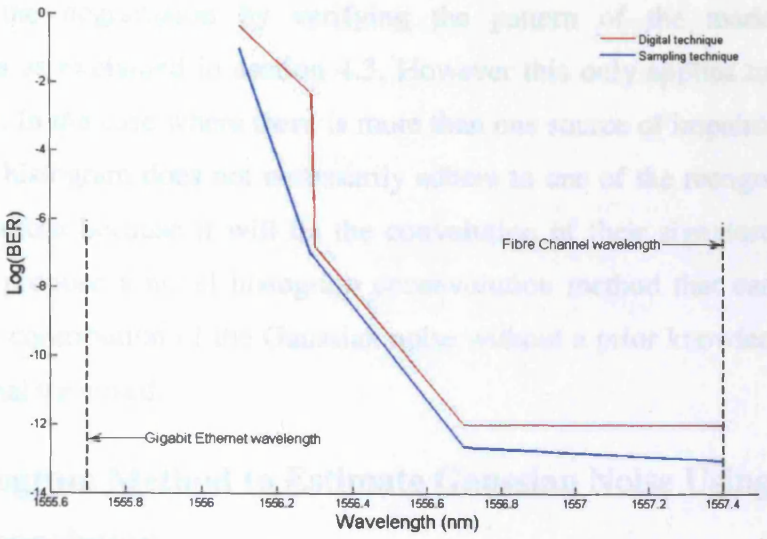

Figure 4.19 The BER of the Gigabit Ethernet channel as a function of the wavelength shift in the adjacent Fibre Channel

The transmission is virtually error free when the wavelength moves from 1557.4 to 1556.7nm although a small degradation in the BER is noticeable with the sampling technique. The BER increases rapidly afterwards where it reaches 1.6×10^{-7} at 1556.3nm and finally 10^{-1} at 1556.1nm. It can be observed that there is a good correlation between the digital and the analogue monitoring methods although the latter gives a slightly lower BER probably because we were using a narrower optical filter than the ones used in the transponders.

4.4.3 Summary and Conclusions

In this section we investigated the accuracy of the sampling technique for performance monitoring of deployed WDM metro networks transporting various protocols. The protocols used were 2.5Gbit/s Synchronous Digital Hierarchy (SONET/SDH), 1.0625Gbit/s Fibre Channel, 2.125Gbit/s Fibre Channel and 1.25Gbit/s Gigabit Ethernet. We examined the effect of two sources of degradation on the metro network: amplifier noise and in-band crosstalk. We found that this technique can accurately estimate the BER for both impairments and regardless of the protocol used (protocol independent). In addition we found that the sampling technique can sense the degradation in the quality of service well before it reaches the critical BER threshold of 10^{-12} or 10^{-9} and therefore can be used as a pre-emptive maintenance tool. Furthermore, although the built-in digital performance monitoring techniques (BIP, CRC) can correctly detect bit errors, they cannot indicate the root cause of the degradation. The sampling technique on the other hand can reveal the

source of the degradation by verifying the pattern of the marks and spaces distributions as explained in section 4.3. However this only applies to single source degradation. In the case where there is more than one source of impairment, the shape of the final histogram does not necessarily adhere to one of the recognisable patterns discussed before because it will be the convolution of their signatures. In the next section we propose a novel histogram deconvolution method that can estimate and subtract the contribution of the Gaussian noise without a prior knowledge of the path that the signal traversed.

4.5 Histogram Method to Estimate Gaussian Noise Using Deconvolution

As mentioned in the previous chapter and discussed in section 4.3, the histogram and especially the marks' histogram takes a distinctive shape for every source of impairment and this could be used to determine the root cause of signal degradation during transmission. In general, the histogram reflects a combination of distortion and noise existing on the transmission path. In other words, the different signatures appearing on the histogram and originating from different sources of degradation are convolved together and could be separated by using the FFT deconvolution method. This technique was first proposed by Weinert et al [Wei'00a] to evaluate crosstalk in an environment dominated by Gaussian noise. However, unless the exact amount of Gaussian noise is known, the use of this technique will not lead to the correct detection of crosstalk [Wei'00a]. In this section, we present a novel way of evaluating the Gaussian noise from the marks' histogram without prior knowledge of the transmission path and then use this result to detect other sources of distortion. This technique is then extended to deal with more than two sources of degradation and the limitations of its use are also investigated.

4.5.1 Deconvolution Algorithm

White noise is mainly introduced in the network through amplified spontaneous emission (ASE) of the erbium-doped fibre amplifiers. This noise is random and can be assumed to have a Gaussian distribution. As mentioned earlier, the marks' histogram, sampled at decision times, can be seen as a convolution of different shapes, each resulting from a specific type of degradation. Convolution of two functions can be

written as a product of their Fourier transforms in the Fourier domain. Assuming that the histogram $h(v)$ contains some Gaussian elements, it can be written as:

$$h(v) = \exp\left(\frac{-v^2}{2\sigma^2}\right) * f(v) \tag{4.2}$$

where σ is unknown and f is an arbitrary function that can, for example, represent the pattern of chromatic dispersion and/or the initial histogram without distortion. Equation 4.2 can be written in the Fourier domain as:

$$H(\omega) = \exp\left(-\alpha\omega^2\right)F(\omega) \tag{4.3}$$

where $\alpha = \frac{\sigma^2}{2}$, H is the Fourier transform of h and F is the Fourier transform of the arbitrary function f. Our proposed technique involves multiplying the function H with an exponential function so that it cancels out the Gaussian function. This can be written as:

$$H(\omega)\exp\left(\beta\omega^2\right) = \exp\left((\beta-\alpha)\omega^2\right)F(\omega) \tag{4.4}$$

When β is greater than α in equation (4.4), the resultant function is a parabolic function and has two peaks, one on each side of the spectrum. However when β approaches α, the first term on the right hand side becomes more of a unit step function and therefore F starts to appear. By varying the width of the exponential function (i.e. varying β) and tracking the side peaks, it is possible to obtain a good approximation of α. Figure 4.20 shows the application of this method to a histogram that contains a Gaussian and another arbitrary function in the Fourier domain.

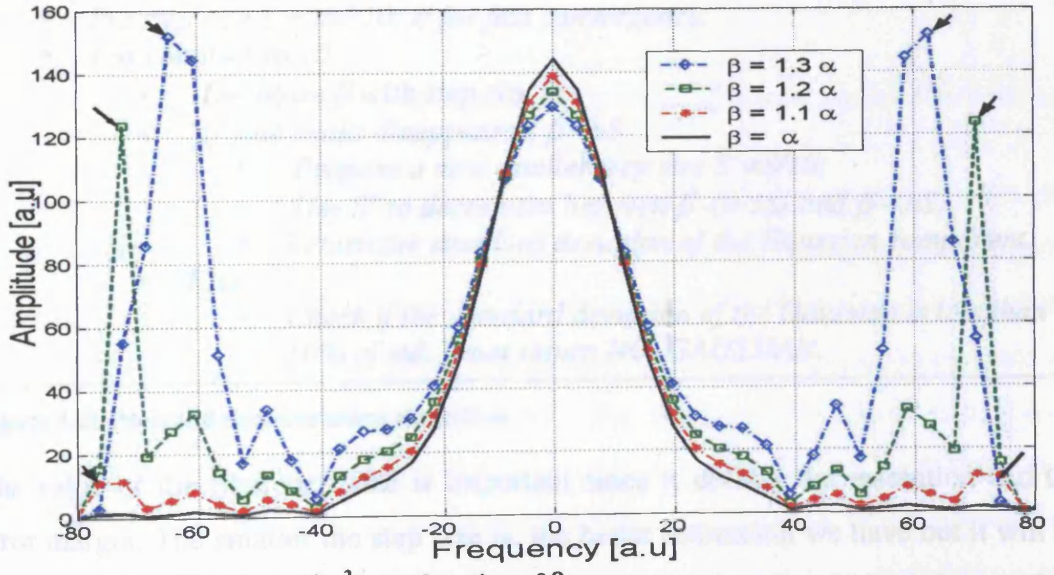

Figure 4.20 Plot of H(w) exp(βw²) as a function of β

First the variance of the exponential function is chosen to be equal to the variance of the histogram so that we can ensure that β is greater than α (the variance of the histogram is equal to the sum of variances of the deconvolved functions). Following this, β is decreased gradually and the side peaks are monitored and compared to the amplitude of the centre of the spectrum. The peaks are identified by their sharp edges which usually do not exist in the Fourier transform of stable functions. Moreover, as β is decreased these peaks move further from the centre of the spectrum (as indicated by arrows in Figure 4.20). Finally, when the amplitude of the peaks is less than 1% of the peak at the center of the spectrum, the function is inverse Fourier transformed and the deconvolved function is obtained. The standard deviation of the Gaussian pulse is given by:

$$\sigma = \sqrt{2\beta} \tag{4.5}$$

The step size has to be sufficiently large at the start to guarantee a fast convergence of the algorithm and to ensure that the original histogram does contain a Gaussian element (if the side peaks do not subside, the histogram does not contain a Gaussian component). From simulations, an initial step size of 5% to 10% of the variance was found to be sufficient to reveal the existence of Gaussian elements and to confine them in an interval within a low number of iterations (at most 10 to 20). After this, a smaller step size is chosen and the above operation is repeated again. Figure 4.21 shows an example of the algorithm.

In the F-domain

- *Start with β equal to the standard deviation (std) of the histogram;*
- *Put step size S = std/10; // for fast convergence.*
- *For count=1 to 10*
  - *Decrease β with step size S;*
  - *If side peaks disappear at β - nS*
    - *Propose a new smaller step size S'=S/10;*
    - *Use S' to decrement between β-(n-1)S and β – nS*
    - *Return the standard deviation of the Gaussian component.*
  - *Else*
    - *Check if the standard deviation of the Gaussian is less than 10% of std. If not return NO_GAUSSIAN.*

Figure 4.21 Proposed deconvolution algorithm

The value of the final step size is important since it defines the resolution and the error margin. The smaller the step size is, the better estimation we have but it will be more time consuming. It was found that an error in the estimation of the standard

deviation of +/- 5% will not greatly affect the deconvolution result. Therefore aiming at a 5% error margin in the estimation is a good trade off between processing time and result accuracy.

4.5.2 Numerical Simulation

The technique was tested by numerical simulation in an environment dominated by Gaussian noise and one source of distortion. We investigated two types of distortion: chromatic dispersion and crosstalk. The simulation setup shown in Figure 4.22 was used to introduce residual dispersion. A 2^{13} pseudo random bit sequence NRZ signal was generated at 10Gbit/s and transmitted through a loop consisting of an EDFA with a noise figure (F_n) of 6dB and a 100km single mode fibre (SMF) followed by dispersion compensating fibre (DCF). The dispersion coefficients were 17ps/nm.km for the SMF and -85ps/nm.km for the DCF. The optical signal was circulated 6 times around the loop (total of 600Km of SMF) before it was terminated by a square law detector. The EDFA compensated exactly for the fibre loss of each span.

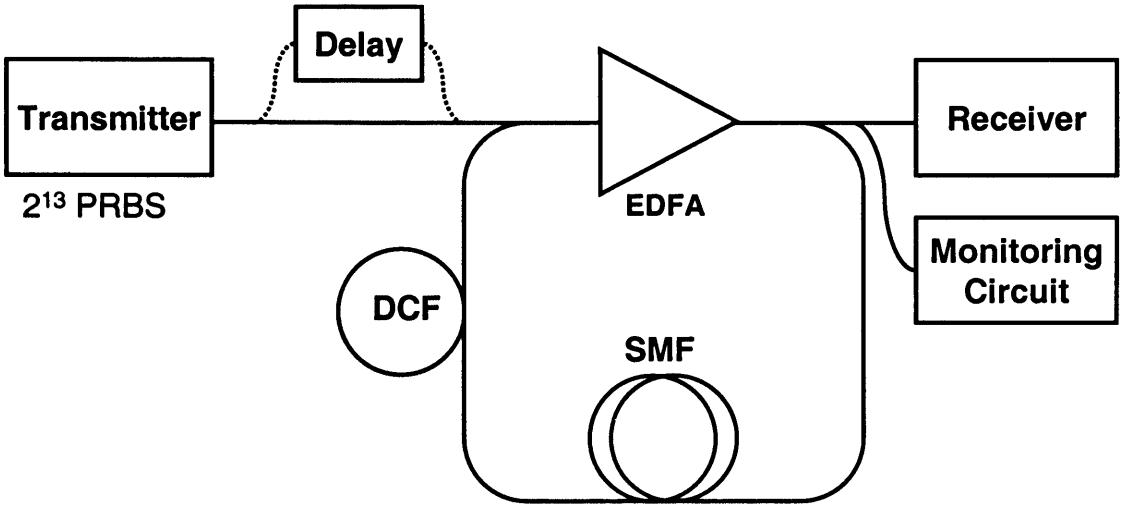

Figure 4.22 Simulation setup to verify the accuracy of the histogram deconvolution method. SMF: single mode fibre; DCF: dispersion compensating fibre.

The DCF was set so that it did not fully compensate for dispersion and the total residual dispersion at the end of the link was 918ps/nm. Nonlinear effects were ignored at this stage. The monitoring circuit consisted of two D-type flip-flops followed by an XOR gate as explained in section 3.4.2. This was used to generate the histograms of the channel at decision times. The clock utilised was a high-Q filter based clock recovery. Our deconvolution technique was applied to the histogram of the sampled signal and the obtained marks distribution before and after deconvolution is displayed in Figure 4.23(a). It can be observed that the ones histogram has a slight

signature of chromatic dispersion although it is partially masked by the effects of ASE noise. After deconvolution the two effects are separated and the signature of dispersion, with its three distinct levels, can be clearly seen.

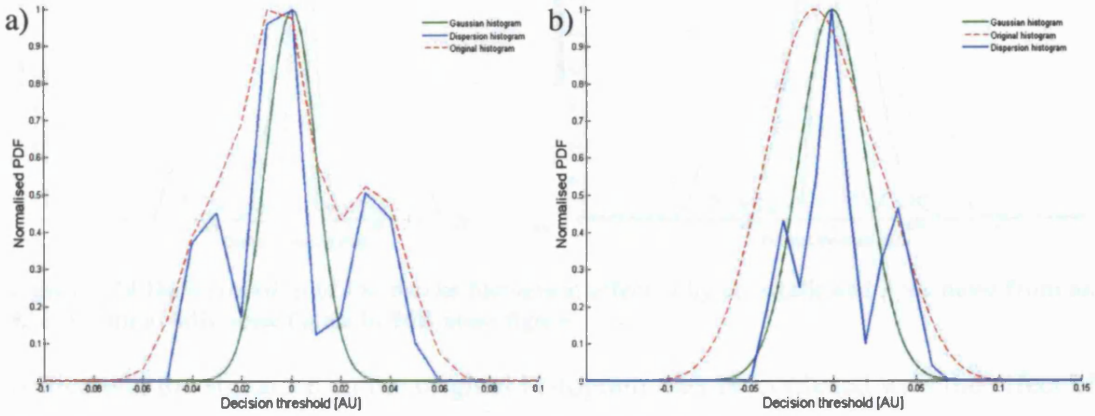

Figure 4.23 Deconvolution of the marks histogram affected by dispersion and ASE noise from an EDFA with a) 6dB noise figure b) 9dB noise figure

The above experiment was repeated but with the amount of residual dispersion kept constant, the ASE noise in the system was increased by increasing the noise figure of the amplifier to 9dB. The obtained marks histogram before and after deconvolution is shown in Figure 4.23(b). The distribution of the marks before deconvolution has a Gaussian shape (although not truly Gaussian) because ASE noise is now the most dominant source of degradation. It can also be noticed that although residual dispersion was not modified, the distribution due to CD changed slightly compared with Figure 4.23(a). This is because in the presence of heavy Gaussian noise our deconvolution technique converges quickly resulting in a small overestimation of the noise and hence a slight alteration in the expected results.

The simulation was rerun with 14dB in-band crosstalk and without chromatic dispersion. Crosstalk was introduced at the start of the link by tapping a portion of the signal out, delaying then reintroducing it as demonstrated in Figure 4.22. The noise figure of the amplifier was reset to 6dB. After sampling the signal at decision times, we applied our deconvolution technique to the obtained histogram and the results are shown in Figure 4.24(a).

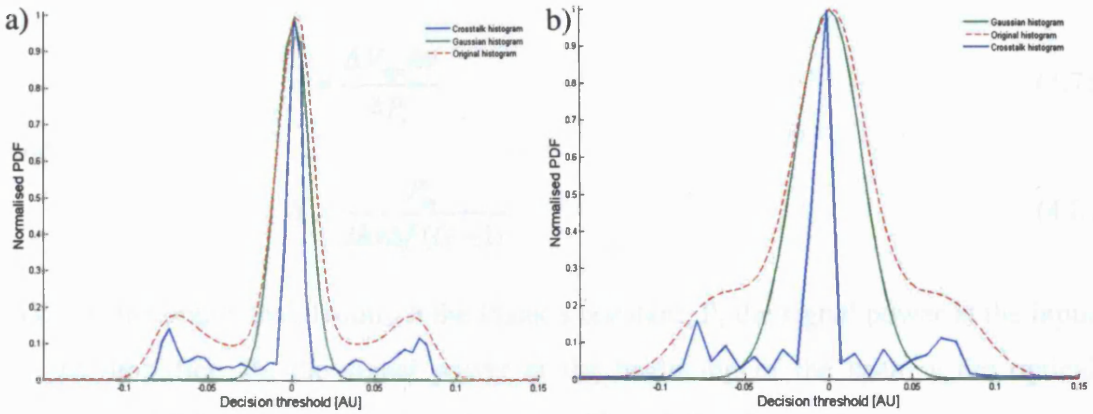

Figure 4.24 Deconvolution of the marks histogram affected by crosstalk and ASE noise from an EDFA with a) 6dB noise figure b) 9dB noise figure

Notice that the signature on the original histogram may be confused with the effect of dispersion (three distinct levels) but it is clear that, after deconvolution, the channel suffered from coherent crosstalk (appearance of the plateau around the centre peak). This simulation was repeated with the noise figure of the amplifier increased to 9dB in order to increase the ASE noise in the system. The histogram before and after deconvolution is illustrated in Figure 4.24(b). It can be observed that our technique correctly detects an increase in the ASE noise contribution. In addition, it can be seen that the shape of the crosstalk distribution changed slightly compared to Figure 4.24(a) because our technique converged before reaching the actual standard deviation of the noise. Nevertheless, this does not greatly affect the accuracy of the outcome.

We saw in the previous section that not only does the sampling monitoring technique accurately evaluate the BER of the system but it can also detect degradation in the quality of the service before reaching a critical level. In addition, by analysing the shape of histograms, the root cause of this drop in quality may be assessed. However, as we saw in these simulations, when more than one impairment coexist in the same channel the final histogram may have an unrecognisable shape. Using our deconvolution technique, we showed that the Gaussian noise contribution can be removed and hence a clearer picture on what caused the degradation can be drawn. Moreover, the BER due to ASE noise can be estimated and the noise figure of the system can be assessed. This is given by (see appendix 7):

$$BER = \tfrac{1}{2} erfc\left(\frac{\sqrt{b}}{\sqrt{a F_n} + \sqrt{F_n}}\right) \tag{4.6}$$

where

$$a = \frac{\Delta V_{opt} hv}{4P_s} \tag{4.7}$$

and

$$b = \frac{P_{in}}{2hv\Delta f(G-1)} \tag{4.8}$$

ΔV_{opt} is the optical bandwidth, h the Plank's constant, P_s the signal power at the input of the amplifier, P_{in} the signal power at the beginning of the span, v the optical frequency, Δf the receiver (electrical) bandwidth and G is the amplifier gain.

The major drawback of using this deconvolution technique is that it does not function well in the presence of nonlinearities. While impairments such as noise, dispersion and crosstalk are combined by multiplying their transfer functions in the Fourier domain, nonlinear effects such as self-phase modulation have their transfer functions convolved in this domain. In other words, linear effects are combined in the Fourier domain whereas the nonlinearities are combined in the time domain. To understand this, let us consider the following example. Assuming the signal after the first loop is only affected by chromatic dispersion and noise, its Fourier transform F_1 can be written as:

$$F_1 = G \times D \tag{4.9}$$

where G and D are the transfer functions of the Gaussian noise and dispersion respectively. Now assume after the second loop the signal is affected by noise, dispersion and nonlinearity. Its Fourier transform (F_2) is then given by:

$$F_2 = (F_1 \times G \times D) * N \tag{4.10}$$

where N is the transfer function of the nonlinear effects. Our method will try to multiply equation 4.10 with an exponential to cancel out G, but this will inevitably lead to erroneous results.

4.5.3 Experimental validation

The deconvolution technique was experimentally tested at 10Gbit/s and the setup is shown in Figure 4.25. First, the output from the Mach-Zehnder modulator was fed into a dispersion compensating grating module, designed to compensate 40 km of single mode fibre, to generate a fixed amount of dispersion. A variable attenuator was placed at the output to control the optical power input into the erbium-doped fibre

amplifier (EDFA) and therefore allowed the amount of ASE noise to be varied. A 3nm bandpass filter was used to avoid the saturation of the receiver. Finally a monitoring circuit based on the dual decision circuit configuration (section 3.4.2) was used.

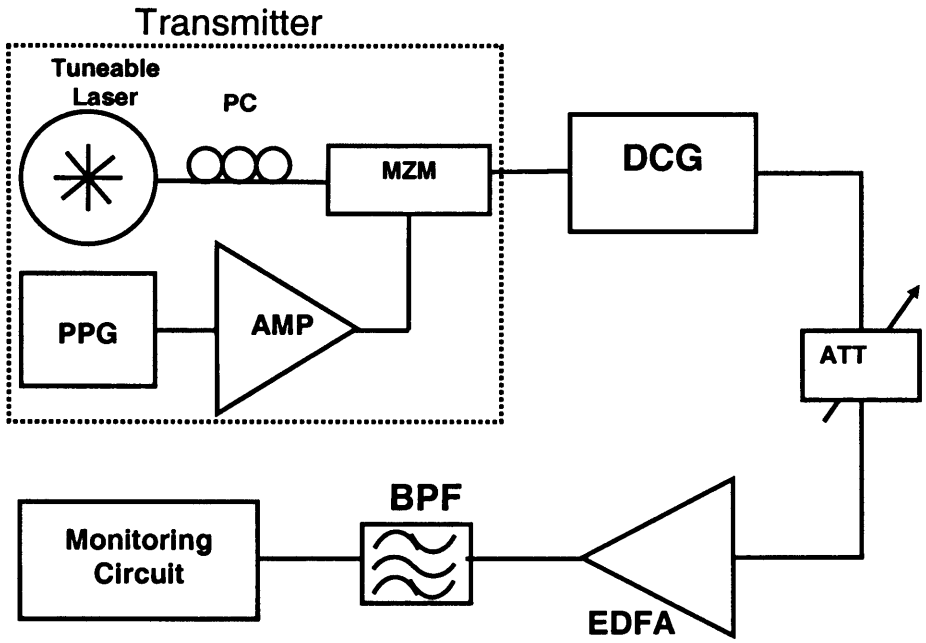

Figure 4.25 Experimental setup to verify the accuracy of the deconvolution technique

The noise figure of the EDFA was 6dB, the optical bandwidth was 375GHz and electrical bandwidth was approximately 14GHz. The optical power incident on the EDFA was varied by varying the optical attenuator preceding the amplifier. This leads to a change in the amplifier gain and thus a change in the contribution of the ASE noise towards the total degradation (i.e. higher gain leads to higher amplifier noise). A histogram was generated for every optical power at the input of the EDFA. It is important to note that dispersion was kept fixed using the same wavelength and the same room temperature and any change in the overall degradation will come from the change in the noise generated by the amplifier. In this experiment we estimated the standard deviation of the ASE noise using the novel deconvolution technique described earlier and compared it with the theoretical values. We applied this technique to the marks distribution because they are affected by both the signal-spontaneous and spontaneous-spontaneous beat noise whereas the spaces are only affected by spontaneous-spontaneous noise. The theoretical values of the signal-spontaneous and spontaneous-spontaneous variances are governed by [Agr'02]:

$$\sigma^2_{sig-sp} = 2(q\eta)^2 F_n \frac{\Delta f}{h\nu} G^2 P \qquad (4.11)$$

and

$$\sigma_{sp-sp}^2 = (q\eta F_n)^2 \Delta f \Delta v_{opt} G^2 \tag{4.12}$$

The total standard deviation of the marks due to ASE noise is given by:

$$\sigma_{Marks} = \sqrt{\sigma_{sig-sp}^2 + \sigma_{sp-sp}^2} \tag{4.13}$$

Equations 4.9, 4.10 and 4.11 were used to calculate the theoretical values of the standard deviation. The deconvolution technique was applied to the marks histogram and the results plotted in Figure 4.26 were obtained.

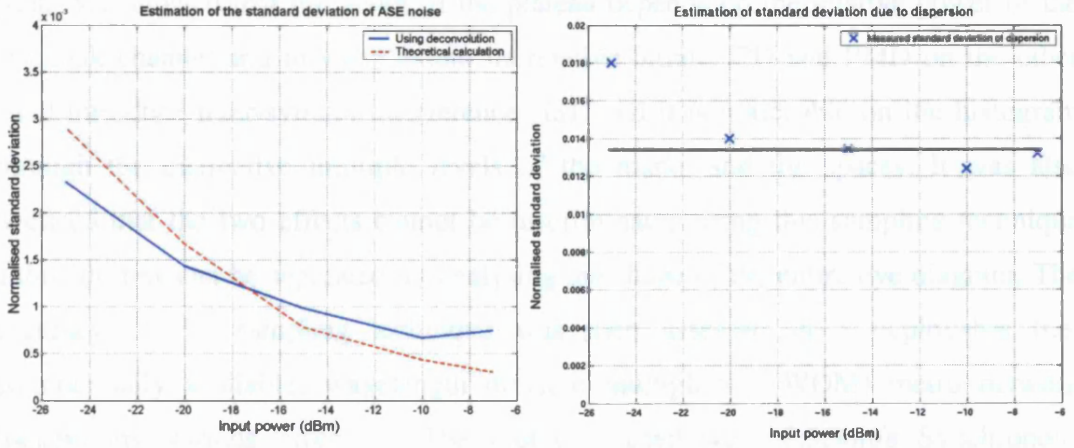

Figure 4.26 a) Theoretical Vs. measured standard deviation of ASE noise b) Measured standard deviation of dispersion

Figure 4.26(a) shows a comparison between the theoretical and the estimated (using deconvolution) normalised standard deviations of the marks as a function of the input power to the EDFA. The standard deviations have been normalised by dividing them by the difference between the mean value of the ones and the mean value of the zeros (i.e. divided by μ_1-μ_0). From the graph, it can be seen that there is a good correlation between the two although the algorithm tends to slightly overestimate noise when the input power is greater than -10dBm and slightly underestimate it in the region less than -24dBm.

Figure 4.26(b) shows the normalized standard deviation of the non-Gaussian component (i.e. due to dispersion) after deconvolution. It can be observed that the standard deviation is almost constant for input power levels greater than -20dBm, as expected, since distortion due to dispersion does not vary with power. However it slightly increases at lower powers because the algorithm underestimated the standard deviation due to ASE noise ($\sigma^2_{total}=\sigma^2_{disp}+\sigma^2_{noise}$).

4.6 Summary

In this chapter the synchronous sampling technique for performance monitoring of optical networks was investigated. We started by experimentally analysing the effects of crosstalk, chromatic dispersion (CD) and polarisation mode dispersion (PMD) on the histograms. The pattern of these impairments on the histogram can potentially be utilised for root cause analysis. We demonstrated that crosstalk affects mainly the marks (ones) histograms and leads to the appearance of a plateau around the centre peak. We showed that the width of the plateau depends on the relative power of the crosstalk channel and to some extent its relative bitrate. CD and PMD on the other hand introduce inter-symbol interference (ISI) and it is noticeable on the histogram through the distinctive multiple levels of the marks and the spaces. It was also deduced that the two effects cannot be discriminated using this sampling technique although they can be separated by analysing the shape of the entire eye diagram. The accuracy of the sampling technique was then assessed in a deployable (i.e. commercially available) wavelength division multiplexed (WDM) metro network transporting various protocols. The protocols used were 2.5Gbit/s Synchronous Digital Hierarchy (SONET/SDH), 1.0625Gbit/s Fibre Channel, 2.125Gbit/s Fibre Channel and 1.25Gbit/s Gigabit Ethernet. We examined the effect of amplifier (ASE) noise and in-band crosstalk in the WDM system and we showed that the sampling technique can detect the degradation in the quality of the service before reaching a critical level (BER of 10^{-12}). This characteristic can be utilised as a pre-emptive maintenance tool so that service providers can anticipate service degradation before they are noticed by the clients. Moreover, this method can accurately determine the BER and is protocol and bitrate independent. Furthermore, although the built-in digital performance monitoring techniques (BIP, CRC) can correctly detect bit errors, they cannot indicate the root cause of the malfunctioning. The sampling technique on the other hand can reveal the source of the degradation by verifying the shape of the marks and spaces distributions. These distribution shapes however can be composed of different patterns convolved together in the case of multiple impairments. We proposed a novel deconvolution method that can be applied to the histograms in order to evaluate the Gaussian noise without prior knowledge of the transmission path. This can be used to separate the contribution of distortion from the contribution of noise and hence provide advanced root cause analysis.

Chapter 5 PMD Effects on the Clock Recovery

5.1 Introduction and Problem Formulation

As the bit rate and distance of optical fibre transmission systems continue to increase, the understanding of polarisation-mode dispersion (PMD) and its impairments on the system performance are becoming ever more important. First order PMD can be represented by a differential group delay (DGD) $\Delta\tau$, between orthogonally polarised components of the input power waveform $P_{in}(t)$. Both the DGD and the principal states of polarisation (PSP) are random and depend on the birefringence details along the entire fibre. The output waveform can be written as [Poo'91]:

$$P_{out} = \gamma P_{in}\left(t + \frac{\Delta\tau}{2}\right) + (1-\gamma)P_{in}\left(t - \frac{\Delta\tau}{2}\right) \tag{5.1}$$

where $0< \gamma <1$ is the ratio of powers launched into the two principal states. In the absence of PMD and neglecting all other impairments, P_{in} and P_{out} are equal. In a network where chromatic dispersion is exactly compensated for, PMD becomes the main linear distortion that degrades the quality of service. The effects of PMD on the eye closure, the bit error rate (BER) and SNR/Q-factor have been described in many previous works [Poo'91],[Ian'93],[Mor'94]. However, there has been no analysis of the effect of PMD on the clock recovery behaviour and thus on the sampling time, key in determining the consequences of PMD on the BER or the Q-factor in transmission systems. Unlike noise and dispersion, in the presence of PMD the sampling time based on the recovered clock may not be at the centre of the eye and may shift depending on the differential group delay $\Delta\tau$ and the ratio of powers in the two principal states of polarisation (γ).While some have chosen to ignore this factor completely (e.g. [Kim'02]) others have proposed rough assumptions for their calculations. For instance, in [Ian'93], where the error probability due to PMD is analysed, the clock phase is assumed to change linearly with the differential group delay and the power ratio and is given as:

$$t_S = t_0 + \gamma\Delta\tau \tag{5.2}$$

where t_0 is the sample time in the absence of PMD. In [Gal'01] on the other hand, the probability density function of the Q-factor due to PMD is defined on the basis that

the clock recovery samples at the centre of mass of the pulses in the received signal. The shift in the sampling time is governed by:

$$t_S = t_0 + (2\gamma - 1)\frac{\Delta\tau}{2} \tag{5.3}$$

Intuitively this assumption seems more probable because, as one might expect, when the two PSPs have equal power (γ =0.5) there should not be any phase shift. Bearing in mind these two different assumptions, the question that arises is how PMD actually affects the phase of the recovered clock. This problem is important to accurately define a relationship between the BER/Q-factor and PMD and even more crucial for PMD monitoring techniques utilising clock recovery circuits (see Literature Review chapter) as they must take into account the PMD-induced phase shift (since it leads to different measured eye opening). This is what we will try to answer in this chapter. The chapter is organised as follow: section 5.2 introduces the different clock recovery methods used in telecommunication networks. It is divided into phase locked loop and high-Q filter methods. Section 5.3 discusses the effect of PMD on some selected high-Q filter clock configurations.

5.2 Clock Recovery Circuits

The clock recovery circuits are an essential part of the receivers in telecommunication systems and their primary task consists of synchronising the incoming bits with the decision circuit. This is carried out by isolating the spectral component at the bitrate frequency which contains information about the phase of the bit slot, a crucial element in the decision process. In the case of return-to-zero (RZ), a spectral component at the bitrate frequency is present as shown in Figure 5.1a for a 10Gbit/s system and can be easily extracted using a narrow-bandpass filter.

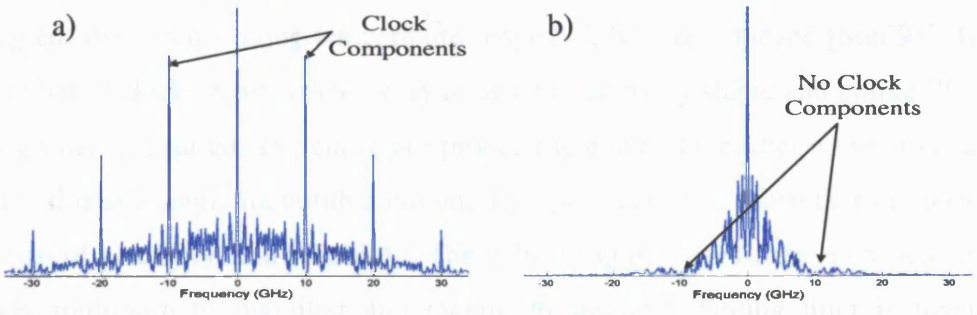

Figure 5.1 10Gbit/s spectrum of a 2^6-1PRBS (a) 40% duty cycle RZ format (b) NRZ format

The non-return-to-zero (NRZ) format, however, is widely used in current lightwave systems because it has a better bandwidth efficiency and is simpler to generate. Recovering the clock of a NRZ data stream is slightly more problematic because it has little or no component at the bitrate frequency (null in the Fourier transform) as can be observed in Figure 5.1b. Consequently, the clock signal has to be regenerated by means of a nonlinear, pre-processing circuit before the filtering process. Different schemes of nonlinear pre-processing have been proposed and the extensively used methods are transition/edge detectors and square-law (absolute value) units. These will be discussed in more details in section 5.3. The subsequent filtering stage is achieved by utilising either an open-loop structure or a closed-loop, adaptive structure. The former is implemented by means of high-Q filters while the latter is realised using the phase-locked loop (PLL) technique. This is considered next.

5.2.1 High-Q Filter

High-Q filters can be implemented using two different technologies namely transversal surface-acoustic-wave (SAW) filters or dielectric resonator (DR) filters. For transmission rates up to a few Gbit/s, bandpass filters have been typically fabricated using the SAW technology. However, these filters exhibit excessive losses for higher bitrates and are more difficult to manufacture because the inter-digital electrode spacing becomes very small [Mon'92]. DR filters on the other hand have low losses and are relatively easy to manufacture. They have been successfully used for data synchronisation in systems functioning at bitrates of 20Gbit/s and above [Mon'94], [Yoo'95]. The main disadvantage of using this technology is that the resonance frequency of the DR is temperature sensitive and a large change in the ambient temperature may lead to a significant phase shift in the extracted clock. This can be corrected by using an automatic phase controller where a phase variation of $< \pm 6$ degrees over an operating temperature range 0-75^{0}C was achieved [Son'95]. High-Q filter based clock recoveries are easy to design, relatively stable and unlike PLL, no locking time is required. The entire pre-processing unit and the filtering section can be integrated into a single monolithic circuit. This provides clear advantages in terms of size, cost of assembly, and reliability. The value of Q in these filters is chosen so that it gives minimum timing jitter and maximum stability. Timing jitter is inversely proportional to $\sqrt{Q}$ and therefore increasing this latter results in a reduction of the jitter [Fih'90]. However, filter detuning places an upper limit because it leads to a

phase shift that is proportional to Q. To have a good trade off between the two, it was argued that Q should be in the range between 300 and 800 [Fih'90]. Most of the filters currently in use and reported in the literature utilize filters with Q in this range [Mon'94], [Yoo'95].

5.2.2 Phase-Lock Loop (PLL)

A phase-locked loop operates as an active filter for selecting the clock frequency. Any PLL must include three basic components which are a phase detector, a (loop) low pass filter and a voltage controlled oscillator (VCO). The functional block diagram is shown in Figure 5.2.

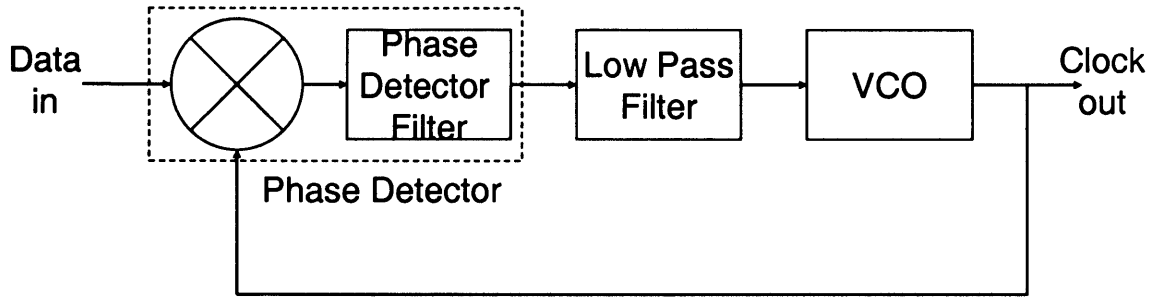

Figure 5.2 Block diagram of PLL

The first stage measures the phase difference between the incoming data and the sinusoidal signal output of the VCO using a phase detector. In its simplest form, the phase detector consists of a multiplier followed by a low pass filter to remove the unwanted high frequencies. It can also be implemented using an exclusive OR (XOR) gate. The loop filter provides the error signal that drives the VCO. This produces a periodical signal which frequency changes based on the applied external signal. A null error signal results in the VCO emitting at its central frequency (quiescent frequency). When the reference clock and the feedback clock are aligned, the PLL is locked. Since PLLs operate on the phase of signals, they are susceptible to phase noise or jitter [Raz'96]. Excessive jitter on the input clock can cause the PLL to lose lock. Additionally, if there is a sudden, drastic phase change of the input clock, the PLL may not be able to react quickly enough to maintain lock. PLLs are more complex to implement and cannot be implemented in truly monolithic form for high bitrates (>10Gbit/s) because they need external components such as high frequency VCO's [Mur'99].

5.3 The Effect of PMD on the Sampling Time

5.3.1 The System and PMD Model

The transmitted signal in our numerical model is a 10Gbit/s, 2^{11} NRZ pseudo-random bit sequence (PRBS). Since neither the Q-factor nor the eye opening penalty will be assessed in this chapter, the extinction ratio of the system was considered to be infinite. The transmitted pulses have Gaussian-like edges and a 10-90% rise time of 33ps. First order PMD is generated using the principal state model (Jones space) shown in Figure 5.3. The signal launched from the transmitter is linearly polarised. It is then split into two parts with equal amplitudes using, for instance, a polarisation beam splitter (PBS). While one section is multiplied by $\sqrt{\gamma}$ ($0<\gamma<1$) and retarded by an amount of $\Delta\tau/2$, the other one is multiplied by $\sqrt{1-\gamma}$ and advanced by $\Delta\tau/2$. The two segments are finally recombined and detected by a square-law receiver. Its bandwidth is assumed to be large enough so that the shape of the pulses is not altered.

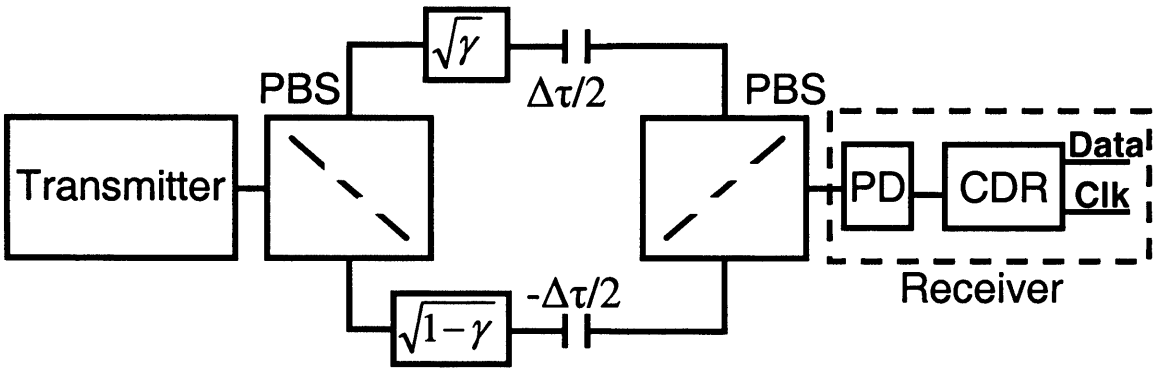

Figure 5.3 PMD model used in the numerical simulation

The clock recovery circuit (CRC) considered here is a high-Q filter based. The band pass filter (BPF) is assumed to be a square filter centred at 10GHz with a bandwidth of approximately 5.5 MHz corresponding to a Q-value of 1800 ($BW=\omega_0/Q$) [Has'98], [Sed'97]. Other sources of impairments such as noise and dispersion were ignored so that solely the effect of PMD on the clock recovery is examined.

5.3.2 No Pre-processing Circuit

In a NRZ system, the electrical power spectrum contains no clock frequency component because after detection (quadratic) the upper and lower optical clock sidebands beat with the carrier and cancel each other out [Hei'03]. Therefore to recover the clock of a NRZ signal, a high-Q filter at half the bit rate frequency is used.

It is usually followed by a full wave rectifier to double the clock to the desired frequency. RZ format however contains a clock component at the bit rate frequency and a band-pass filter at 10GHz is sufficient to extract the clock.

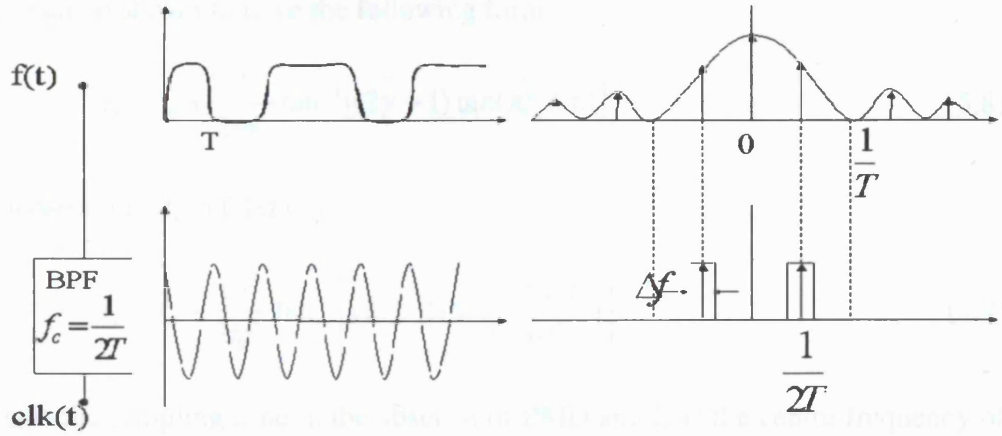

Figure 5.4 Clock recovery configuration for NRZ format with no pre-processing circuit

Figure 5.4 shows the clock extraction from a NRZ data stream without a pre-processing circuit. First let us assume that f(t) is the data arriving at the receiver without suffering from PMD. According to Figure 5.4, the clock signal can be written as:

$$clk(t) = \Im^{-1}\left(F(\omega).H(\omega)\right) \tag{5.4}$$

where $\Im^{-1}$ indicates the inverse Fourier transform, H(ω) is the filter transfer function and F(ω) is the Fourier transform of f(t). Now assume that $f_{PMD}(t)$ is the same data stream arriving at the receiver, but having experienced a certain amount of PMD. Working with the principal state model, it can be expressed as:

$$f_{PMD}(t) = \gamma f\left(t + \frac{\Delta\tau}{2}\right) + (1-\gamma) f\left(t - \frac{\Delta\tau}{2}\right) \tag{5.5}$$

Notice that in the absence of PMD (i.e. $\Delta\tau=0$), $f_{PMD}(t) = f(t)$. Using the two above equations, it can be deduced that the clock expression of $f_{PMD}(t)$ is governed by (see Appendix 2):

$$clk_{PMD}(t) = \Im^{-1}\left\{\left[\gamma e^{-i\omega\Delta\tau/2} + (1-\gamma)e^{i\omega\Delta\tau/2}\right]F(\omega)H(\omega)\right\} \tag{5.6}$$

Or can simply be expressed as:

$$clk_{PMD}(t) = \gamma clk(t + \Delta\tau/2) + (1-\gamma)clk(t - \Delta\tau/2) \tag{5.7}$$

Thus the clock signal in the presence of PMD is the sum of the clock signals of the two principal states of polarisation. By applying trigonometric properties to the above equation (refer to Appendix 2), the PMD-induced time shift t_S, for both RZ and NRZ formats, can be shown to have the following form:

$$t_s = t_0 + \frac{1}{2\pi f_c}\tan^{-1}\left[(2\gamma - 1)\tan(\pi f_c \Delta\tau)\right] \tag{5.8}$$

Or in picoseconds (f_c in GHz):

$$t_s = t_0 + \frac{10^3}{2\pi f_c}\tan^{-1}\left[(2\gamma - 1)\tan\left(\frac{\pi f_c \Delta\tau}{10^3}\right)\right] \tag{5.9}$$

where t_0 is the sampling time in the absence of PMD and f_c is the centre frequency of the high Q filter. In a 10Gbit/s system, f_c = 5GHz for NRZ and 10GHz for RZ format. It can be noticed that when γ =0.5 or $\Delta\tau$ =0, t_s is the same as t_0. This equation was confirmed by numerical simulation at 10Gbit/s using the model described in section 5.3.1. The simulated clock recovery consisted of a high-Q filter centred at 5GHz and the results are shown in Figure 5.5 with t_0 assumed to be zero.

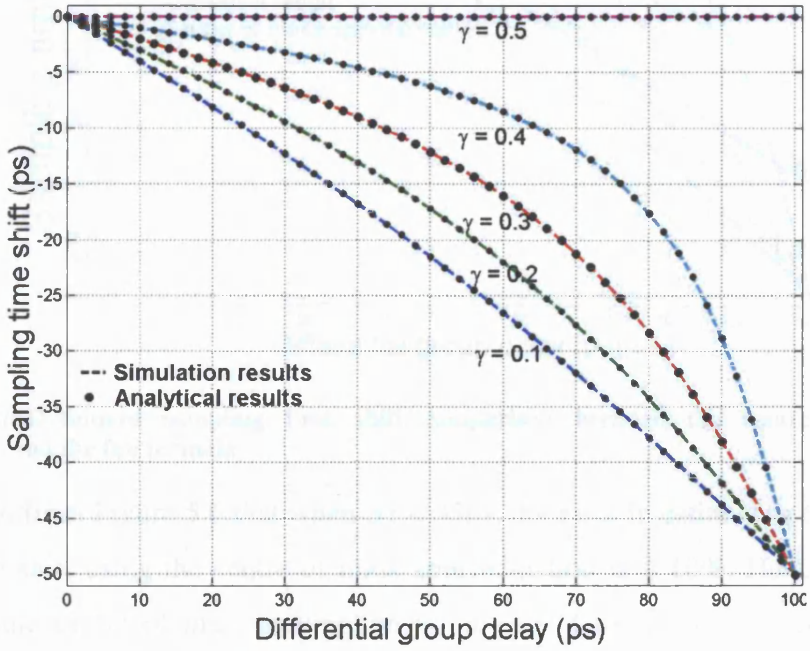

Figure 5.5 Sampling time shift induced by PMD of a clock recovery with no pre-processing circuit

Figure 5.5 shows the sampling time shift induced by PMD for values of γ between 0 and 0.5 with steps of 0.1. Curves for 1-γ (i.e. between 0.5 and 1) can be obtained by taking a mirror copy of the curve at γ wrt the x-axis at zero. It can be seen from the

graph that the decision time does not change when the power is evenly split between the two states of polarisation. However it increases rapidly when most of the power is travelling in one state of polarisation (e.g. γ=0.1 or 0.9) or with increasing differential group delay. Equation 5.9 can be expanded by using the Taylor series to give:

$$t_s = t_0 + \frac{2\gamma - 1}{2}\Delta\tau + \frac{2}{3}\gamma(1-\gamma)(2\gamma-1)\pi^2 f^2 \Delta\tau^3 + \ldots \qquad (5.10)$$

As reported in section 5.1 (equation 5.3) the second term in the right hand side of this equation represents the centre of mass of the incoming pulses. Hence the centre of mass assumption is valid as long as the other higher terms can be neglected. To assess the extent to which this assumption is applicable, the full equation and the centre of mass approximation are compared in the plot below.

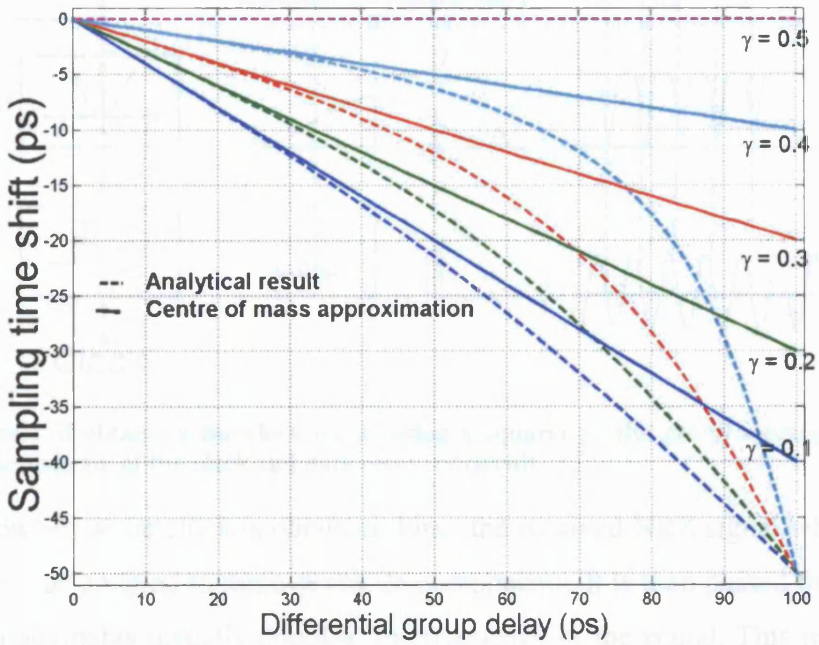

Figure 5.6 PMD-induced sampling time shift comparison between the centre of mass approximation and the full formula

It can be seen from Figure 5.6 that when $\Delta\tau < 35$ps, the error in estimating the PMD-induced time shift using the centre of mass approximation is $\leq 10\%$. Hence we can deduce that the centre of mass assumption is only valid for a DGD range 0-35ps. Equation 5.8 is periodic with a period equivalent to 100ps (one bit period) and is valid for any DGD range.

Although widely utilised in RZ systems, this type of clock recovery is more difficult to implement for NRZ formats. The reason is that the phase of the 5GHz signal randomly shifts by 180^0 making data synchronisation and sampling unstable [Ans'95].

This is why most clock recovery circuits include a pre-processor unit to create a tone at the bitrate frequency.

5.3.3 Using a Squarer

One of the most common methods of regenerating the clock component of a NRZ signal is to utilise non-linear circuit that emulates a square-law device. This can be achieved by means of a field effect transistor (FET) operating in the non-linear region where the output source drain current is approximately the square of the input (gate) voltage [Lim'98]. The schematic diagram of the clock and data recovery module is shown in the inset of the figure below.

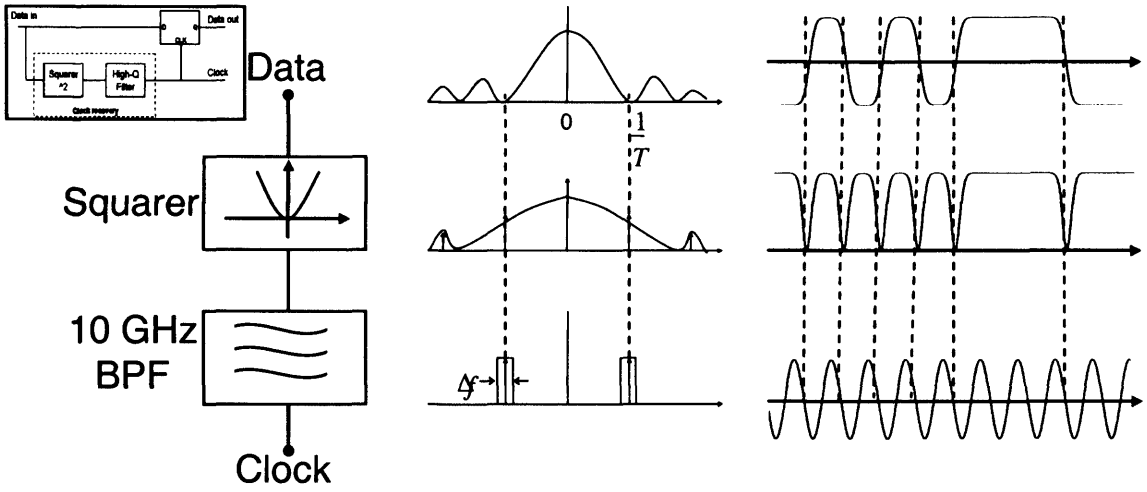

Figure 5.7 Process of obtaining the clock signal using a squarer as the pre-processing circuit. Inset: Schematic diagram of the clock and data recovery circuit

Figure 5.7 shows how the clock is obtained. First, the received NRZ signal which has no clock tone, is ac coupled to remove any dc components. It is then passed through a squarer which augments (usually doubles) the frequency of the signal. This results in the regeneration of the frequency component at 10GHz. Finally, this tone is filtered out using a high-Q filter and a clock signal is obtained. The clock in this case is the convolution between the square of the signal $f(t)$ and filter's transfer function $h(t)$ and can be written as:

$$clk = f^2(t) * h(t) \tag{5.11}$$

Starting from this equation and equation 5.5, it can be shown that the PMD-induced time shift using this type of clock recovery is governed by:

$$t_s = t_0 + \frac{1}{2\pi f_c}\tan^{-1}\left[\frac{(2\gamma-1)\sin(\pi f_c \Delta\tau)}{(\gamma^2+(1-\gamma)^2)\cos(\pi f_c \Delta\tau)+2\gamma(1-\gamma)P(\Delta\tau)}\right] \quad (5.12)$$

where t_0 is the sampling time in the absence of PMD and f_c is the centre frequency of the high Q filter. $P(\Delta\tau)$ is the patterning effect of the signal and is dependent on the shape of the waveform (i.e. power distribution) and the bit sequence of ones and zeros. The full derivation can be found in Appendix 3. Note that when $\Delta\tau = 0$ or $\gamma = 0.5$, PMD does not induce a clock phase shift. Before continuing this analysis, the patterning characteristics need to be discussed first. We will then return to equation 5.12.

5.3.3.1 Patterning Effects Due to the Squarer Pre-processor

The patterning effect in the clock recovery due to the squarer finds its origins in the fact that two identical copies of the signal, shifted, due to PMD, by $\Delta\tau$ from each other, are multiplied together giving rise to a pattern-dependent spectral component at the clock frequency. This can be easily seen when squaring equation 5.5 to give:

$$f_{PMD}^2(t) = \gamma^2 f^2\left(t+\frac{\Delta\tau}{2}\right)+(1-\gamma)^2 f^2\left(t-\frac{\Delta\tau}{2}\right)+2\gamma(1-\gamma)f\left(t-\frac{\Delta\tau}{2}\right)f\left(t+\frac{\Delta\tau}{2}\right) \quad (5.13)$$

The first and the second terms on the right hand side have a fixed clock tone for a given $\Delta\tau$ whereas the spectrum of the third term depends on the bit sequence of f(t). This is illustrated in Figure 5.8 for three rectangular-bit patterns with $\Delta\tau = 50$ps.

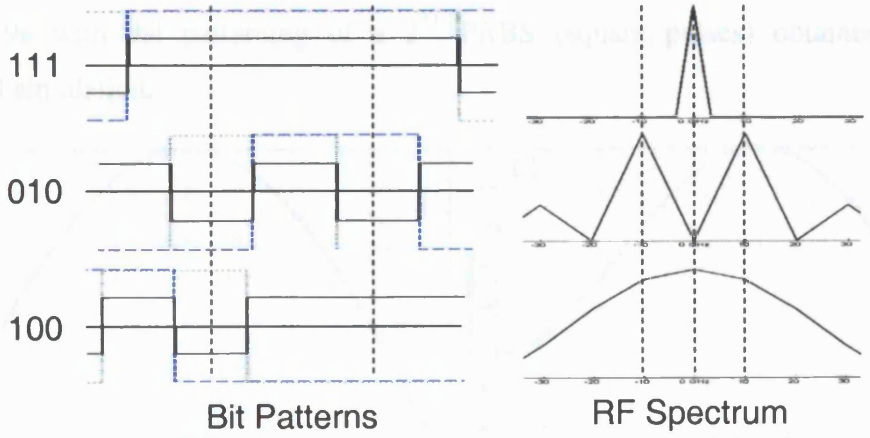

Figure 5.8 Dependency of the clock spectrum on the patterns 111, 010 and 100

Figure 5.8 shows the product (black solid line) of the two delayed replicas and their corresponding spectrum for the three-bit patterns 111, 010 and 100. The dashed blue

waveforms are the sequences at $+\Delta\tau/2$ while the dotted green waveforms are at $-\Delta\tau/2$. It can be observed that, unlike the 111 sequence, all other combinations have a component at the clock frequency which is added to the spectrum of the squared terms in equation 5.13. To describe the impact of patterning on the phase shift of the clock recovery for a DGD of up to 200ps, it is sufficient to consider a pattern combination of 3 bits (i.e. 2^3=8). If all three-bit combinations have equal probability of occurring, the patterning contribution to the clock phase-shift can be written as:

$$P(\Delta\tau)=\frac{1}{6}\sum_{i=1}^{6}\frac{\{f_i(t+\Delta\tau/2).f_i(t-\Delta\tau/2)\}*h(t)}{f_i^{\,2}(t)*h(t)} \tag{5.14}$$

where h(t) is the filter transfer function and $f_i(t)$ is a three bit pattern (excluding 000 and 111). The patterning effect is mainly caused by the two sequences 010 and 101 i.e. when there is an isolated one or zero. It is demonstrated in Appendix 3 that the above equation can be approximated by considering only the patterning of a 010 sequence (or a 101). Therefore $P(\Delta\tau)$ becomes:

$$P(\Delta\tau)\approx\frac{\{f_{010}(t+\Delta\tau/2).f_{010}(t-\Delta\tau/2)\}*h(t)}{f_{010}^{\,2}(t)*h(t)} \tag{5.15}$$

For square pulses, the above equation can be reduced to:

$$P(\Delta\tau)=\frac{1}{\lambda f_c}\sin(\lambda f_c\Delta\tau) \tag{5.16}$$

where f_c is the centre frequency of the high Q filter. This equation is compared in Figure 5.9a with the patterning of a 2^{11} PRBS (square pulses) obtained using numerical simulation.

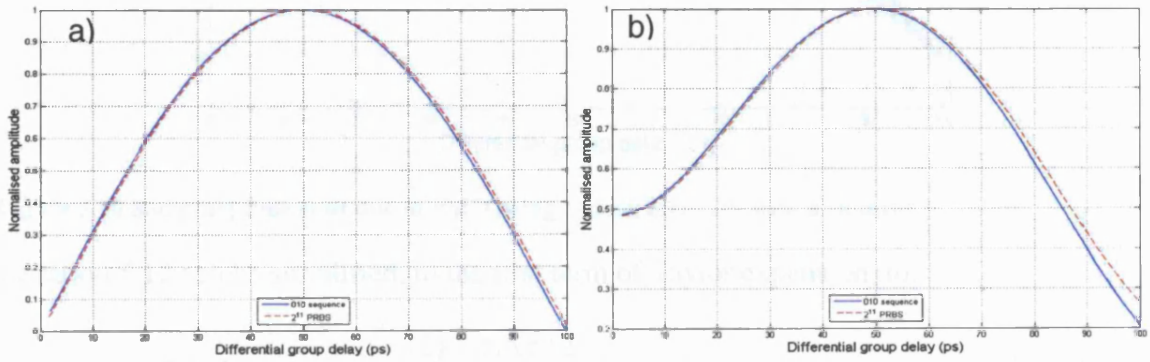

Figure 5.9 Amplitude variation (normalised) of the clock component in the beating terms for (a) square-shaped waveform (b) theoretical model waveform

It can be observed that there is a good agreement between the approximation and the patterning due to the PRBS. Additionally, it can be noticed that the patterning effect is maximum when the differential group delay is equal to half of the bit period ($\sin(\lambda f_c \Delta\tau)=1$ in equation 5.16). Similarly, the NRZ, 2^{11} PRBS data described previously in our system model was used with this clock recovery. The normalised amplitude variation of the clock component in the two beating terms is plotted in Figure 5.9b for the complete PRBS and for a 010 sequence. It can be seen that this component also has a maximum when $\Delta\tau$ = 50ps. Furthermore, when comparing Figure 5.9 (a) and (b) it can be noticed that, unlike the arbitrary waveforms, the beatings between the square pulses have no clock tone when $\Delta\tau$ tends to 0. Now that we have analytically obtained P($\Delta\tau$) of our system (Figure 5.9b), we can go back and substitute it in equation 5.12. Figure 5.10 compares the PMD-induced sampling time shift obtained from numerical simulation (dashed lines) and the analytical expression given by equation 5.12. A good agreement between the theory and the simulation can be clearly seen.

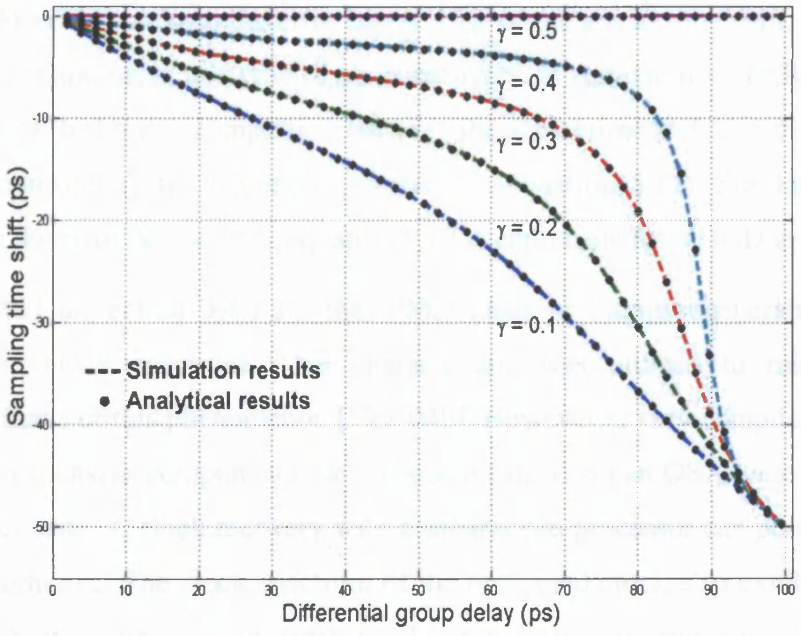

Figure 5.10 Sampling time shift due to PMD using a clock recovery with a squarer

Equation 5.12 can be simplified, to the first term of Taylor expansion, to:

$$t_s = t_0 + \frac{(2\gamma - 1)\Delta\tau / 2}{2\gamma^2\left(1 - P(\Delta\tau)\right) - 2\gamma\left(1 - P(\Delta\tau)\right) + 1} \tag{5.17}$$

If the patterning effect is ignored ($P(\Delta\tau)=1$), equation 5.17 reduces to the centre of mass expression. To verify to what extent this is valid, a graph comparing the sampling time shift using the centre of mass assumption and the full equation given in 5.12 is plotted in Figure 5.11a.

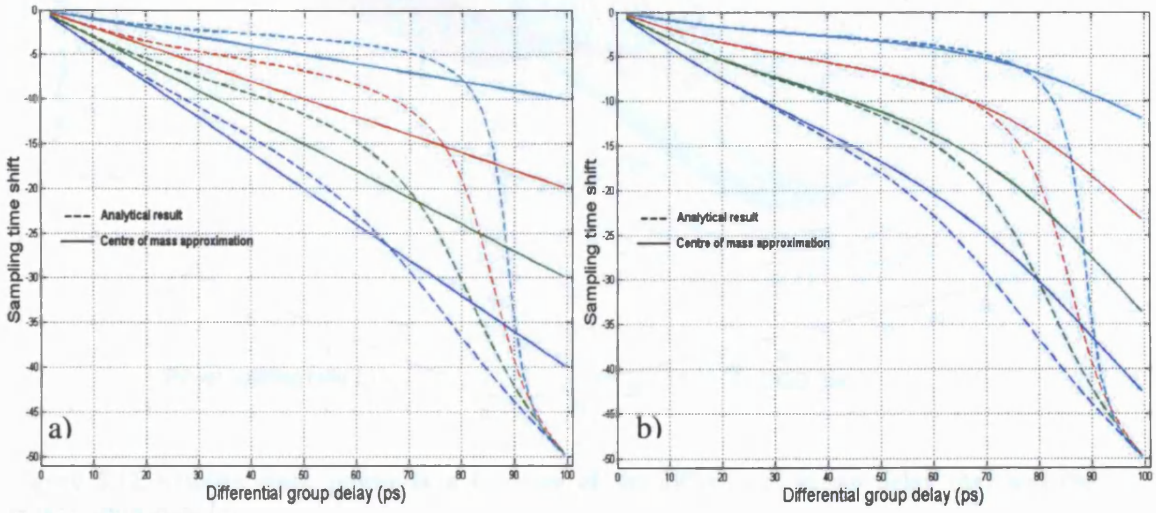

Figure 5.11Centre of mass approximation (a) without patterning (b) considering patterning

It can be deduced that to keep the error below 10% of the actual time shift, the centre of mass assumption, using this type of clock recovery, is suitable for a DGD range 0-25ps. Figure 5.11b shows a comparison between the actual time shift and the centre of mass while considering the patterning effects (i.e. equation 5.17). Similarly and in order to keep the error below 10%, equation 5.17 is applicable for a DGD up to 60ps.

It was reported in section 3.4.1.2.2 that PMD leads to fading/regeneration in the power of the clock spectrum. This characteristic was utilised to mitigate the deleterious effects of this phenomenon [Nez'04b]. However, a very complicated setup that includes expensive components such as notch filters and an OSA were needed to track the clock tone. A clock recovery with a squarer pre-processor can potentially be a cheaper alternative. The clock spectrum of the recovered clock also exhibits fading due to PMD and this can be used in the same way to mitigate PMD. The fading/regeneration of the clock tone can be described by equation A3.25 given in Appendix 3. Figure 5.12 illustrates how the clock power changes with varying γ and $\Delta\tau$.

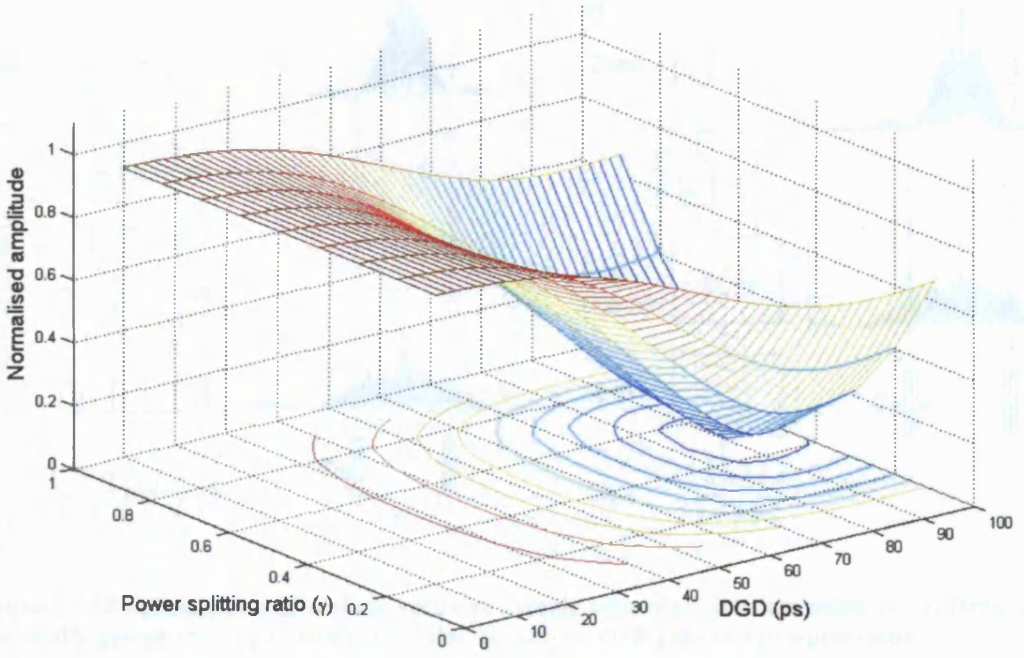

Figure 5.12 Relative clock power as a function of the differential group delay (Δτ) and the polarisation state (γ)

It can be observed that the clock power gradually decreases until it reaches a minimum at $\Delta\tau$ = 90ps after which it starts rising. If there was no patterning effects, the minimum would occur at $\Delta\tau$ = 50ps (see Appendix 3). More investigations need to be carried out to determine the validity of this method and especially the effect of the combined PMD-chromatic dispersion on the clock power. This will be investigated in the future.

5.3.4 Using an Edge Detector

5.3.4.1 The Theory

One of the conventional ways of regenerating the clock signal of a NRZ signal is to double its frequency by means of an edge detector, also known as transition detector. This can be implemented using two distinct pre-processing circuits, namely "differentiate and rectify" or a "delay and multiply" [Yur'96] as can be seen in Figure 5.13.

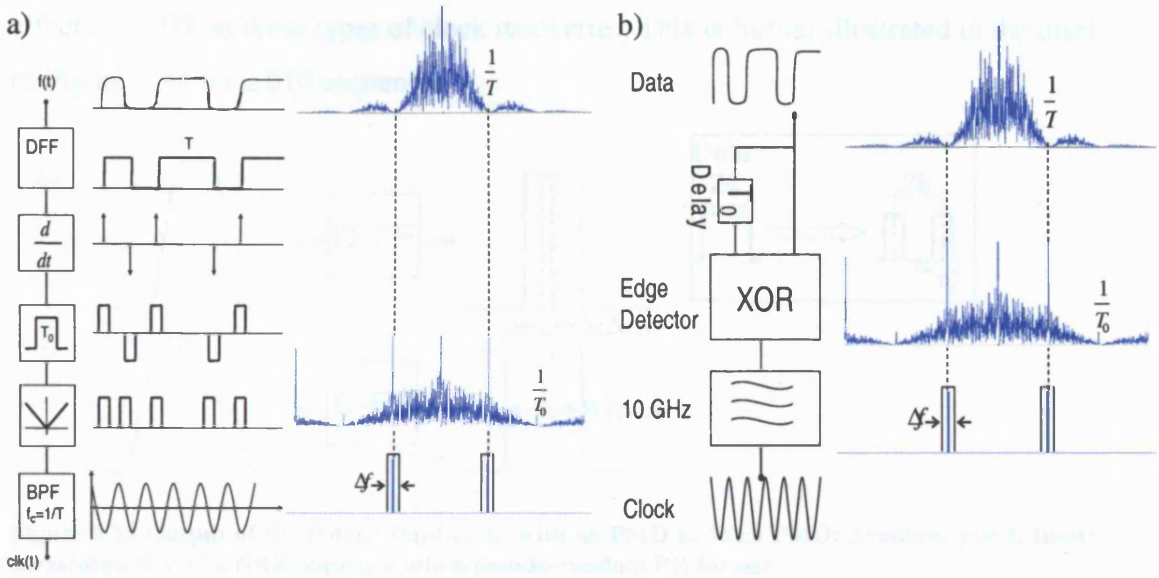

Figure 5.13 Configuration of a clock recovery circuit with edge detector using (a) differentiate and rectify pre-processing circuit (b) A delay line and a XOR gate as a pre-processor

The advantage of using this type of nonlinear circuit, compared to all commonly used nonlinearities, is that they are the least affected by amplitude fluctuations of the input signal [Dav'89]. Figure 5.13a shows how the differentiate and rectify circuit is utilised to create a clock frequency. First the signal is regenerated and passed through a differentiator which creates very narrow pulses (delta function) at positive and negative transitions of the input data. This can be implemented using a C-R network. The data is then regenerated to give a bipolar pseudo-random RZ pattern [Wan'91]. This pattern is transformed into a unipolar RZ format by means of full-wave rectifier. This random RZ signal contains a clock tone at the bitrate frequency which can be extracted using a high-Q passband filter. Because differentiation and rectification is performed by passive components, high speed operation can be achieved.

Figure 5.13b demonstrates how the clock recovery is obtained using the delay and multiply concept. The multiplication can be performed using a Gilbert multiplier [Yur'96] or simply an exclusive OR (XOR) gate [Mur'99]. The delay line has a direct impact on the power of the recovered clock and it has been shown that the power is maximised when the delay is equal to half the bit period [Imb'83]. The output from the XOR gate is also a pseudo-random RZ data which contain a clock signal. Both mentioned methods have in common the property of transforming a NRZ data stream into a pseudo-random RZ (PRZ) sequence containing a clock component at the bitrate frequency. This is an important characteristic to comprehend in order to define the

effect of PMD on these types of clock recoveries. This is further illustrated in the inset of Figure 5.14 for a 010 sequence.

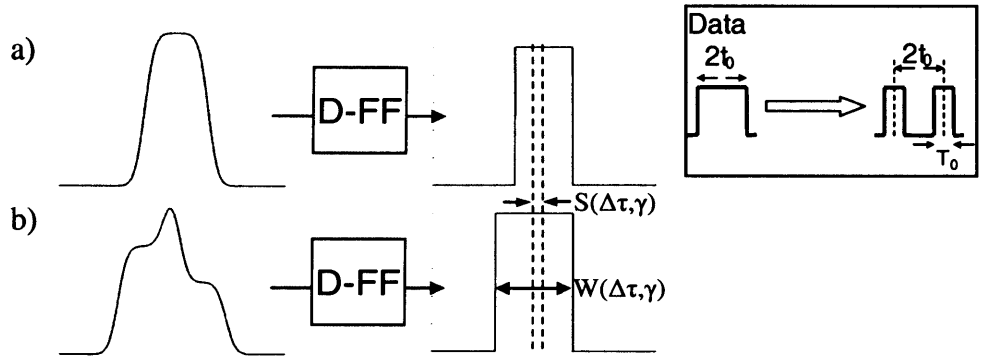

Figure 5.14 Output of the D-type flip-flop a) with no PMD b) With PMD: Δτ=80ps, γ=0.4. Inset: transformation of a NRZ sequence into a pseudo-random RZ format

The D-type flip-flop (D-FF) (or the XOR gate) in Figure 5.13 reshapes the input signal so that the output pulses are rectangular of a width equal to the full width at half maximum (FWHM) of the original pulses as shown in Figure 5.14a. In the presence of PMD, the FWHM of the input pulse changes according to its shape and the two parameters γ and $\Delta\tau$ as demonstrated in Figure 5.14b. The FWHM in the presence of PMD can be represented by the function $W(\Delta\tau, \gamma)$. In addition, there is a certain time shift between the output pulse (from the D-type flip-flop) without PMD and in the presence of PMD that also depends on the above parameters. This time shift of the centre of the pulse is shown in the figure above and will be named $S(\Delta\tau, \gamma)$. Both functions $W(\Delta\tau, \gamma)$ and $S(\Delta\tau, \gamma)$ define how the sampling time shifts with changing PMD. Unlike the squarer-based clock, this one does not depend on the different combinations of bits but mainly on the shape of the transmitted signal. This will be considered next.

First let us assume that the input data to our system consists of rectangular waveforms. In this case and in the presence of PMD, the FWHM of the distorted waveform is always equal to the bit period (i.e. $W(\Delta\tau, \gamma) = T_b$). The exception is when $\gamma = 0.5$, the width of output waveform is $T_b + \Delta\tau$. The shift in the output pulse (after the D-FF) follows the polarisation state with the highest power and thus $S(\Delta\tau, \gamma) = \Delta\tau/2$ ($S(\Delta\tau, \gamma)=0$ for $\gamma = 0.5$). Now if a waveform that has Gaussian shaped edges and a rise time of 33ps (taken from the aforementioned system model) is considered, $W(\Delta\tau, \gamma)$ and $S(\Delta\tau, \gamma)$ will change according to Figure 5.15(a) and (b) respectively.

The time shift for γ>0.5 can be deduced by mirroring Figure 5.15b with respect to the x-axis (There is no time shift when γ =0.5).

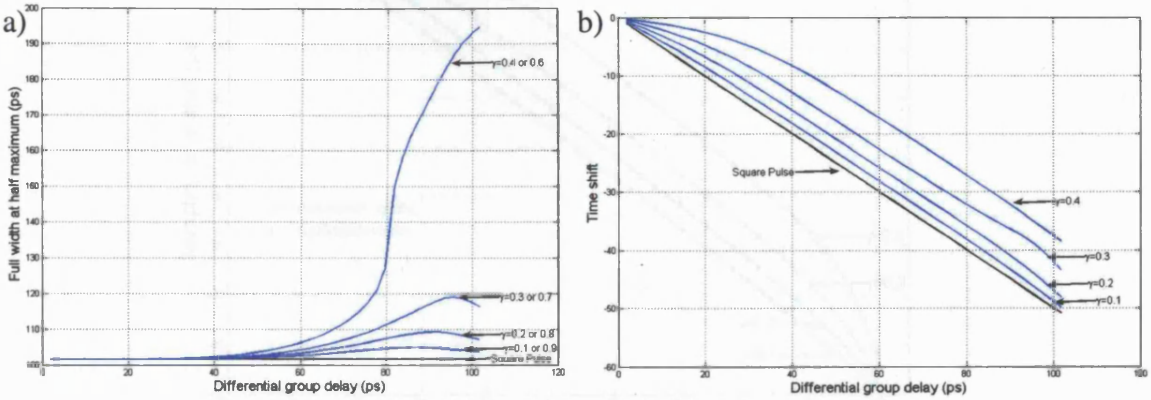

Figure 5.15 a) Change in the FWHM of the pulse (W(Δτ ,γ)) at the output of the DFF due to PMD (b) Time shift of the output pulse S(Δτ ,γ)

It can be observed that the FWHM of the output pulse increases gradually with increasing differential group delay and becomes significant when Δτ >80ps. Additionally, the width increases substantially when γ tends to 0.5. The time shift on the other hand also increases with increasing Δτ but it is more pronounced when γ tends to 0.1 (or 0.9). It is shown in Appendix 4 that most waveforms at 10Gbit/s would follow the time shift pictured in Figure 5.15b. In the same appendix, the overall sampling time shift of the clock recovery circuit due to the effect of PMD is shown to be:

$$t_s = t_0 + \mathrm{Real}\left[\frac{1}{j\omega}\ln\left(-\cos\left(W(\Delta\tau,\gamma)\omega/2\right)\exp\left(jS(\Delta\tau,\gamma)\omega\right)\right)\right] \qquad (5.18)$$

where t_0 is the sampling time in the absence of PMD. The accuracy of the above equation was verified using numerical simulation. The delay and multiply clock recovery circuit shown in Figure 5.13b was used to recover the random pattern affected by PMD with Δτ and γ ranging between 0-100ps and 0.1-0.5 respectively. The good agreement between equation 5.18 and the simulation results can be clearly observed in Figure 5.16.

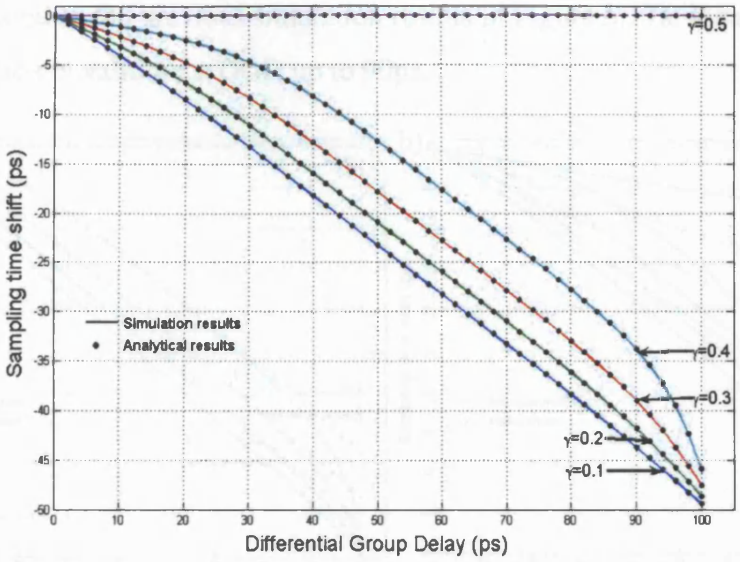

Figure 5.16 Comparison between the analytical and simulation PMD-induced sampling time shift for a clock recovery using edge detection

Curves for 1-γ (i.e. for values 0.5 - 1) can be obtained by taking a mirror copy of the curve at γ wrt the x-axis. Although equation 5.18 is very accurate, it is extremely difficult to see how the PMD-induced sampling time shift is affected by the parameters γ and Δτ. Additionally, the PMD-induced time shift can only be obtained using simulation, a method which is not practical in real systems. A much simpler equation is derived in Appendix 4 where the time shift due to PMD is shown to be governed by:

$$t_s = t_0 + \frac{\alpha}{4\pi f_c}\sinh^{-1}[(2\gamma-1)\sinh(2\pi f_c \Delta\tau/\alpha)] \tag{5.19}$$

where

$$\alpha = \frac{\pi T_r}{\tanh^{-1}(0.8)T_b} \tag{5.20}$$

T_r is the 10-90% rise time and T_b is the bit period. Assuming a 10-90% rise time between 32 and 35ps, it is shown in Appendix 4 that this expression can be approximated by:

$$t_s = t_0 + \frac{1}{4\pi f_c}\sinh^{-1}[(2\gamma-1)\sinh(2\pi f_c \Delta\tau)] \tag{5.21}$$

where f_c is the central frequency of the high Q filter. This new expression is simpler and it can be intuitively deduced that $t_s = t_0$ when γ =0.5 or when Δτ =0. Equation

5.19 is compared to the previous simulation results in Figure 5.17a. It can be observed that the equation is valid for a DGD up to 90ps.

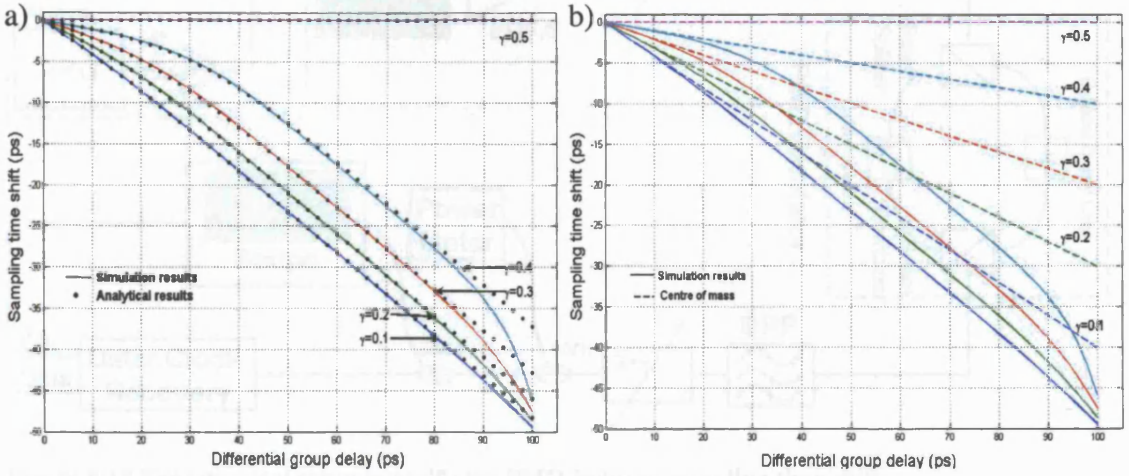

Figure 5.17 a) Comparison between the simplified expression and the simulation results b) Comparison between the centre of mass expression and the simulation results

Equation 5.21 can be expanded using Taylor series to give:

$$t_s = t_0 + \frac{2\gamma - 1}{2}\Delta\tau + \frac{4}{3}\gamma(1-\gamma)(2\gamma-1)\pi^2 f^2 \Delta\tau^3 + \ldots \qquad (5.22)$$

The second term in this equation represents the centre of mass of the pulses in the incoming signal given in section 5.1 (equation 5.3). Therefore the centre of mass assumption can be used as long as the higher terms of this expansion are negligible. The centre of mass expression is compared to the simulated sampling time shift in Figure 5.17b. It can be deduced that this assumption is only valid for a differential group delay up to approximately 25ps in a 10Gbit/s system.

5.3.4.2 Experimental verification

The effect of PMD on the clock recovery was verified experimentally with the experimental setup shown in Figure 5.18. In the transmitter, one input of the Mach-Zehnder modulator (MZM) is connected to a tuneable laser source emitting at 1554nm. The polarisation of this light is stabilised by means of a polarisation controller (PC1). A pulse pattern generator (PPG) followed by a high-power RF amplifier were used to generate a 9.953Gbit/s 2^{11}-1 NRZ, pseudo-random bit sequence (PRBS) data stream that was fed to the second arm of the modulator. The rise and fall times of the system were 32 and 35ps respectively.

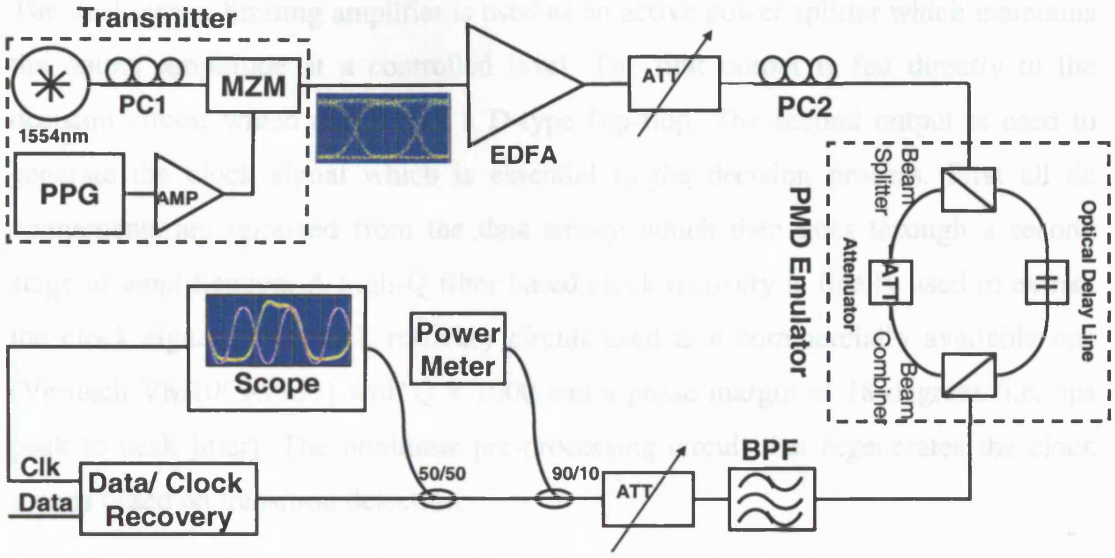

Figure 5.18 Experimental setup to verify the PMD-induced sampling time shift

The modulated light from the MZM was boosted by an EDFA and the optical power input to the PMD emulator was maintained at 3dBm by means of an optical attenuator. The PMD emulator employed in this experiment (JDS PE4+1FP) divided the incoming light into two discrete polarisation paths using a polarisation beam splitter. One of the paths passes through an optical delay element while the other was passed through a matching attenuator before they were recombined at the output. The optical delay element allowed precise control of the time delay between the two polarisation states ($\Delta\tau$) while the polarisation controller (PC2) was used to control the power ratio (γ) between them. The signal was then passed through a 100GHz bandpass optical filter to remove the ASE noise introduced by the EDFA. A second optical attenuator was used to keep the optical power at the input of both the oscilloscope and the clock/data recovery circuit at -6dBm. A schematic diagram of the clock and data recovery circuit is presented in Figure 5.19.

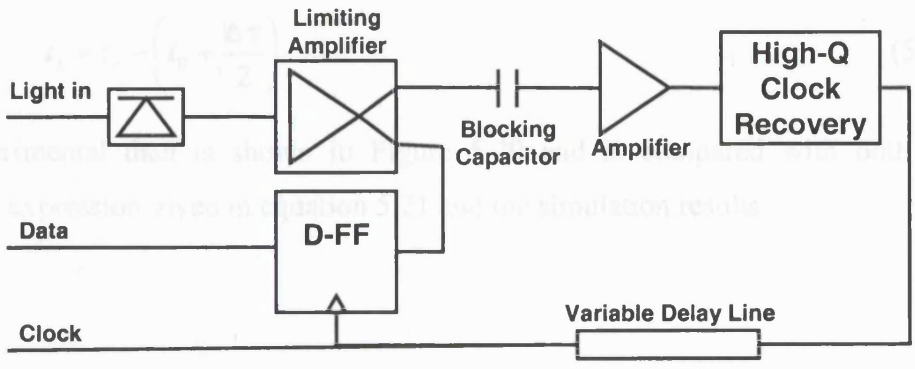

Figure 5.19 Schematic diagram of the data and clock recovery circuit used

The dual output limiting amplifier is used as an active power splitter which maintains the output amplitude at a controlled level. The first output is fed directly to the decision circuit which consists of a D-type flip-flop. The second output is used to generate the clock signal which is essential to the decision process. First all dc components are removed from the data stream which then goes through a second stage of amplification. A high-Q filter based clock recovery is finally used to extract the clock signal. The clock recovery circuit used is a commercially available one (Veritech VM10CR9953) with Q = 1000 and a phase margin of 18 degrees (i.e. 5ps peak to peak jitter). The nonlinear pre-processing circuit that regenerates the clock tone is based on transition detection.

The PMD emulator was used to vary the differential group delay from 5 to 100ps with 5ps resolution while the power splitting ratio in the fast polarisation axis was increased from 10 to 50% of the total power with steps of 10%. The oscilloscope was employed to assess the PMD-induced sampling time shift and was triggered from the PPG. First the clock phase when $\Delta\tau = 0$ was recorded and the transition of the rising edge of the clock was used as a time reference. This will be referred to as t_0. After this, $\Delta\tau$ was increased for every polarisation state and the new position of the same rising edge was recorded. This new time reading will be referred to as t_r. Recall, in our PMD model described in section 5.3.1, that the DGD was introduced by delaying one polarisation state by $\Delta\tau/2$ and accelerating the other by the same amount. However, in practice the DGD is introduced by delaying one copy by a total of $\Delta\tau$. Therefore, in order to compare the simulation with the experimental results, the reference point in the experimental data always needs to be halfway between the two delayed copies and thus at $t_0 + \Delta\tau/2$. The shift in sampling time (t_s) due to PMD is thus calculated using the following equation:

$$t_s = t_r - \left(t_0 + \frac{\Delta\tau}{2}\right) \tag{5.23}$$

The experimental data is shown in Figure 5.20 and is compared with both the analytical expression given in equation 5.21 and the simulation results.

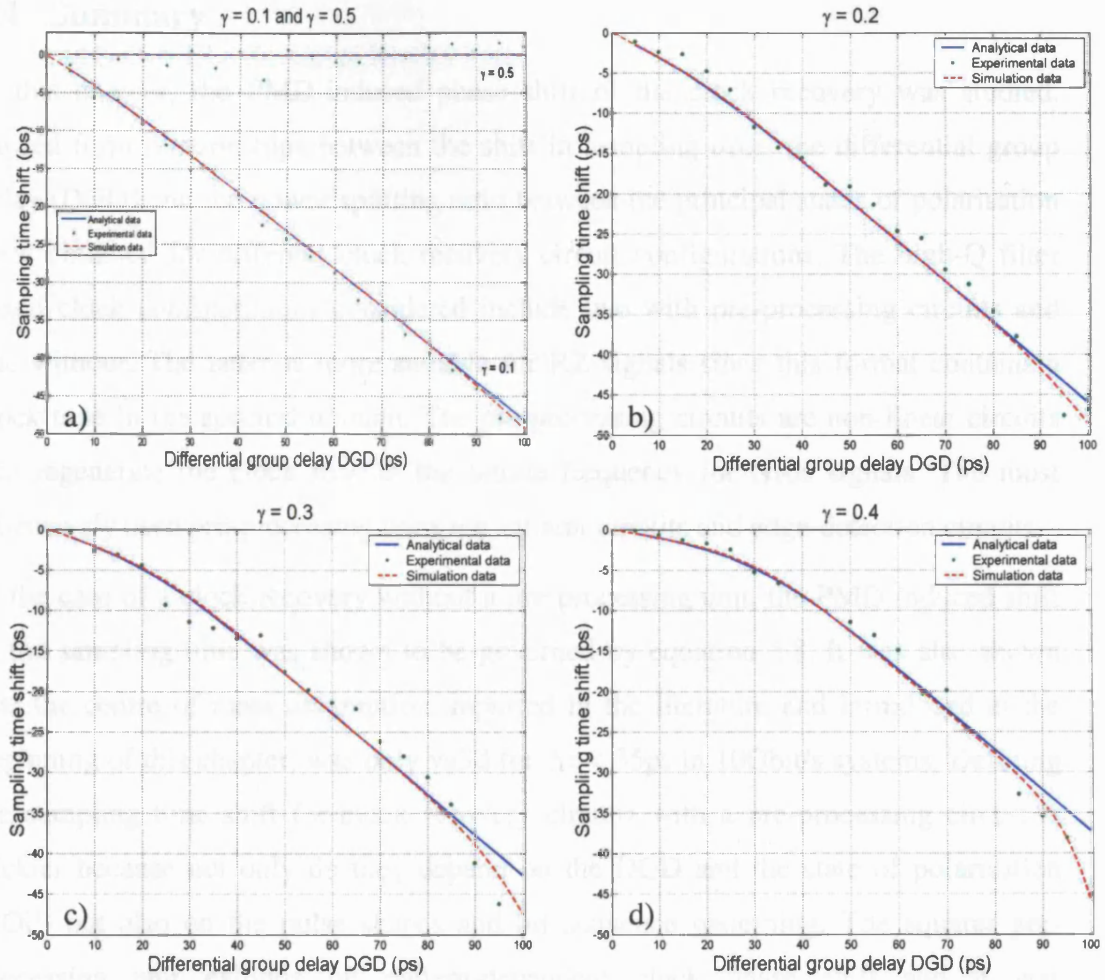

Figure 5.20 PMD-induced sampling time shift comparison between experimental (dots), analytical (solid) and simulation (dashed) for a) γ= 0.1 and 0.5 b) γ= 0.2 c) γ= 0.3 d) γ= 0.4

The good agreement between the experimental and the simulation result can be clearly seen. This experiment also confirms the fact that the simplified equations 5.19 and 5.21 are adequate for a DGD up to 90ps. The small deviations between the experimental and the theoretical data are due to two factors. The first one is the time jitter which is provoked by either the pulse pattern generator or more importantly by the clock recovery circuit. This can be considered as phase noise with zero mean and a certain standard deviation. The second factor consists of the minute and instantaneous changes in the signal's SOP due to laboratory conditions (temperature, vibrations …) and the imperfect nature of the polarisation controller at the input of the PMD emulator.

5.4 Summary

In this chapter, the PMD-induced phase shift of the clock recovery was studied. Closed form relationships between the shift in sampling time, the differential group delay (DGD) and the power splitting ratio between the principal states of polarisation were obtained for different clock recovery circuit configurations. The high-Q filter based clock configurations considered include two with pre-processing circuits and one without. The latter is more suitable for RZ signals since this format contains a clock tone in the spectral domain. The pre-processing circuits are non-linear circuits that regenerate the clock tone at the bitrate frequency for NRZ signals. The most extensively used pre-processing units are squarer circuits and edge-detection circuits.

In the case of a clock recovery without a pre-processing unit, the PMD-induced shift in the sampling time was shown to be governed by equation 5.8. It was also shown that the centre of mass assumption, reported in the literature and introduced at the beginning of this chapter, was only valid for $\Delta\tau < 35$ps in 10Gbit/s systems. Defining the sampling time shift for clock recovery circuits with a pre-processing circuit is trickier because not only do they depend on the DGD and the state of polarisation (SOP) but also on the pulse shapes and bit sequence patterning. The squarer pre-processing unit exhibits bit pattern-dependent clock phase shift and it was demonstrated that the bit sequence where there is an isolated mark or space (010/101) has the most dominant effect. This patterning effect is described by equation 5.15 whereas the PMD-induced time shift using this configuration is given by equation 5.12. Furthermore, the centre of mass assumption was shown to be suitable for a DGD up to 25ps in this case. The transition/edge detector unit on the other hand is more dependent on the rise and fall times of the system (pulse shape). A simple equation describing the PMD-induced sampling time shift was derived (5.19). This equation however is valid for a DGD up to 90ps. Moreover, the theoretical clock phase shift due to PMD has been confirmed experimentally using a commercial high-Q filter based clock recovery circuit. The good match between the theoretical and experimental data can be clearly observed in Figure 5.20. The centre of mass assumption in this case was shown to be valid for a DGD less than 25ps in 10Gbit/s systems.

The results obtained from this study of the clock recovery behaviour under the effects of PMD will allow a better determination of its effects on the signal quality such as the Q-factor, SNR and eye closure. It will also provide a more accurate evaluation of PMD in synchronous sampling-based PMD monitoring techniques as they rely on estimating the eye opening at decision times. Finally, if $\Delta\tau$ and γ are known, the obtained equations would provide feedback to enable a rapid and efficient variation in the temporal sampling point, to minimise the bit error rate.

Chapter 6 Three-Section Eye Sampling Technique

6.1 Introduction

Performance monitoring techniques, which can be divided into sampling and spectral methods, were described in chapter 3. The sampling approach is sensitive to all kinds of impairments as noise and distortion have a direct impact on the histogram of the monitored channel. It was also shown that each type of impairment gives the histogram a distinctive shape or signature which can be used to determine the source of the degradation (root cause analysis) and hence facilitate troubleshooting and problem isolation. In addition, this technique can be used to evaluate the Q-factor, OSNR, the relative intra-band crosstalk and assess PMD. We have seen in chapter IV that by deconvolving the histograms, the Gaussian noise contribution can be separated from the effect of other impairments and the noise figure of the system can be evaluated. Additionally, it was shown that the PMD and dispersion signatures on the histograms are similar despite resulting from different phenomena. Sampling methods have a great deal of potential for performance monitoring purposes but have been under-exploited thus far. They still suffer from the following problems:

1. While spectral methods can estimate the group velocity dispersion (GVD) and differential group delay (DGD) by analysing specific components of the electrical spectrum, sampling methods can only detect their signatures (dispersion and PMD). Even though the sampling-based eye opening technique used for PMD mitigation (section 3.4.2.3.1) can track this distortion, it retains information on all optical penalties and not just the PMD effect. This can lead to erroneous PMD estimation in the event of several impairments acting simultaneously as all of them contribute to eye closure at the decision times.
2. PMD and dispersion have similar signatures on the histogram sampled at decision time and therefore sampling methods cannot discriminate between the two phenomena making the fault isolation task more difficult.

This is where the technique of three-section eye diagram sampling becomes useful. The concept of adding a sampling section on both edges of the eye was developed after observing the distinctive characteristics of the PMD-affected eye demonstrated in chapter 4. Unlike dispersion, PMD leads to a temporal asymmetry where the

closure on one side is more pronounced than the other. Moreover, the side of the closure reveals which polarisation axis contains more power; if most of the power is travelling in the fast axis then the right side of the eye is affected. Conversely, if most of the power is travelling in the slow axis then the closure comes from the left. The method is based on sampling on both sides of the eye diagram so that the level of the signal transitions (leading/trailing edges) can be compared and hence PMD signature can be detected. In addition, these levels can be used to precisely estimate both the DGD and the state of polarisation (SOP) of the monitored channel. Moreover, this powerful technique also has dispersion monitoring capabilities where the GVD can be accurately assessed over a very large range. Finally, this sampling approach can have other useful applications such as inline mask testing and detecting laser overshoots.
This chapter is divided as follows; the first section discusses the concept of the three-point sampling technique and its implementation in more depth. The second section shows how it can be used for PMD detection and evaluation. The third section examines the capability of this method to monitor and estimate dispersion. The fourth section shows other potential utilisation of this technique.

6.2 The System and PMD Model

The system and PMD model used in this chapter is similar to the model used in chapter 5. The transmitted data in our simulations is a 10Gbit/s, 2^{11} NRZ pseudo-random bit sequence (PRBS). The transmitted pulses have Gaussian-like edges and 10-90% rise and fall times of 33ps. First-order PMD simulation is performed in Jones space by varying the magnitude and phase of the two polarisation states using the setup shown in Figure 5.3 (the same approach is used for experimental PMD emulation). First, a linearly polarised signal is launched from the transmitter. It is then split into two parts with equal amplitudes using, for instance, a polarisation beam splitter (PBS). While one section is multiplied by γ ($0< \gamma<1$) and retarded by an amount of $\Delta\tau/2$, the other one is multiplied by $1-\gamma$ and advanced by $\Delta\tau/2$. The power splitting ratio γ represents the proportion of the power travelling in the slow polarisation axis. The two segments are finally recombined and detected by a square-law receiver. This contains no filter and its bandwidth is assumed to be infinite. The square-law detector is followed by a high-Q filter based clock recovery circuit. It utilises an edge detector pre-processing circuit type discussed in the previous chapter.

6.3 Three-section Eye Diagram Sampling Technique

6.3.1 Concept

As mentioned earlier, the concept of sampling the eye diagram at three distinctive temporal points was developed after observing the asymmetric manifestation of PMD. Synchronous sampling techniques reported in the literature obtain the histogram of the transmitted signal at decision time, which is generally situated around the centre of the eye as shown in Figure 6.1. The novelty is to introduce predetermined delays in the recovered clock and obtain the histograms of the two sides of the eye diagram and hence three-section eye sampling. While the histogram obtained at decision time is used for BER evaluation and root cause analysis, the side histograms can be used for PMD detection and the evaluation of the DGD and GVD as will be shown subsequently. The middle histogram will be ignored in the following discussion and we will concentrate on the side histograms instead.

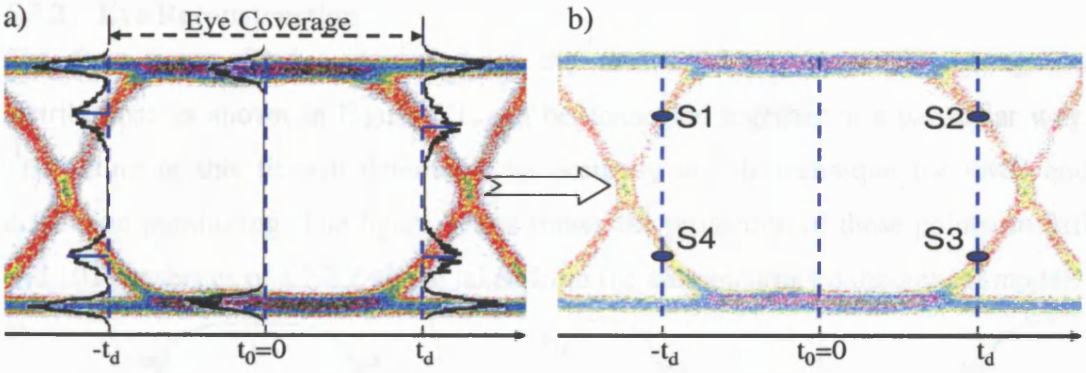

Figure 6.1 Three-section eye diagram sampling concept shown on an experimental 10Gbit/s eye diagram

Sampling is performed on both edges of the eye diagram and the corresponding side histograms are acquired as demonstrated in Figure 6.1(a). The means of the distributions of the marks, spaces, rising and falling edges are then calculated. The mean, also known as the first moment, is given by:

$$\mu = \frac{\Sigma Hist \times v}{\Sigma Hist} \tag{6.1}$$

where *Hist* is the obtained histogram and *v* is the voltage axis. The marks and spaces means are used to normalise the eye so that its amplitude (marks level – spaces level) equates to 1. By normalising the means of the inner distributions of the two side histograms (rising and falling edges), values for the points labelled S1, S2, S3 and S4 in Figure 6.1(b) can be determined. PMD and dispersion can be effectively assessed

by comparing these normalised values at the transmitter with the ones at the receiver. The decision time at the centre of the eye is denoted t_0 and will be considered the origin of the time axis. The side sampling delay t_d is chosen so that the distribution of the rising and falling edges can easily be distinguished from that of the spaces and marks (at least from the transmitter side). In practice this could be the point where the rising and falling edges reach 80 and 20% of the average amplitude respectively. In this case the side delay t_d is given by:

$$t_d = \frac{T_b - T_r}{2} \tag{6.2}$$

where T_b is the bit period and T_r is the 20-80% rise time. Eye coverage (EC) is another parameter which is independent of the bitrate and expressed as a percentage of the bit period. For instance, an 80% eye coverage is equivalent to a t_d of 40ps in a 10Gbit/s system and 10ps at 40Gbit/s ($t_d = EC \times T_b/2$).

6.3.2 Eye Reconstruction

The four points S1-4, obtained from the means of the inner side-histograms distributions as shown in Figure 6.1, can be connected together in a particular way. The nature of this fit will determine the accuracy of this technique for PMD and dispersion monitoring. The figure below shows the projection of these points on 010 and 101 sequences of a NRZ signal taken from the aforementioned theoretical model.

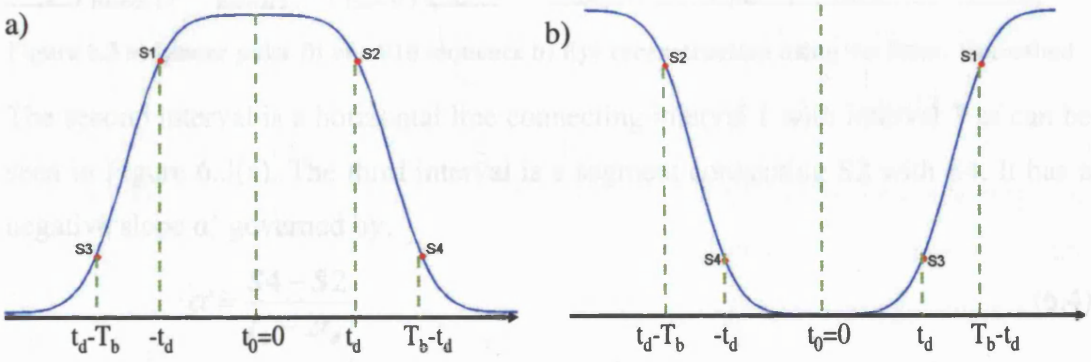

Figure 6.2 Projection of the side distribution means on 101 and 010 sequences

Comparing the above figure with Figure 6.1, it can be observed that for the 010 sequence the sample points S3 and S4 are now on the left and right of decision point respectively. This is because S3 is on the rising edge whereas S4 is on the falling edge of the eye diagram. Both S1 and S2 in this bit-sequence are situated at distance t_d from the centre of the eye while S3 and S4 are T_b -t_d away from decision time. Similarly the position of S1 and S2 are swapped in the 101 sequence because S1 is on the 0 to 1

transition and S2 is on the 1 to 0 transition on the eye diagram. In this case S1 and S2 are T_b -t_d from the centre whereas S3 and S4 are at distance t_d. Using this information all three-bit sequence combinations (2^3=8) can be fitted and hence the entire eye diagram can be reconstructed using the four points S1-4. We will consider three types of fitting algorithms: linear, raised cosine and hyperbolic tangent.

Linear Fit

The most straightforward method of linking the above four points is to join the two segments crossing the pair of points (S3, S1) and (S4, S2) at the mark's or the space's level as shown in the figure below for a 010 sequence. The linear fit is defined over three discrete intervals. The first interval is a straight line with a positive slope α linking S1 with S3. The slope α is given by

$$\alpha = \frac{S1 - S3}{T_b - 2t_d} \tag{6.3}$$

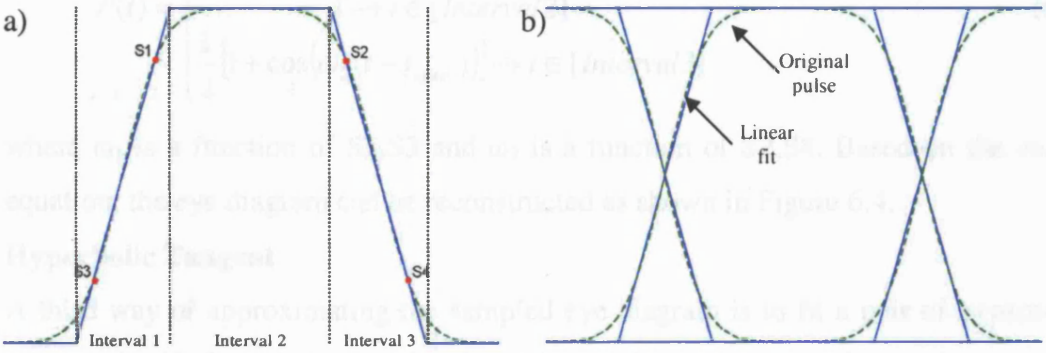

Figure 6.3 a) Linear pulse fit of a 010 sequence b) Eye reconstruction using the linear fit method

The second interval is a horizontal line connecting interval 1 with interval 3 as can be seen in Figure 6.3(a). The third interval is a segment connecting S2 with S4. It has a negative slope α' governed by:

$$\alpha' = \frac{S4 - S2}{T_b - 2t_d} \tag{6.4}$$

α and α' are equal if S1=S2 and S3=S4. All other bit combinations can be approximated using this linear fit and the entire eye diagram can be reconstructed as shown in Figure 6.3(b). This technique however is not very accurate as it ignores the roll-off between the edges and the marks/spaces levels.

Raised Cosine

Raised cosine is a function commonly used in telecommunication to describe a pulse shape or the shape of a filter's transfer function. The pulse is also described by three

discrete intervals where the first and the third intervals are defined as raised cosines while the second interval is a horizontal line as shown in Figure 6.4(a).

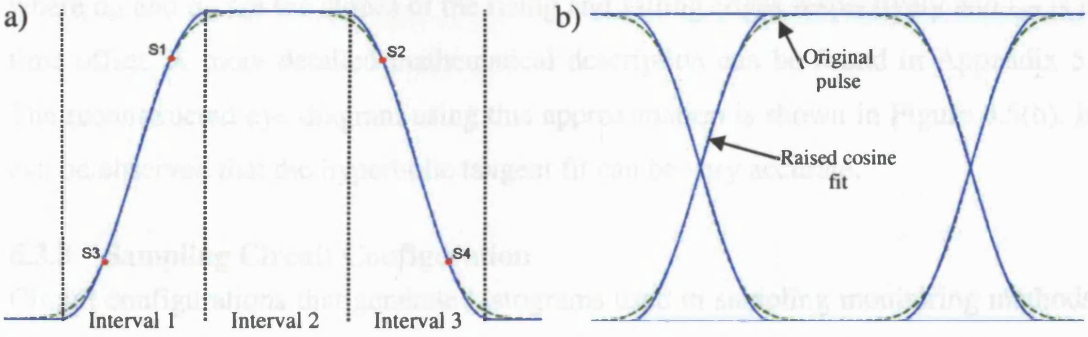

Figure 6.4 a) Raised cosine pulse fit of the sequence 010 b) Eye reconstruction using the raised cosine fit method

Mathematically this is defined as:

$$P(t) = \begin{cases} \frac{1}{2}\left[1+\cos\left(\omega_1 (t+t_{offset})\right)\right] \rightarrow t \in [Interval1] \\ 1 \rightarrow t \in [Interval2] \\ \frac{1}{2}\left[1+\cos\left(\omega_2 (t-t_{offset})\right)\right] \rightarrow t \in [Interval3] \end{cases} \quad (6.5)$$

where ω_1 is a function of S1,S3 and ω_2 is a function of S2,S4. Based on the above equation, the eye diagram can be reconstructed as shown in Figure 6.4.

Hyperbolic Tangent

A third way of approximating the sampled eye diagram is to fit a pair of hyperbolic tangent (tanh) functions, one for the rising and one for the falling edge such as illustrated in Figure 6.5(a). Unlike the previous methods, this approach is defined over the entire range (no discrete intervals) because two tanh functions can be chosen so that they add up constructively over a certain range and destructively over the rest.

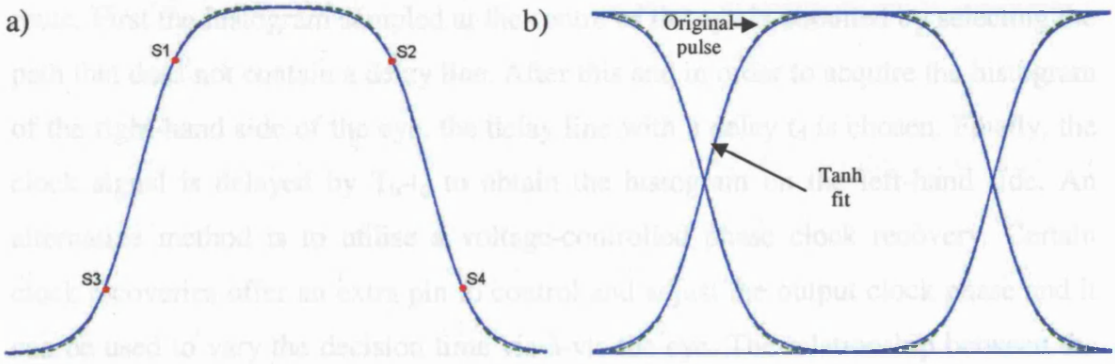

Figure 6.5 a) hyperbolic tangent pulse fit of the sequence 010 b) Eye reconstruction using the tanh approximation

Mathematically the 010 pulse can be expressed as:

$$P(t) = \frac{1}{2}\left(\tanh\left(\alpha_R\left(t + t_{off}\right)\right) + \tanh\left(\alpha_F\left(t + t_{off}\right)\right)\right) \quad (6.6)$$

where α_R and α_F are the slopes of the rising and falling edges respectively and t_{off} is a time offset. A more detailed mathematical description can be found in Appendix 5. The reconstructed eye diagram using this approximation is shown in Figure 6.5(b). It can be observed that the hyperbolic tangent fit can be very accurate.

6.3.3 Sampling Circuit Configuration

Circuit configurations that generate histograms used in sampling monitoring methods were discussed in section 3.4.2.1. The sampling can be done either electrically or optically and they generally need a clock signal that can either be internal or external (e.g. from a clock recovery). Three-section eye diagram sampling technique can be achieved using the same configurations albeit with a minor modification of the input clock signal as shown in Figure 6.6(a).

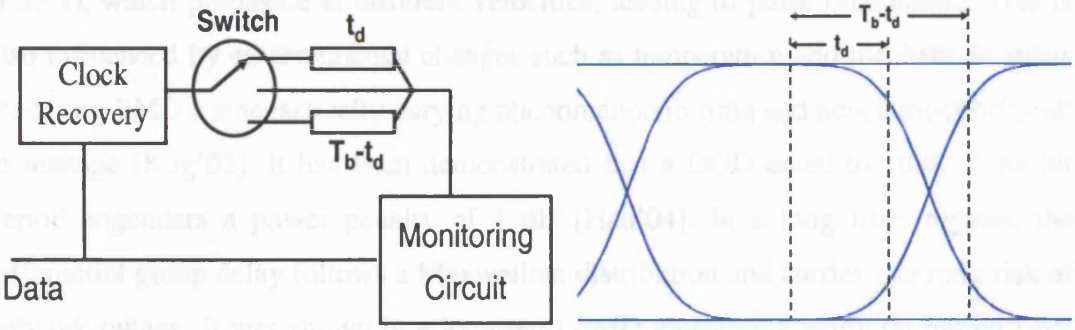

Figure 6.6 a) Conceptual configuration for the three-section eye diagram sampling technique b) The three temporal sampling points on the eye (T_b is the bit period)

Instead of feeding the clock signal directly to the monitoring circuit, two paths with different propagation delays can be added. A switch is utilised to select any particular route. First the histogram sampled at the centre of the eye is obtained by selecting the path that does not contain a delay line. After this and in order to acquire the histogram of the right-hand side of the eye, the delay line with a delay t_d is chosen. Finally, the clock signal is delayed by T_b-t_d to obtain the histogram on the left-hand side. An alternative method is to utilise a voltage-controlled phase clock recovery. Certain clock recoveries offer an extra pin to control and adjust the output clock phase and it can be used to vary the decision time vis-à-vis the eye. The relationship between the voltage and the output phase is generally linear and a phase control of $0\text{-}360^0$ is common (e.g. Elcom SCDR-192 clock and data recovery module). A single vertical scan of the eye takes approximately 2ms if dual-decision monitoring circuit is used

[Buc'01]. Therefore the three section eye diagram sampling takes less than 10ms if transition and stabilisation time is considered. This is relatively rapid for the rate of change of most impairment such as chromatic dispersion or PMD which changes on the scale of hours [Nag'00].

6.4 First-Order PMD Monitoring

Polarization-mode dispersion (PMD) has become a major source of impairment since transmission rates have increased to 10Gbit/s and beyond especially in networks with high-PMD fibre legacy. This is further accentuated in amplified systems where it has been shown that optical components such as EDFAs, isolators and couplers can add up to 7ps of differential group delay (DGD) in each fibre span [Gal'92]. First order PMD emanates from the fact that, in single mode fibre, the signal energy is resolved into two orthogonal polarization modes, known as the principal states of polarization (PSP's), which propagate at different velocities, leading to pulse broadening. This is also influenced by environmental changes such as temperature and mechanical stress rendering PMD a stochastically varying phenomenon in time and hence more difficult to manage [Kog'02]. It has been demonstrated that a DGD equal to 10% of the bit period engenders a power penalty of 1 dB [Hau'04]. In a long fibre regime, the differential group delay follows a Maxwellian distribution and carries a certain risk of network outage. It was shown in a long-term PMD monitoring study on buried fibre optic cables that DGD peaks exceeding three times the mean DGD regularly occur [Nag'00]. Numerous techniques to monitor PMD have been proposed in the literature and are reported in chapter 3. They either rely on measuring the degree of polarisation (DOP) of the signal or the fading/regeneration of a particular spectral component (clock-power detection and pilot tones). These approaches are usually expensive to deploy and lack versatility (dedicated to PMD only). In addition, they cannot separate the differential group delay (DGD) from the state of polarization of the signal and can only detect either their combined effects or just the DGD. Separating the two parameters may lead to a simpler design of PMD compensators, whether electrical or optical. For instance, to dynamically compensate for PMD optically, it is more convenient to align the polarization of the incoming signal to one of the principal states of polarization.

6.4.1 Concept

As mentioned in previous chapters, first order PMD can be represented phenomenologically by a differential group delay time $\Delta\tau$ between orthogonally polarised components of the input power waveform $P_{in}(t)$. Both the DGD and PSP are random and depend on the birefringence details along the entire fibre. The output waveform can be written as:

$$P_{out} = \gamma P_{in}\left(t + \frac{\Delta\tau}{2}\right) + (1-\gamma)P_{in}\left(t - \frac{\Delta\tau}{2}\right) \tag{6.7}$$

where $0< \gamma <1$ reflects the relative power launched in the two principal states. Notice that in the absence of PMD P_{in} and P_{out} are equal. If the shape of the waveform at the transmitter is known, the shape of the signal at the receiver (P_{out}) can be predicted using the equation above. Remember that by applying the three-point sampling technique to the signal at the transmitter, as explained in the previous section, we obtain four normalised amplitudes denoted S_T1, S_T2, S_T3 and S_T4 in Figure 6.7(a). These amplitudes can then be used to approximate the shape of the waveform of the transmitter using one of the fitting approaches discussed in section 6.3.2. Finally by applying the sampling technique to the transmitted signal, the four normalised amplitudes S_R1, S_R2, S_R3 and S_R4 of Figure 6.7(b) are obtained at the receiver and PMD can be assessed by comparing them with the predicted ones based on the approximation.

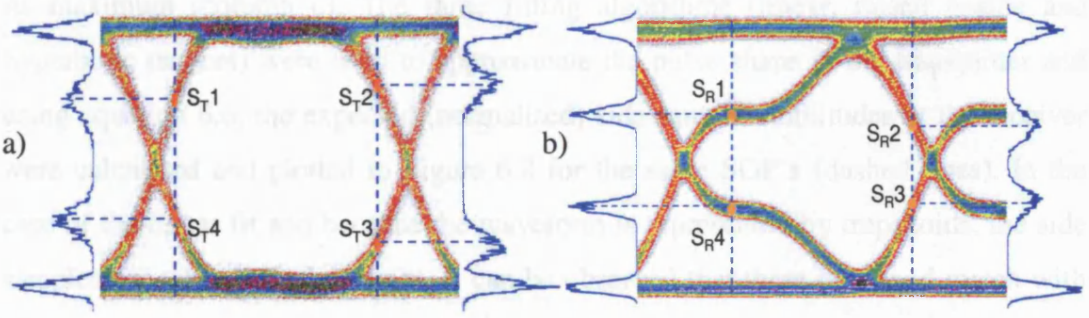

Figure 6.7 a) 10Gbit/s experimental eye diagram at the transmitter b) Eye diagram at the receiver affected by PMD ($\Delta\tau$=70ps and γ=0.7)

To illustrate this, let us first look at the progression of the side samples of our theoretical model with increasing DGD. The four side samples taken at ±37.5ps from decision time at the receiver are shown in Figure 6.8 (solid lines) for three states of polarisation (SOP): $\gamma = 0.1$ (column a), 0.3 (column b) and 0.5 (column c). Since first-order PMD is symmetrical, the side amplitudes for γ are the same as 1- γ but with S1

swapped with S2 and S3 interchanged with S4 (E.g. the graphs of $\gamma = 0.1$ and 0.3 are similar to 0.9 and 0.7 respectively).

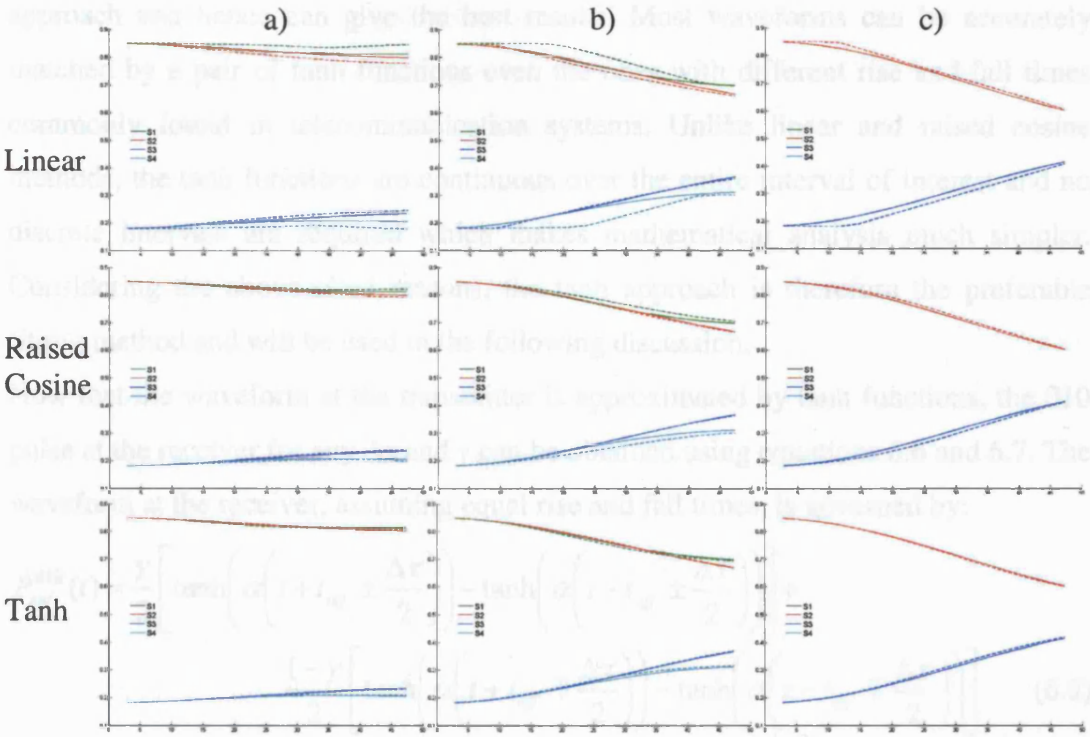

Figure 6.8 Comparison between the normalised side samples of the original pulse (solid lines) and the three approximations (dashed lines) as a function of the DGD for a) γ=0.1 b) γ=0.3 c) γ=0.5

It can be observed that the rate of change in the amplitude of the side samples is small when γ approaches 1 or 0 and substantially increases as γ tends to 0.5 where it reaches its maximum (column c). The three fitting algorithms (linear, raised cosine and hyperbolic tangent) were used to approximate the pulse shape at the transmitter and using equation 6.6, the expected (normalised) side sample amplitudes at the receiver were calculated and plotted in Figure 6.8 for the same SOP's (dashed lines). In the case of the linear fit and because the waveform is represented by trapezoids, the side samples progress in straight lines. It can be observed that there is a good match with the samples of the original waveform on the side where the eye closure is more pronounced i.e. the right-hand side in this case (S2 and S3). This is because, as shown in the previous chapter, the shift in the sampling time of the clock recovery due to PMD is less than $\Delta\tau/2$ and considering that each polarisation state shifts by $\pm\ \Delta\tau/2$, the side sampling now occurs above S1 and below S4 in the fast axis (Figure 6.3) where the approximation is the least accurate and moves slightly below S2 and above S3 where the approximation is still precise. The raised cosine approach is more accurate than the linear fit especially for the curves S1 and S4 although minor

discrepancies, when compared with the original curves, can be noticed for the same reasons explained above. The hyperbolic tangent approximation is the most precise approach and hence can give the best results. Most waveforms can be accurately matched by a pair of tanh functions even the ones with different rise and fall times commonly found in telecommunication systems. Unlike linear and raised cosine methods, the tanh functions are continuous over the entire interval of interest and no discrete intervals are required which makes mathematical analysis much simpler. Considering the above cited reasons, the tanh approach is therefore the preferable fitting method and will be used in the following discussion.

Now that the waveform at the transmitter is approximated by tanh functions, the 010 pulse at the receiver for any $\Delta\tau$ and γ can be obtained using equations 6.6 and 6.7. The waveform at the receiver, assuming equal rise and fall times, is governed by:

$$P_{out}^{010}(t) = \frac{\gamma}{2}\left[\tanh\left(\alpha\left(t+t_{off} \pm \frac{\Delta\tau}{2}\right)\right) - \tanh\left(\alpha\left(t-t_{off} \pm \frac{\Delta\tau}{2}\right)\right)\right] + \frac{1-\gamma}{2}\left[\tanh\left(\alpha\left(t+t_{off} \mp \frac{\Delta\tau}{2}\right)\right) - \tanh\left(\alpha\left(t-t_{off} \mp \frac{\Delta\tau}{2}\right)\right)\right] \quad (6.8)$$

Similarly, the output waveform for a 101 sequence, as demonstrated in Appendix 5, is given by:

$$P_{out}^{101}(t) = \frac{\gamma}{2}\left[\tanh\left(\alpha\left(t-t_{off} \pm \frac{\Delta\tau}{2}\right)\right) - \tanh\left(\alpha\left(t+t_{off} \pm \frac{\Delta\tau}{2}\right)\right)\right] + \frac{1-\gamma}{2}\left[\tanh\left(\alpha\left(t-t_{off} \mp \frac{\Delta\tau}{2}\right)\right) - \tanh\left(\alpha\left(t+t_{off} \mp \frac{\Delta\tau}{2}\right)\right)\right] + 1 \quad (6.9)$$

In equations 6.8 and 6.9, t is the sampling time of the eye diagram and is equal to $\pm t_d$ or to $\pm(T_b - t_d)$ as explained in section 6.3.2. This is true if the transmitter and the receiver have the same clock source such as the clock output of a pulse pattern generator in the laboratory. However in real networks clock recoveries are utilised and as shown in the previous chapter, PMD leads to a phase shift in the recovered clock which must be accommodated in the above equations. Not only does it depend on $\Delta\tau$ and γ but also on the type of clock recovery circuit utilised. For instance if the "differentiate and rectify" type clock recovery is deployed, the sampling time t will obey the following expression:

$$t = t_0 + \frac{1}{4\pi f_c}\sinh^{-1}\left[(2\gamma - 1)\sinh(2\pi f_c \Delta\tau)\right] \quad (6.10)$$

where t_0 equates $\pm t_d$ or $\pm(T_b-t_d)$ and f_c is the central frequency of the high-Q filter. Since S_R1-4 are the means of the inner distributions of the side histograms, they are mainly defined by the average values of the 101 and 010 sequences. Therefore, the curves in Figure 6.8 for the tanh approximation can be expressed as the average of equations 6.8 and 6.9. In other words they are governed by:

$$P_{out}(t) = \frac{P_{out}^{010}(t) + P_{out}^{101}(t)}{2} \tag{6.11}$$

Finally PMD can be assessed by solving the equation:

$$P_{out}(t) = S_R \tag{6.12}$$

where S_R is one of the normalised means at the receiver (S_R1, S_R2, S_R3 or S_R4). If γ is known and $\Delta\tau$ is unknown, solving one equation is sufficient to determine the DGD. The power ratio γ can be evaluated in the laboratory by calculating the relative power of the two polarisation states using a polarisation beam splitter (PBS) and a power meter. On the other hand, if both $\Delta\tau$ and γ are unknown then we need to equate P_{out} to two different means (e.g. S_R1 and S_R3) and solve a set of two simultaneous equations. A lookup table can also be generated based on equations 6.8 to 6.11 in order to evaluate PMD. It could be either one or two dimensional depending on whether γ is known or not. This has the advantage of a faster processing time and also any error in the estimation of the means of the side histograms can be averaged out.

To summarise, first-order PMD can be monitored by first applying the three-section eye sampling technique to the transmitter. The obtained normalised side means S_T1-4 in Figure 6.7(a) are utilised to reconstruct the eye and especially the two sequences 010 and 101 using the hyperbolic tangent approximation (section 6.3.2 and Appendix 5). Note that sampling the transmitter is not necessary if the rise and fall times of the system are known since they can be used to obtain the tanh approximation. The sampling technique is performed on the received signal and the normalised means S_R1-4 are acquired. Finally by considering the PMD-induced time shift (equation 6.10) and solving equation 6.12 for one or two unknowns, the DGD and the power splitting ratio between the two polarisation states can be evaluated.

6.4.2 Simulation Results

The PMD was simulated using the simulation model described in section 5.3.1. First we will assume that the power ratio between the polarisation states (γ) is known and

try to evaluate the DGD. After this both $\Delta\tau$ and γ will be treated as unknown variables and verify the accuracy of this technique.

a) Predetermined γ

As mentioned earlier, γ can be estimated by means of a polarisation beam splitter and a power meter and therefore we assume that it is accurately determined. The three-section eye sampling technique was applied to the signal at the transmitter and the four normalised means were obtained. Based on these values, the slope (α) and the time offset (t_{off}) of equations 6.8 and 6.9 were calculated as shown in Appendix 5. After introducing PMD, the sampling technique was performed at the receiver and the quantities S_R1-4 were acquired. Because of the symmetric nature of first-order PMD, working with power splitting ratios ranging between 0 and 0.5 suffices. γ was gradually increased by steps of 0.1 while the DGD was varied between 4 and 100ps with approximately 4ps resolution. The DGD was estimated by means of a lookup table which was constructed by evaluating P_{out} in equation 6.11 for S_R1, S_R2, S_R3 and S_R4. An example of this database is shown in Figure 6.10 for γ= 0.1, 0.3 and 0.5 (dashed lines) along with the side samples of the actual PRBS (solid lines). The good agreement between the estimated $\Delta\tau$ and the actual differential group delay for all power splitting ratios ($0.1 \leq \gamma \leq 0.5$) is shown in Figure 6.9(a).

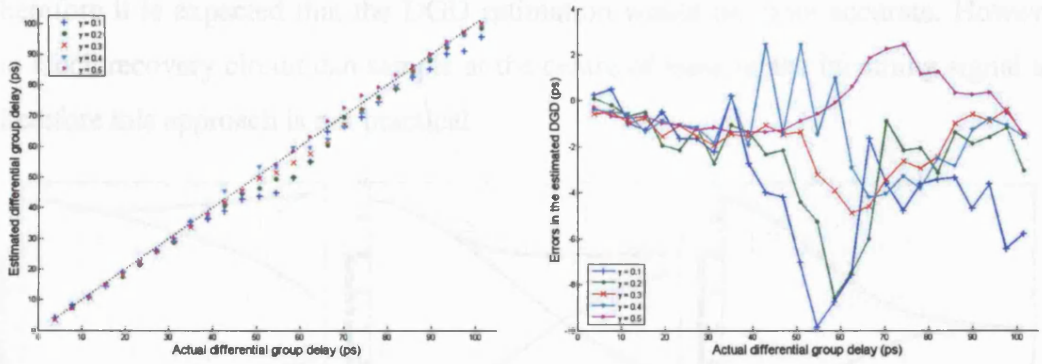

Figure 6.9 a) Estimated differential group delay (DGD) as a function of the actual DGD b) Errors in the estimated DGD as a function of the actual DGD

Figure 6.9(b) shows the error in the estimation which is the difference between the calculated and the actual DGD. It can be seen that errors increase with decreasing γ where the maximum observed error for γ=0.5 is around 2.5ps while it increases to approximately 10ps for γ=0.1. It therefore can be deduced that the errors in the DGD estimation increases as γ tends to 0 or 1 and decreases as γ approaches 0.5. This is because the side samples of the eye diagram, when one polarisation state contains most of the power, change only slightly with increasing DGD as shown in Figure

6.10a leading to more errors in the estimation. However, when the power is equally split the rate of change of the side samples as $\Delta\tau$ increases, is important (Figure 6.10b). In addition, it can be observed that the errors increase in the DGD range 40 to 70ps.

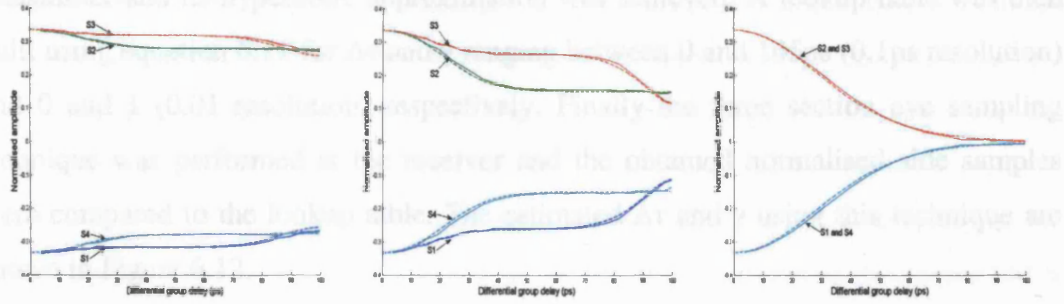

Figure 6.10 Comparison between the progression of the side samples of the simulated PRBS (solid) and the tanh approximation (dashed) when using a clock recovery for a) $\gamma = 0.1$ b) $\gamma = 0.3$ c) $\gamma = 0.5$

This is because, when deploying a clock recovery circuit, the decision time shifts to where the eye is most open leading to a flat progression of the side samples within this interval especially when γ tends to 0 (or 1) as demonstrated in Figure 6.10. Compare this with Figure 6.11 where the decision time is taken at the centre of mass of the incoming pulses. The rate of change of the side samples is more important and therefore it is expected that the DGD estimation would be more accurate. However, no clock recovery circuit can sample at the centre of mass of the incoming signal and therefore this approach is not practical.

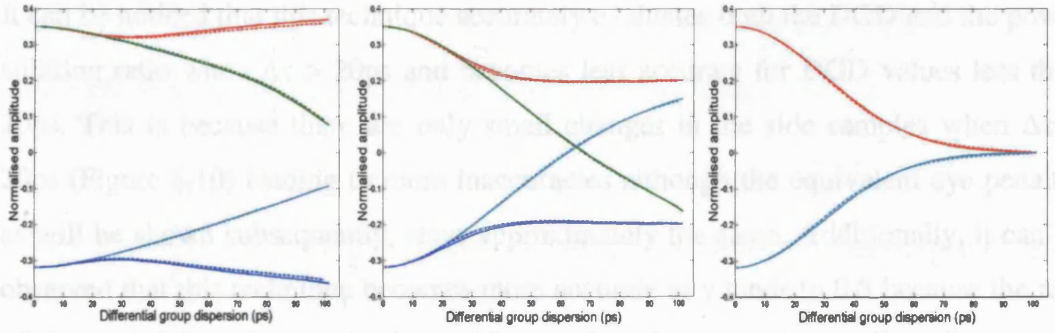

Figure 6.11 Comparison between the progression of the side samples of a simulated 010 sequence (solid) and the tanh approximation (dashed) when sampling at the centre of mass of the incoming pulse for a) $\gamma = 0.1$ b) $\gamma = 0.3$ c) $\gamma = 0.5$

Three section-eye diagram technique using commercially available clock recovery circuits can nevertheless estimate the DGD with high precision, infinite resolution and over a large range. The range is equivalent to one bit period and is only matched by the degree of polarisation (DOP) techniques described in section 3.4.1.1.3.

b) Both γ and Δτ unknown

As in the previous section, first-order PMD was modelled by increasing the differential group delay (Δτ) from 4 to 100ps (4ps resolution) while varying the power splitting ratio γ between 0.1 and 0.5. Our sampling technique was first applied to the transmitter and its hyperbolic approximation was achieved. A lookup table was then built using equation 6.11 for Δτ and γ ranging between 0 and 105ps (0.1ps resolution) and 0 and 1 (0.01 resolution) respectively. Finally the three section eye sampling technique was performed at the receiver and the obtained normalised side samples were compared to the lookup table. The estimated Δτ and γ using this technique are shown in Figure 6.12.

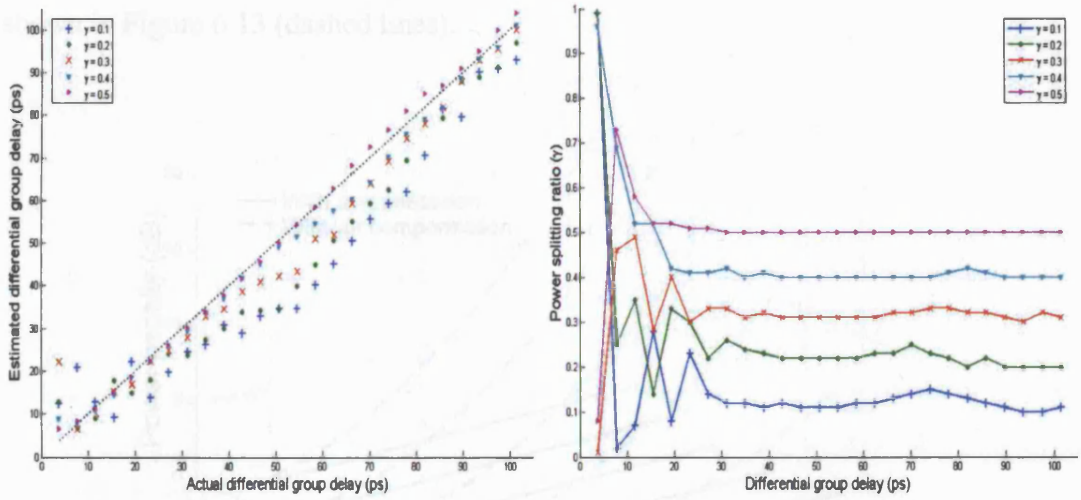

Figure 6.12 a) Estimated Vs actual differential group delay (DGD) b) Corresponding estimated power splitting ratio γ as a function of the DGD

It can be noticed that this technique accurately evaluates both the DGD and the power splitting ratio when Δτ > 20ps and becomes less accurate for DGD values less than 20ps. This is because there are only small changes in the side samples when Δτ < 20ps (Figure 6.10) leading to more inaccuracies although the equivalent eye penalty, as will be shown subsequently, stays approximately the same. Additionally, it can be observed that this technique becomes more accurate as γ tends to 0.5 because the rate of change of the side samples is significant when the power is equally split between the two polarisation states.

To fully evaluate this technique, one can assess the amount by which the power penalty can be reduced if this technique is used to control a PMD compensator. Power penalty due to first order PMD is given by [Poo'91] [Kog'02]:

$$\varepsilon(dB) = \frac{A}{T^2}\Delta\tau^2\gamma(1-\gamma) \qquad (6.13)$$

where T is the bit period and *A* is a dimensionless parameter that depends on pulse shape, modulation format and receiver characteristics. For pin receivers, *A* may vary between 10 to 40 for NRZ and from 20 to 40 for RZ [Kog'02]. For optically pre-amplified receivers, it ranges between 10 to 70 and 10 to 40 for NRZ and RZ respectively. In the system considered here, A=70. The power penalty in equation 6.13 depends on the two variables $\Delta\tau$ and γ and increases with increasing DGD and /or when γ tends to 0.5. By considering the above equation, it can be seen that although our technique is inaccurate for $\Delta\tau < 20$ps it still gives the correct power penalty (we can have the same penalty for different combinations of $\Delta\tau$ and γ). The power penalty (ε) due to PMD without any form of compensation in our system is shown in Figure 6.13 (dashed lines).

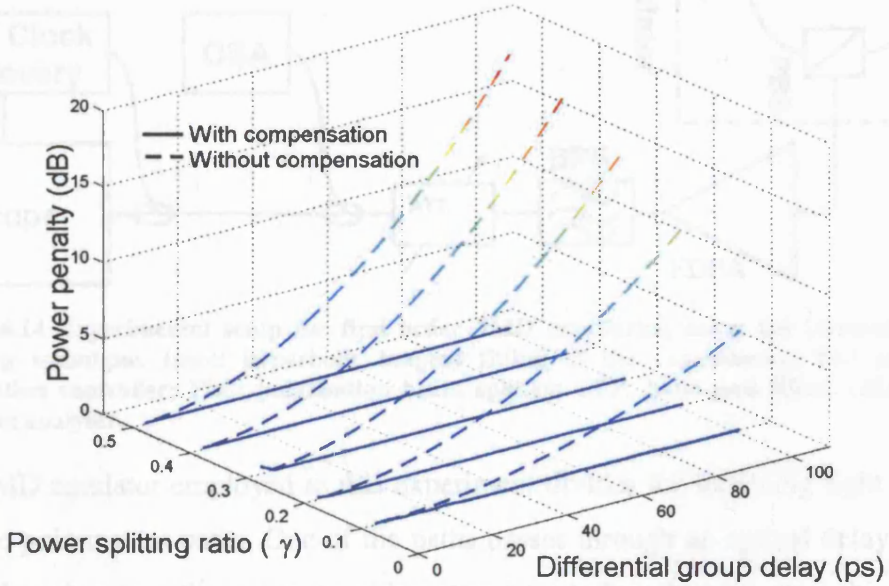

Figure 6.13 Power penalty as a function of $\Delta\tau$ and γ with (solid lines) and without (dashed lines) compensation

The solid lines in Figure 6.13 represent the power penalty after compensating for PMD, assuming that our technique is used as a feedback signal to a PMD compensator that compensates for both $\Delta\tau$ and γ. It can be observed that using this method leads to a significant improvement of up to 17.5dB in the power penalty with a maximum penalty of less than 0.5 dB.

6.4.3 Experimental Validation

A 10Gbit/s experiment was carried out to verify the accuracy of this technique as shown in Figure 6.14. A 9.953Gbit/s, 2^{31}-1PRBS optical signal was generated using a Mach-Zehnder modulator. The rise and fall times of the system were 31.7 and 35ps

respectively while the extinction ratio was approximately 13dB. The signal is coupled with an amplified spontaneous emission (ASE) noise source in order to control the OSNR. This is achieved by regulating the relative power between them using the two deployed attenuators. The OSNR was initially set to 34dB corresponding to a BER $<10^{-12}$. First order PMD is then introduced by means of a PMD emulator.

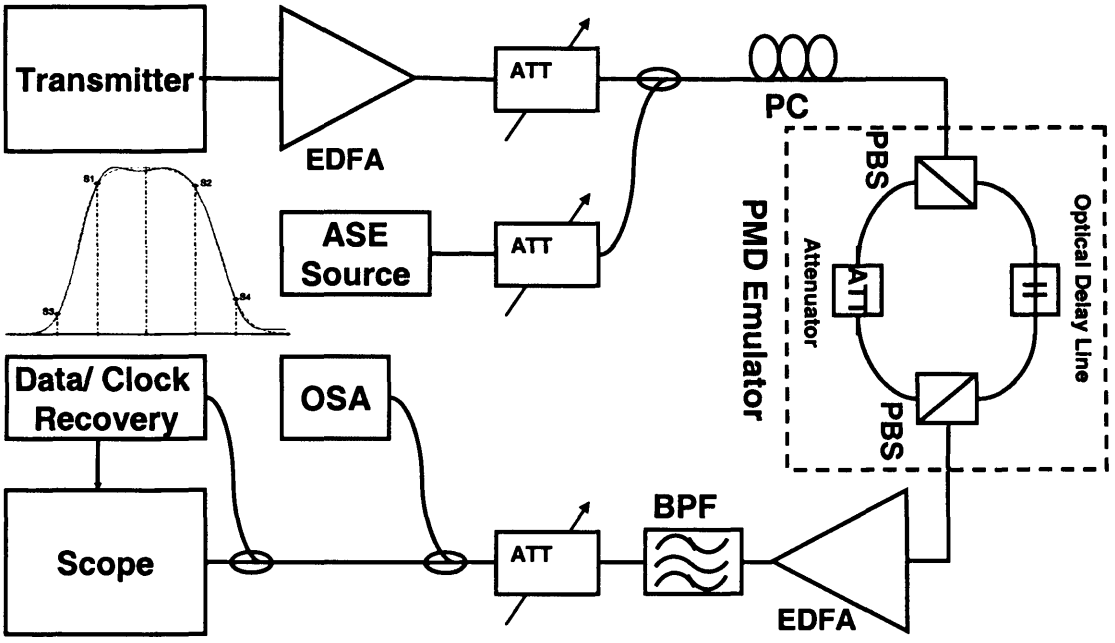

Figure 6.14 Experimental setup for first order PMD monitoring using the three-section eye sampling technique. Inset: hyperbolic tangent fitting of the experimental 010 pulse. PC: polarisation controller; PBS: polarisation beam splitter; BPF: band-pass filter; OSA: optical spectrum analyser.

The PMD emulator employed in this experiment divides the incoming light into two discrete polarization paths. One of the paths passes through an optical delay element while the other goes through a matching attenuator before they are recombined at the output. The optical delay element allows precise control of the time delay between the two polarization states ($\Delta\tau$) while the polarization controller is used to control the power ratio between them (γ). An EDFA is used at the output of the PMD emulator to boost the signal and pre-compensate for the loss of the 100GHz optical band-pass filter (~8dB insertion loss). 10% of the signal is then tapped out and fed to an optical spectrum analyser (OSA) to measure the OSNR. Finally the signal is split into two; one part is fed to the clock and data recovery module whereas the other part is connected to a digital sampling oscilloscope which was used as our monitoring circuit. The clock extraction circuit utilised is a high-Q filter based circuit described in section 5.3.4.2 of the previous chapter. The generated clock signal was fed to the sampling oscilloscope and our sampling technique was applied to the incoming data.

First order PMD was introduced as follow: using the polarisation controller, the power in the slow axis was gradually increased from 10 to 90% of the total power in steps of 20% (i.e. γ= 0.1, 0.3, 0.5, 0.7 and 0.9). For each polarisation state the differential group delay was varied from 10 to 100ps using 10ps resolution. The three-section eye sampling method was applied to the transmitted waveform where the side samples were taken at 40ps from the decision times and the four normalised means, denoted S_T1, S_T2, S_T3 and S_T4 in Figure 6.7(a), were obtained. The close match between the experimental (solid line) and the fitted tanh approximation (dashed line) in the inset of Figure 6.14 highlights the accuracy of this fitting method. Based on these values, a lookup table with a γ resolution of 0.01 and a DGD resolution of 0.1ps was generated. Since the type of the clock recovery circuit deployed here is a "differentiate and rectify", equation 6.10 was employed to describe the shift in decision times with respect to PMD. Finally the distorted signal arriving at the receiver was also sampled using the same approach and the normalised means were compared to the lookup table. The results, which are shown in Figure 6.15, were chosen on the basis of the closest match to the database in the Cartesian space.

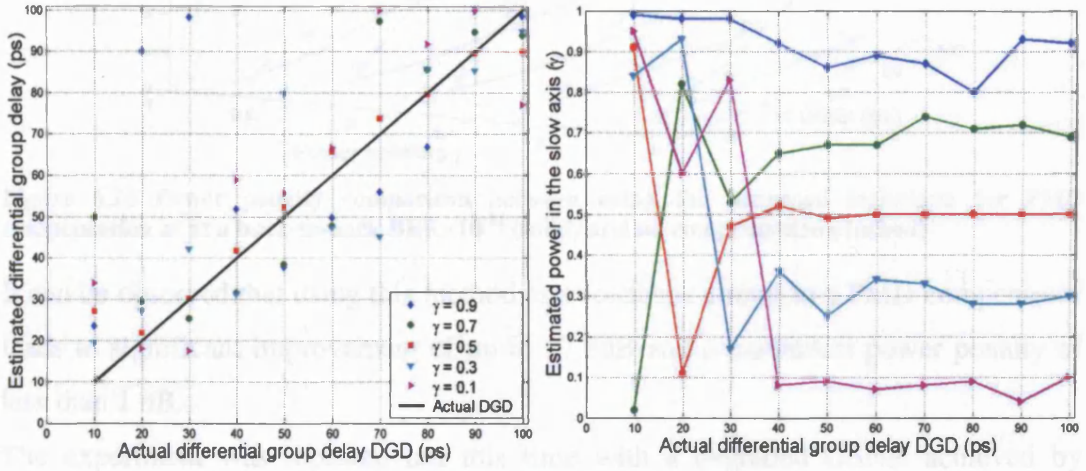

Figure 6.15 a) Differential group delay (DGD) estimation for a back to back BER<10^{-12} b) Corresponding estimated power splitting ratio γ in the slow polarization state

Figure 6.15 (a) and (b) show the estimated differential group delay and the corresponding power ratio in the slow polarisation state as a function of the real DGD. As expected from the simulation results, this method is more accurate for $\Delta\tau$ > 20ps especially when estimating the state of polarisation. It can also be observed that this technique is very precise when the power is equally divided between the two polarisation states (i.e. γ tends to 0.5) indicating that it works better in the worst case scenarios. In addition, clock jitter contributes to the inaccuracies in estimating PMD

especially when γ moves away from 0.5 because one side of the eye becomes steeper and any change in the sampling time leads to a significant change in the distributions of the side samples. This is why some points corresponding to γ= 0.1 and γ= 0.9 in Figure 6.15 (a) are out of range. Furthermore, we noticed when γ=0.5 and Δτ =100ps, the clock recovery intermittently loses synchronization since it tries to recover two identical signals shifted by a bit period from each other leading to errors in the DGD estimation. Using the above results and assuming this technique is used to drive a PMD compensator, the PMD-induced power penalties before and after compensation are shown in Figure 6.16.

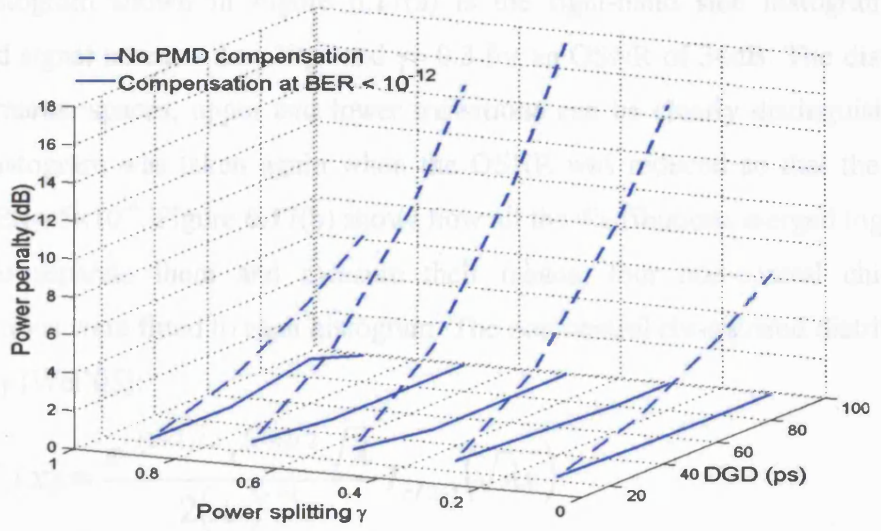

Figure 6.16 Power penalty comparison between using the proposed technique for PMD compensation at at a back-to-back BER<10^{-12} (solid) and no compensation (dashed)

It can be observed that using this method as a feedback circuit to a PMD compensator leads to significant improvement of up to 17.5dB and a maximum power penalty of less than 1 dB.

The experiment was repeated but this time with a degraded OSNR achieved by introducing more ASE noise into the system (DGD resolution was 20ps). The OSNR was set so that the bit error rates in the back to back configuration, measured with a bit error detector, were 10^{-9} and 5×10^{-4}. The noise increases the standard deviation of all distributions and they become indistinguishable from each other as demonstrated in Figure 6.17.

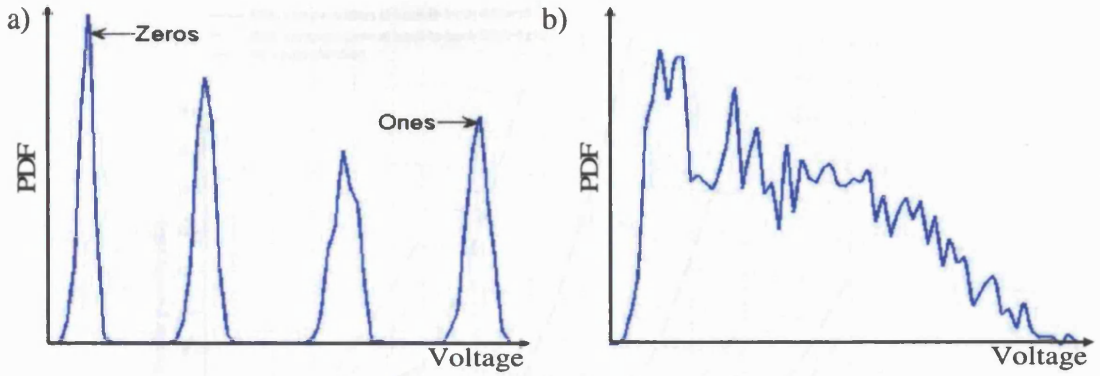

Figure 6.17 Experimental histogram of the right-hand side of the eye diagram with Δτ= 60ps and γ= 0.3 at a back-to-back BER of a) BER $<10^{-12}$ b) BER $=5\times10^{-4}$

The histogram shown in Figure 6.17(a) is the right-hand side histogram of the received signal taken at Δτ= 70ps and γ= 0.3 for an OSNR of 34dB. The distribution of the marks, spaces, upper and lower transitions can be clearly distinguished. The same histogram was taken again when the OSNR was reduced so that the back to back BER= 5×10^{-4}. Figure 6.17(b) shows how all the distributions merged together. In order to separate them and measure their means, four non-central chi-squared distributions were fitted to each histogram. The non-central chi-squared distribution is given by [Wei'05]:

$$P_r(x) = \frac{e^{-(x+\lambda)/2} x^{(r-1)/2} \sqrt{\lambda}}{2(\lambda x)^{r/4}} I_{r/2-1}\left(\sqrt{\lambda x}\right) \tag{6.14}$$

where $I_n(x)$ is a modified Bessel function of the first kind. The mean of the distribution is $\mu = r + \lambda$. Using the normalised means, Δτ and γ were calculated from the lookup table and the power penalties corresponding to each back-to-back BER are displayed in Figure 6.18. It can be observed that the power penalty at BER=10^{-9} is very similar to the error-free case with a maximum penalty <1dB for all states of polarisation. Additionally, it can be seen that it is slightly more accurate when γ approaches 0.5. For the back-to-back BER= 5×10^{-4} the trend is slightly different. We chose this BER because it is possible to achieve error-free detection at this sort of BER using forward error correction (FEC). It was reported in [Aza'02] that using Reed–Solomon RS(255, 239) code, error free detection (BER= 10^{-15}) can be obtained at an input BER of 10^{-4}.

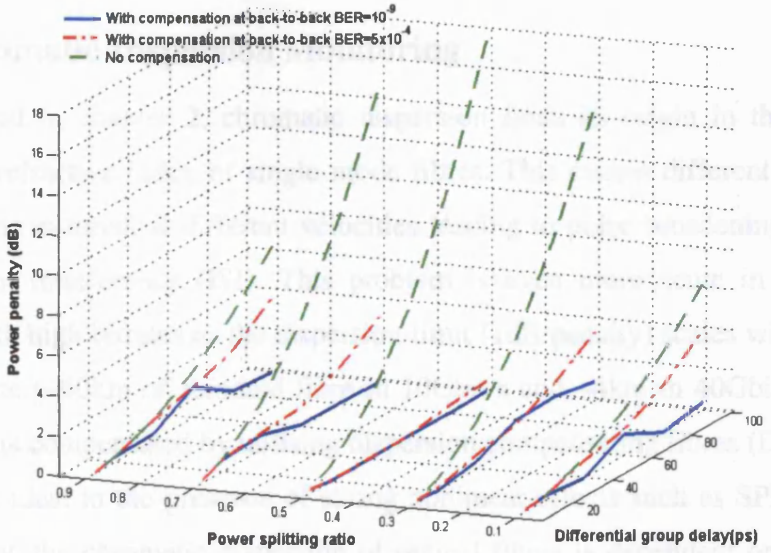

Figure 6.18 Power penalty comparison between using the proposed technique for PMD compensation at a back-to-back BER=10^{-9} (solid), BER=5×10^{-4} (dash-dot) and no compensation (dashed).

It is worth noting that the BER after introducing PMD is much worse than 5×10^{-4} in our experiment and therefore error-free transmission cannot be achieved even when utilising FEC. What we want to understand is to what extent PMD can be predicted and compensated for so that its contribution to the BER degradation can be removed. It can be observed from Figure 6.18 that using this sampling technique to drive a PMD compensator reduces the power penalty in all cases especially when γ tends to 0.5 (worst case). This sampling technique is not as accurate as in the previous cases because the power of the noise is now comparable to the power of the signal itself and therefore the mean of the noise is comparable to the means of the histogram distributions. Furthermore, the noise affects the means of the distributions in different way. For instance the noise increases the mean and the standard deviation of the marks and the upper-transition distributions more than those of the spaces and the lower transitions. This in turn leads to a disproportionate resizing of all the means when normalised with respect to the means of the ones and the zeros. This is further accentuated when γ tends toward 1 or 0 because the upper-transition distribution is always close to the marks distribution and both suffer from signal-spontaneous and spontaneous-spontaneous noise whereas the lower-transition distribution remains close to the zeros and are mainly affected by spontaneous-spontaneous contribution. Nevertheless, using this sampling technique in a feedback circuit to a first-order PMD compensator leads to significant savings in the power penalty.

6.5 Chromatic Dispersion Monitoring

As discussed in chapter 2, chromatic dispersion finds its origin in the frequency-dependent refractive index of single mode fibres. This causes different wavelengths (frequencies) to travel at different velocities leading to pulse broadening and thus to inter-symbol interference (ISI). This problem is even more acute in transmission systems with high bitrates as the dispersion limit (1dB penalty) scales with the square of the bitrate (~60km of standard fibre in 10Gbit/s and ~4km in 40Gbit/s) [Ber'02]. Dispersion is compensated by utilising dispersion compensating fibres (DCF) but they may not be ideal in the presence of strong nonlinear effects such as SPM and XPM. Additionally, the chromatic dispersion of optical fibres is dependent on the ambient temperature and it has been shown in [Wal'02] that the peak to peak seasonal variation can range between 375 and 570ps/nm in ultra-long-haul routes. In order to maintain the signal quality at an acceptable level, dynamic compensation within tight tolerance must be used. This can be achieved either electrically or optically. The former comprises methods such as decision-feedback equalization (DFE) and maximum-likelihood sequence estimation (MLSE) [Aga'05]. Tuneable optical dispersion compensation can be achieve by using, for instance, nonlinearly chirped fibre Bragg gratings [Pan'02] or adaptive planar lightwave circuit (PLC) [Sec'03]. The different performance monitoring techniques reported in chapter 3 can be utilised as feedback circuits to drive these compensators. Most of the spectral methods, however, suffer from the fact that they have a short monitoring range, scale badly with the bitrate or may even necessitate transmitter modification (pilot tones). Furthermore, their accuracy is affected by filter characteristics (transfer function, detuning), nonlinear effects and sometimes bit patterning. Sampling methods, on the other hand, have been used to detect dispersion signature on the histogram, used essentially for troubleshooting and root cause analysis. However, they have not been exploited to their full potential and to date there has not been any work showing how these techniques can estimate the group velocity dispersion (GVD) of a dispersive link. This is what we will demonstrate using the three-point sampling technique. The next section explains the concept of utilising the three-section eye sampling technique for chromatic dispersion evaluation purposes. Section 6.5.2 discusses the results obtained from our theoretical model and finally an experimental validation of this technique is shown in section 6.5.3.

6.5.1 Concept

The GVD estimation can be achieved using two methods. The first approach consists of approximating the optical field by a pair of hyperbolic tangent functions in the same manner as the electrical signal shown in the previous sections. A single equation relating the shape of the signal with respect to the propagation distance can be derived. By sampling the signal at the receiver and comparing it with this equation, the GVD estimation is attained. The second method consists of obtaining an approximation of the electrical eye then transforming it into an optical field. A database relating the side samples with the propagation distance can be acquired and used for GVD evaluation. This method is easier and more convenient to apply.

Method 1

The side samples of the transmitter's eye diagram, as shown in Figure 6.19a, are obtained after a square law detector. Assuming the optical signal has a constant phase (no chirp), the optical pulse envelope is proportional to the square root of the electrical waveform. Therefore the amplitude of the incident field at the side sampling times is the square root of the amplitudes denoted S1, S2, S3 and S4.

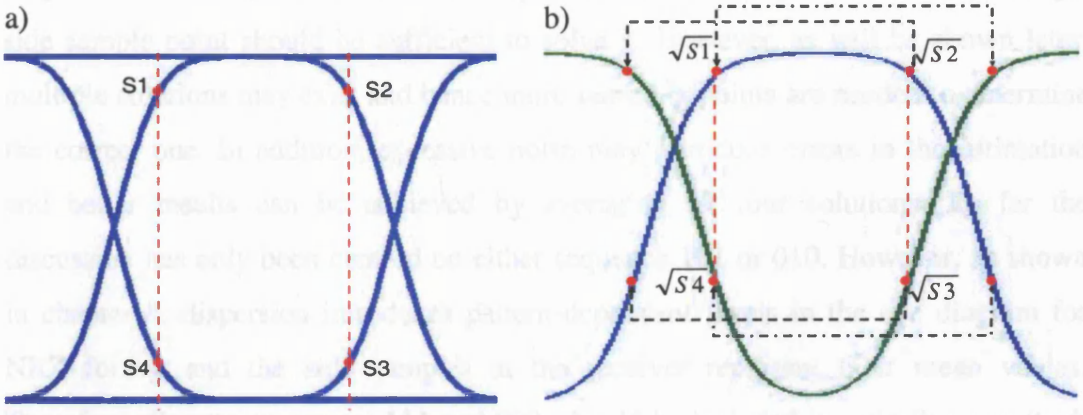

Figure 6.19 a) Eye diagram of the signal at the transmitter b) Tanh approximation of the optical pulse envelope

The optical envelope can then be approximated by hyperbolic tangent (tanh) functions. Figure 6.19b shows the tanh fit for sequences 010 and 101. For identical rise and fall times, a 010 (or 101) sequence at the transmitter can be expressed as:

$$U_{010} = \frac{1}{2}\left[\tanh\left(\alpha_o\left(t + t_{off}\right)\right) - \tanh\left(\alpha_o\left(t - t_{off}\right)\right)\right] \tag{6.15}$$

where α_o is the optical slope (to be differentiated from the electrical slope). The Fourier transform of a tanh function is given in [Bra'99] as:

$$\Im\{\tanh(\alpha_o t)\} = \frac{-i\pi}{\alpha_o}\cos ech\left(\frac{\pi\omega}{2\alpha_o}\right) \tag{6.16}$$

Using equations 6.15 and 6.16, the Fourier transform of our 010 sequence is therefore:

$$\tilde{U}_{010}(\omega) = \frac{\pi}{\alpha_o}\cos ech\left(\frac{\pi\omega}{2\alpha_o}\right)\sin\left(t_{off}\omega\right) \tag{6.17}$$

where $\tilde{U}_{010}$ is the transform of U_{010}. The pulse shape due to group velocity dispersion after L km of fibre is given by [Gov'01]:

$$U_L = \Im^{-1}\left\{\tilde{U}_{010}(\omega).\exp\left(\frac{i}{2}\beta_2 L\omega^2\right)\right\} \tag{6.18}$$

The product $\beta_2 L$ (or DL) can be assessed by equating the square of the above equation to the side samples of the eye at the receiver i.e.

$$U_L = \sqrt{S_{Rx}} \tag{6.19}$$

where S_{Rx} represents the four side samples of the signal at the receiver (after the detector). Unfortunately there is no closed form formula for U_L in this case and can only be numerically evaluated. Since equation 6.19 has only one variable, a single side sample point should be sufficient to solve it. However, as will be shown later, multiple solutions may exist and hence more sampling points are needed to determine the correct one. In addition, excessive noise may introduce errors in the estimation and better results can be achieved by averaging all four solutions. So far the discussion has only been centred on either sequence 101 or 010. However, as shown in chapter 4, dispersion introduces pattern-dependent levels in the eye diagram for NRZ format and the side samples at the receiver represent their mean values. Therefore all patterns, except 111 and 000, should be included in a similar way (tanh approximation). For upper side samples ($S_{Rx}1$ or $S_{Rx}2$), equation 6.19 becomes:

$$\frac{1}{3}\Im^{-1}\left\{\left[\tilde{U}_{010}(\omega)+\tilde{U}_{011}(\omega)+\tilde{U}_{110}(\omega)\right]\exp\left(\frac{i}{2}\beta_2 L\omega^2\right)\right\} = \sqrt{S_{Rx}(1|2)} \tag{6.20}$$

Similarly for the lower side samples ($S_{Rx}3$ or $S_{Rx}4$), equation 6.19 yields:

$$\frac{1}{3}\Im^{-1}\left\{\left[\tilde{U}_{001}(\omega)+\tilde{U}_{100}(\omega)+\tilde{U}_{101}(\omega)\right]\exp\left(\frac{i}{2}\beta_2 L\omega^2\right)\right\} = \sqrt{S_{Rx}(3|4)} \tag{6.21}$$

For RZ format on the other hand, if the (electrical) waveform is fitted using a Gaussian pulse, a closed form expression can be obtained. First, let us assume the incident field is given by:

$$U_0 = \exp\left(-\frac{t^2}{2T_0^2}\right) \tag{6.22}$$

where T_0 is the half-width at 1/e intensity point. The optical amplitude at any distance L along the fibre (ignoring fibre attenuation) can be shown to be [Agr'01]:

$$U_L = \frac{T_0}{\sqrt{T_0^2 - i\beta_2 L}} \exp\left(-\frac{t^2}{2(T_0^2 - i\beta_2 L)}\right) \tag{6.23}$$

The product $\beta_2 L$ for RZ signals is easily evaluated by substituting the above equation into equation 6.19 and solving a simple equation.

Method 2

Figure 6.20(a) shows the 10Gbit/s eye diagram of a transmitter using an externally-modulated Mach-Zehnder interferometer. First, the signal at the transmitter is sampled on both sides and histograms similar to the ones shown in Figure 6.20(a) are obtained.

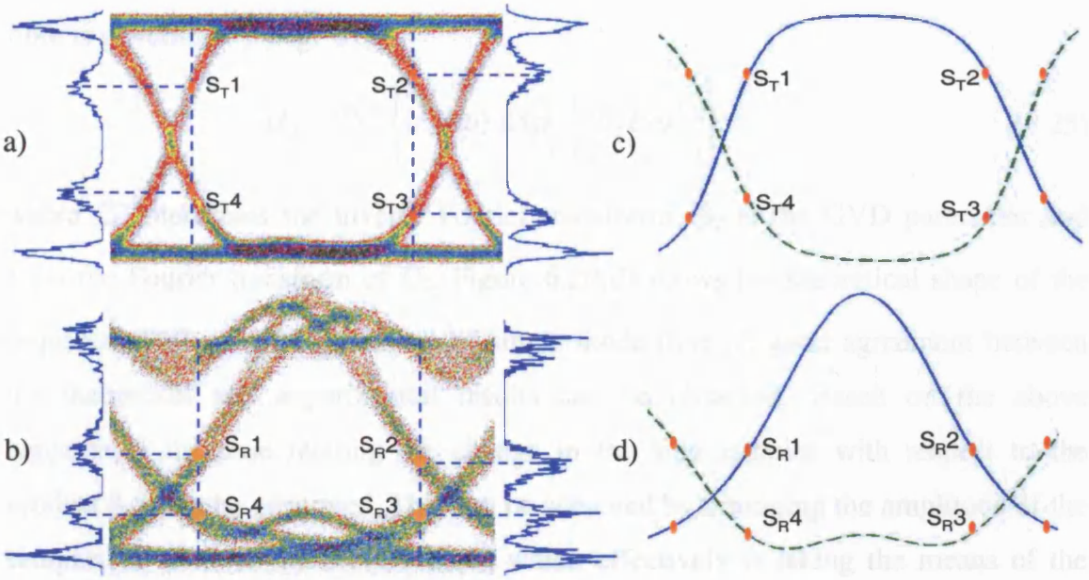

Figure 6.20 a) Experimental 10Gbit/s eye diagram of the transmitter b) 10Gbit/s eye diagram after 50km of SMF c) Hyperbolic tangent approximation of sequences 010 and 101 at the transmitter d) Simulated 010 and 101 sequences after 50km of SMF

By taking the means of their inner distributions, values for the points labelled S_T1-4, normalized with respect to the marks and spaces, are determined. The side sampling delay is chosen so that the distributions can be easily distinguished and is achieved by introducing fixed delay lines to the recovered clock signal or by utilizing a voltage-controlled phase clock recovery. Similarly at the receiver, the side histograms are obtained by sampling a tapped portion of the incoming signal and the means labelled S_R1-4 in Figure 6.20 (b) are determined. The sampling points at the transmitter can be used to generate a unique pair of hyperbolic tangent functions, one for the rising and

one for the falling edge, to approximate the shape of the transmitted waveform. Figure 6.20(c) illustrates this fit for bit sequences 010 and 101. A normalized formula for these two sequences has the form:

$$f_0 = \frac{1}{2}\left(\tanh\left(\alpha_R\left(t + t_{off}\right)\right) + \tanh\left(\alpha_F\left(t - t_{off}\right)\right)\right) \tag{6.24}$$

where α_R and α_F determine the slopes of the rising and falling edges respectively and t_{off} is the time offset defined in Appendix 5. Note that if the rise and fall times of the transmitter were known, then it would not be necessary to sample the transmitted signal as the tanh approximation can be achieved using these parameters. The photocurrent at the receiver is directly proportional to the incident optical power [Agr'02]. In other words, assuming the transmitted signal has a constant phase (no chirp), the optical pulse envelope U_0 is proportional the square root of the electrical waveform i.e. $U_0 \sim \sqrt{f_0}$. The normalized optical amplitude at any distance L along the fibre is governed by [Agr'01]:

$$U_L = \Im^{-1}\left\{\tilde{U}_0(\omega).\exp\left(\frac{i}{2}\beta_2 L\omega^2\right)\right\} \tag{6.25}$$

where $\Im^{-1}$ represents the inverse Fourier transforms, β_2 is the GVD parameter and $\tilde{U}_0$ is the Fourier transform of U_0. Figure 6.20(d) shows the theoretical shape of the sequences 010 and 101after 50km of single mode fibre. A good agreement between the theoretical and experimental results can be observed. Based on the above equation, a database relating the change in the side samples with respect to the product $\beta_2 L$ can be generated. This can be achieved by averaging the amplitude of the samples of all three-bit combinations, which effectively is taking the means of the side samples of a reconstructed eye diagram. However since dispersion affects mainly isolated bits, a database containing the averaged values of sequences 010 and 101 is sufficient. The experimental sample points S_R1-4 are then compared with the database and the GVD of the signal is deduced.

6.5.2 Theoretical Results

This sampling technique was applied to the theoretical model described in section 5.3.1. The second method was chosen to generate a database based on sampling points obtained at ± 37.5ps from the decision time (centre of the eye diagram). The two-dimensional database which relates how the side samples progress with accumulated dispersion (DL product) is depicted in the graphs below. Figure 6.21(a) compares the

change in the side samples (S_R1-4) of the PRBS with the ones of the database at 10Gbit/s. The PRBS side samples were obtained by first recovering the signal after a distance L using a high-Q filter clock recovery then applying the three-point sampling technique. Although there is a good agreement between these two, minor discrepancies can be observed. This is due to the slight mismatch between the shape of the original waveform and the fitted tanh approximation. The rate of change in the amplitude of the samples, and especially the upper ones (S_R1-2), is significant between 0 and 1870ps/nm. It reduces considerably above 1870ps/nm (110km of SMF) to become almost zero after 2500ps/nm.

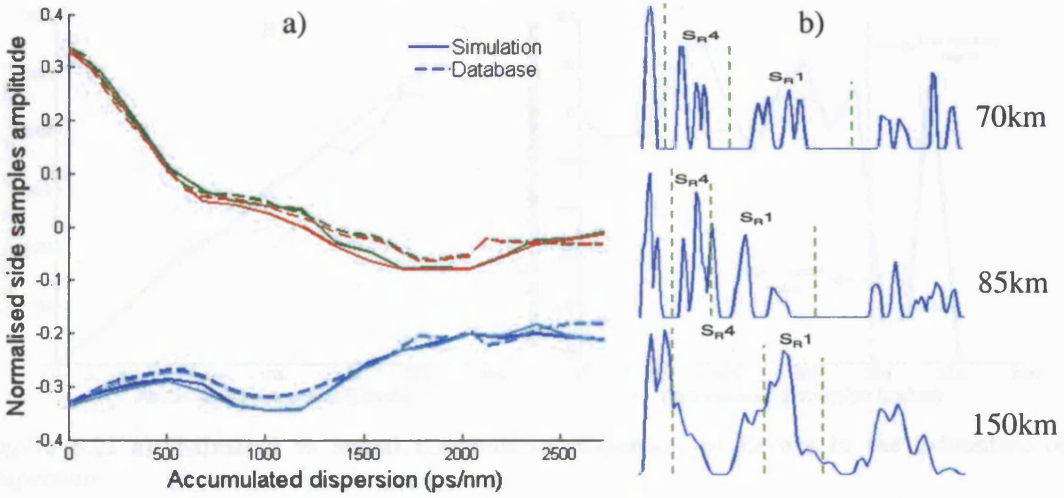

Figure 6.21 a) The normalised amplitude of the side samples wrt accumulated dispersion of the simulated PRBS (solid) and the database (dashed) at 10Gbit/s b) Left-side distributions at 70, 90 and 140km of SMF

This is because the upper and lower inner histograms start to overlap after approximately 80km of standard fibre but they can still be separated, by evaluating their median (since rising and falling edges have equal probability of occurrence) as shown in Figure 6.21(b). After ~140km of SMF however, the two histograms are completely fused together and their median becomes constant. This is the reason why the upper and lower samples progress in almost two parallel lines after 2500ps/nm. Therefore this technique has a monitoring range of 0-2500ps/nm. This range scales with the square of the bitrate because dispersion is proportional to the square of the frequency and reduces to approximately 156ps/nm (~9.2km) for a 40Gbit/s system. The resolution of this method depends on the resolution of the database and can potentially be very high. The side samples of the PRBS data were compared to the database by finding the closest match in the Cartesian space over a distance ranging between 0 and 150km of standard fibre (D=17ps/nm). Figure 6.22(a) reveals the

accuracy of this technique in estimating dispersion. Normally one sampling point (e.g. S_R4) should be sufficient in determining dispersion since we are trying to find only one variable. However, one side sample value may give more than one solution and dispersion may not be unambiguously evaluated. For instance, when the normalised amplitude of the lower samples is -0.3, the DL product can have three values (200, 800 or 1260ps/nm) and therefore correlating it with the upper samples would give the correct solution. An additional benefit of using all four samples is in the case where an error occurs in evaluating one of the histogram means, this error would be averaged out and an accurate assessment can still be obtained.

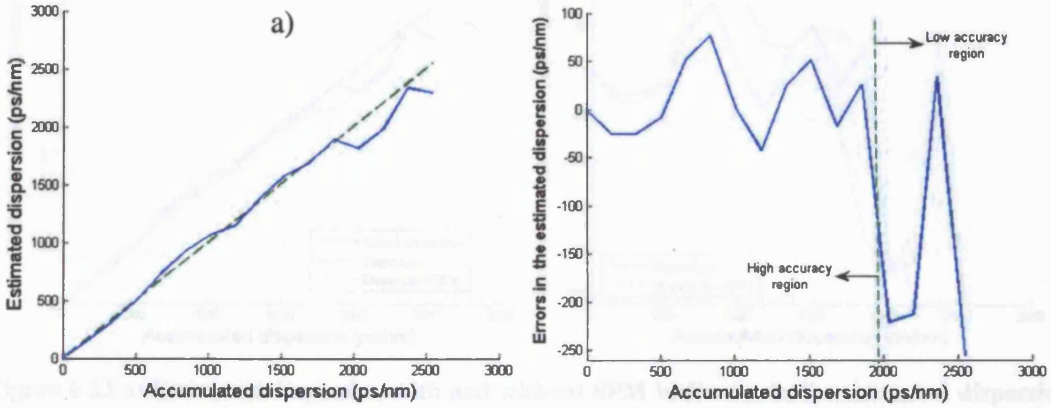

Figure 6.22 a) Estimated vs actual accumulated dispersion b) Errors in the estimation of dispersion

Figure 6.22(b) shows that the technique has a high accuracy within the range 0-1870ps/nm (0-110km) above which it slightly degrades. This, as explained earlier, is due to the fact that the rate of change of the side samples within this range is substantial and reduces above 110km where little information can be extracted. However, the maximum error obtained was around -250ps/nm (14.7km) which can be negligible in a 10Gbit/s system. In addition, the small errors in dispersion evaluation observed in the high accuracy region result from the small mismatch between the actual shape of the PRBS waveform and the hyperbolic approximation.

In theory this monitoring approach is immune to the effect of ASE noise in the system. Assuming it has a Gaussian distribution with zero mean, noise will lead to the broadening of the side histograms. But since we are measuring the means of the distributions, these remain constant. As a result, the amplitude of the side samples with and without noise should be approximately the same leading to similar results as shown in Figure 6.22. Nonlinear effects on the other hand may influence the measurement technique, as they actively interact with dispersion in shaping and

distorting the eye diagram. The nonlinear effect considered in this case is self-phase modulation (SPM). In the anomalous-dispersion regime of the fibre, the combination dispersion-SPM leads to a reduced pulse broadening [Agr'01]. This can be understood by noting that SPM introduces a positive chirp to the signal while dispersion-induced chirp is negative (when $\beta_2<0$). As a consequence, the two phenomena partially compensate for each other especially at the start of the link. The effect of SPM reduces as the pulses propagate along the fibre since the signal power decreases due to fibre loss.

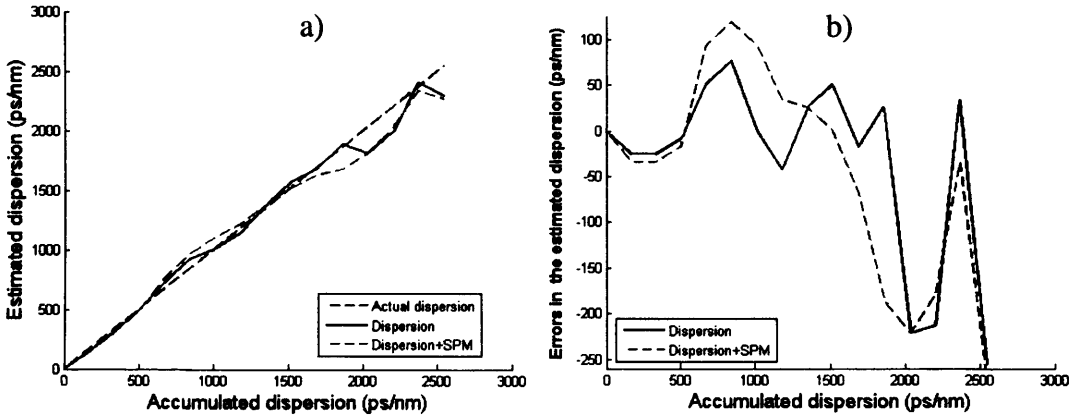

Figure 6.23 a) Estimated dispersion with and without SPM b) Errors in the estimated dispersion with and without SPM

The fibre nonlinearities were modelled by increasing the launch power to 6dBm and using the split-step Fourier method. This method consists of splitting the fibre into a number of longitudinal subsections along which the signal is passed [Low'02]. In each section fibre dispersion then a nonlinear phase shift are applied to the signal. The dispersion is implemented in the Fourier domain while the nonlinear phase shift is implemented in the time domain. More information on this method can be found in Appendix 6. Figure 6.23 compares the results previously obtained without SPM with the estimated DL product in the presence of both dispersion and SPM (fibre nonlinear coefficient $\gamma= 1W^{-1}km^{-1}$). It can be observed that dispersion is slightly underestimated in the intervals 0-510 and 1400-2550ps/nm and overestimated between 510 and 1400ps/nm. As mentioned earlier, SPM and dispersion counteract each other leading to a slower pulse broadening than in the absence of SPM. In other words, we expect the eye to be more open in the presence of SPM and hence this sampling technique should yield an underestimation of dispersion. However the accumulated dispersion is overestimated in the interval 510-1400ps/nm which coincides with the interval where the discrepancies between the actual side-samples and the database is the highest

(Figure 6.21a). We therefore conclude that this is an error due to the minor mismatch between the actual waveform shape and the tanh approximation.

6.5.3 Experimental Validation

The three-point sampling technique for chromatic dispersion monitoring was verified experimentally with the setup shown in Figure 6.24.

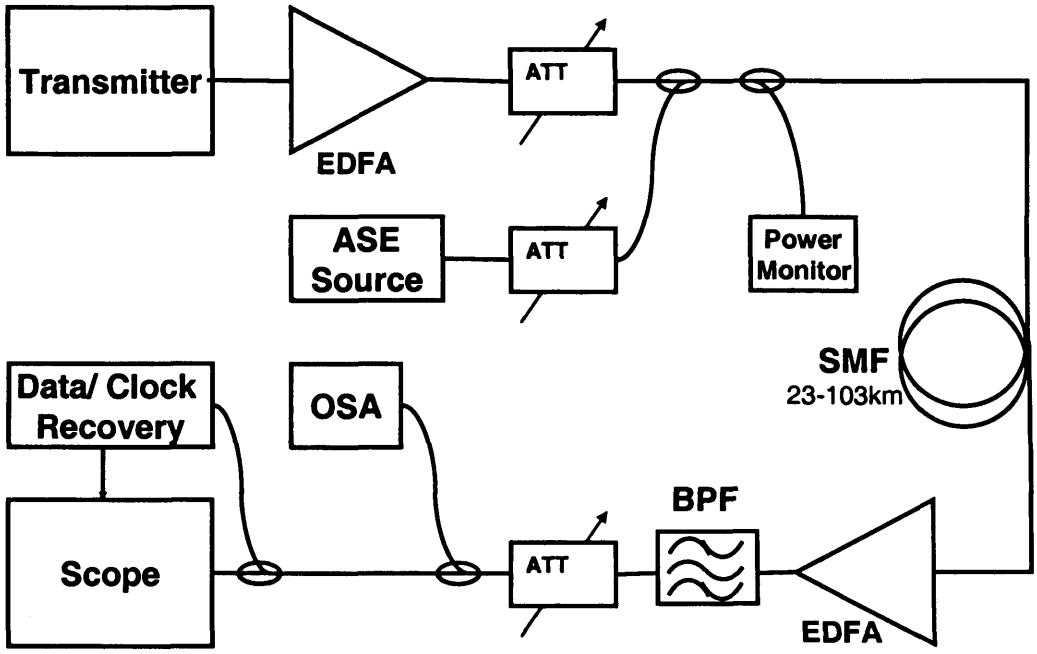

Figure 6.24 Experimental setup of dispersion monitoring using three-point sampling

An externally modulated 9.953Gbit/s, 2^{31}-1PRBS optical signal was generated then coupled with an ASE source in order to control the OSNR. The OSNR was initially set to 34dB (0.1nm resolution bandwidth). Variable attenuators were utilized to keep the power at the input of the SMF constant at 0dBm. The lengths of the fibre spans used were 23, 40, 50, 63, 73, 80, 90 and 103 km. An EDFA was used to boost the signal power at the output of the fibre, followed by a 100GHz optical bandpass filter. An optical attenuator was utilised to maintain the power at the receiver at -7dBm. In addition an optical spectrum analyser was used to measure the signal OSNR. Finally a clock and data recovery circuit was employed for data termination and a digital sampling oscilloscope was utilized to sample the eye.

First the three-section eye sampling technique was applied to the signal at the transmitter where the side samples were performed at 40ps from the centre of the eye diagram (decision time). After processing the side histograms, the points denoted S_T1-4 in Figure 6.20 were obtained. Based on these values, a database was generated using the second method described in section 6.5.1, with a resolution of 8.5ps/nm (i.e.

0.5km propagation distance). The three-point sampling technique was then applied to the received signal for every fibre length, where the side samples were also performed on either side at 40ps from decision time. The normalised means of the histograms were compared to the database and the results are shown in Figure 6.25.

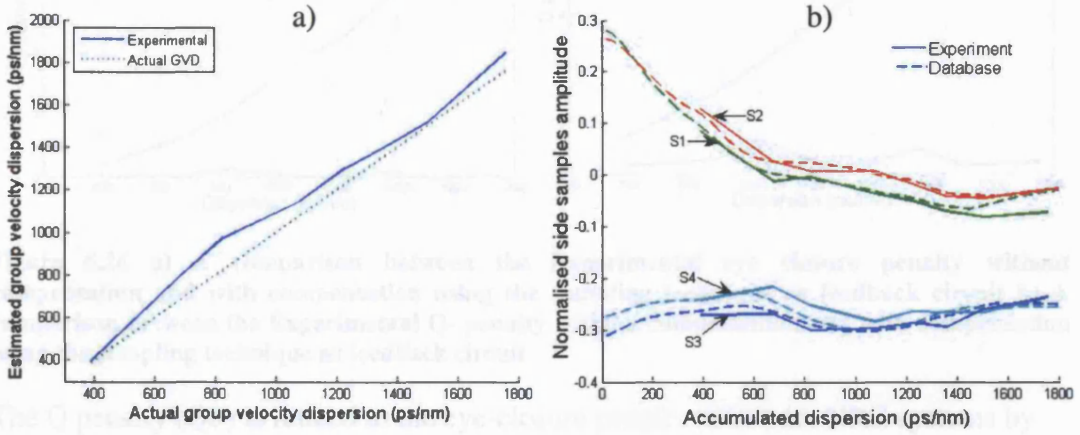

Figure 6.25 a) Estimated dispersion for OSNR = 34dB b) The normalised amplitude of the side samples wrt accumulated dispersion of the experimental eye and the database

Figure 6.25(a) compares the actual with the estimated GVD where the maximum error in the estimated GVD was 110ps/nm. The small errors in the measured results are due to the slight mismatch between the actual pulse shape and the tanh approximation. In addition, the clock recovery jitter which introduces amplitude noise in the histogram will increase these errors. Figure 6.25(b) shows the good agreement in the side-sample amplitudes between the experiment and the database (theoretical). Next we investigated the reduction in Q-penalty that can be achieved with this technique being used as a feedback circuit to a dynamic dispersion compensator. The experimental eye closure penalty (ECP) was measured for every fibre length as illustrated in Figure 6.26(a) (dashed line). The eye closure/opening penalty measurement is explained in the theory chapter.

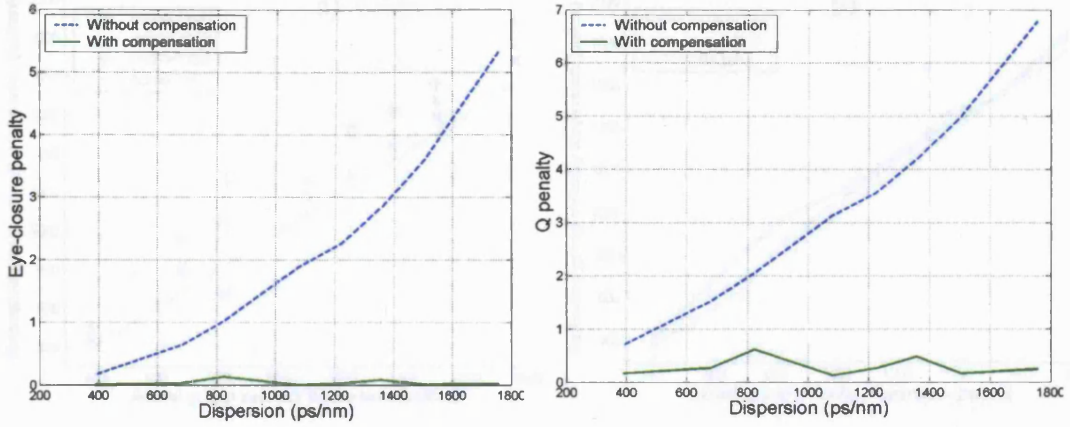

Figure 6.26 a) A comparison between the Experimental eye closure penalty without compensation and with compensation using the sampling technique as feedback circuit b) A comparison between the Experimental Q- penalty without compensation and with compensation using the sampling technique as feedback circuit

The Q penalty (QP) is related to the eye-closure penalty (ECP) for NRZ systems by [Dow'05]:

$$QP = ECP.\frac{1+\sqrt{\frac{ECP-1}{ECP+1}}}{\sqrt{1+\frac{ECP-1}{ECP+1}}} \tag{6.26}$$

The equivalent Q-penalty for every fibre span is shown in Figure 6.26(b). The estimated ECP and QP if this monitoring technique was used as a feedback circuit to a dynamic dispersion compensator are shown in Figure 6.26(a) and (b) (solid lines). Note that compensation was not achieved experimentally and the estimated ECP and QP after compensation were obtained by numerical simulation. It can be observed that by using this technique, the Q-penalty can be kept below 0.6dB up to a dispersion-induced Q-penalty of approximately 7dB.

The relative power of the ASE source was gradually increased so that the OSNR was decreased to 27, 22 and finally 17dB. The electrical bandwidth of the sampling scope, which was used as a monitoring circuit, was 30 GHz. Considering that the extinction ratio of the signal was 13dB, the BER of the system at an OSNR of 22 and 17dB was approximately 10^{-9} and 5×10^{-4} respectively (see theory chapter for formula). This is the equivalent of having an OSNR of 17 and 12dB for a receiver with 10GHz electrical bandwidth. In the presence of noise, the means were obtained by fitting four non-central Chi square distributions to the side histograms as discussed in section 6.4.3. Figure 6.27(a) shows the GVD estimation for different OSNRs.

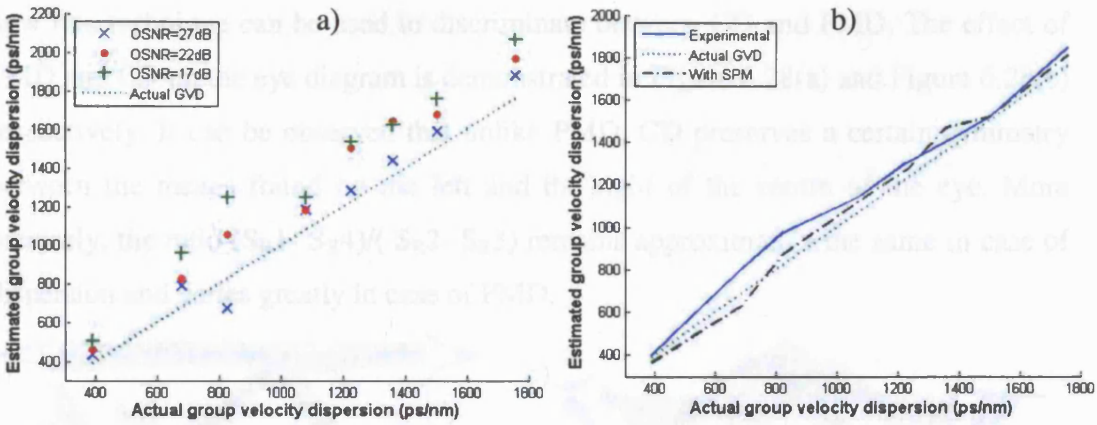

Figure 6.27 a) Dispersion estimation with varying OSNR values b) Dispersion estimation with and without SPM.

It can be seen that the errors increase with decreasing ONSR but they represent less than 1dB penalty in the worst case. In the literature, ASE noise is widely modelled as additive white Gaussian noise (AWGN) with zero mean and a certain variance [Cai'03]. However, in practice we noticed that the noise was not Gaussian and did have a non-zero mean which introduced errors in the evaluation of dispersion.

Finally the input power to the fibre span was increased from 0 to 5.8dBm (no ASE noise was introduced) to investigate the impact of self phase modulation on the CD measurement technique. The OSNR of the system in this case was >34dB. Figure 6.27 (b) shows that the measurement is not greatly affected by the effects of moderate levels of SPM. However we note that the dispersion is underestimated by approximately 7 to 11% up to distances of 40km. Due to fibre loss, the effect of SPM is largest over the effective length at the start of the link and thus the interaction between SPM and dispersion leads to a reduction in the effective dispersion accumulated by the signal. In other words, the nonlinear effect may compensate for part of the dispersion and our technique can only detect their combined product. This characteristic may be beneficial so that the received signal is not overcompensated.

In this experiment we effectively showed that a digital sampling oscilloscope can be used as a dispersion analyser using our sampling technique. This is a very cheap method to estimate fibre dispersion over this sort of range (~110km) when compared with using an optical dispersion analyser.

As a final note, since we analysed the effect of chromatic dispersion and PMD on the eye diagram and in particular on the side histograms, we will discuss in more detail

how this technique can be used to discriminate between CD and PMD. The effect of PMD and CD on the eye diagram is demonstrated in Figure 6.28(a) and Figure 6.28(c) respectively. It can be observed that unlike PMD, CD preserves a certain symmetry between the means found on the left and the right of the centre of the eye. More precisely, the ratio (S_R1- S_R4)/(S_R2- S_R3) remains approximately the same in case of dispersion and varies greatly in case of PMD.

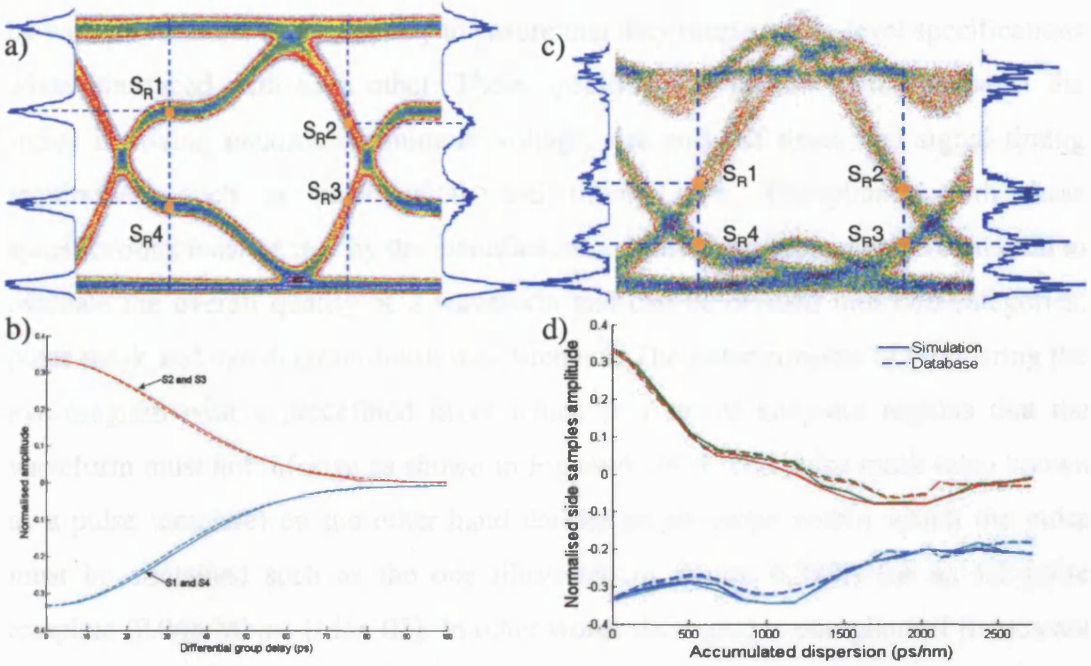

Figure 6.28 a) 10Gbit/s Eye diagram affected by PMD ($\Delta\tau$= 70ps, γ=0.7) b) Normalised amplitude of the side samples as a function of DGD for γ=0.5 c) 10Gbit/s eye diagram after 50km of SMF d) Normalised amplitude of the side samples as a function of accumulated dispersion

This ratio increases if the most of the power travels in the slow axis and decreases if the majority of this power is in the fast polarisation state. The exception is when there is equal power in the two states (i.e. γ= 0.5). In this case the above mentioned ratio remains the same. In order to differentiate between PMD and CD when γ= 0.5, we need to compare Figure 6.28 (b) with (d). The first one shows the progression of the amplitude of the side samples when the DGD is varied whereas the second figure shows how these amplitudes change with accumulated dispersion. The difference is, unlike in figure (d), the upper (S_R1 and S_R2) and lower (S_R3 and S_R4) amplitudes in figure (b) are symmetric about a certain axis. In case $S_R1 \neq S_R2$ there will be two axes representing the means of S_R1 with S_R4 and S_R2 with S_R3 respectively. Since these axes are the same for the side sample amplitude at the transmitter (S_T1-4) which are known, it is easy to verify if the signature is due to PMD or CD by calculating the

average of the pairs (S_R1, S_R4), (S_R2, S_R3) and comparing them with the average of (S_T1, S_T4) and (S_T2, S_T3).

6.6 Potential Utilisation of the Three-Point Sampling Technique

6.6.1 Inline Mask Measurement

In today's complex telecommunication networks with different components supplied by various vendors, it is necessary to ensure that they meet system-level specifications when interfaced with each other. These specifications pertain to the shape of the signal including maximum/minimum voltage, rise and fall times and signal timing requirement such as pulse width and timing jitter. Compliance with these specifications must be met by the manufacturers. Mask measurement are often used to evaluate the overall quality of a waveform and can be divided into two categories: pulse mask and eye diagram mask measurement. The latter consists of comparing the eye diagram with a predefined mask which is a set of keep-out regions that the waveform must not infringe as shown in Figure 6.29(a). The pulse mask (also known as a pulse template) on the other hand defines an envelope within which the pulse must be contained such as the one illustrated in Figure 6.29(b) for an E1 pulse template (2.048 Mbps) [Max'02]. In other words the signal is compliant if it does not exceed any of the mask boundaries.

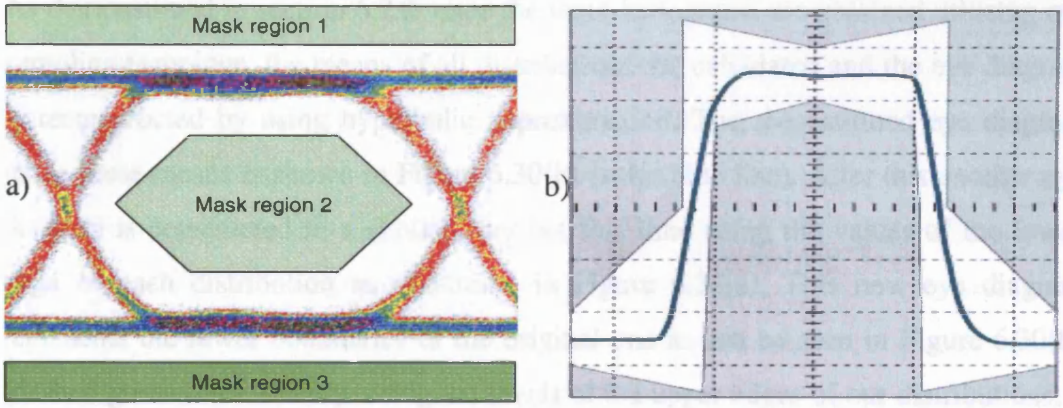

Figure 6.29 a) Concept of eye-diagram mask test b) E1 pulse template mask ([Max'02])

Eye diagrams are the most common method used to verify the overall quality of telecommunication systems. Because they consist of various bit-pattern combinations superimposed in time, impairments such as noise and excessive jitter as well as pulse parameters such as rise/fall time and overshot can be easily observed. To verify that a transmission channel complies with a certain telecommunication standard, an eye

mask test is usually performed. This is done by placing predefined polygons in and around the eye diagram. A compliant eye diagram surrounds the hexagonal centre-mask region and remains between the top and bottom regions. Eye-mask tests are carried out using oscilloscopes which also have the capability of counting the number of samples that fall outside the standard mask limit. In real networks, because of component aging and degradation, eye mask tests are performed regularly at every node which can be very costly since it involves having mobile units and may sometimes necessitate taking links out of service. Three-section eye sampling technique can be used to reconstruct the eye diagram and therefore can be utilised as a cheap, inline eye-mask test unit. This is demonstrated in Figure 6.30.

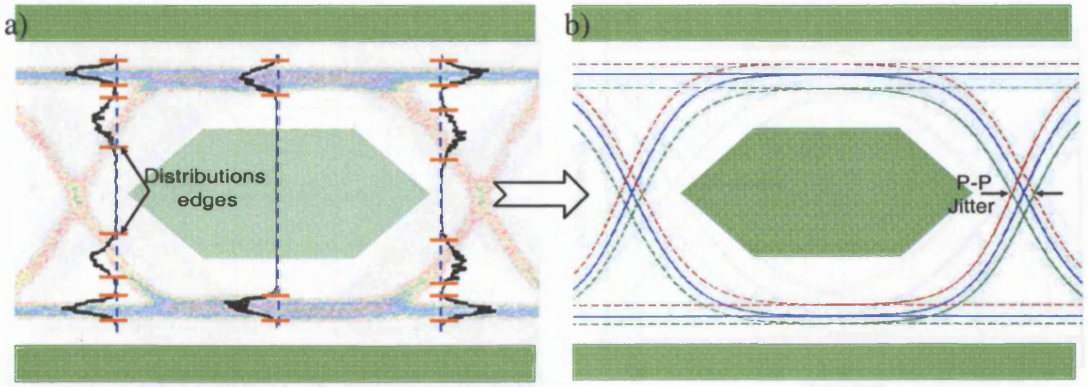

Figure 6.30 a) Eye-mask test of an experimentally obtained eye diagram. Also showing the three-section eye sampling technique b) Eye-mask test performed on the reconstituted eye diagram

As demonstrated in section 6.2.2, once the three histograms are obtained utilising our sampling technique, the means of all distributions are calculated and the eye diagram is reconstructed by using hyperbolic approximation. The reconstituted eye diagram using these means is shown in Figure 6.30(b) (solid blue line). After this another eye diagram is constructed in a similar way but this time using the values of the lower edge of each distribution as illustrated in Figure 6.30(a). This new eye diagram represents the lower boundaries of the original one as can be seen in Figure 6.30(b) (dashed green line). Finally, using the levels of the upper edges of our distributions, a third eye diagram representing the upper boundaries of the original eye can be obtained (dashed red line). Using these upper and lower boundaries, it is simple to verify that our system complies with the standards. Moreover, in case of a mask violation, the number of samples falling outside the correct region can be estimated by calculating the probability of a sample falling in the tail of the distributions crossing the mask. Furthermore, the peak-to-peak jitter can be approximated by calculating the time difference between the upper and lower boundaries at the eye crossing level as

demonstrated in Figure 6.30(b). Similarly, the temporal eye opening can also be evaluated by measuring the temporal distance of the two intersecting points between the upper and lower eye boundaries. As a proof of principle, time jitter estimation using this technique was verified by realising the following experiment. A 10Gbit/s PRBS signal was generated by means of a Mach-Zehnder modulator then transmitted over a short distance fibre. The optical signal was then passed through a clock and data recovery circuit and the eye diagram was viewed on a digital sampling oscilloscope. Time jitter was introduced by externally adding phase noise to the clock signal and the peak-to-peak jitter measured using the digital oscilloscope varied between 20.5 and 25.5ps as demonstrated in Figure 6.31(a).

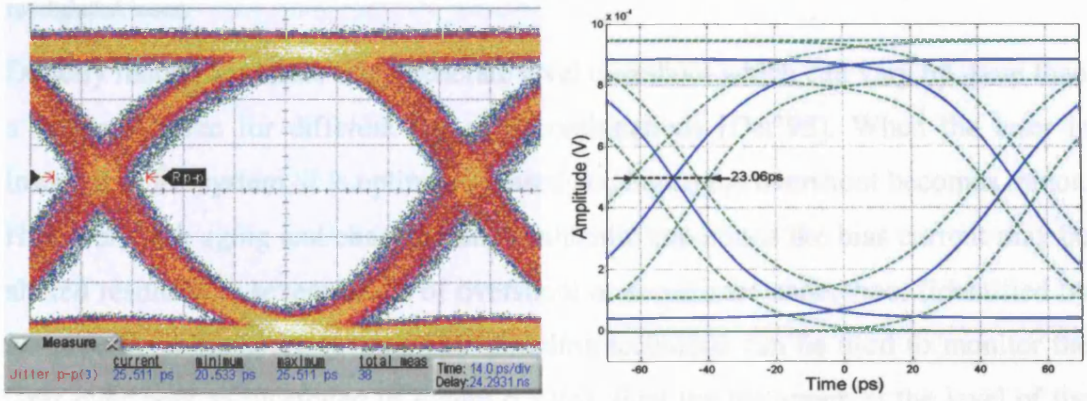

Figure 6.31 a) 10Gbit/s eye diagram exhibiting a peak-to-peak time jitter between 20.5 and 25.5ps b) The corresponding mean eye (solid) and its contour (dashed) obtained using the three section eye sampling technique. The estimated peak-to-peak jitter is 23.06ps

Three section eye sampling technique was applied to the received signal and the obtained mean-eye and its contour (upper and lower boundaries) are shown in Figure 6.31(b). The time jitter, estimated from the distance between outer boundaries at the mean-eye crossing level, is approximately 23ps. This value is in good agreement with the results obtained using the oscilloscope.

6.6.2 Inline Transmitter Monitoring

The output eye diagram from a transmitter may change over time due to aging or a change in the optimum settings without necessarily failing the standard eye-mask test. However tracking these changes may be beneficial for network operators to prevent or anticipate future degradations (pre-emptive maintenance). Two types of transmitter lasers will be considered here: directly modulated and externally modulated. Figure 6.32 shows an example of the output waveforms of commercially available

SONET/SDH transievers, one using directly modulated laser (Figure 6.32a) and other one externally modulated laser (Figure 6.32b).

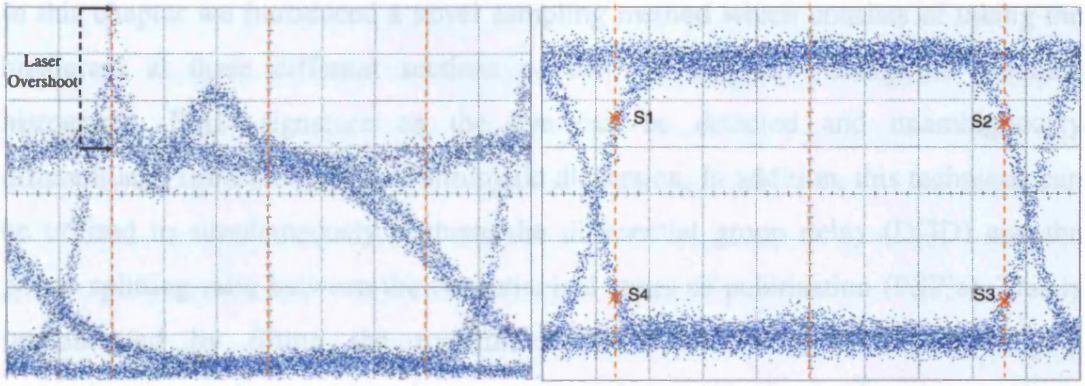

Figure 6.32 2.5Gbit/s SONET/SDH eye diagram for a) directly modulated laser b) externally modulated laser.

Directly modulated lasers often generate level overshoot which can vary by more than a factor of three for different one-zero combinations [Der'98]. When the laser is installed in the system, it is optimally biased and hence the overshoot becomes minor. However, with aging and changing environmental conditions the bias current may be altered resulting in severe levels of overshoot or sometimes undershoot (identified by an increase in the space levels). Our sampling technique can be used to monitor the laser overshoot as illustrated in Figure 6.32(a). First the histogram at the level of the overshoot is taken and stored just after installing the laser. The overshoot amplitude is calculated by comparing the voltage-peak value of this histogram with the mean of the ones taken from the other two histograms. This test can be carried out regularly and the change in the laser overshoot can be monitored over time. Similarly the three-section eye sampling technique can be used to monitor the eye diagram of an externally modulated laser. The change in the transmitter's characteristics in this case may come from an alteration in the bias of the laser resulting in a modification of the extinction ratio or the bias of the modulator leading to an alteration in the eye closure. By measuring the means of the side histograms at setup time and comparing them with the values of subsequent tests, any change in the transmitter characteristics can be detected.

6.7 Summary

In this chapter we introduced a novel sampling method which consists of taking the histogram at three different sections of the eye diagram. Using the obtained histograms, PMD signature on the eye can be detected and unambiguously differentiated from the effects of chromatic dispersion. In addition, this technique can be utilised to simultaneously evaluate the differential group delay (DGD) and the power splitting ratio between the two principal states of polarisation (PSP's). This is implemented by fitting the transmitted waveform using hyperbolic tangent approximation and comparing the output waveform with the predicted one. Using simulation and then confirmed experimentally, it was shown that a DGD of up to 100ps (one bit period) can be unambiguously estimated with a high resolution in a 10Gbit/s system. This is a relatively large range compared with the range of other PMD monitoring techniques described in the literature and reported in chapter 3 (see summary of chapter 3). It was also shown that this method can reduce the PMD-induced power penalty by up to 17.5dB (worst case) if used to control a PMD compensator. Significant power penalty reductions can also be achieved in the presence of moderate or excessive noise. Moreover, this technique also has chromatic dispersion monitoring capabilities. Not only does it detect its signature but also can accurately estimate the residual chromatic dispersion. It was demonstrated that using this approach, a large dispersion range of up to 2500ps/nm equivalent to 147km of uncompensated single mode fibre can be accurately evaluated. It was also shown that significant eye closure penalty or Q penalty reductions can be obtained if our monitoring circuit is used to control a dynamic dispersion compensator. We experimentally proved that this technique is immune to amplified spontaneous emission (ASE) noise and that it detects the combined effects of dispersion and nonlinearities which is very useful to avoid overcompensation.

Three-section eye sampling technique is relatively cheap and very fast to operate (10 ms). It also offers easy and quick inline eye mask testing and can evaluate the temporal eye opening and the peak to peak time jitter. In addition, it can be used to monitor laser overshoot of directly modulated lasers or indirectly monitor the bias current of an externally modulated transmitter by regularly measuring its rise and fall times. Furthermore, this technique gives the bit error rate (BER) of the system and is

scalable in large networks since only little information is circulated requiring very low bandwidth.

In future work, a thorough investigation on assessing the combined effects of chromatic dispersion and PMD using three-section eye sampling is required. This will still involve fitting the transmitted pulses with hyperbolic tangent functions but it will probably necessitate some kind of convolution between the lookup tables related to dispersion and PMD. The most likely method of achieving this is to reconsider the time impulse response of first order PMD and introduce the group velocity dispersion factor for both polarisation states. In other word, rewrite the first order PMD equation of the output electrical field as (see the Theory chapter):

$$\vec{E}_{out}(t) = a_+ |p_+\rangle E_{out}\left(t - \frac{\Delta\tau}{2}\right) + a_- |p_-\rangle E_{out}\left(t + \frac{\Delta\tau}{2}\right) \tag{6.27}$$

where

$$E_{out} = \Im^{-1}\left\{\tilde{E}_{in}(\omega)\exp\left(\frac{i}{2}\beta_2 L\omega^2\right)\right\} \tag{6.28}$$

$\Im^{-1}$ is the inverse Fourier transform and $\tilde{E}_{in}$ is the Fourier transform of the input electrical field E_{in}. This will create a three dimensional lookup table relating the side samples to the DGD, the power split ratio between the polarisation states and the dispersion product DL. The challenge is to find a unique correlation between the three mentioned parameters and the values of the side samples. In addition, second order PMD can also be included in the calculations by considering the time impulse response of the second order PMD. Unlike first order, second order PMD creates six replicas in each polarisation axis and their combination depends on the rotation of the principal states of polarisation with frequency and the polarisation-dependent chromatic dispersion (PCD). This latter may combine with fibre dispersion and may either increase it or compensate for a part of it. The extent to which this affects the accuracy of the three-section eye sampling technique should be examined further.

Chapter 7 Summary and conclusions

This thesis investigated advanced performance monitoring of future all-optical fibre networks using the synchronous sampling technique. Current networks are based on simple engineering rules and heavily rely on the design and the allocated margins to provide an acceptable service quality. The signal quality is verified by ensuring that different network elements are functioning properly. This is achieved by means of indirect indicators such as drive currents, power loss, over temperature and frequency drift. Recently, the assessment of optical signal-to-noise ratio (OSNR) was introduced in certain systems (Nortel Networks OPTera metro for example), but the correlation between the OSNR and the end-node signal quality is poor since it does not measure distortion. These techniques for assessing the quality of service are no longer valid in next generation transparent optical networks where added complexities such as dynamic link reconfiguration and fault localisation and management have to be addressed. Advanced optical performance monitoring (OPM) is a potential mechanism to improve quality assessment, fault management and resource allocation in these future networks. OPM can be used to verify service level agreement (SLA) between service providers and their customers classically achieved by means of opaque (protocol-dependent) techniques such as bit-interleaved parity (BIP) checking in SONET/SDH. Since OPM has the capability of detecting anomalies, it can be used to isolate the faulty part of the network and enable restoration through the unaffected redundant resources. This feature can also be used by field engineers to rapidly locate and repair the faults. Ideally, OPM techniques can be utilised as pre-emptive maintenance tools that track changes in the network parameters and anticipate major service degradation. Furthermore, they can enable novel ways of routing data such as impairment-based routing where connections are established based on the expected quality of service.

Numerous OPM techniques have been proposed in the literature and were reported in chapter 3. These were divided into two main categories: spectral methods and sampling methods. Spectral methods were further divided into optical and electrical spectrum techniques. The optical spectrum is measured by using highly sensitive optical components and can provide the OSNR and channel identification. Unfortunately, as mentioned earlier, there is not a strong correlation between the optical spectrum measurements and the end-node signal quality since it does not

measure signal distortion. Electrical spectrum monitoring, which assesses the encoded signal, is a better measure of the signal quality because it is sensitive to both noise and distortion. However, most of these techniques are dedicated to monitor only one source of impairments. Sampling methods on the other hand are sensitive to all kind of impairments and can be exploited to monitor all of them simultaneously. They are generally used to measure the Q-factor which is strongly related to the BER and thus sensitive to the same impairments as the end-node receiver. Sampling methods can generate histograms either synchronously or asynchronously. The asynchronously-generated histograms differ from the synchronous ones as they include the transitions between the marks and the spaces, making it more difficult to evaluate their average levels and the noise level around them. In this work we chose to implement advanced OPM using sampling technique because it allows accurate bit error rate (BER) assessment and degradation root cause analysis. Prior to this research no published work had shown how this method can be employed to estimate residual chromatic dispersion or the differential group delay (DGD) between the polarisation modes due to polarisation mode dispersion (PMD). Additionally we demonstrated that this approach has the capability to discriminate between the effects of dispersion and PMD on signal degradation.

Initially we started by experimentally analysing the effects of crosstalk, chromatic dispersion (CD) and polarisation mode dispersion (PMD) on the histograms. The pattern of these impairments on the histogram can potentially be utilised for root cause analysis. We demonstrated that crosstalk affects mainly the marks (ones) histograms and leads to the appearance of a plateau around the centre peak. We showed that the width of the plateau depends mainly on the relative power of the crosstalk channel and to some extent its relative bitrate compared with the crosstalk channel. CD and PMD on the other hand introduce inter-symbol interference (ISI) and it is noticeable on the histogram through the distinctive multiple levels of the marks and the spaces. It was also deduced that the two effects cannot be discriminated by sampling at the centre of the eye diagram. However, unlike CD, PMD introduces temporal asymmetry to the eye diagram which can be exploited to differentiate between the two. As a result we proposed to use a variable delay line for the clock signal and sample at the two edges of the eye, a technique we referred to as three-section eye sampling method.

The accuracy of the sampling technique to estimate the BER was then assessed in a commercially available wavelength division multiplexed (WDM) metro system transporting various protocols. The protocols used were 2.5Gbit/s Synchronous Digital Hierarchy (SONET/SDH), 1.0625Gbit/s Fibre Channel, 2.125Gbit/s Fibre Channel and 1.25Gbit/s Gigabit Ethernet. We examined the effects of amplifier (ASE) noise and in-band crosstalk in the WDM system and we showed that the sampling technique can detect the degradation in the quality of the service before reaching a critical level (BER of 10^{-12}). This characteristic can be utilised as a pre-emptive maintenance tool so that service providers can anticipate service degradation before they are noticed by the clients. Moreover, this method can accurately determine the BER and is protocol and bitrate independent. Furthermore, although the built-in digital performance monitoring techniques (BIP, CRC) can correctly detect bit errors, they cannot indicate the root cause of the malfunctioning. The sampling technique on the other hand can reveal the source of the degradation by verifying the pattern on the marks and spaces distributions. These patterns however can be composed of different patterns convolved together in the case of multiple impairments. We proposed a novel deconvolution method that can be applied to the histograms in order to evaluate the Gaussian noise without prior knowledge of the transmission path. Although limited by nonlinear effects, this method can be used to separate the contribution of distortion from the contribution of noise and hence provide advanced root cause analysis.

The three-section eye sampling technique proposed to discriminate between the effects of PMD and chromatic dispersion has a much greater potential. We demonstrated that it can also be used to accurately assess PMD and residual dispersion. Since we were using synchronous sampling, the effects of PMD on the sample time had to be first determined. Since the early 90's it was assumed the sampling time simply followed the centre of mass of the incoming pulses. However, we discovered that this was not always the case and for the first time closed form relationships between the shift in sampling time, the differential group delay (DGD) and the power splitting ratio between the principal states of polarisation were obtained for different clock recovery circuit configurations. Three types of high-Q filter based clock recoveries were considered: without pre-processing circuit, with an edge-detection circuit and a squarer pre-processing circuit. In the case of a high-Q filter

based clock recovery without a pre-processing unit, the centre of mass assumption is only valid for DGD < 35ps in 10Gbit/s systems. In the case of clock recoveries with pre-processing circuits we showed that the centre of mass assumption is only valid for DGD<25ps. The results obtained from the study of the clock recovery behaviour under the effects of PMD will allow a better determination of its effects on the signal quality such as the Q-factor, SNR and eye closure. It will also provide a more accurate evaluation of PMD in synchronous sampling-based PMD monitoring techniques as they rely on estimating the eye opening at decision times. Finally, if $\Delta\tau$ and γ are known, the obtained equations would provide feedback to enable a rapid and efficient variation in the temporal sampling point, to minimise the bit error rate.Based on the above results, we demonstrated that the three-section eye sampling technique can be utilised to simultaneously evaluate the differential group delay (DGD) and the power splitting ratio between the two principal states of polarisation (PSP's). This is carried out by fitting the transmitted waveform using hyperbolic tangent approximation and comparing the output waveform with the predicted one. Using simulation and then confirmed experimentally, it was shown that a DGD of up to 100ps (one bit period) can be unambiguously estimated with a high resolution in a 10Gbit/s system. This is a relatively large range compared with the range of other PMD monitoring techniques found in the literature. In addition, it was shown that this method can reduce the PMD-induced power penalty by up to 17.5dB (worst case) if used to control a PMD compensator. Significant power penalty reductions can also be achieved in the presence of moderate or excessive noise. Moreover, this technique also has chromatic dispersion monitoring capabilities. Not only does it detect its signature but it can also accurately estimate the residual chromatic dispersion. It was demonstrated that using this approach, a large dispersion range of up to 2500ps/nm equivalent to 147km of uncompensated single mode fibre can be accurately evaluated. It was also shown that significant eye closure penalty or Q penalty reductions can be obtained if our monitoring circuit was used to drive a dynamic dispersion compensator. We experimentally proved that this technique is immune to amplified spontaneous emission (ASE) noise and that it detects the combined effects of dispersion and nonlinearities which is very useful to avoid overcompensation. The three-section eye sampling technique is relatively cheap and very fast to operate (10 ms). It also offers easy and quick inline eye mask testing and can evaluate the temporal eye opening and the peak to peak time jitter. In addition, it can be used to

monitor laser overshoot of directly modulated lasers or indirectly monitor the bias current of an externally modulated transmitter by regularly measuring its rise and fall times. Furthermore, this technique gives the bit error rate (BER) of the system and is scalable in large networks since only little information is circulated requiring very low bandwidth.

In future work, a thorough investigation on how to assess the combined effects of chromatic dispersion and PMD using three-section eye sampling is required. This will still involve fitting the transmitted pulses with hyperbolic tangent functions but it will probably necessitate some kind of convolution between the lookup tables related to dispersion and PMD. The most likely method of achieving this is to reconsider the time impulse response of first order PMD and introduce the group velocity dispersion factor for both polarisation states. In other word, rewrite the first order PMD equation of the output electrical field as (see the Theory chapter):

$$\vec{E}_{out}(t) = a_+ |p_+\rangle E_{out}\left(t - \frac{\Delta\tau}{2}\right) + a_- |p_-\rangle E_{out}\left(t + \frac{\Delta\tau}{2}\right)$$

where

$$E_{out} = \Im^{-1}\left\{\tilde{E}_{in}(\omega)\exp\left(\frac{i}{2}\beta_2 L\omega^2\right)\right\}$$

$\Im^{-1}$ is the inverse Fourier transform and $\tilde{E}_{in}$ is the Fourier transform of the input electrical field E_{in}. This will create a three dimensional lookup table relating the side samples to the DGD, the power split ratio between the polarisation states and the chromatic dispersion-distance product DL. The challenge is to find a unique correlation between these three parameters and the values of the side samples. In addition, second order PMD can also be included in the calculations by considering the time impulse response of the second order PMD. Unlike first order, second order PMD creates six replicas in each polarisation axis and their combination depends on the rotation of the principal states of polarisation with frequency and the polarisation-dependent chromatic dispersion (PCD). This latter may combine with fibre dispersion and may either increase it or compensate for a part of it. The extent to which this affects the accuracy of the three-section eye sampling technique should be examined further.

Chapter 8 Appendices

8.1 Appendix 1: Digital Performance Monitoring

Digital methods for monitoring the end to end performance of an optical channel consist of detecting errors in block codes i.e. block of bits. Blocks are scrutinised by means of Error Detection Code (EDC), which allows the detection of erroneous *codewords* with a certain probability. Different transport protocols utilise different performance monitoring techniques in search of errors on a transmission link. These protocols can be divided into two categories: protocol dependent and protocol independent.

Synchronous optical network or synchronous digital hierarchy (SONET/SDH) are ubiquitous protocol-aware standards that provide a robust solution to carry voice and data over optical networks [Bal'89]. They include a technique to analyse errors called *bit-interleaved parity-8* (BIP-8) (see Figure 8.1) [Par'02]. The BIP bin is transmitted one frame behind the corresponding data (one frame lag) to give the receiver time to calculate its own BIP code and compare them (they should be different if an error occurred). The BIP code is found in the SONET/SDH frame header and it is referred to as B1 (section overhead), B2 (line overhead) and B3 (path overhead) bytes. It is suggested in [ITU'99] that the probability of detecting an error event is greater than 90% assuming Poisson error distribution. Using the BIP-8 technique, the following monitoring metrics have been introduced:

- Coding Violations (CVs): refer to an occurrence of BIP errors in the incoming signal.
- Errored Seconds (ES): a count of the number of seconds in which at least one CV has occurred.
- Severely Errored Seconds (SES): a count of seconds in which multiple CVs have occurred.
- Unavailable Seconds (UAS): the total number of seconds when the service is not available.

These metrics are used by service providers to set up service level agreements (SLAs) with their customers to guarantee a minimum level of service e.g. service will be guaranteed 99.99% during a year. The BER calculation is based on the number of CVs occurring within a determined period of time. However as explained in the next section, some errors can go undetected using the BIP-8 technique and therefore the BER is never truly measured in SONET/SDH.

There are growing interests in creating similar metrics and SLAs for next generation non-SONET/SDH services such as Gigabit Ethernet (GbE) and Fibre Channel (FC). These services use *cyclic redundancy coding* (CRC-32) for error monitoring and this technique is explain in subsequent sections.

Protocol independent services such as Digital Wrappers and Generic Framing Procedure (GFP) have been introduced recently to bring the technology one step closer to realising the original vision of optical transport networks (OTNs) [Bon'00]. Digital wrapper technology provides management functions described in ITU-T

recommendation G.907 (or G.872) such as performance monitoring, forward error correction (FEC), protection and network restoration on a per-wavelength basis independent of the input signal format. The error monitoring technique used in G.907 is the same as used in SONET/SDH BIP-8 except for two minor differences. Unlike SONET, the BIP bin in this case is delayed by two frames instead of one. Also in SONET the BIP is applied to the entire frame whereas in G.907 the parity is applied to only some portions of the frame. GFP on the other hand use CRC-16 for the header frame and CRC-32 for the payload frame in order to protect the integrity of the information [Her'02].

8.1.1.1.1 Bit-Interleaved Parity

Parity is a method of encoding such that the number of 1's in a frame or a stream of bits is even or odd. Figure 8.1demonstrates an example of BIP-8 encoding. The first groups of bytes (8 bits) are stacked on the top of each other and the number of 1's in every column is counted. If this number is even, a 0 is placed in the bin and if the number is odd a 1 is added to the corresponding column in the bin so that the total number of 1's in every column is even.

Sent Data: 01101000 10101110 10001101 00101001

0	1	1	0	1	0	0	0
1	0	1	0	1	1	1	0
1	0	0	0	1	1	0	1
0	0	1	0	1	0	0	1

0	1	1	0	0	0	1	0	← BIP bin

Figure 8.1 Illustration of the BIP-8

However and as illustrated in Figure 8.2, this method detects an error only if an odd number of bits is disturbed. An even number of errors within the same column will be self-compensating and go undetected. It can be seen from the figure below that the BIP bin is identical to the bin in the previous figure although the received data is different (shaded boxes).

Received Data: 11101000 10101100 10001111 10101001

1	1	1	0	1	0	0	0
1	0	1	0	1	1	0	0
1	0	0	0	1	1	1	1
1	0	1	0	1	0	0	1

0	1	1	0	0	0	1	0	← BIP bin

Figure 8.2 Limits of the BIP method; shaded boxes represent errors.

8.1.1.1.2 Cycle Redundancy Checking (CRC)

The CRC is both a powerful and easy-to-implement technique used to check data reliability in digital systems [Crc'94]. It consists of appending an extra n-bit sequence (at the transmitting node) to every frame called Frame Check Sequence (FCS). The FCS holds redundant information about the frame that helps the receiving end to detect errors in the frame. The main advantages of using this technique are: good error detection capabilities, ease of implementation and light overheads.

The algorithm treats the bit streams as binary polynomials; for instance, if the data consists of the pattern 10100011 it is translated to the polynomial $X^7 + X^5 + X + 1$. Given the original frame, the transmitter generates a FCS such that the resulting frame (original frame + FCS) is divisible by a predefined polynomial. The latter is called the CRC polynomial. For a more elaborate explanation consider the following definitions:

- We call 'M' the original frame to be transmitted. M has a length of *k* bits.
- 'F' is the FCS of length *n* to be added to M.
- 'T' is the concatenated frame that consists of M and F and thus it has a length of k + n bits.
- 'P' is n+1bits long and represents the predefined CRC polynomial.

First, the frame M is shifted n-bits to the left or, in polynomial terms, M is multiplied by X^n. After this, the product $M*X^n$ is divided by the CRC polynomial P and the remainder is the frame check sequence F that will be appended to the raw data. The final frame T that will be transmitted can be written as:

$$T = M * X^n + F \qquad \text{(A1.1)}$$

Finally, when the frame arrives at the receiver it will be divided by the CRC polynomial (i.e. P) and if the remainder is not zero then the frame is corrupted. The algorithm can either be implemented in hardware or software.

8.1.1.1.3 Bit Error Rate (BER) and Forward Error Correction (FEC)

Any method that can correct errors at the receiver without the need for a retransmission of the frame is referred to as *forward error correction* (FEC). Many algorithms have been proposed and the most popular ones are summarised in table 8.1 [Rod'95]. The bit stream at the source is partitioned into binary words and extra bits are added to every word in order to perform forward error correction. This operation is known as *block encoding*. The binary words, before going through the block encoder are referred to as *datawords* and after being encoded are called *codewords*. Each dataword contains k bits and each codeword contains n bits so that the total number of added bits (for error correction) is n-k. The symbol *t* in the table denotes the number of errors that can be corrected in a codeword.

Code Name	n	k	t	Notes
Hamming	2^m-1	n-*m*	1	m is an integer
Golay	23	12	3	
Bose-Chaudhuri-Hocquenghem (BCH)	2^m-1	≥ n- *mt*	t	Multiple error correction
Reed-Solomon (RS)	2^m-1	n- 2t	t	Designed to cope with burst errors

Table 8.1. Examples of block codes. After ref [Rod'95]

Currently there are two FEC standards; "in-band" FEC is used in SONET/SDH protocol, where the extra bits are inserted inside available overhead bytes. Because of the limited number of available bytes (only three bytes for end-to-end path function) [Gro'90], the code chosen was a 3-bit-error-correcting BCH code [Kam'02]. Out-of-band FEC is used in submarine systems and digital wrappers and it adds an additional ~7% bandwidth overhead. The code is based on Reed-Solomon(255,239), which can correct up to t=8 random symbol errors. In addition, the code has a coding gain of approximately 5.5 dB at a BER of 10^{-12} (see Figure 8.3) and can correct bursts of length up to 64 bits.

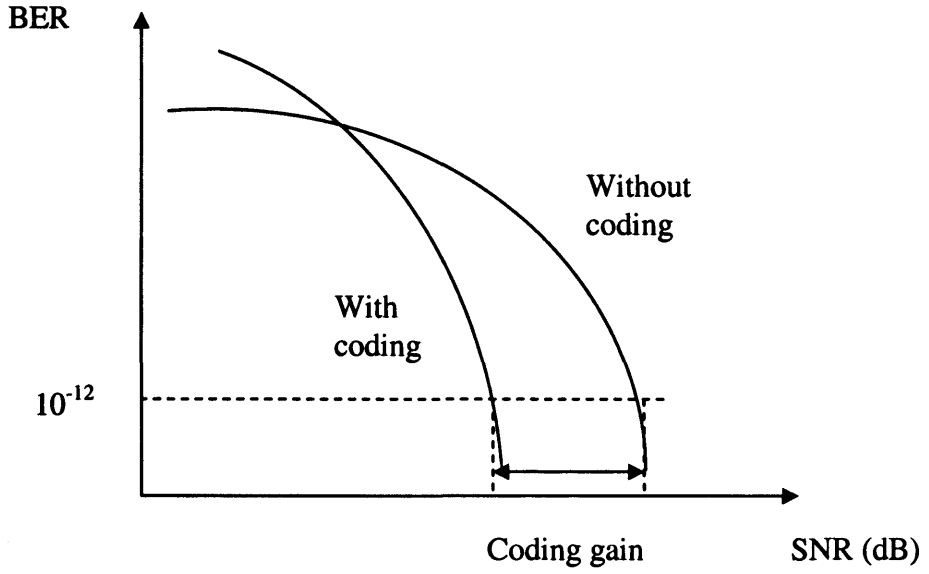

Figure 8.3 The coding gain

The bit error rate after coding, which will be referred to as BER_C, is different from the BER of the transmission channel and does not affect it in any way. The BER of the transmission channel is determined by the signal to noise ratio (SNR) while the BER_C depends on the capability of error detection and correction of a given block code. In fact, coding makes the probability of bit error worse assuming the same transmission rate.

Suppose the probability of coded bit error is P_e, then the probability of i errors occurring in a n-bit codeword is:

$$P_i = P_e^i (1- P_e)^{n-i} \tag{A1.2}$$

Usually $P_e \ll 1$ and hence $P_i \cong P_e^i$. The number of combinations of i errors in a n-bit codeword is:

$$C_{i,n} = \frac{n!}{i!(n-i)!} \tag{A1.3}$$

Therefore the probability of receiving a codeword with i errors is:

$$P_{i,n} = C_{i,n} P_i \tag{A1.4}$$

Sometimes it is necessary to know the probability of a codeword containing at least i errors. This will be denoted as P_{we} and given as:

$$P_{we} = P_{i,n} + P_{i+1,n} + P_{i+2,n} + \ldots\ldots + P_{n,n} \qquad \text{(A1.5)}$$

Since $P_e \ll 1$, the probability of getting more than i errors is negligible compared to the probability of getting i errors and thus P_{we} could be approximated to $P_{i,n}$. Now suppose that FEC code can correct or detect errors up to a maximum number of t-bits. The probability of receiving a codeword with at least $i = t + 1$ errors is the same as the probability of receiving i errors and is given by

$$P_{we} = \frac{n!}{i!(n-i)!} P_e^i \qquad \text{(A1.5)}$$

Usually a transmission contains W number of words and the number of erroneous words that can go undetected is $W_E = W\ P_{we}$. Since there are i error bits in every undetected word, the total number of corrupted bits in the transmission is iWP_{we}. Assuming a uniform distribution of errors among the n codeword bits, the fraction of errors expected in the k data bits is $r = k/n$ (r is also called the code rate). Hence the average number of data bits in error is $irWP_{we}$. The BER based on the relative frequency definition is the ratio between the average number of erroneous data bits and the total number of data bits (kW) and is given as:

$$BER_C = \frac{irWP_{we}}{kW} = \frac{(n-1)!}{t!(n-1-t)!} P_e^{t+1} \qquad \text{(A1.6)}$$

Without coding the bit error rate (BER) is equal to P_e.

8.2 Appendix 2: PMD Effects on Clock Recovery Modules without Pre-processing Circuits

In this section the behaviour of high-Q filter clock recovery is studied under the influence of first order PMD. An analytical equation describing the shift of decision point with respect to differential group delay (DGD) and the principal states of polarisation (PSP's) is defined for clock circuit without a pre-processing unit.

First order PMD can be represented by a differential group delay time $\Delta\tau$ between orthogonally polarised components of the input power waveform $P_{in}(t)$[1]. Both the DGD and PSP are random and depend on the birefringence details along the entire fibre. The output waveform can be written as:

$$P_{out} = \gamma P_{in}\left(t+\frac{\Delta\tau}{2}\right)+(1-\gamma)P_{in}\left(t-\frac{\Delta\tau}{2}\right) \qquad \text{(A2.1)}$$

where $0< \gamma <1$ reflects the relative power launched in the two principal states. In the absence of PMD P_{in} and P_{out} are the same. Using a high Q filter clock recovery, the clock signal of P_{in} can be defined as:

$$clk_1(t) = \Im^{-1}\left(P(\omega).H(\omega)\right) \qquad \text{(A2.2)}$$

where P(ω) represents the Fourier transform of P_{in} and H(w) is the filter's transfer function. In the presence of PMD the clock signal of P_{out} becomes:

$$clk_2(t) = \Im^{-1}\left\{\left[\gamma e^{-i\omega\Delta\tau/2}+(1-\gamma)e^{i\omega\Delta\tau/2}\right]P(\omega)H(\omega)\right\} \qquad \text{(A2.3)}$$

Using equation A2.2 the above equation can be rewritten as:

$$clk_2(t) = \gamma clk_1(t+\Delta\tau/2)+(1-\gamma)clk_1(t-\Delta\tau/2) \qquad \text{(A2.4)}$$

Thus the clock in the presence of PMD is the sum of the clock signals of the two principal states of polarisation.

First assuming the clock function for P_{in} is a sinusoidal function, then it can be written as $clk_1(t) = \cos(\omega t+\theta)$. Substituting in equation A2.4 gives

$$clk_2 = \gamma\cos\left[\omega\left(t+\frac{\Delta\tau}{2}\right)+\theta\right]+(1-\gamma)\cos\left[\omega\left(t-\frac{\Delta\tau}{2}\right)+\theta\right] \qquad \text{(A2.5)}$$

Using trigonometric properties, the above equation can be simplified to

[1] C. D. Poole et al "Phenomenological approach to polarisation dispersion" Electronic Letters, Vol.22 pp. 1029-1030, 1986.

$$clk_2 = \cos(\omega t + \theta)\cos\left(\frac{\omega\Delta\tau}{2}\right) + (2\gamma - 1)\sin(\omega t + \theta)\sin\left(\frac{\omega\Delta\tau}{2}\right) \quad \text{(A2.6)}$$

Putting the first derivative of clk_2 (wrt t) equal to zero to find how the peaks change with DGD:

$$(2\gamma - 1)\sin\left(\frac{\omega\Delta\tau}{2}\right)\cos(\omega t + \theta) = \cos\left(\frac{\omega\Delta\tau}{2}\right)\sin(\omega t + \theta) \quad \text{(A2.7)}$$

$$\tan(\omega t + \theta) = (2\gamma - 1)\tan\left(\frac{\omega\Delta\tau}{2}\right) \quad \text{(A2.8)}$$

Assuming $\theta=0$, this becomes:

$$t = \frac{1}{\omega}\tan^{-1}\left[(2\gamma - 1)\tan\left(\frac{\omega\Delta\tau}{2}\right)\right] \quad \text{(A2.9)}$$

Or in ps (f_c in GHz)

$$t(ps) = \frac{10^3}{2\pi f_c}\tan^{-1}\left[(2\gamma - 1)\tan\left(\frac{\pi f_c\Delta\tau}{10^3}\right)\right] \quad \text{(A2.10)}$$

The following section is a complementary section that shows that the above equation is still valid even if the clock signal is not truly sinusoidal. We now assume the clock signal is a cycloid which is defined by:

$$\begin{cases} x = t - \sin(\omega t) \\ y = 1 - \cos(\omega t) \end{cases} \quad \text{(A2.11)}$$

where x is the new time axis and y is the amplitude. The figure below compares the cycloid given in equation A2.11 (solid line) with a sinusoidal (1-cos(ωt)).

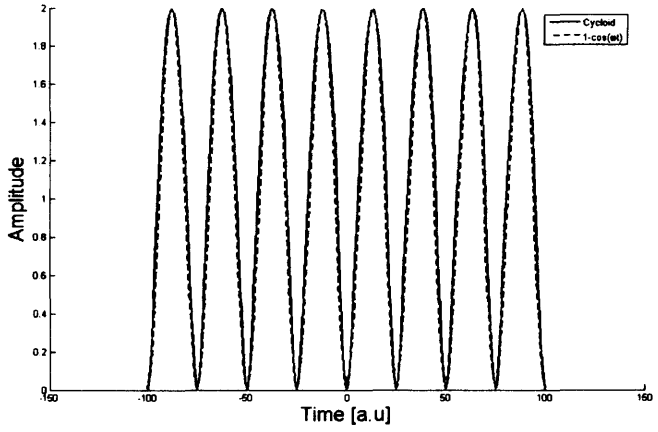

Figure 8.4 Comparison between a cycloid and a sinusoidal signal

In the presence of PMD the clock of the first axis would be

$$\begin{cases} x_1 = t - \Delta\tau/2 - \sin(\omega(t - \Delta\tau/2)) \\ y_1 = \gamma[1 - \cos(\omega(t - \Delta\tau/2))] \end{cases} \quad \text{(A2.12)}$$

while the second axis is:

$$\begin{cases} x_2 = t + \Delta\tau/2 - \sin(\omega(t + \Delta\tau/2)) \\ y_2 = (1-\gamma)[1 - \cos(\omega(t + \Delta\tau/2))] \end{cases} \quad \text{(A2.13)}$$

Also clk_2 is defined as:

$$\begin{cases} x = \frac{1}{2}(x_1 + x_2) \\ y = y_1 + y_2 \end{cases} \quad \text{(A2.14)}$$

Thus

$$\begin{cases} x = t - \cos(\omega\Delta\tau/2)\sin(\omega t) \\ y = 1 + (1-2\gamma)\sin(\omega\Delta\tau/2)\sin(\omega t) - \cos(\omega\Delta\tau/2)\cos(\omega t) \end{cases} \quad \text{(A2.15)}$$

Differentiating the above equation with respect to time we get

$$\begin{cases} \frac{dx}{dt} = 1 - \cos(\omega\Delta\tau/2)\cos(\omega t) \\ \frac{dy}{dt} = (1-2\gamma)\sin(\omega\Delta\tau/2)\cos(\omega t) + \cos(\omega\Delta\tau/2)\sin(\omega t) \end{cases} \quad \text{(A2.16)}$$

Putting $\frac{dy}{dx} = 0$ gives:

$$\tan(\omega t) = (2\gamma - 1)\tan\left(\frac{\omega\Delta\tau}{2}\right) \quad \text{(A2.17)}$$

Thus

$$t = \frac{1}{\omega}\tan^{-1}\left[(2\gamma - 1)\tan\left(\frac{\omega\Delta\tau}{2}\right)\right] \quad \text{(A2.18)}$$

Or

$$t = \frac{1}{2\pi f_c}\tan^{-1}[(2\gamma - 1)\tan(\pi f_c\Delta\tau)] \quad \text{(A2.19)}$$

8.3 Appendix 3: PMD Effects on Clock Recovery Modules with Squarer Pre-processing Circuits

In this appendix the behaviour of a high-Q filter based clock recovery using a squarer, as a pre-processor circuit, to double the frequency of the signal is studied under the influence of first order PMD. An analytical equation describing the shift of decision point with respect to differential group delay (DGD) and the principal states of polarisation (PSP's) is defined. We will start by rewriting the PMD equation using the principal state model. In the presence of PMD, the received signal can be expressed as:

$$f_{PMD}(t) = \gamma f\left(t+\frac{\Delta\tau}{2}\right)+(1-\gamma)f\left(t-\frac{\Delta\tau}{2}\right) \tag{A3.1}$$

The schematic diagram, showing how the clock signal using a squarer is obtained, is repeated in Figure 1 for convenience.

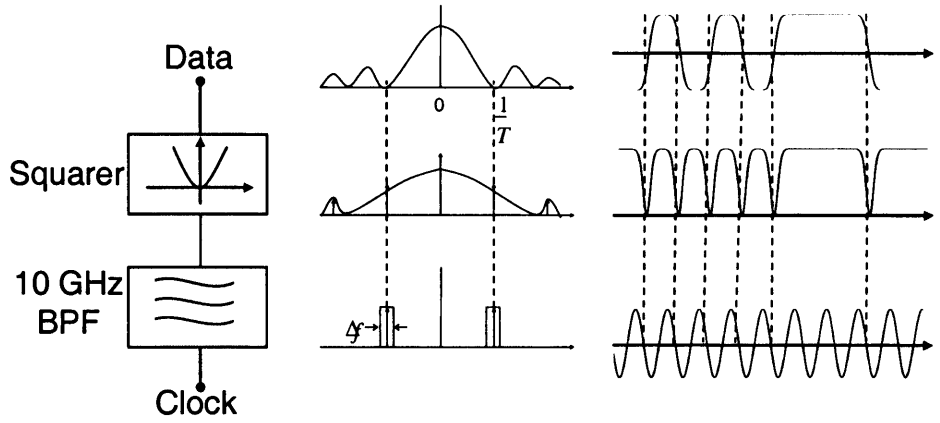

Figure 8.5 Clock recovery configuration

The clock of the signal in the absence of PMD can be written as:

$clk = f^2(t) * h(t)$

where h(t) is the transfer function of the filter. In the frequency domain, the same equation can be expressed as:

$$CLK(\omega) = F(\omega).H(\omega) \tag{A3.2}$$

where $F(\omega) = \Im\{f(t)^2\}$ and CLK(ω) is the transform of clk(t). For simplicity and convenience, we will introduce the following notation:

$$f_+ = f\left(t+\frac{\Delta\tau}{2}\right) \tag{A3.3}$$

$$f_- = f\left(t - \frac{\Delta\tau}{2}\right) \tag{A3.4}$$

$$\gamma' = 1 - \gamma \tag{A3.5}$$

Therefore, in the presence of PMD, the PMD equation becomes:

$$f_{PMD}(t) = \gamma f_+ + \gamma' f_- \tag{A3.6}$$

Equation A3.2 can then be rewritten as:

$$CLK(\omega) = \Im\{\gamma^2 f_+^2 + \gamma'^2 f_-^2 + 2\gamma\gamma' f_+ f_-\} H(\omega) \tag{A3.7}$$

Using the distributive properties of the Fourier transform, the clock in the time domain becomes:

$$clk = \gamma^2 (f_+^2 * h(t)) + \gamma'^2 (f_-^2 * h(t)) + 2\gamma\gamma' (f_+ f_- * h(t)) \tag{A3.8}$$

It is known in Fourier transform theory that a time domain shift leads to a multiplication with an exponential in the frequency domain. For instance, considering the first term in equation A3.8

$$\Im(f_+^2 * h(t)) = F(\omega).\exp(i\omega\Delta\tau/2).H(\omega) \tag{A3.9}$$

Using the commutative property of multiplication and equation A3.2

$$\Im(f_+^2 * h(t)) = [F(\omega).H(\omega)]\exp(i\omega\Delta\tau/2) = CLK(\omega)\exp(i\omega\Delta\tau/2) \tag{A3.10}$$

Finally, using the previous notation:

$$f_+^2 * h(t) = clk\left(t + \frac{\Delta\tau}{2}\right) = clk_+ \tag{A3.11}$$

Similarly equation A3.8 can be written as:

$$clk = \gamma^2 clk_+ + \gamma'^2\, clk_- + 2\gamma\gamma' (f_+ f_- * h(t)) \tag{A3.12}$$

The first and second terms of this equation represent the clock without the effect of PMD shifted by $\pm\Delta\tau/2$ and having different weights. The third term in the equation gives a clock that is in phase with PMD-free clock signal but its amplitude depends on both $\Delta\tau$ and the bit sequence of f(t). This pattern dependent amplitude gives rise to a pattern dependent phase of clk in the above equation since we are summing three sinusoidal waveforms and the final product depends on both their relative phases and their amplitudes. Thus it can be written as:

$$clk = \gamma^2 clk_+ + \gamma'^2\, clk_- + 2\gamma\gamma' clk.P(\Delta\tau) \tag{A3.13}$$

where $P(\Delta\tau)$ is the patterning term. We will study this effect after we define the PMD-induced time shift. Equation A3.13 can be expressed as:

$$clk = \gamma^2 \cos\left(\omega\left(t-\frac{\tau}{2}\right)\right) + \gamma'^2 \cos\left(\omega\left(t+\frac{\tau}{2}\right)\right) + 2\gamma\gamma' P(\tau)\cos(\omega t) \quad \text{(A3.14)}$$

Using trigonometric identities, the clock expression can be simplified to:

$$clk = \left[(\gamma^2+\gamma'^2)\cos\left(\omega\frac{\tau}{2}\right) + 2\gamma\gamma' P(\tau)\right]\cos(\omega t) + (\gamma^2-\gamma'^2)\sin\left(\omega\frac{\tau}{2}\right)\sin(\omega t) \quad \text{(A3.15)}$$

Equation A3.15 defines the envelope of the clock. In order to find the rate of change of t as a function of $\Delta\tau$, we need to differentiate the clock wrt to t. Clk'=0 gives:

$$\left[(\gamma^2+\gamma'^2)\cos\left(\omega\frac{\tau}{2}\right) + 2\gamma\gamma' P(\tau)\right]\sin(\omega t) = (\gamma^2-\gamma'^2)\sin\left(\omega\frac{\tau}{2}\right)\cos(\omega t) \quad \text{(A3.16)}$$

Rearranging,

$$t = \frac{1}{\omega}\tan^{-1}\left[\frac{(2\gamma-1)\sin\left(\omega\frac{\tau}{2}\right)}{(\gamma^2+\gamma'^2)\cos\left(\omega\frac{\tau}{2}\right) + 2\gamma\gamma' P(\tau)}\right] \quad \text{(A3.17)}$$

Considering that $\omega = 2\pi f_c$, the above equation yields to:

$$t = \frac{1}{2\pi f_c}\tan^{-1}\left[\frac{(2\gamma-1)\sin(\pi f_c \Delta\tau)}{(\gamma^2+(1-\gamma)^2)\cos(\pi f_c \Delta\tau) + 2\gamma(1-\gamma)P(\tau)}\right] \quad \text{(A3.18)}$$

Equation A3.18 represents the PMD-induced time shift as a function of $\Delta\tau$ and γ. The patterning effect is studied next.

To describe the impact of patterning on the phase shift of the clock recovery for a DGD of up to 200ps, it is sufficient to consider a pattern combination of 3 bits (i.e. 2^3=8). These combinations can be divided into 3 groups; the first is when there are three similar consecutive bits and these are 000 and 111. The second group is where there is an isolated 1 or 0 such as in 010 and 101. The third group is where there is an occurrence of two similar consecutive bits. The spectra of some selected patterns are shown in the figure below.

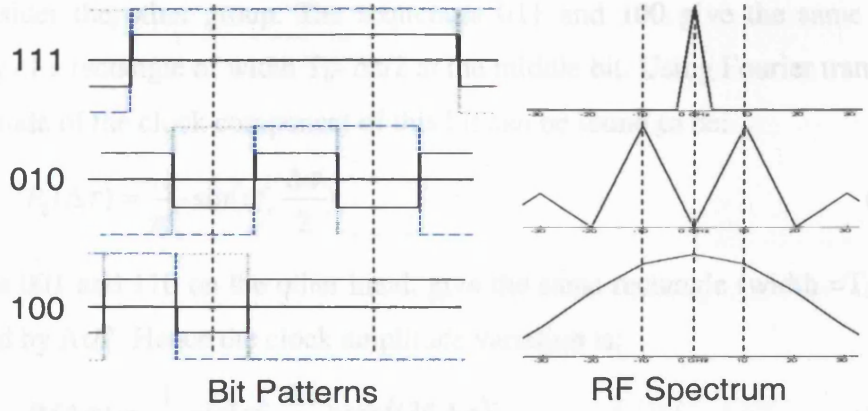

Figure 8.6 Patterning and spectrum of bit sequences 111, 010 and 100

The first group can be considered as a dc offset that has no effects on the clock spectral frequency and hence can be disregarded. As can be observed from the above graph, the second and third group have spectral frequencies at 10GHz and thus they contribute to the patterning effect. Assuming they all have equal probability of occurring, the patterning contribution to the clock phase-shift can be written as:

$$P(\Delta\tau) = \frac{1}{6}\sum_{i=1}^{6}\frac{\{f_i(t+\Delta\tau/2).f_i(t-\Delta\tau/2)\}*h(t)}{f_i^{\,2}(t)*h(t)} \qquad \text{(A3.19)}$$

where h(t) is the filter transfer function and $f_i(t)$ is a three bit pattern (excluding 000 and 111). The sequences 010 and 101 give the same pattern consisting of a rectangle of width T_b- $\Delta\tau$ at the middle bit as illustrated in the figure above (T_b is the bit period). Using Fourier transforms, the amplitude of the clock component of this bit is:

$$P_1(\Delta\tau) = \frac{1}{\pi f_c}\sin(\pi f_c \Delta\tau) \qquad \text{(A3.20)}$$

This was verified by comparing it to the amplitude variation of a simulated 010 sequence and the good agreement between the two is shown in Figure 8.7a.

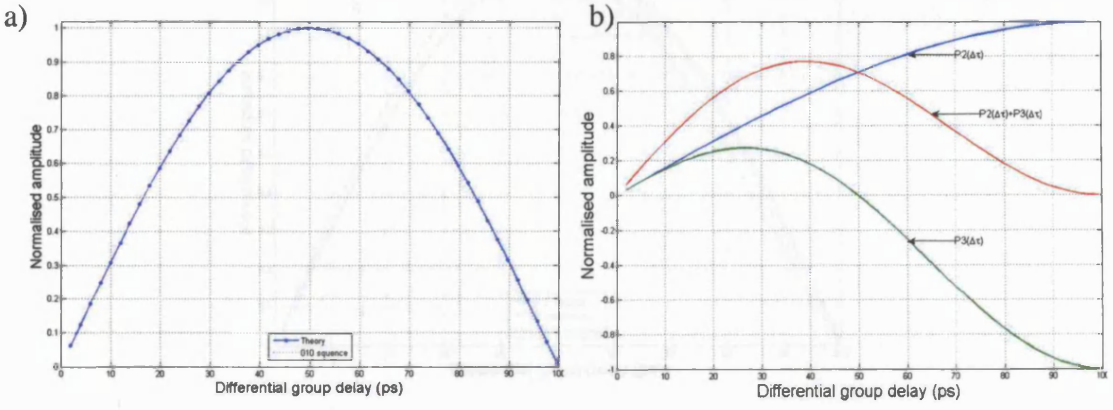

Figure 8.7 Square pulse patterning for a) group 2 sequences b) group 3 sequences

Now consider the other group. The sequences 011 and 100 give the same pattern consisting of a rectangle of width T_b- $\Delta\tau/2$ at the middle bit. Using Fourier transforms, the amplitude of the clock component of this bit can be found to be:

$$P_2(\Delta\tau) = \frac{1}{\pi f_c}\sin(\pi f_c \frac{\Delta\tau}{2}) \tag{A3.21}$$

Sequences 001 and 110 on the other hand, give the same rectangle (width =T_b- $\Delta\tau/2$) but shifted by $\Delta\tau/2$. Hence the clock amplitude variation is:

$$P_3(\Delta\tau) = \frac{1}{\pi f_c}\sin(\pi f_c \frac{\Delta\tau}{2})\exp(i\lambda f_c \Delta\tau) \tag{A3.22}$$

Rewriting equation A3.19 for rectangular waveforms:

$$P(\Delta\tau) = \frac{1}{6}\left(2P_1(\Delta\tau) + 2P_2(\Delta\tau) + 2P_3(\Delta\tau)\right) \tag{A3.23}$$

Equation A3.21 and A3.22 adds up in a destructive manner when $\Delta\tau$ >50ps (see Figure 8.7b) and therefore the effect of the sequences in the third group will cancel each other out. In addition their amplitudes, compared with equation A3.20, for $\Delta\tau$ <50ps are relatively small. This leads us to conclude that in general the sequences 101 and 010 have the most dominant effect. As a result, equation A3.19 can be approximated to:

$$P(\Delta\tau) \approx \frac{\left\{f_{010}(t+\Delta\tau/2).f_{010}(t-\Delta\tau/2)\right\} * h(t)}{f_{010}{}^2(t) * h(t)} \tag{A3.24}$$

A comparison between the theoretical P($\Delta\tau$) expressed in equation A3.23, the patterning of a 010 sequence and a randomly generated 2^{11} PRBS is shown in the figure below.

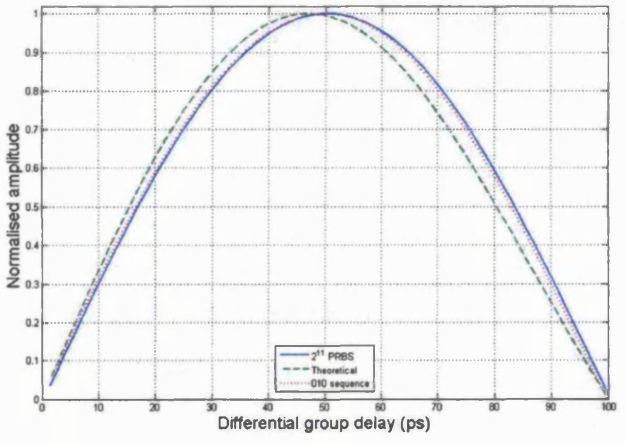

Figure 8.8 Comparison between the average theoretical patterning and the patterning of a 010 sequence and a 2^{11} PRBS

It can be observed that there is a slight difference between the theory and the patterning due to the generated PRBS. This is probably because the randomly generated sequence had more 010/101 sequences than the rest. However, there is a good agreement between the 010 sequence and the PRBS.

Finally, it is well known that PMD leads to fading in the power of the clock spectrum. This can be seen in the equation below obtained by normalising equation A3.13 by the factor $F(\omega).H(\omega)$.

$$CLK(\omega) = [\gamma^2 \exp(i\omega\Delta\tau/2) + (1-\gamma)^2 \exp(-i\omega\Delta\tau/2)] + 2\gamma(1-\gamma)P(\Delta\tau) \quad \text{(A3.25)}$$

If patterning is ignored and $\gamma = 0.5$, the above equation becomes proportional to $\cos(\omega\Delta\tau/2)$. This is illustrated in the figure below.

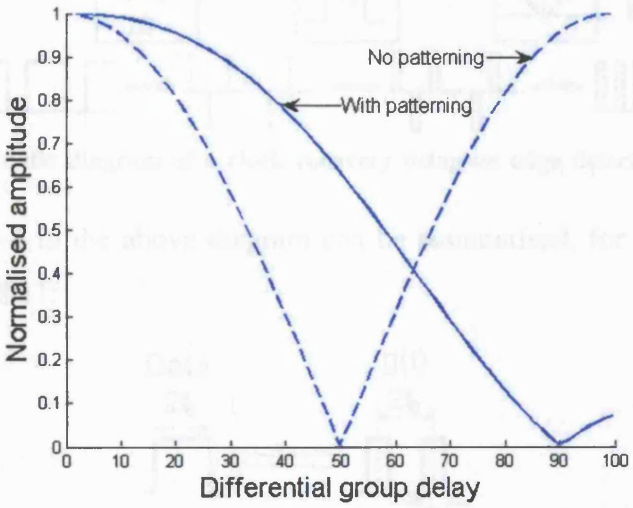

Figure 8.9 Comparison between the clock fading with and without patterning for $\gamma = 0.5$

8.4 Appendix 4: PMD Effects on Clock Recovery Modules with Edge Detection Pre-processing Circuits

In this section the behaviour of high Q filter clock recovery is studied under the influence of first order PMD. An analytical equation for the PMD-induced time shift on the clock recovery, with respect to differential group delay (DGD) and the principal states of polarisation (PSP's), is obtained. The clock recovery under study is based on edge detection and a high-Q filter. This can be implemented using the circuit shown below or by simply using an XOR gate followed by the high-Q filter.

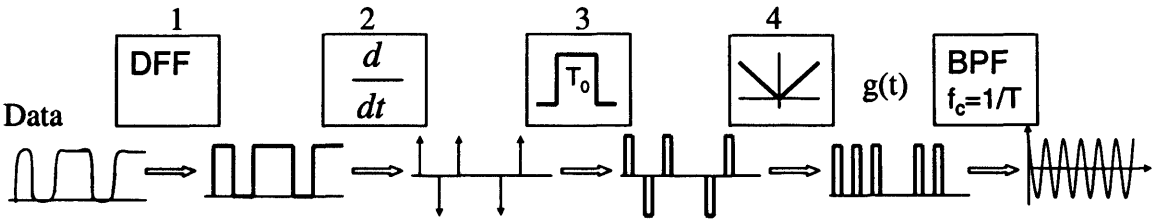

Figure 8.10 Schematic diagram of a clock recovery using an edge detector as a pre-processing circuit

Stages from 1 to 4 in the above diagram can be summarised, for a 010 sequence as shown in Figure 8.11:

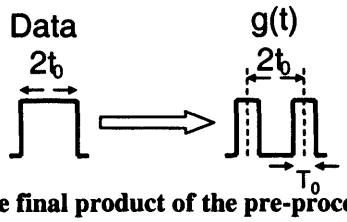

Figure 8.11 The final product of the pre-processing circuit

The bit period is equivalent to $2t_0$. The function g(t) in the above graph can be represented, for a single pulse, as a convolution between two delta functions and a rectangle. This is illustrated in Figure 8.12:

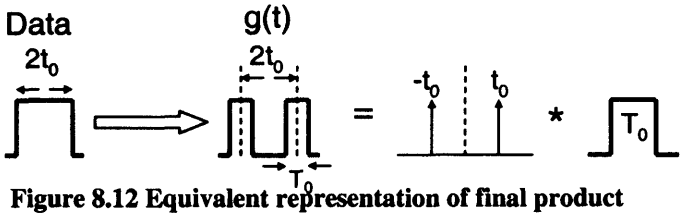

Figure 8.12 Equivalent representation of final product

The function g(t) can be therefore be written as:

$$g(t) = \left(\delta(t - t_0) + \delta(t + t_0)\right) * \mathrm{Re}ct(T_0) \qquad \text{(A4.1)}$$

where T_0 is the width of the rectangle Rect. Now using Fourier transforms, this equation can be expressed in the frequency domain as:

$$G(\omega) = 4T_0 \cos(t_0\omega).\sin c(T_0\omega/2) \quad \text{(A4.2)}$$

The D-type flip-flop (or XOR gate) at stage 1 in Figure 8.10 reshapes the input signal so that the output pulses are rectangular of a width equal to the FWHM of the original pulses. In the presence of PMD, the FWHM of the input pulses changes according to their shape and the two parameters γ and $\Delta\tau$. The FWHM in the presence of PMD can be represented by the function $W(\Delta\tau, \gamma)$. In addition, there is a certain time shift between the output pulse (from the D-FF) without PMD and in the presence of PMD that also depends on the above parameters. This time shift of the centre of the pulse is shown in the figure below will be named $S(\Delta\tau, \gamma)$.

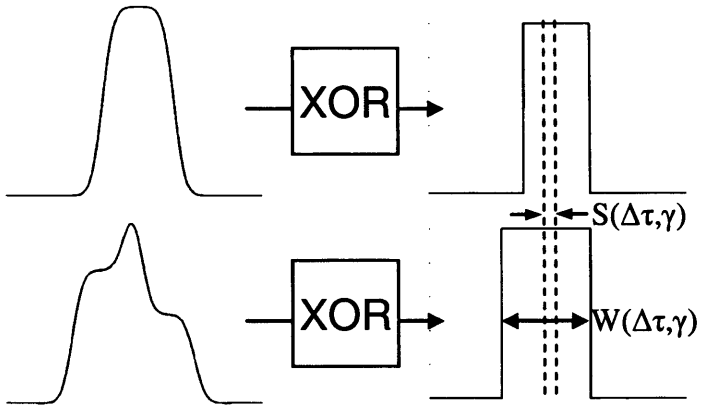

Figure 8.13 The effects of the reshaping process on the output waveform

In the presence of PMD, equation A4.2 becomes:

$$G(\omega) = 4T_0 \cos(W(\Delta\tau,\gamma)\omega/2).\sin c(T_0\omega/2).\exp(jS(\Delta\tau,\gamma)\omega) \quad \text{(A4.3)}$$

where the exponential term represents the time shift defined by S. At $\Delta\tau$=0 this equation is governed by:

$$G_0(\omega) = 4T_0 \cos(T_b\omega/2)\sin c(T_0\omega/2) \quad \text{(A4.4)}$$

where T_b is the bit period. However $\cos(T_b\omega/2)$ = -1, and hence the above equation becomes:

$$G_0(\omega) = -4T_0 \sin c(T_0\omega/2) \quad \text{(A4.5)}$$

Considering equation A4.4, equation A4.3 can be rewritten as:

$$G(\omega) = -G_0(\omega)\cos(W(\Delta\tau,\gamma)\omega/2)\exp(jS(\Delta\tau,\gamma)\omega) \quad \text{(A4.6)}$$

The second and third terms on the right hand side in the above equation lead to a change in the amplitude of the clock spectrum. To see how they translate into a shift in the time domain, one can write A4.6 as:

$$G(\omega) = G_0(\omega)\exp(j\omega t_s) \tag{A4.7}$$

where ts is the time shift due to PMD. Therefore, by comparing A4.6 and A4.7 we can conclude that:

$$\exp(j\omega t_s) = -\cos(W(\Delta\tau,\gamma)\omega/2)\exp(jS(\Delta\tau,\gamma)\omega) \tag{A4.8}$$

Finally t_s can be deduced as:

$$t_s = \frac{1}{j\omega}\ln(-\cos(W(\Delta\tau,\gamma)\omega/2)\exp(jS(\Delta\tau,\gamma)\omega)) \tag{A4.9}$$

Since the above equation contains complex components, the time shift is then given by:

$$t_s = \text{Real}\left[\frac{1}{j\omega}\ln(-\cos(W(\Delta\tau,\gamma)\omega/2)\exp(jS(\Delta\tau,\gamma)\omega))\right] \tag{A4.10}$$

This type of clock recovery is dependent on a certain patterning. Unlike the squarer-based clock, this one does not depend on the different combinations of bits but on the shape of the transmitted signal. As was shown in Figure 8.11, any three-bit combination would produce two rectangles of width T_0 which are $W(\Delta\tau, \gamma)$ (or a multiple of it) apart from each other. Hence the patterning comes from the two function W and S which are solely dependent on the shape of the pulse. To comprehend how this shape-dependent patterning works, let's consider two 10GHz pulses: a rectangular and an arbitrary-shaped pulse with a 32ps rise time. These are shown in the inset of the figure below.

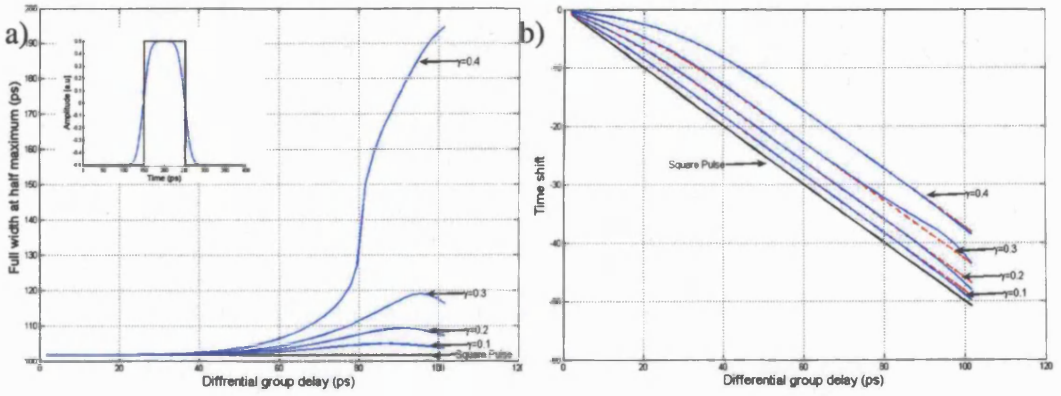

Figure 8.14 a) Change in the FWHM of the pulse at the output of the DFF due to PMD (b) Time shift of the output pulse

Figure 8.14a shows W($\Delta\tau$,γ), the change in the FWHM at the output of the DFF, for different values of γ as $\Delta\tau$ is increased. It can be seen that while the width of the rectangular pulse does not change, the width of the second waveform increases with increasing γ and $\Delta\tau$. Figure 8.14b shows the function S($\Delta\tau$,γ) for the same waveforms. As expected with the rectangular shape, the time shift follows the polarisation state which has the higher power and moves by an amount of $\Delta\tau/2$ for any γ. The second pulse on the other hand shifts by an amount which depends on both γ and $\Delta\tau$ (solid lines). To quantify this value, we need to approximate the shape of any pulse to a shape we know. We will assume here that the rising edge of our arbitrary pulse is a hyperbolic tangent and hence can be written as:

$$f(t) = \tanh(at) \tag{A4.11}$$

where a is the slope. In order to make our calculations simpler and without loss of generality, the 10-90% rise time can be assumed to be T_b/π. This is equivalent to 31.8ps in a 10Gbit/s system. The slope 'a' in this case is approximately equal to $2\pi/T_b = \omega$. In the presence of PMD, equation A4.11 becomes:

$$f(t) = \gamma \tanh(\omega(t + \Delta\tau/2)) + (1-\gamma)\tanh(\omega(t - \Delta\tau/2)) \tag{A4.12}$$

S($\Delta\tau$,γ) is simply the solution to the above equation. Equation A4.12 was solved using MatLab and the full expression is given at the end of this appendix (because it is cumbersome). This will be referred to as equation A4.13. S($\Delta\tau$,γ) obtained using the tanh approximation is plotted in Figure 8.14b (dashed lines) and the close match with the arbitrary pulse (solid lines) can be observed. Now that we acquired S($\Delta\tau$,γ) and W($\Delta\tau$,γ), they can be substituted in equation A4.9 to be compared with the simulated PMD-induced time shift. This is shown in Figure 8.15.

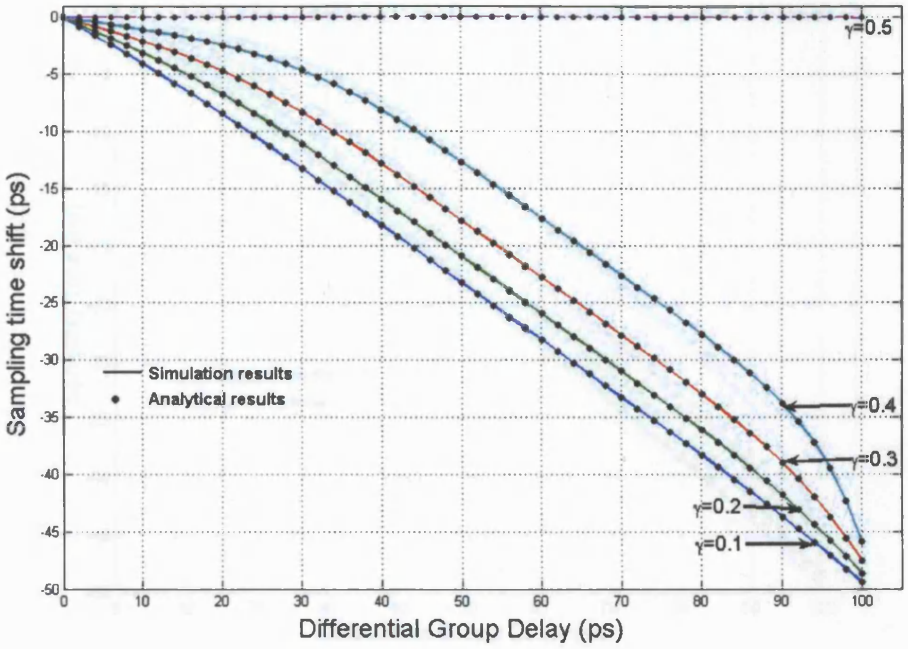

Figure 8.15 Comparison between the analytical and simulation PMD-induced sampling time shift for a clock recovery using edge detection

Although equation A4.9 is very accurate, it is extremely difficult to see intuitively how it might be affected by the parameters γ and Δτ. The next section deals with how this expression can be simplified.

We will start by assuming that the term $\cos(W(\Delta\tau,\gamma)\omega/2)$ in equation A4.9 can be neglected. This is generally valid for Δτ<80ps or for γ∉ [0.4 0.6] as can be observed in Figure 8.14a. Therefore equation A4.9 becomes:

$$t_s = S(\Delta\tau,\gamma) \tag{A4.14}$$

The PMD-induced time shift in this case is dictated by equation A4.13. Taking its Taylor expansion to the fifth term, it can be reduced to:

$$t_s = (2\gamma-1)\frac{\Delta\tau}{2} + \frac{1}{3}\omega^2\Delta\tau^3\gamma(2\gamma-1)(1-\gamma) - \frac{1}{15}\omega^4\Delta\tau^5\gamma(1-\gamma)(2\gamma-1)(3\gamma-1)(3\gamma-2) + \ldots \tag{A4.15}$$

This expansion has the same terms as the Taylor series of the following equation:

$$t_s = \frac{1}{2\omega}\sinh^{-1}[(2\gamma-1)\sinh(\omega\Delta\tau)] \tag{A4.16}$$

This equation is much simpler and it is straightforward to see the effects of γ and Δτ. The following figure shows how the above equation compares with the simulation results of Figure 8.15.

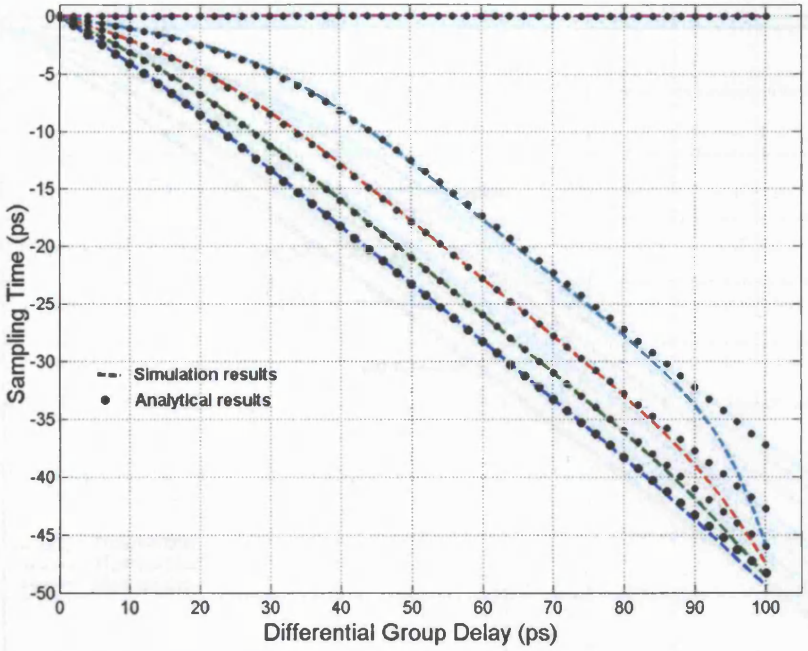

Figure 8.16 Sampling shift comparison between the simulation and the approximation

The good match between the two plots can be observed up to $\Delta\tau$ = 90ps. It can also be noticed that the drift is more pronounced for 0.3 < γ <0.7 (if symmetry is considered). Equation A4.12 is derived based on the approximation that the slope equates to $2\pi/T_b$. In reality the slope is equal to:

$$a = \frac{2\tanh^{-1}(0.8)}{T_r} \tag{A4.17}$$

where T_r is the rise time ($\tanh^{-1}(0.8)$ = 1.098). For any given rise time, equation A4.16 can be rewritten as:

$$t_s = \frac{\alpha}{2\omega}\sinh^{-1}\left[(2\gamma-1)\sinh(\omega\Delta\tau/\alpha)\right] \tag{A4.18}$$

where

$$\alpha = \frac{\pi T_r}{\tanh^{-1}(0.8)T_b} \tag{A4.19}$$

For instance α=1 for T_r =35ps and α=0.77 for T_r =27ps. The figure below compares the sampling time shift for rise times 27, 32 and 35ps.

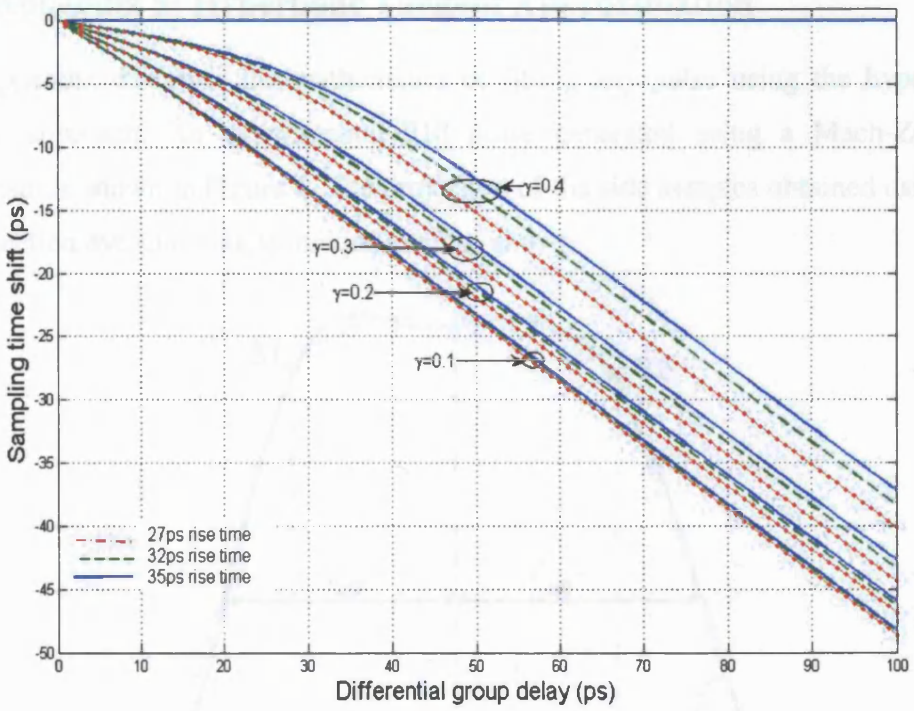

Figure 8.17 Comparison of the PMD-induced sampling time shift for different rise times

It can be deduced that equation A4.12 is valid for rise times ranging between 32 and 38ps ($0.9< \alpha<1.1$). For any other rise time, the factor α should be introduced for more accuracy.

$$S(\Delta\tau,\gamma) =$$

$$\log\Big(1/2\,\big(4\gamma^4 - 2 + 2\exp(1/2\,\omega\,\Delta\tau)^4 - 4\gamma^4\exp(1/2\,\omega\,\Delta\tau)^4 + 2\,(4\gamma^4 - 4\gamma^2 + 8\gamma^4\exp(1/2\,\omega\,\Delta\tau)^4 - 8\gamma^2\exp(1/2\,\omega\,\Delta\tau)^4 + 1 + 2\exp(1/2\,\omega\,\Delta\tau)^8 + \exp(1/2\,\omega\,\Delta\tau)^8 - 4\exp(1/2\,\omega\,\Delta\tau)^8\gamma^2 + 4\gamma^4\exp(1/2\,\omega\,\Delta\tau)^8\big)^{1/2}\big)^{1/2}/\exp(1/2\,\omega\,\Delta\tau)\Big)/\omega \qquad \text{(A4.13)}$$

8.5 Appendix 5: Hyperbolic Tangent Approximation

This appendix describes the mathematics of fitting any pulse using the hyperbolic tangent approach. An experimental 010 pulse generated using a Mach-Zehnder modulator is shown in Figure 1. The projection of the side samples obtained using the three-section eye sampling technique are also shown.

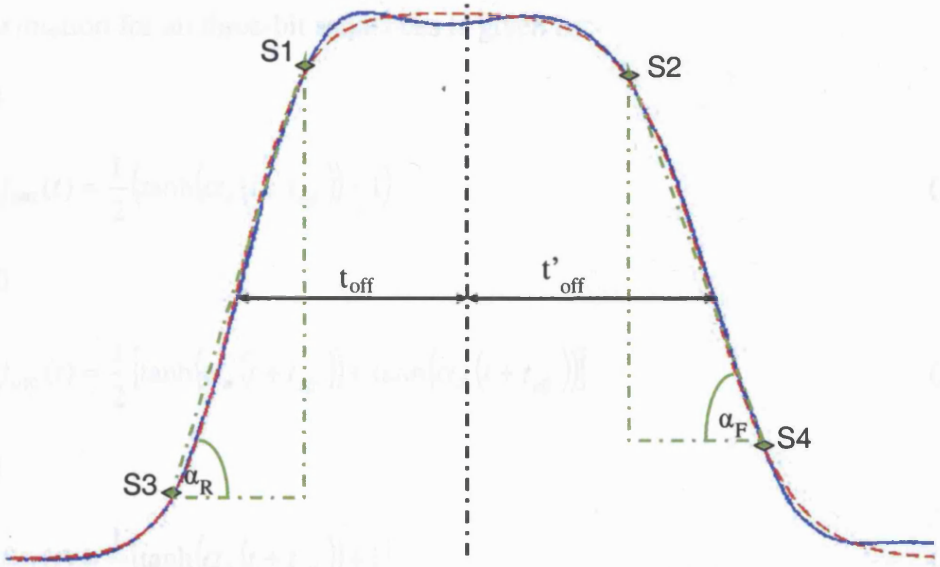

Figure 8.18 Figure showing the approximation of an experimental 010 pulse (solid) by a pair of hyperbolic tangent functions (dashed)

First we define the following parameters:

Time offset of the rising edge t_{off}:

$$t_{off} = \frac{t_{S3}\tanh^{-1}(2S_1 - 1) - t_{S1}\tanh^{-1}(2S_3 - 1)}{\tanh^{-1}(2S_3 - 1) - \tanh^{-1}(2S_1 - 1)} \quad \text{(A5.1)}$$

Time offset of the falling edge t'_{off}:

$$t'_{off} = \frac{t_{S4}\tanh^{-1}(2S_2 - 1) - t_{S2}\tanh^{-1}(2S_4 - 1)}{\tanh^{-1}(2S_4 - 1) - \tanh^{-1}(2S_2 - 1)} \quad \text{(A5.2)}$$

The slope of the rising edge α_R:

$$\alpha_R = \frac{\tanh^{-1}(2S_1 - 1)}{t_{off} + t_{S1}} \quad \text{(A5.3)}$$

The slope of the falling edge α_F:

$$\alpha_F = \frac{\tanh^{-1}(2S_2 - 1)}{t_{off}' + t_{S2}} \tag{A5.4}$$

Now using the above defined parameters, the normalised hyperbolic tangent approximation for all three-bit sequences is given by:

a) 001

$$f_{001}(t) = \frac{1}{2}\left(\tanh\left(\alpha_R\left(t + t_{off}'\right)\right) + 1\right) \tag{A5.5}$$

b) 010

$$f_{010}(t) = \frac{1}{2}\left[\tanh\left(\alpha_R\left(t + t_{off}\right)\right) + \tanh\left(\alpha_F\left(t + t_{off}'\right)\right)\right] \tag{A5.6}$$

c) 011

$$f_{011}(t) = \frac{1}{2}\left(\tanh\left(\alpha_R\left(t + t_{off}\right)\right) + 1\right) \tag{A5.7}$$

d) 100

$$f_{100}(t) = \frac{1}{2}\left(\tanh\left(\alpha_F\left(t + t_{off}\right)\right) + 1\right) \tag{A5.8}$$

e) 101

$$f_{101}(t) = \frac{1}{2}\left[\tanh\left(\alpha_R\left(t + t_{off}'\right)\right) + \tanh\left(\alpha_F\left(t + t_{off}\right)\right)\right] + 1 \tag{A5.9}$$

f) 110

$$f_{110}(t) = \frac{1}{2}\left(\tanh\left(\alpha_F\left(t + t_{off}'\right)\right) + 1\right) \tag{A5.10}$$

Using the principal state model, the received signal in the presence of PMD can be expressed as:

$$f_{PMD}(t) = \gamma f\left(t + \frac{\Delta\tau}{2}\right) + (1 - \gamma) f\left(t - \frac{\Delta\tau}{2}\right) \tag{A5.11}$$

Using this model and equation (A5.6), the 010 pulse at the receiver, in the presence of PMD, is given by:

$$f_{010}^{out} = \frac{\gamma}{2}\left[\tanh\left(\alpha_R\left(t + t_{off} \pm \frac{\Delta\tau}{2}\right)\right) + \tanh\left(\alpha_F\left(t + t'_{off} \pm \frac{\Delta\tau}{2}\right)\right)\right] + \frac{1-\gamma}{2}\left[\tanh\left(\alpha_R\left(t + t_{off} \mp \frac{\Delta\tau}{2}\right)\right) + \tanh\left(\alpha_F\left(t + t'_{off} \mp \frac{\Delta\tau}{2}\right)\right)\right] \quad \text{(A5.12)}$$

Similarly, the 101 sequence at the receiver is governed by:

$$f_{101}^{out} = \frac{\gamma}{2}\left[\tanh\left(\alpha_R\left(t + t'_{off} \pm \frac{\Delta\tau}{2}\right)\right) + \tanh\left(\alpha_F\left(t + t_{off} \pm \frac{\Delta\tau}{2}\right)\right)\right] + \frac{1-\gamma}{2}\left[\tanh\left(\alpha_R\left(t + t'_{off} \mp \frac{\Delta\tau}{2}\right)\right) + \tanh\left(\alpha_F\left(t + t_{off} \mp \frac{\Delta\tau}{2}\right)\right)\right] + 1 \quad \text{(A5.13)}$$

If the waveform has equal rise and fall time (i.e. $|\alpha_R| = |\alpha_R| = |\alpha|$ and $t_{off} = -t'_{off}$) equations A5.12 and A5.13 become:

$$f_{010}^{out} = \frac{\gamma}{2}\left[\tanh\left(\alpha\left(t + t_{off} \pm \frac{\Delta\tau}{2}\right)\right) - \tanh\left(\alpha\left(t - t_{off} \pm \frac{\Delta\tau}{2}\right)\right)\right] + \frac{1-\gamma}{2}\left[\tanh\left(\alpha\left(t + t_{off} \mp \frac{\Delta\tau}{2}\right)\right) - \tanh\left(\alpha\left(t - t_{off} \mp \frac{\Delta\tau}{2}\right)\right)\right] \quad \text{(A5.14)}$$

$$f_{101}^{out} = \frac{\gamma}{2}\left[\tanh\left(\alpha\left(t - t_{off} \pm \frac{\Delta\tau}{2}\right)\right) - \tanh\left(\alpha\left(t + t_{off} \pm \frac{\Delta\tau}{2}\right)\right)\right] + \frac{1-\gamma}{2}\left[\tanh\left(\alpha\left(t - t_{off} \mp \frac{\Delta\tau}{2}\right)\right) - \tanh\left(\alpha\left(t + t_{off} \mp \frac{\Delta\tau}{2}\right)\right)\right] + 1 \quad \text{(A5.15)}$$

8.6 Appendix 6: Split-Step Fourier Algorithm

The split-step Fourier algorithm is the most widely used method to model fibre nonlinearities [Low'02]. It was first applied in 1973 and gained more popularity because it utilises fast Fourier transforms (FFT) and hence has a fast execution time. This technique numerically calculates a solution for the nonlinear Schrödinger equation given by:

$$\frac{\partial A}{\partial z}\left(\hat{D}+\hat{N}\right)A \tag{A5.1}$$

where

$$\hat{D}=-\frac{i\beta_2}{2}\frac{\partial^2}{\partial T^2}+\frac{\beta_3}{6}\frac{\partial^3}{\partial T^3}-\frac{\alpha}{2} \tag{A5.2}$$

and

$$\hat{N}=i\gamma|A|^2 \tag{A5.3}$$

$\hat{D}$ represents the dispersion and absorption in a linear medium and $\hat{N}$ accounts for the effect of fibre nonlinearities on pulse propagation. Generally, the linear and nonlinear effects act simultaneously along the propagation length. The split step Fourier method assumes that the two effects are independent over a small distance h. In other words, the propagation from z to z + h can be executed in two steps. First nonlinearity is applied alone ($\hat{D}$=0) then the dispersion operator is applied while setting $\hat{N}$ =0. This is equivalent to:

$$A(z+h,T)=\exp(h\hat{D})\exp(h\hat{N})A(z,T) \tag{A5.4}$$

While the nonlinear phase shift is applied in the time domain, dispersion is implemented in the Fourier domain by means of FFT. The accuracy of this method is assessed by the Baker-Hausdorff formula for two non-commuting operators and was shown to be accurate to the second order in the step size h (~ ½ h^2) [Agr'02]. This accuracy can be further improved to the third order in step size h by adopting the procedure shown in the figure below. This is known as the symmetrised split-step Fourier method.

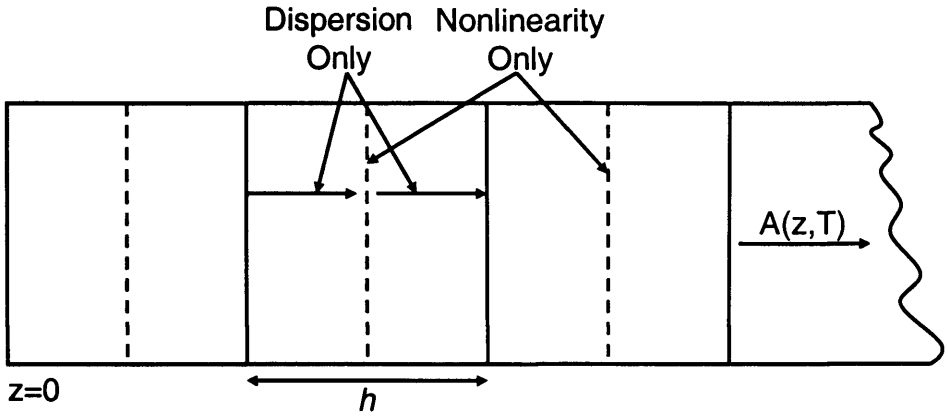

The main difference from the previous method is that nonlinear effects are introduced in the middle of the segment as opposed to segment boundaries. First the fibre is split into many equally spaced segments of length h. The optical field is propagated for a distance $h/2$ under the influence of linear effects (dispersion + fibre loss). After this, at $z + h/2$, the complex field is multiplied by the nonlinear term representing the nonlinear effects over the entire segment h. Finally the field is propagated through the last section of the segment ($h/2$) with linear effects only.

8.7 Appendix 7: Relationship between the BER and Noise Figure of EDFAs

We assume the configuration in Figure 1 where post compensation is used and each amplifier gain matches exactly the loss in the span. In this case the noise figure (NF) of the overall path is simply the sum of the NF's of the individual amplifiers [Bec'99].

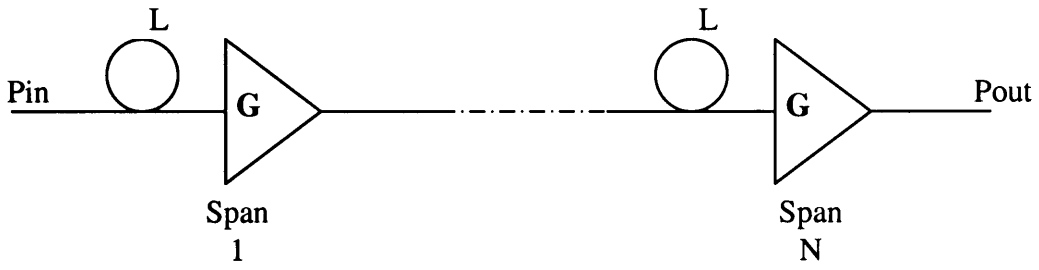

Figure 8.19 Post compensation of fibre loss

In an intensity modulation with direct detection (IMDD) system, the noise current σ_1 and σ_0 are defined as [Agr'02]:

$$\sigma_1 = \sqrt{\sigma_{sig-sp}^2 + \sigma_{sp-sp}^2} \tag{A7.1}$$

$$\sigma_0 = \sigma_{sp-sp} \tag{A7.2}$$

where the signal-spontaneous noise σ_{sig-sp} and the spontaneous-spontaneous noise σ_{sp-sp} are defined as:

$$\sigma_{sig-sp}^2 = 2(q\eta G)^2 FnP_s \Delta f / h\nu \tag{A7.3}$$

$$\sigma_{sp-sp}^2 = (q\eta GFn)^2 \Delta\nu_{opt} \Delta f \tag{A7.4}$$

ΔV_{opt} is the optical bandwidth, h the Plank's constant, P_s the signal power at the input of the amplifier, ν the optical frequency, Δf the receiver (electrical) bandwidth, G is the amplifier gain, η the quantum efficiency and Fn is the noise figure.

Dividing (A7.4) by (A7.3) we get:

$$\sigma_{sp-sp}^2 = aFn\sigma_{sig-sp}^2 \tag{A7.5}$$

where

$$a = \frac{\Delta\nu_{opt} h\nu}{4P_s} \tag{A7.6}$$

From equation (A7.5) we notice that $\sigma_{sp\text{-}sp} \ll \sigma_{sig\text{-}sp}$ especially when an optical filter is used (Δv_{opt} is even smaller) and hence the spontaneous-spontaneous noise can be neglected in equation (A7.1) i.e. $\sigma_1 = \sigma_{sig\text{-}sp}$.

The Q-factor is defined as:

$$Q = \frac{I_1 - I_0}{\sigma_1 + \sigma_0} \tag{A7.7}$$

By assuming that $I_0 \cong 0$ and using (A7.5)

$$Q = \frac{I_1}{(1+\sqrt{aFn})\sigma_{sig-sp}} \tag{A7.8}$$

But

$$SNR = \frac{I_1^2}{\sigma_1^2} \tag{A7.9}$$

Thus

$$Q = \frac{\sqrt{SNR}}{1+\sqrt{aFn}} \tag{A7.10}$$

Since the white noise is assumed to have Gaussian statistics, BER can be written as

$$BER = \tfrac{1}{2} erfc(\frac{Q}{\sqrt{2}}) \tag{A7.11}$$

In addition, SNR is also defined as [Bec'99]

$$SNR = \frac{Pin}{Fnhv\Delta f(G-1)} \tag{A7.12}$$

Substituting (10) and (12) in equation (11) we get

$$BER = \tfrac{1}{2} erfc(\frac{b}{\sqrt{aFn}+\sqrt{Fn}}) \tag{A7.13}$$

where

$$b = \frac{Pin}{2hv\Delta f(G-1)} \tag{A7.14}$$

8.8 Appendix 8: Glossary

AM	Amplitude modulation
AON	All optical networks
APD	Avalanche photodiode
ASE	Amplified spontaneous emission
ASM	Analogue symbol monitoring
AWG	Arrayed waveguide grating
BER	Bit error rate
BIP-8	Bit-interleaved parity-8
BPF	Band-pass filter
CD	Chromatic dispersion
CDR	Clock and data recovery
CNR	Carrier to noise ratio
CRC	Cycle redundancy code/checking
DBR	Distributed Bragg reflector
DCF	Dispersion compensating fibre
DEMUX	Demultiplexer
DFB	Distributed feed-back
D-FF	D-type flip-flop
DGD	Differential group delay
DOP	Degree of polarisation
DSF	Dispersion shifted fibre
DSL	Digital subscriber loop
DWDM	Dense WDM
ECP	Eye closure penalty
EDC	Error detection code
EDFA	Erbium-doped fibre amplifier
FEC	Forward error correction
FET	Field effect transistor
FM	Frequency modulation
FWHM	Full width at half maximum
FWM	Four wave mixing
GbE	Gigabit Ethernet
GFP	Generic framing procedure
GVD	Group velocity dispersion
IM/DD	Intensity-modulated direct-detection
ISI	Intersymbol interference
ITU-T	International Telecommunication Union- Telecommunication Standardization sector
LO	Local oscillator
LOS	Loss of signal
MEMS	Micro-electro-mechanical systems
MLSE	Maximum-likelihood sequence estimation
MUX	Multiplexer
NLSE	Nonlinear Schrödinger Equation
NRZ	Non-return to zero
OADM	Optical add-drop multiplexer
OEO	Optical-electrical-optical

OPM	Optical performance monitoring
OSA	Optical spectrum analyser
OSNR	Optical signal to noise ratio
OTN	Optical transport networks
OXC	Optical cross-connect
PBS	Polarisation beam splitter
PC	Polarisation controller
PCD	Polarisation-dependent chromatic dispersion
PD	Photodetector
PDF	Probability density function
PDL	Polarisation dependent loss
PIN	p-type, intrinsic, n-type
PLC	Planar lightwave circuit
PLL	Phase-locked loop
PM	Phase modulation
PMD	Polarisation mode dispersion
PRBS	Pseudo Random Bit Sequence
PSD	Power spectral density
PSP	Principal state of polarisation
QoS	Quality of service
RIN	Relative intensity noise
RWA	Routing and wavelength assignment
RZ	Return to zero
SCM	Subcarrier multiplexing
SCR	Signal to crosstalk ratio
SDH	Synchronous digital hierarchy
SLA	Service level agreement
SMF	Single mode fibre
SNR	Signal to noise ratio
SONET	Synchronous optical network
SOP	State of polarisation
SPM	Self phase modulation
SRS	Stimulated Raman Scattering
VCO	Voltage controlled oscillator
VSB	Vestigial side bands
WDM	Wavelength division multiplexing
XOR	Exclusive or
XPM	Cross phase modulation

Chapter 9 References

[Aga'05] Agazzi, O.E.; Hueda, M.R.; Carrer, H.S.; Crivelli, D.E.; "Maximum-likelihood sequence estimation in dispersive optical channels", J. Lightwave Technol, Volume 23, Issue 2, Feb. 2005 pp:749 - 763

[Agr'01] Govind P. Agrawal; "Nonlinear Fiber Optics", third edition, Academic Press Inc. (London) Ltd, 2001, ISBN: 0-12-045143-3

[Agr'97] G. P. Agrawal; "Fiber-Optic Communication Systems", Second Edition, ISBN: 0-471-17540-4, John Wiley & Sons Inc 2002

[Agr'02] G. P. Agrawal; "Fiber-Optic Communication Systems", Third Edition, ISBN: 0-471-21571-6, John Wiley & Sons Inc 2002

[Ali'02] Ali, M.; Tancevski, L.; "Impact of polarization-mode dispersion on the design of wavelength-routed networks", IEEE Photon. Technol. Lett., Volume 14, Issue 5, May 2002 pp:720 - 722

[Ali'01] Ali, M.; Elie-Dit-Cosaque, D.; Tancevski, L.; "Network optimization with transmission impairments-based routing", in Proc. 27th European Conf. on Optical Commun. (ECOC) 2001, Volume 1, pp:42 - 43

[Amr'99] Amrani, A.; Roldan, J.; Prat, J.; Rafel, A.; Junyent, G.; "Optical spectrum explorer for maintenance of optical networks", in Proc. Lasers and Electro Optics Society Conference (LEOS). Volume 2, 8-11 Nov. 1999 pp:649 - 650

[Amr'00] A. Amrani, G. Junyent, J. Prat, J. Comellas, I. Ramdani; "Performance monitoring for all-optical networks based in homodyne spectroscopy", IEEE Photon. Technol. Lett. Vol.12, No11, November 2000 pp.1564-1566

[And'01] Andre, P.S.B.; Teixeira, A.L.J.; Lima, M.J.N.; Pinto, J.L.; da Rocha, J.R.F., "Optical performance monitor based on asynchronous detection", in Proc. Lasers and Electro Optics Society Conference (LEOS) 2001,Volume: 1, pp:30 - 31, 12-13 Nov. 2001

[And'04] Andre, P.S.B.; Luis, A.J; Teixeira, A.L.J.; Lima, M.J.N and Monteiro, P.N, "Asynchronous sampled amplitude histogram models for optical performance monitoring in high-speed networks", J. Optic. Networking, Volume 3, No. 8, pp: 636 – 642, August 2004

[Ans'95] Andersson, L.I.; Rudberg, B.G.R.; Lewin, P.T.; Reed, M.D.; Planer, S.M.; Sundaram, S.L.;"Silicon bipolar chipset for SONET/SDH 10 Gb/s fiber-optic communication links", IEEE J. Solid-State Circ., Volume 30, Issue 3, March 1995 pp:210 – 218

[Aza'02] Azadet, K.; Haratsch, E.F.; Kim, H.; Saibi, F.; Saunders, J.H.; Shaffer, M.; Song, L.; Meng-Lin Yu;"Equalization and FEC techniques for optical transceivers", IEEE J. Solid-State Circ., Volume 37, Issue 3, March 2002, pp:317 - 327

[Bal'89] Ralph Ballart & Yau-Chau Ching "SONET: Now it's the standard optical network", IEEE Comm. Magazine Vol. 27, Issue 3 (1989)

[Bec'99] Becker, P. C.; Olsson, N.A.; Simpson J.R.; "Erbium-Doped Fiber Amplifiers: Fundamentals and Technology" ,AP Professional. 1999, ISBN: 0120845903

[Ben'00] G. Bendelli, C. Cavazzoni, R. Girardi, R. Lano; "Optical performance monitoring techniques", in Proc. European Conf. on Optical Commun. (ECOC) Munich 2000. V4 pp. 113-116

[Ben'03a] Benlachtar, Y.; Killey, R.; Bayvel, P.; "Identification of sources of degradation in optical channels using deconvolution technique", in Proc. Optical Fiber Commun. Conf. (OFC), 2003, 23-28 March 2003 pp:109 - 110, vol.1

[Ben'03b] Benlachtar, Y.; Killey, R.; Bayvel, P.;"Novel Histogram Method for Estimating Gaussian White Noise in Optical Channels and Its Application in Identifying Different Sources of Degradation", Postgrad. Research Conf. Elec., Photon., Comm. And Software (PREP2003), 14-16 April 2003, Exeter University, UK.

[Ben'03c] Benlachtar, Y.; Killey, R.; Bayvel, P.; "Experimental investigation of a deconvolution technique for identification of channel impairment", in Proc. Lasers and Electro Optics Society Conference (LEOS) 2003, Volume 1, 27-28 Oct. 2003 pp:146 - 147

[Ben'05a] Benlachtar, Y.; Killey, R.; Bayvel, P.; "Novel Three-Point Sampling Technique for Detection of First Order PMD", e-Photon ONe Winter School on Optical Core Network Technologies, Aveiro, 23-25 February 2005. Portugal

[Ben'05b] Benlachtar, Y.; Scopes, M.; Killey, R. I.; Bayvel, P.; "Novel Eye Monitoring Technique for Detection of First Order PMD", in Proc. Conf. on Lasers and Electro-Optics Society (CLEO/QELS) 2005, Baltimore. JThE77. May 22 - May 27, 2005

[Ben'05c] Benlachtar, Y.; Killey, R.; Bayvel, P.;"Experimental Investigation of Three-Point Sampling Technique for the Estimation of First Order PMD", in Proc. European Conf. on Optical Commun. (ECOC), Sptember 2005, Glascow, We4.P.100

[Ben'05d] Benlachtar, Y.; Killey, R.; Bayvel, P.;"Effects of first-order polarisation-mode dispersion on clock recovery", Electron. Lett., Volume 41, Issue 21, 13 Oct. 2005 pp:1190 - 1191

[Ber'93] Bergano, N.S.; Kerfoot, F.W.; Davidsion, C.R.; "Margin measurements in optical amplifier system", IEEE Photon. Technol. Lett., Volume 5, Issue 3, March 1993 pp:304 - 306

[Ber'02] Neal S. Bergano; "Optical Fiber Telecommunications Systems v. IV-B", Academic Press Inc. (London) Ltd, ISBN:0-12-395173-9, 2002

[Bon'00] P. Bonenfant, A. Rodriguez-Moral; "Optical data networking", IEEE comm. Magazine Vol. 38, Issue 3 (2000)

[Bra'99] R.N. Bracewell; "The Fourier Transform and Its Applications", McGraw-Hill Education (ISE Editions), ISBN: 0-07-116043-4, 1999.

[Buc'01] Buchali, F.; Lanne, S.; Thiery, J.-P.; Baumert, W.; Bulow, H.; "Fast eye monitor for 10 Gbit/s and its application for optical PMD compensation", in Proc. Optical Fiber Commun. Conf. (OFC), 2001, Volume 2, 2001 pp:TuP5-1 - TuP5-3

[Buc'02] Buchali, F.; Baumert, W.; Bulow, H.; Poirrier, J.; "A 40 Gb/s eye monitor and its application to adaptive PMD compensation", in Proc. Optical Fiber Commun. Conf. (OFC), 2002, 17-22 Mar 2002 pp:202 – 203

[Cai'03] Yi Cai; Morris, J.M.; Adali, T.; Menyuk, C.R.;"On turbo code decoder performance in optical-fiber communication systems with dominating ASE noise", J. Lightwave Technol, Volume 21, Issue 3, March 2003 pp:727 - 734

[Car'05] Cardillo, R.; Curri, V.; Mellia, M.; "Considering transmission impairments in wavelength routed networks", in Proc. Conf. on Optic. Network Design and Mod. 2005, Feb. 7-9, 2005 pp:421 – 429

[Chs'00] H.S. Chung et al; "Effects of stimulated Raman scattering on pilot tone based WDM supervisory technique", in Proc. Optical Fiber Commun. Conf. (OFC), 2000. WK7-1 pp. 185-187

[Chu'04] Chun-Liang Yang; San-Liang Lee; "OSNR monitoring using double-pass filtering and dithered tunable reflector", IEEE Photon. Technol. Lett., Volume 16, Issue 6, June 2004 pp:1570 - 1572

[Crc'94] Cyclic redundancy check (CRC) tutorial
http://www.rad.com/networks/1994/err_con/crc.htm

[Dav'89] Davidson, F.M.; Sun, X.;"Slot clock recovery in optical PPM communication systems with avalanche photodiode photodetectors", IEEE Trans. on Comm., Volume 37, Issue 11, Nov. 1989 pp:1164 - 1172

[Dav'02] Davey, R.; Payne, D.; Lord, A.;" Optical networks: a pragmatic European operator's view" in Proc. Optical Fiber Commun. Conf. (OFC) 2002, 17-22 Mar 2002 pp:41 – 42

[Dav'05] Davey, R.; Payne, D.; "The future of optical transmission in access and metro networks- an operator's view", in Proc. European Conf. on Optical Commun. (ECOC), Sptember 2005, Glascow, We2.1.3

[Der'98] Dennis Derickson; "Fiber Optic Test and Measurement", Hewlett-Packard Professional Books, Prentice Hall PTR; 1st edition (January 15, 1998), ISBN: 0135343305

[Des'02] Desurvire, E.; "Erbium-Doped Fiber Amplifiers: Principles and Applications", John Wiley & Sons, 2002, ISBN: 0471264342

[Dim'00] Dimmick, T.E.; Rossi, G.; Blumenthal, D.J.; "Optical dispersion monitoring technique using double sideband subcarriers", IEEE Photon. Technol. Lett., Volume 12, Issue 7, July 2000 pp:900 - 902

[Dow'01] Downie, J.D.; Tebben, D.J.; "Performance monitoring of optical networks with synchronous and asynchronous sampling", in Proc. Optical Fiber Commun. Conf. (OFC) 2001, Volume 3, pp:WDD50-1 - WDD50-3

[Dow'05] Downie, J.D.; "Relationship of Q penalty to eye-closure penalty for NRZ and RZ signals with signal-dependent noise", J. Lightwave Technol, Volume 23, Issue 6, June 2005 pp:2031 - 2038

[Ess'02] René-Jean Essiambre; Gregory Raybon and Benny Mikkelsen; "Optical Fiber Telecommunications Systems v. IV-B", Academic Press Inc. (London) Ltd, ISBN: 0-12-395173-9, 2002

[Fci'05] Fibre Channel Industry Association, http://www.fibrechannel.org/

[Fra'99] Francia, C.; Bruyere, F.; Thiery, J.P.; Penninckx, D.; "Simple dynamic polarisation mode dispersion compensator", Electron. Lett., Volume 35, Issue 5, 4 March 1999 pp:414 - 415

[Fih'90] Fishman, D.A.; "A narrow bandpass microstrip filter for high-speed fiber optic systems", IEEE Trans. on Comm., Volume 38, Issue 8, Aug. 1990 pp:1122 - 1124

[Fis'97] Daniel A. Fishman; B. Scott Jackson; "Optical Fiber Telecommunications IIIB", Academic Press, ISBN: 0123951712, 1997

[Fis'01] Fischler, W.; Richter, A.; Bock, H.; Elbers, J.-P.; Glingener, C., "Monitoring the optical performance in a transparent and configurable metro area network", in Proc. Lasers and Electro Optics Society Conference (LEOS), Volume: 2 , pp:479 - 480, 12-13 Nov. 2001

[Fra'98a] Francia, C.; Penninckx, D.; Bruyere, F.; Chbat, M.W.; "Time impulse response of second order PMD in single-mode fibers", in Proc. European Conf. on Optical Commun. (ECOC), 1998, Volume 1, 20-24 Sept. 1998 pp:143 - 144

[Fra'98b] Francia, C.; Bruyere, F.; Penninckx, D.; Chbat, M.;"PMD second-order effects on pulse propagation in single-mode optical fibers", IEEE Photon. Technol. Lett., Volume 10, Issue 12, Dec. 1998 pp:1739 - 1741

[Fra'99] Francia, C.; Penninckx, D.; "Polarization mode dispersion in single-mode optical fibers: time impulse response", IEEE Inter. Conf. on Comm. (ICC '99), Volume 3, 6-10 June 1999 pp:1731 - 1735

[Gal'92] Galtarossa, A.; Schiano, M.;"Complete characterisation of polarisation mode dispersion in erbium doped optical amplifiers", Electron. Lett., Volume 28, Issue 23, 5 Nov. 1992 pp:2143 - 2144

[Gal'01] Galtarossa, A.; Pizzinat, A.; Matera, F.;' Statistical description of optical system performances due to random coupling on the principal states of polarization'. Photonics Technol. Lett., Vol.13, (12), 2001 pp.1307 – 1309

[Gre'01] Green, P.; "Progress in optical networking", IEEE Comm. Magazine, Volume 39, Issue 1, Jan. 2001 pp:54 - 61

[Gro'90] W. D. Grover & T. E. Moore; "Design and characterization of an error-correcting code for the SONET", IEEE Trans. on Comm.. Vol. 38, Number 4 (1990)

[Ham'97] Hamazumi, Y.; Koga, M.; "Transmission capacity of optical path overhead transfer scheme using pilot tone for optical path network", J. Lightwave Tech., Volume 15, Issue 12, Dec. 1997 pp:2197 - 2205

[Han'98] N. Hanik, A. Gladisch, C. Caspar and B. Strebel, "Application of amplitude histograms to monitor performance of optical channels", in Proc. European Conf. on Optical Commun. (ECOC) Madrid. pp. 707-708, 1998

[Has'98] Hansryd, J.; Andrekson, P.A.; Bakhshi, B.;"A simple, low timing jitter, sub-multiple clock recovery technique", ," in Proc. European Conf. on Optical Commun. (ECOC), Volume 1, 20-24 Sept. 1998 pp:471 - 472

[Hau'04] Haunstein, H.F.; "PMD and chromatic dispersion control for 10 and 40 Gbps systems", in Proc. Optical Fiber Commun. Conf. (OFC) 2004, Volume 2, 23-27 Feb. 2004 pp:3 pp.

[Hei'03] Heismann, F.; "Origin of clock-frequency components in NRZ-formatted optical signals", IEEE Photon. Technol. Lett., Volume 15, Issue 7, July 2003 pp:912 - 914

[Her'02] E. Hernandez-Valencia, M. Scholten, Z. Zhu; "The generic framing procedure (GFP). An overview.", IEEE comm. Magazine Vol. 40, Issue 5 (2002)

[Hil'93] Hill, G.R.; Chidgey, P.J.; Kaufhold, F.; Lynch, T.; Sahlen, O.; Gustavsson, M.; Janson, M.; Lagerstrom, B.; Grasso, G.; Meli, F.; Johansson, S.; Ingers, J.; Fernandez, L.; Rotolo, S.; Antonielli, A.; Tebaldini, S.; Vezzoni, E.; Caddedu, R.; Caponio, N.; Testa, F.; Scavennec, A.; O'Mahony, M.J.; Zhou, J.; Yu, A.; Sohler, W.; Rust, U.; Herrmann, H.; "A transport network layer based on optical network elements", J. Lightwave Tech., Volume 11, Issue 5, May-June 1993 pp:667 – 679

[Hor'05] Hornung, S.; Payne, D.; Davey, R.; "New architecture for an all optical network", in Proc. Optical Fiber Commun. Conf. (OFC) 2005, Volume 2, 6-11 March, OTuH7

[Ian'93] Iannone, E. et al.;' Effect of polarization dispersion on the performance of IM-DD communication systems'. Photonics Technol. Lett., Vol.5, (10), 1993 pp. 1247 – 1249

[Ian'99] E. Iannone et al, "Modelling of In-band Crosstalk in WDM Optical Networks", IEEE J. Lightwave Tech.. Vol. 17, Number 7, 1999

[Imb'83] Imbeaux, J.-C.;"Performances of the Delay-Line Multiplier Circuit for Clock and Carrier Synchronization in Digital Satellite Communications", IEEE J. on Selec. Areas in Comm., Volume 1, Issue 1, Jan 1983, pp:82 - 95

[ITU'99] ITU-T Recommendation G.826, Feb 1999

[Jin'04] Jing Zhang; Mukheriee, B.;"A review of fault management in WDM mesh networks: basic concepts and research challenges", IEEE Network, Volume 18, Issue 2, Mar-Apr 2004 pp:41 – 48

[Kam'02] Kamran Azadet et al; "Equalization and FEC techniques for optical tranceivers", IEE J. of Solid-State Circ. Vol. 37, Number 3 (2002)

[Kat'95] Katzela, I.; Ellinas, G.; Stern, T.E.; "Fault Diagnosis in the Linear Lightwave Network", Flat Panel Display Technology/Technologies for a Global Information Infrastructure/ICs for New Age Lightwave Communications/RF Optoelectronics, 1995 Digest of the LEOS Summer Topical Meetings

[Kat'01] Katzela, I.; Ellinas, G.; Yoon, W., S.; Stern, T.E.; "Fault Diagnosis in Optical Networks", J. of High Speed Networks, Volume 10, Issue 4, 2001, pp: 269-291

[Kil'02] D. C. Kilper, S. Chandrasekhar, L. Buhl, A. Agarwal, and D. Maywar,

"Spectral monitoring of OSNR in high speed networks," in Proc. European Conf. on Optical Commun. (ECOC), 2002, p. 7.4.4.

[Kil'04] Kilper, D.C.; Bach, R.; Blumenthal, D.J.; Einstein, D.; Landolsi, T.; Ostar, L.; Preiss, M.; Willner, A.E.; "Optical performance monitoring", J. Lightwave Technol, Volume 22, Issue 1, Jan. 2004 pp:294 – 304

[Kim'02] Kim, C.H.; Kim, H.; Winzer, P.J.; Jopson, R.M.; "Dependence of polarization-mode dispersion penalties on receiver characteristics", IEEE Photon. Technol. Lett., Volume 14, Issue 11, Nov. 2002 pp:1629 - 1631

[Klo'98] A. Kloch et al.; "Pilot tones in networks with nonlinear elements", IEEE Photon. Technol. Lett., Vol. 10, No. 3, 1998

[Kik'01] Kikuchi, N.; "Analysis of signal degree of polarization degradation used as control signal for optical polarization mode dispersion compensation", J. Lightwave Technol, Volume 19, Issue 4, April 2001 pp:480 - 486

[Kog'02] Herwig Kogelnik; Robert M. Jopson and Lynn E. Nelson; "Optical Fiber Telecommunications Systems v. IV-B", Academic Press Inc. (London) Ltd, ISBN:0-12-395173-9, 2002

[Kon'99] E. Kong et al; "Pilot tone based optical-path supervisory scheme for optical cross connects", Electron. Lett. Vol.35 No.17, pp.1481-1483. 1999

[Kwa'00] Kwang-Uk Chu et al; "Scalable optical-path supervisory scheme using pilot tones and channel equalisers", Electron. Lett., Vol.36 No.9, pp.817-818. 2000

[Lee'01] Lee, J.H.; Chung, Y.C.; "Improved OSNR monitoring technique based on polarisation-nulling method", Electron. Lett., Volume 37, Issue 15, 19 Jul 2001 pp:972 - 973

[Leg'96] Legg, P.J.; Tur, M.; Andonovic, I., "Solution paths to limit interferometric noise induced performance degradation in ASK/direct detection lightwave networks", J. Lightwave Technol ,Volume: 14 , Issue: 9, pp:1943 – 1954, Sept. 1996

[Lev'01] Levandovsky, D.; "Wavelength routing based on physical impairments", in Proc. Optical Fiber Commun. Conf. (OFC) 2001, Volume 2, pp:TuG7-1 - TuG7-3 vol.2

[Lim'98] Lima, M.J.; Monteiro, P.P.; Ferreira da Rocha, J.; Teixeira, A.; Matos, J.N.;"Design of clock-recovery GaAs ICs for high-speed communication systems", IEEE Inter. Conf. on Electron., Circ. and Systems, Volume 3, 7-10 Sept. 1998 pp:205 - 208 vol.3

[Low'02] Arthur J. Lowery; "Optical Fiber Telecommunications Systems v. IV-B", Academic Press Inc. (London) Ltd, ISBN:0-12-395173-9, 2002

[Lui'04] Luis, R.; Teixeira, A.; Andre, P.; Monteiro, P.; "Evaluation of Intra-Band Crosstalk Using Asynchronous Histograms", Networks & Optical Communications (NOC) 2004.

[Maf'04] Martins-Filho, J.F.; Bastos-Filho, C.J.A.; Arantes, E.A.J.; Oliveira, S.C.; Nunes, F.D.; Dante, R.G.; Fontana, E.;"Impact of device characteristics on network performance from a physical-impairment-based routing algorithm", in Proc. Optical Fiber Commun. Conf. (OFC) 2004, Volume 1, 23-27 Feb. 2004

[Mas'00] Mas, C.; Thiran, P.; "An efficient algorithm for locating soft and hard failures in WDM networks", IEEE J. on Selected Areas in Comm., Volume 18, Issue 10, Oct. 2000 pp:1900 - 1911

[Mas'05] Mas, C.; Tomkos, I.; Tonguz, O.K.; "Failure Location Algorithm for Transparent Optical Networks", IEEE J. on Selected Areas in Comm., Volume 23, Issue 8, Aug. 2005 pp:1508 – 1519

[Max'02] Maxim Integrated Products; "Measuring Telecom Systems Against a Pulse Mask Template", http://www.maxim-ic.com/appnotes.cfm/appnote_number/1797, December 2002.

[Mel'92] L. Melkonian, "Improving A/D Converter Performance Using Dither", National Semiconductor Application Note 804, www.national.com/an/AN/AN-804.pdf, February 1992

[Mon'92] Monteiro, P.; Matos, J.N.; Gameiro, A.; da Rocha, J.R.F.; "10 Gbit/s timing recovery circuit using dielectric resonator and active bandpass filters", Electron. Lett., Volume 28, Issue 9, 23 April 1992 pp:819 - 820

[Mon'94] Monteiro, P.; Matos, J.N.; Gameiro, A.; Da Rocha, J.R.F.; "20 Gbit/s DR based timing recovery circuit", Electron. Lett., Volume 30, Issue 10, 12 May 1994 pp:799 - 800

[Mor'94] Morkel, P.R.; Syngal, V.; Butler, D.J.; Newman, R.;' PMD-induced BER penalties in optically-amplified IM/DD lightwave systems'. Electron. Lett. Vol. 30, (10), 1994 pp. 806 - 807

[Mue'99] K. Mueller, N. Hanik, A. Gladisch, C. Caspar, H. M. Foisel, "Application of amplitude histograms for quality of service measurements of optical channels and fault identification", Electron. Lett.., Vol.35, No.5 pp. 403-404, March 4th 1999

[Muk'04] Mukherjee, B.; Huang, Y.; Heritage, J.P.; "Impairment-aware routing in wavelength-routed optical networks" in Proc. Lasers and Electro

Optics Society Conference (LEOS) 2004, Volume 1, 7-11 Nov. 2004 pp:428 – 429

[Mur'95] Murakami, M.; Amemiya, M.; "Simple and accurate zero dispersion wavelength measurement for long haul optical amplifier systems using induced phase to amplitude modulation conversion", Electron. Lett., Volume 31, Issue 8, 13 April 1995 pp:666 – 668

[Mur'99] Koichi Murata and Taiichi Otsuji; "A Novel Clock Recovery Circuit for Fully Monolithic Integration", IEEE Trans. on microwave theory and tech., Vol. 47, No. 12, December 1999. pp:2528-2533

[Nag'00] Nagel, J. A.; Chbat, M. W.; Garrett, L. D.; Soigne J. P.; Weaver, N. A.; Desthieux, B. M.; Bulow, H.; McCormick, A. R.; Derosier R. M.; "Long-term PMD mitigation at 10Gb/s and time dynamics over high-PMD installed fiber", in Proc. European Conf. on Optical Commun. (ECOC) 2000, Volume 2, pp: 31-32

[Nak'03] Nakamura, K.; Saitoh, T.; Takahashi, Y.; "High-speed optical performance monitor for WDM network using MEMS scanning mirror", Optical MEMS, in Proc. Lasers and Electro Optics Society Conference (LEOS) 18-21 Aug. 2003 pp:97 - 98

[Nez'04a] Nezam, S.M.R.M.; McGeehan, J.E.; Willner, A.E.; "Degree-of-polarization-based PMD monitoring for subcarrier-multiplexed signals via equalized carrier/sideband filtering", J. Lightwave Technol Volume 22, Issue 4, April 2004 pp:1078 – 1085

[Nez'04b] Nezam, S.M.R.M.; Yong-Won Song; Changyuan Yu; McGeehan, J.E.; Sahin, A.B.; Willner, A.E.; "First-order PMD monitoring for NRZ data using RF clock regeneration techniques", J. Lightwave Technol., Volume 22, Issue 4, April 2004 pp:1086 - 1093

[Oht'99] S. Ohteru and N Takachio, "Optical signal quality monitor using direct Q-factor measurement," IEEE Photon. Technol. Lett.. Vol.11, No.10 pp.1307-1309, October 1999.

[Par'02] Park, E.;"Error monitoring for optical metropolitan network services" IEEE Comm. Magazine, Volume 40, Issue 2, Feb. 2002 pp:104 – 109

[Pak'02a] Park, K.J.; Youn, C.J.; Lee, J.H.; Chung, Y.C.; "Chromatic dispersion monitoring technique in WDM network", in Proc. Optical Fiber Commun. Conf. (OFC) 2002, 17-22 Mar, pp:735 - 737

[Pak'02b] Park, K.J.; Youn, C.J.; Lee, J.H.; Chung, Y.C.; "Effect of self-phase modulation on group-velocity dispersion measurement technique using PM-AM conversion", Electron. Lett., Volume 38, Issue 21, 10 Oct. 2002 pp:1247 - 1248

[Pak'03] Park, K.J.; Youn, C.J.; Lee, J.H.; Chung, Y.C.; "Performance comparisons of chromatic dispersion-monitoring techniques using pilot tones", IEEE Photon. Technol. Lett., Volume 15, Issue 6, June 2003 pp:873 – 875

[Pak'04] Park, K.J.; Youn, C.J.; Lee, J.H.; Chung, Y.C.; "Optical path, wavelength and power monitoring technique using frequency-modulated pilot tones", in Proc. Optical Fiber Commun. Conf. (OFC) 2004, Volume 2, 23-27 Feb. pp:3 pp. vol.2

[Pan'01] Pan, Z.; Yu, Q.; Xie, Y.; Havstad, S.A.; Willner, A.E.; Starodubov, D.S.; Feinberg, J.; "Chromatic dispersion monitoring and automated compensation for NRZ and RZ data using clock regeneration and fading without adding signalling", in Proc. Optical Fiber Commun. Conf. (OFC) 2001, Volume 3, pp:WH5-1 - WH5-3

[Pan'02] Pan, Z.; Song, Y.W.; Yu, C.; Wang, Y.; Yu, Q.; Popelek, J.; Li, H.; Li, Y.; Willner, A.E.;"Tunable chromatic dispersion compensation in 40-Gb/s systems using nonlinearly chirped fiber Bragg gratings", J. Lightwave Technol, Volume 20, Issue 12, Dec. 2002 pp:2239 - 2246

[Pen'03] Penninckx, D.; Perret, C.; "New physical analysis of 10-Gb/s transparent optical networks", IEEE Photon. Technol. Lett., Volume 15, Issue 5, May 2003 pp:778 – 780

[Pem'04] Petersson, M.; Sunnerud, H.; Karlsson, M.; Olsson, B.-E.; "Performance monitoring in optical networks using Stokes parameters", IEEE Photon. Technol. Lett., Volume 16, Issue 2, Feb. 2004 pp:686 - 688

[Pet'02] Petersen, M.N.; Pan, Z.; Lee, S.; Havstad, S.A.; Willner, A.E.; "Online chromatic dispersion monitoring and compensation using a single inband subcarrier tone", IEEE Photon. Technol. Lett., Volume 14, Issue 4, April 2002 pp:570 – 572

[Poo'86] Poole, C. D.; Wagner R. E.; "Phenomenological approach to polarization dispersion in long single-mode fibers", Electron. Lett. ,Volume: 22 , pp:1029 – 1030, 1986

[Poo'91] Poole, C.D.; Tkach, R.W.; Chraplyvy, A.R.; Fishman, D.A.;"Fading in lightwave systems due to polarization-mode dispersion", IEEE Photon. Technol. Lett.,Volume 3, Issue 1, Jan. 1991 pp:68 - 70

[Ram'03] S. Ramamurthy, L. Sahasrabuddhe, and B. Mukherjee, "Survivable WDM Mesh Networks," IEEE J. Lightwave Tech., vol. 21, Apr. 2003, pp. 870–83.

[Ras'99] Rasztovits-Wiech, M.; Studer, K.; Leeb, W.R., "Bit error probability estimation algorithm for signal supervision in all-optical networks", Electron. Lett. ,Volume: 35 , Issue: 20, pp:1754 – 1755, 30 Sept. 1999

[Raz'96] Behzad B. Razavi; "Monolithic Phase-locked Loops and Clock Recovery Circuits: Theory and Design", John Wiley & Sons Inc, ISBN: 0780311493, 1996

[Ric'01] Richter, A.; Bock, H.; Fischler, W.; Elbers, J.-P.; Glingener, C.; Bach, R.; Grupp, W., "Field trial of optical performance monitor in dynamically configurable DWDM network", Electron. Lett., Volume: 37 , Issue: 6 , pp:370 – 371,15 Mar 2001

[Ric'02] Richter, A.; Fischler, W.; Bock, H.; Bach, R.; Grupp, W., "Optical performance monitoring in transparent and configurable DWDM networks", Optoelectronics, IEE Proceedings- ,Volume: 149 , Issue: 1, pp:1 - 5, Feb. 2002

[Rod'95] D. Roddy, J. Coolen; "Electronic communications 4th edition", Prentice Hall International Editions. 1995

[Ros'00] Giammarco Rossi, T. E. Dimmick and D. J. Blumanthal; "Optical performance monitoring in reconfigurable WDM optical networks using subcarrier multiplexing", J. Lightwave Tech.. Vol.18 No12, December 2000 pp.1639-1648

[San'96] Sano, A.; Kataoka, T.; Tomizawa, M.; Hagimoto, K.; Sato, K.; Wakita, K.; Kato, K.; "Automatic dispersion equalization by monitoring extracted-clock power level in a 40-Gbit/s, 200-km transmission line", in Proc. 22th European Conf. on Optical Commun. (ECOC), Volume 2, 15-19 Sept. 1996 pp:207 - 210

[Sav'02] Stanic, S.; Subramaniam, S.; Choi, H.; Sahin, G.; Hyeong-Ah Choi; "On monitoring transparent optical networks", in Proc Inter. Con. on Parallel Processing Workshops, 18-21 Aug. 2002 pp:217 – 223

[Sav'03] Stanic, S.; Subramaniam, S.; Hongsik Choi; Sahin, G.; Hyeong-Ah Choi; "Efficient alarm management in optical networks", in Proc Information Survivability Conference and Exposition, Volume 1, 22-24 April 2003 pp:252 - 260

[Sec'03] Secondini, M.; Forestieri, E.; Prati, G.;"Adaptive minimum MSE controlled PLC optical equalizer for chromatic dispersion compensation", J. Lightwave Technol, Volume 21, Issue 10, Oct. 2003 pp:2322 - 2331

[Sed'97] Adel S. Sedra; Kenneth C. Smith; K. C. Smith; "Microelectronic Circuits", Oxford University Press; 4th Bk&Cdr edition (June, 1997), ISBN: 0195116631

[Sen'92] John M. Senior; "Optical Fiber Communications: Principles and Practice", Edition: 2, 1992, Prentice Hall PTR, ISBN:0136354262

[Sha'98] Shake, I.; Takara, W.; Kawanishi, S.; Yamabayashi, Y., "Optical signal quality monitoring method based on optical sampling", Electron. Lett., Volume: 34 , Issue: 22, pp:2152 – 2154, 29 Oct. 1998

[Sha'00] Shake, I.; Otani, E.; Takara, H.; Uchiyama, K.; Yamabayashi, Y.; Morioka, T., "Bit rate flexible quality monitoring of 10 to 160 Gbit/s optical signals based on optical sampling technique", Electron. Lett., Volume: 36 , Issue: 25, pp:2087 - 2088, 7 Dec. 2000.

[Sha'02] Shake, I.; Takara, H., "Averaged Q-factor method using amplitude histogram evaluation for transparent monitoring of optical signal-to-noise ratio degradation in optical transmission system", J. Lightwave Technol ,Volume: 20 , Issue: 8, pp:1367 – 1373, Aug. 2002.

[Sha'03a] Shake, I.; Takara, H.; Kawanishi, S., "Simple Q factor monitoring for BER estimation using opened eye diagrams captured by high-speed asynchronous electrooptical sampling", IEEE Photon. Technol. Lett. ,Volume: 15 , Issue: 4, pp:620 - 622, April 2003

[Sha'03b] Shake, I.; Takara, H., "Chromatic dispersion dependence of asynchronous amplitude histogram evaluation of NRZ signal", J. Lightwave Technol ,Volume: 21 , Issue: 10, pp:2154 – 2161, Oct. 2003

[Sha'04] Shake, I.; Takara, H.; Kawanishi, S., "Simple measurement of eye diagram and BER using high-speed asynchronous sampling", J. Lightwave Technol ,Volume: 22 , Issue: 5, pp:1296 - 1302, May 2004

[Son'95] Jae Ho Song; Tae Whan Yoo; Moon Soo Park;'10 Gbit/s clock recovery circuit using temperature compensated dielectric resonator filter'. Electron. Lett. Vol.31, Issue 17, 1995. pp:1458 - 1460

[Str'01] Strand, J.; Chiu, A.L.; Tkach, R.; "Issues for routing in the optical layer", IEEE Comm. Magazine, Volume 39, Issue 2, Feb. 2001 pp:81 – 87

[Sun'97] Yan Sun et al; "Time dependent perturbation theory and tones in cascaded Erbium-Doped fiber amplifier systems", J. Lightwave Tech. Vol. 15, No. 7, 1997.

[Suz'99] Suzuki, H.; Takachio, N.; "Optical signal quality monitor built into WDM linear repeaters using semiconductor arrayed waveguide grating filter monolithically integrated with eight photodiodes", Electron. Lett., Volume 35, Issue 10, 13 May 1999 pp:836 – 837

[Wal'02] Walter, A.; Schaefer, G.S.;"Chromatic dispersion variations in ultra-long-haul transmission systems arising from seasonal soil temperature variations", in Proc. Optical Fiber Commun. Conf. (OFC) 2002, 17-22 Mar, pp:332 - 333

[Wan'91] Wang, Z.; Langmann, U.; Bosch, B.G.; "Multi-Gb/s silicon bipolar clock recovery IC", IEEE J. on Selected Areas in Comm., , Volume 9, Issue 5, June 1991 pp:656 - 663

[Wei'00a] C. M. Weinert, C. Caspar, M. Konitzer and M. Rohde, "Histogram method for identification and evaluation of crosstalk", Electron. Lett., Vol. 36 No.6 pp.558-559, 16th march 2000

[Wei'00b] C. M. Weinert, "Histogram method performance monitoring of the optical channel", in Proc. European Conf. on Optical Commun. (ECOC) Munich. V4 pp. 121-122, 2000

[Wei'05] Eric W. Weisstein. "Noncentral Chi-Squared Distribution." From MathWorld--A Wolfram Web Resource, "http://mathworld.wolfram.com/NoncentralChi-SquaredDistribution.html"

[Wie'00] Wiesmann, R.; Bleck, O.; Heppner, H., "Cost effective performance monitoring in WDM systems", in Proc. Optical Fiber Commun. Conf. (OFC) 2000 ,Volume: 2 , 7-10, pp:171 - 173, March 2000

[Wra'02] Wrage, M.; Wolf, M.; Neuhauser, R. E.; Spalter, S.; Lanki, B.; "Optical Performance Monitoring by Electrical Amplitude Sampling in Transparent Optical Networks", Networks & Optical Communications (NOC) 2002, A75Wrage.

[Yad'98] Yadlowsky, M.J.; da Silva, V.L.; "Experimental comparison of the effect of discrete and distributed path inband crosstalk on system performance: application to predicting system performance penalties", J. Lightwave Tech., Volume 16, Issue 10, Oct. 1998 pp:1813 - 1821

[Yoo'95] Tae Whan Yoo; Jae Ho Song; Moon Soo Park; Chang Sup Shim; "A novel clock extraction circuit using a new NRZ-to-PRZ converter and a dielectric resonator filter for 10 Gbit/s optical receiver", in Proc. IEEE MTT-S Inter. Microwave Symposium Digest, 16-20 May 1995 pp:1395 - 1398 vol.3

[Yuq'02] Qian Yu; Zhongqi Pan; Lian-Shan Yan; Willner, A.E.; "Chromatic dispersion monitoring technique using sideband optical filtering and clock phase-shift detection", J. Lightwave Tech.. Vol.20 No12, December 2002, pp: 2267- 2271

[Yur'96] Yu, R.; Pierson, R.; Zampardi, P.; Runge, K.; Campana, A.; Meeker, .; Wang, K.C.; Petersen, A.; Bowers, J.; "Packaged clock recovery integrated circuits for 40 Gbit/s optical communication links", in Proc. Gallium Arsenide Integrated Circuit (GaAs IC) Symposium, 3-6 Nov. 1996 pp:129 - 132